

ADVANCED STEEL CONSTRUCTION

An International Journal

Volume 21 Number 5

October 2025

CONTENTS

Technical Papers

Study on Flexural Performance of New Thin-Walled U-Beam-Wood H-Section Combination Beams

Chang Wu, Dong-Dong Ma, Zhi-Jiang Zhao, Ren-Jun Fang and Yie-Gong Xu

Optimal Design and Construction of A Steel Arched Pedestrian Bridge with Structural Enhancement Using UHPC Encasement

Canh-Tuan Nguyen

Design of Single Post-Installed Steel Screw Anchor: A Nomogram Model and Reassessment of Eurocode 2 Part 4

Ng Lieu Thai, Daniel Looi Ting Wee, Jessey Lee, Adeline Ng Ling Ying and S S Ajeesh

Study on the Axial Compression Performance of Concrete Filled Circular Aluminum Alloy Tubular Column with Built-In Hollow Steel Tube

Zheng-Tao Zhang, Bing Li and Zhou Bo

Load-Slip Behavior of Perfobond Shear Connectors Post Hydrochloric Acid Corrosion on Bearing Capacity

Fan Yang, Wen-Jing Qiao, Ting-Kun Zhou, Yun-Long Li, Zhi-Dan Ruan and Shou-Fu Li

Experimental Research on Mechanical Performance of Cold-Formed Thin-Wall Fabricated Rack Columns

Yan-Bo Qu, Gan Tang, Ling-Feng Yin and Ren-Yi Shi

Seismic Performance of Pu-Pai Fang-Dovetail Tenon Joints with Varying Loosening Degrees Reinforced by Steel Sleeve Clamp Hoops

Sen-Long Tan, Yun-Peng Chu, Yao-Peng Liu, Jia-Hao Wang, Si-Qi Wang, Zheng Zhang and Bo Si

Experimental and Numerical Study on Connection Joints Applied to Automatic Construction Device

Xian-Feng Wang, Qian-Xi Zhang, Zhi-Peng Fu, Wei-Lun Wang, Jian Liu, Xiao-Gang Zhang and Shan-Bai Dong

Copyright © 2025 by :

The Hong Kong Institute of Steel Construction

Website: <http://www.hkisc.org>

ISSN 1816-112X

Science Citation Index Expanded, Materials Science Citation Index and ISI Alerting

Cover: Greater Bay Area Cultural and Sports Center, China. Photo@ Li Hua-Bo

e-copy of IJASC is free to download at "www.ascjournal.com" in internet and mobile apps.

ADVANCED STEEL CONSTRUCTION

VOL.21, NO.5 (2025)

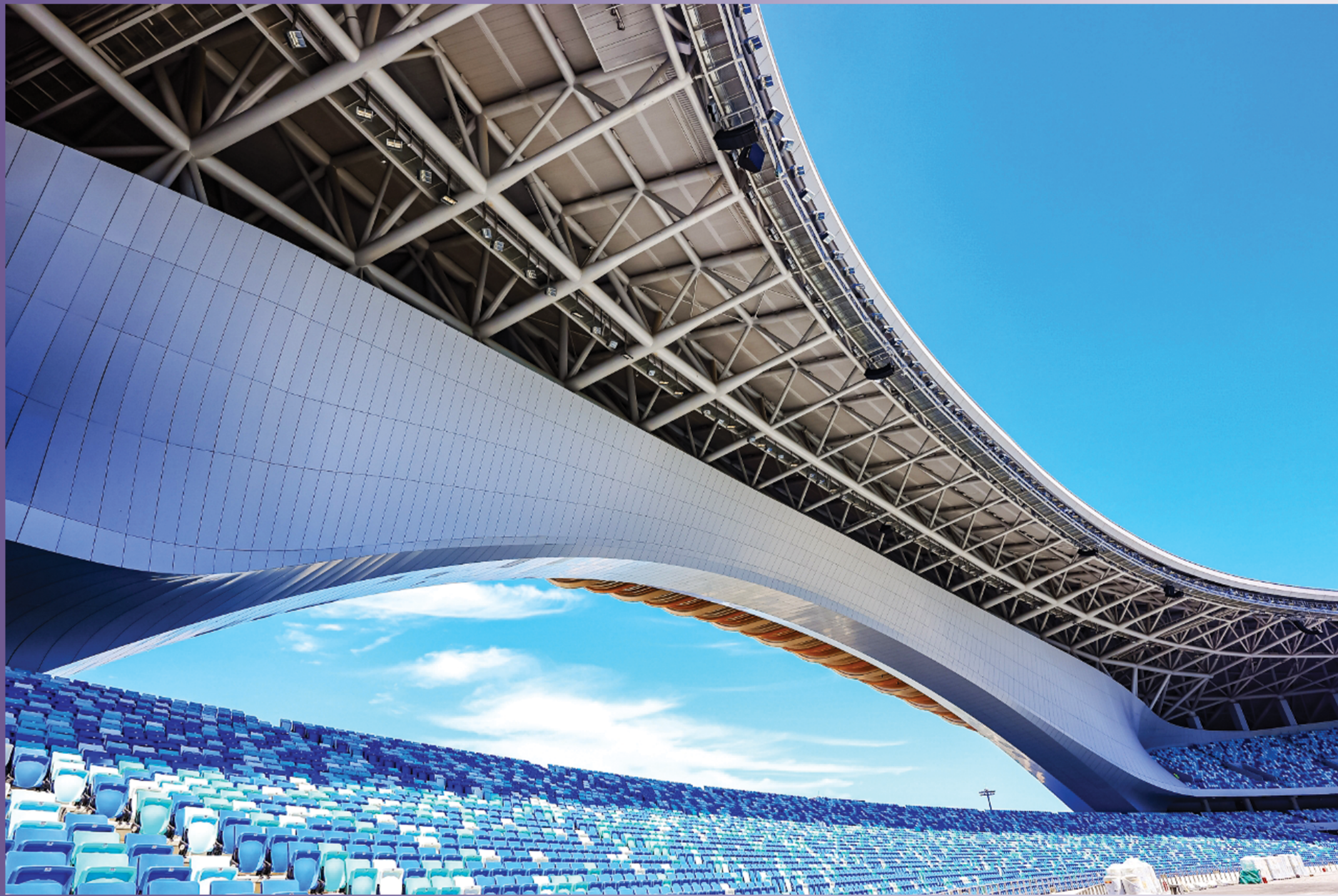
ADVANCED STEEL CONSTRUCTION

an International Journal

ISSN 1816-112X

Volume 21 Number 5

October 2025



Editors-in-Chief

S.L. Chan, South China University of Technology, China

W.F. Chen, University of Hawaii at Manoa, USA

R. Zandonini, Trento University, Italy



ISSN 1816-112X

Science Citation Index Expanded,
Materials Science Citation Index
and ISI Alerting

EDITORS-IN-CHIEF

**Asian Pacific, African
and organizing Editor**
S.L. Chan
South China University of Technology, China

American Editor
W.F. Chen
Univ. of Hawaii at Manoa, USA

European Editor
R. Zandonini
Trento Univ., Italy

ASSOCIATE EDITORS

Y.P. Liu
South China University of Technology, China

S.W. Liu
The Hong Kong Polyt. Univ., Hong Kong, China

INTERNATIONAL EDITORIAL BOARD

F.G. Albermani
Central Queensland Univ., Australia

I. Burgess
Univ. of Sheffield, UK

F.S.K. Bijlaard
Delft Univ. of Technology, The Netherlands

M.A. Bradford
The Univ. of New South Wales, Australia

D. Camotim
Technical Univ. of Lisbon, Portugal

C.M. Chan
Hong Kong Univ. of Science & Technology, Hong Kong, China

T.H.T. Chan
Queensland Univ. of Technology, Australia

T.M. Chan
The Univ. of Hong Kong, Hong Kong, China

Z.H. Chen
Tianjin Univ., China

S.P. Chiew
Nanyang Technological Univ., Singapore

G.G. Deierlein
Stanford Univ., California, USA

L. Dezi
Univ. of Ancona, Italy

D. Dubina
The Politehnica Univ. of Timisoara, Romania

R. Greiner
Technical Univ. of Graz, Austria

L. Gardner
Imperial College of Science, Technology and Medicine, UK

Y. Goto
Nagoya Institute of Technology, Japan

L.H. Han
Tsinghua Univ. China

S. Herion
University of Karlsruhe, Germany

G.W.M. Ho
Ove Arup & Partners Hong Kong Ltd., Hong Kong, China

Todd A. Helwig
University of Texas at Austin, USA

B.A. Izzuddin
Imperial College of Science, Technology and Medicine, UK

J.P. Jaspart
Univ. of Liege, Belgium

S. A. Jayachandran
IIT Madras, Chennai, India

S.E. Kim
Sejong Univ., South Korea

S. Kitipornchai
The Univ., of Queensland, Australia

D. Lam
Univ. of Bradford, UK

H.F. Lam
City Univ. of Hong Kong, Hong Kong, China

G.C. Li
Shenyang Jianzhu Univ., China

G.Q. Li
Tongji Univ., China

J.Y.R. Liew
National Univ. of Singapore, Singapore

E.M. Lui
Syracuse Univ., USA

Y.L. Mo
Univ. of Houston, USA

J.P. Muzeau
CUST, Clermont Ferrand, France

D.A. Nethercot
Imperial College of Science, Technology and Medicine, UK

Y.Q. Ni
The Hong Kong Polyt. Univ., Hong Kong, China

D.J. Oehlers
The Univ. of Adelaide, Australia

J.L. Peng
Yunlin Uni. of Science & Technology, Taiwan, China

K. Rasmussen
The Univ. of Sydney, Australia

J.M. Rotter
The Univ. of Edinburgh, UK

C. Scawthorn
Scawthorn Porter Associates, USA

P. Schaumann
Univ. of Hannover, Germany

Y.J. Shi
Tsinghua Univ., China

G.P. Shu
Southeast Univ. China

L. Simões da Silva
Department of Civil Engineering, University of Coimbra, Portugal

G. Shi
Tsinghua Univ., China

J.G. Teng
The Hong Kong Polyt. Univ., Hong Kong, China

G.S. Tong
Zhejiang Univ., China

K.C. Tsai
National Taiwan Univ., Taiwan, China

C.M. Uang
Univ. of California, USA

B. Uy
University of Western Sydney, Australia

M. Veljkovic
Univ. of Lulea, Sweden

F. Wald
Czech Technical Univ. in Prague, Czech

Y.C. Wang
The Univ. of Manchester, UK

B. Wu
South China University of Technology, China

Y.B. Wang
Tongji Univ., China

D. White
Georgia Institute of Technology, USA

Y.L. Xu
Southwest Jiaotong University, China

E. Yamaguchi
Kyushu Institute of Technology, Japan

Y.B. Yang
National Taiwan Univ., Taiwan, China

Y.Y. Yang
China Academy of Building Research, Beijing, China

B. Young
The Hong Kong Polyt. Univ., Hong Kong, China

X.L. Zhao
The Hong Kong Polyt. Univ., Hong Kong, China

X.H. Zhou
Chongqing University, China

S.Y. Zhu
The Hong Kong Polyt. Univ., Hong Kong, China

R.D. Ziemian
Bucknell Univ., USA

J.X. Zhao
South China University of Technology, China

General Information

Advanced Steel Construction, an international journal

Aims and scope

The International Journal of Advanced Steel Construction provides a platform for the publication and rapid dissemination of original and up-to-date research and technological developments in steel construction, design and analysis. Scope of research papers published in this journal includes but is not limited to theoretical and experimental research on elements, assemblages, systems, material, design philosophy and codification, standards, fabrication, projects of innovative nature and computer techniques. The journal is specifically tailored to channel the exchange of technological know-how between researchers and practitioners. Contributions from all aspects related to the recent developments of advanced steel construction are welcome.

Disclaimer. No responsibility is assumed for any injury and / or damage to persons or property as a matter of products liability, negligence or otherwise, or from any use or operation of any methods, products, instructions or ideas contained in the material herein.

Subscription inquiries and change of address. Address all subscription inquiries and correspondence to Member Records, IJASC. Notify an address change as soon as possible. All communications should include both old and new addresses with zip codes and be accompanied by a mailing label from a recent issue. Allow six weeks for all changes to become effective.

The Hong Kong Institute of Steel Construction

HKISC

c/o Prof. SL Chan,

Unit 209B, Photonics Centre, No. 2 Science Park East Avenue,

Hong Kong Science Park, Shatin, N.T., Hong Kong, China.

Tel: 852- 3595 6150 Fax: 852- 3619 7238

Email: ceslchan@connect.polyu.hk Website: <http://www.hkisc.org/>

ISSN 1816-112X

Science Citation Index Expanded, Materials Science Citation Index and ISI Alerting

Copyright © 2025 by:

The Hong Kong Institute of Steel Construction.



ISSN 1816-112X

Science Citation Index Expanded,
Materials Science Citation Index and
ISI Alerting

EDITORS-IN-CHIEF

Asian Pacific, African and organizing Editor

S.L. Chan

*South China University of
Technology, China*

Email: ceslchan@scut.edu.cn

American Editor

W.F. Chen

Univ. of Hawaii at Manoa, USA

Email: waifah@hawaii.edu

European Editor

R. Zandonini

Trento Univ., Italy

Email: riccardo.zandonini@ing.unitn.it

Advanced Steel Construction

an international journal

VOLUME 21 NUMBER 5

October 2025

Technical Papers

Study on Flexural Performance of New Thin-Walled U-Beam-Wood H-Section Combination Beams 367

Chang Wu, Dong-Dong Ma, Zhi-Jiang Zhao, Ren-Jun Fang and Yie-Gong Xu*

Optimal Design and Construction of A Steel Arched Pedestrian Bridge with Structural Enhancement Using UHPC Encasement 380

*Canh-Tuan Nguyen**

Design of Single Post-Installed Steel Screw Anchor: A Nomogram Model and Reassessment of Eurocode 2 Part 4 390

Ng Lieu Thai, Daniel Looi Ting Wee, Jesse Lee, Adeline Ng Ling Ying and S S Ajeesh*

Study on the Axial Compression Performance of Concrete Filled Circular Aluminum Alloy Tubular Column with Built-In Hollow Steel Tube 413

*Zheng-Tao Zhang, Bing Li and Zhou Bo **

Load-Slip Behavior of Perfobond Shear Connectors Post Hydrochloric Acid Corrosion on Bearing Capacity 425

Fan Yang, Wen-Jing Qiao, Ting-Kun Zhou, Yun-Long Li, Zhi-Dan Ruan and Shou-Fu Li*

Experimental Research on Mechanical Performance of Cold-Formed Thin-Wall Fabricated Rack Columns 436

Yan-Bo Qu, Gan Tang, Ling-Feng Yin and Ren-Yi Shi*

Seismic Performance of Pu-Pai Fang-Dovetail Tenon Joints with Varying Loosening Degrees Reinforced by Steel Sleeve Clamp Hoops 448

Sen-Long Tan, Yun-Peng Chu, Yao-Peng Liu, Jia-Hao Wang, Si-Qi Wang, Zheng Zhang and Bo Si*

Experimental and Numerical Study on Connection Joints Applied to Automatic Construction Device 458

Xian-Feng Wang, Qian-Xi Zhang, Zhi-Peng Fu, Wei-Lun Wang, Jian Liu, Xiao-Gang Zhang and Shan-Bai Dong*

STUDY ON FLEXURAL PERFORMANCE OF NEW THIN-WALLED U-BEAM-WOOD H-SECTION COMBINATION BEAMS

Chang Wu ^{1,2}, Dong-Dong Ma ^{1,*}, Zhi-Jiang Zhao ¹, Ren-Jun Fang ¹ and Yie-Gong Xu ¹

¹ School of Civil Engineering, Lanzhou University of Technology, Lanzhou 730050, China

² Western Center of Disaster Mitigation in Civil Engineering of Ministry of Education, Lanzhou University of Technology, Lanzhou 730050, China

* (Corresponding author: E-mail: 3175275739@qq.com)

ABSTRACT

This study focuses on the analysis of combining the advantages of steel and wood. And then, we propose a new thin-walled H-section steel-wood combination beam, which is connected by a mixture of epoxy resin adhesive and self-tapping screws. In this paper, the bending capacity test is carried out on 7 steel-wood combination beams with the screw spacing, steel profile thickness, web height, and flange board thickness as the influencing factors, and analyze by finite element software modeling. The results show, that the overall performance of the combined beams is good, and the final failure mode of the combined beams is typical bending tensile damage with the tensile cracking of the planks on the tensile side. The change of self-tapping screw spacing on the flange of the combined beam has no obvious influence on the bending load capacity. The increase in the thickness of the flange plank, the thickness of the thin-walled steel section, and the height of the web of the combined beam has a significant increase in the bending load capacity. The adopted finite element model is reasonable and effective, and the calculation results are in good agreement with the test results.

ARTICLE HISTORY

Received: 22 November 2024
Revised: 4 January 2025
Accepted: 8 January 2025

KEYWORDS

Combined steel-wood beams;
Flexural load capacity tests;
Damage mechanisms;
Finite element simulations

Copyright © 2025 by The Hong Kong Institute of Steel Construction. All rights reserved.

1. Introduction

Wood can be recycled many times, which is representative of environmentally reusable building materials. Its processing is convenient and can also be assembled in the field construction. Steel has high strength, good plasticity, and toughness properties. When connecting with different materials or components, it can be connected by bolts, rivets, and other strong and reliable connections. It is a kind of economic, sustainable development of environmentally friendly building materials. Cold-formed thin-walled steel[1-2] is used as a 1.5mm~5mm thin steel plate in the cold state directly bent and processed into a variety of cross-sectional shapes of the steel. However, due to the thin wall thickness, high strength of large cross-sectional openings, and other characteristics, thin-walled steel is prone to instability when subjected to pressure or bending. Steel-wood combination structure combines the good performance of the two, can let them bear the load together, through different ways of combining can play the role of different materials in the structure.

Therefore, scholars at home and abroad began to study the use of wood in combination with steel or other materials to form a combination of members. Shen Yan[3] conducted three sets of tests using three different connections to investigate the full range of behavior of steel beam-column connections. After performing a number of tests, it was found that the variability stems from random changes in geometry and material properties. Guzman[4] had analyzed space lattices with triangular and rectangular cross sections, obtaining a continuous representation model from the energy approach, as well as modeling the lattice as an equivalent property for beams and columns. The results allow us to establish the excellent performance of the equivalent properties obtained for each lattice pattern considered. With the advantage of low computational costs involved in implementation, modeling and processing, a point that deserves more research. Linjie Tian[5] was developed analytical and numerical models for predicting the LTB (The lateral torsional buckling) strength of I-beams arranged by different numbers of lateral braces. And they subjected to two movable concentrated loads during the pre-bending phase. An improved Rayleigh-Ritz method was proposed based on the confinement effect of neighboring beam segments. It was used for parameter selection and LTB strength prediction in the pre-bending stage of steel I-beams, providing a theoretical basis for research in this direction. Haixu Yang[6] studied a new type of cold-formed thin-walled steel and glued laminated timber combination of box girders, the composite beams exhibit higher shear strength than a steel or timber beam. Exploring the effect of parameters on the shear capacity of combined beams, where the shear span ratio has the greatest effect on the shear capacity of combined beams. In the steel skeleton in the form of a box-shaped combination of the cross-sectional shear stiffness does not change much. But shear load carrying capacity than the "I" shaped combination form by 12%. E. McConnell[7], used a series of four-point bending tests that were conducted, under service loads and to failure, found that the stiffness and

bending properties of prestressed tendon-wood composite beams were greatly improved compared with pure glued-laminated timber beams, and the effect of load-carrying capacity improvement was significant. Marco Corradi[8], applied in the region where tensile stresses, with significant cost-savings and higher characteristics in term of "minimum intervention". The improvement of the bending capacity of timber beams under static loads was reinforced with FRP [9-11]. There was a significant improvement in the bending performance of wooden beams under FRP. It was analyzed that imperfections such as cracks and knots in wood beams can make them deform and crack prematurely during the stressing process. He[12], used a general theoretical model considering the typical tensile failure mode, found that the reinforced glulam beams are featured with relatively ductile bending failure, compared to the brittle tensile failure of the unreinforced ones. Hassanieh[13], empirical formulas and load-slip for corrected orthotropic anisotropic glued timber (CLT)-steel composite nodes were obtained by performing indoor pushover tests on CLT-steel-CLT specimens. Wang[14], proposed an approach to improve the bending capacity of wood beams under static loads through the use of self-tapping screws across the beam inclined and staggered along the longitudinal axis of the beam for steel-wood composite connection members. It was shown that the screws have a significant effect on the shear capacity of the members when driven into them at different angles and that they reduce the resisting stiffness. Chiniforush[15], numerical simulation of long-term performance of steel-wood composite structural beams under sustained loading, the results of parametric studies suggest a creep coefficient of 0.35 for 50-years' design life of STC beams. Zhao[16], by three groups of four-point bending tests and finite element simulations, increasing the number of hybrid-anchored screws can significantly improved the slip stiffness of the connection interface of STC beams and reduce the slip. Song[17], proposed a wood-steel tube composite beam consisting of wood and cold-formed thin-walled rectangular steel. The experiments showed that the epoxy adhesive connection alone had better deformation capacity and load-carrying capacity compared to the beam connected by a composite of screws and epoxy adhesive.

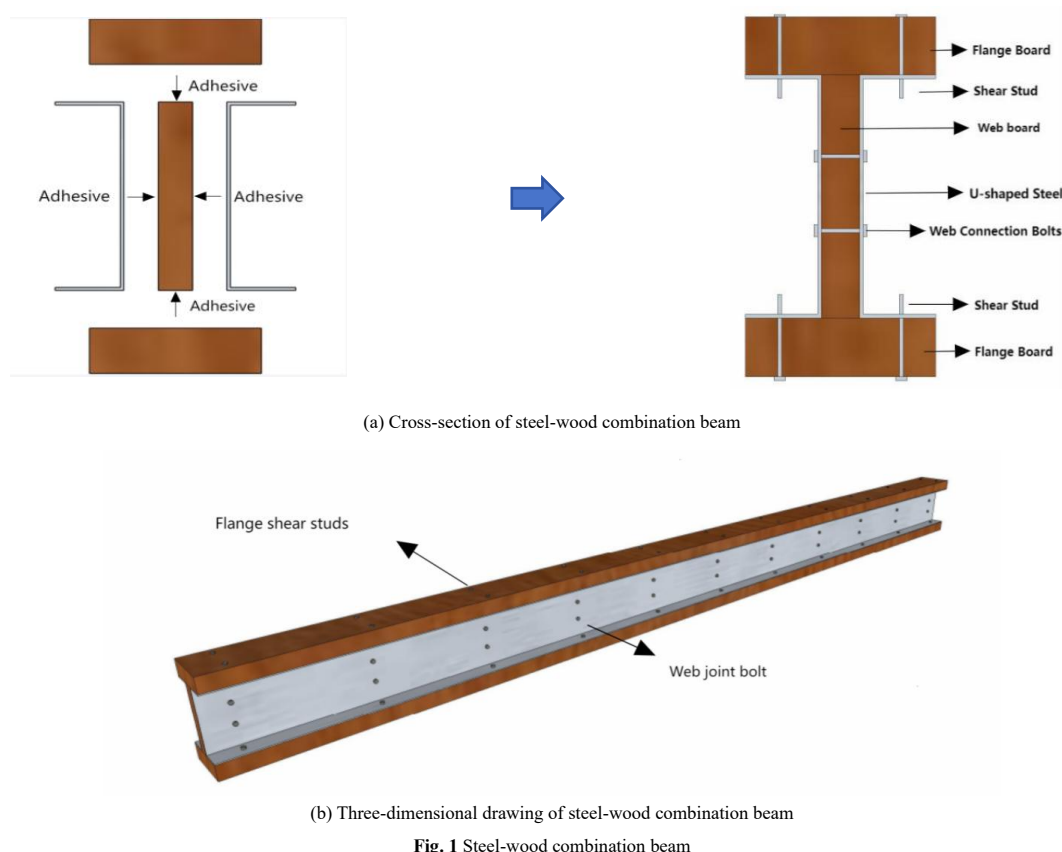
Li[18] found that for every 200% increase in glued wood section, the flexural capacity of the composite beam increased by 16.08%-20.70%, and for a 50% increase in steel thickness, the flexural capacity of the composite beam increased by 33.73%-37.69%. The overall performance of the H-beam larch composite beam was good. Duan[19], three hot-rolled H-beam-larch composite beams and one pure steel beam were tested for bending capacity, found that bonding wood panels to both sides of the steel beam web could increase the load capacity, and the shape of the member was more reasonable and effective. R[20] three hot-rolled H-beam-larch composite beams and one pure steel beam were tested for bending capacity, showed a "two-hinge" yielding mode for all the specimens considered and found that the bolted connection was lower than the self-tapping screw connection in terms of stiffness and ductility. Chen[21] used a four-point bending test to measure

the bending performance of steel-wood composite I-beams under various connection methods, showed that compared to steel-concrete structures, steel-wood hybrid structures have a good performance in terms of flexural load-carrying capacity. Structures, steel-wood hybrid structures have shorter construction times and good seismic performance.

Duan[22] proposed a kind of combined beam with an I-beam cross-section by bonding wood plates at the upper and lower flanges of H-shaped steel, which proved that the combined effect of steel-wood combined beam was significant, the overall synergistic stress performance was good, and the final damage mode of the member was the fracture of wood at the lower flange. Liu Degui[23] designed the thin-walled H-shaped steel wrapped around the wood plate combination beam, compared with pure wood beam combination beam ductility, section stiffness, and bending performance in the presence of steel are greatly increased.

Based on domestic and foreign scholars[24-25] for steel-wood combination beam cross-section combination form, a combination of

connection and force performance[26-29] and other research. This paper proposes two back-to-back and stands U-beams as the skeleton, in the middle of the U-beam, a plank, steel plate, and plank using epoxy resin AB glue[30-32] to combine the initial formation of the steel—wood combination body. Next, in the formation of the combination of the skeleton flange on the superior and lower sides. Respectively, with the structural bonding agent two wooden plates are bonded to form an H-shaped cross-section. Then self-tapping screws and bolts are driven into the flange and web respectively to form a steel-wood combination beam as shown in Fig. 1. To verify the reasonableness of the designed combined beam, the three-point bending test is carried out on the combined beam. The parameters such as self-tapping screw spacing, profile thickness, web height, and flange board thickness of the combined beam are used to study the flexural load capacity of the combined beam. The corresponding finite element simulation analysis is carried out to verify its reasonableness by comparing numerical simulation and test.



2. Test overview

2.1. Specimen design

This test will design 7 thin-walled H-shaped steel-wood combination beams (Specific parameters are shown in Table 1) for bending capacity test, the test to the combination of beam cross-section dimensions like width and

height, shear connectors spacing, and the combination of beam steel plate thickness as a parameter to start. Seven thin-walled H-shaped steel-wood combination beam specimens numbered L-1 to L-7. The combination of beams are 2.5m in length and the calculation of the span of 2.3m. Study the damage process, damage characteristics, and failure modes of the combined beams.

Table 1
Specific parameters of thin-walled H-shaped steel-wood combination beams

Serial number	Plate thickness(mm)	Steel thickness(mm)	Section dimensions of steel	Pitch of	Combined beam cross-section
L-1	30	1.5	30×125×30	240	80×185×80
L-2	30	1.5	40×125×40	240	100×185×100
L-3	30	1.5	40×125×40	180	100×185×100
L-4	30	1.5	40×125×40	120	100×185×100
L-5	30	2.0	40×125×40	120	100×185×100
L-6	40	1.5	40×125×40	120	100×205×100
L-7	30	1.5	40×165×40	120	100×225×100

Note: The thickness of the test beam web planks are 20mm, the axial spacing of the web connecting bolts are 240mm and the height direction spacing is half of the height of the web; the cross-section size of the steel section is the size of the outer edge of the U-type steel plate.

2.2. Specimen production

Timber: Choose Douglas fir timber, the surface of the timber is flat, and no prominent defects or other phenomena. **Steel:** use Q 235 thin-walled steel, through cold processing into the required U-shaped steel size. **Binder** (two-component epoxy resin glue): E44 two-component AB epoxy resin glue is used. **Connectors:** bolts with a diameter of 5mm and a length of 35mm (M5×35mm), countersunk head self-tapping screws with a diameter of 5mm and a length of 50mm (M5×50mm). **Step 1:** Make the timber boards and galvanized thin-walled steel plates needed for the combination beam for the test to the required size. **Step 2:** The surfaces of the timber and thin-walled steel profiles to be sanded were leveled and smoothed. Then wipe off the dust from the surface of the wood. **Step 3:** Apply the structural adhesive on the surface of steel and wood and maintain the combined beam specimen. **Step 4:** After the maintenance retains a certain strength, in the combination of beams on the upper and lower flange according to the design spacing into the self-tapping screws, in the web according to the design spacing holes and tighten the bolts. At this point, the whole steel-wood combination beam specimen production is completed. The complete specimen of the combined beam is shown in Fig. 2.



Fig. 2 Finished steel-wood combination beam member

2.3. Mechanical properties test of epoxy resin adhesive

2.3.1. Determination of modulus of elasticity, tensile strength

The modulus of elasticity and tensile strength of the epoxy resin AB adhesive material used in the test were determined as follows. The dimensions were designed in accordance with the General Principles of Test Methods for Properties of Resin Casting Bodies (GB/T 2567-2008) and Test Methods for Tensile Properties of Resin Casting Bodies (GB/T 2568-2008). The production requires mixing the two at 1:1 and pouring them into the mold when uncured. At room temperature 25°, leave for 2 days to fully cure, during which time it should not be moved.

The tensile strength of epoxy resin AB adhesive is calculated according to eq. 1:

$$\sigma_t = \frac{F}{bh} \quad (1)$$

Where, σ_t is tensile strength of epoxy resin AB adhesive, units is MPa; F is destructive load, units is kN; b is width of the specimen, units is mm; h is thickness of the specimen, units is mm.

The modulus of elasticity of the epoxy resin AB adhesive is calculated by eq. 2:

$$E = \frac{Fl}{A\Delta l} \quad (2)$$

Where, E is modulus of elasticity of epoxy resin AB adhesive, units is MPa; F is destructive load, units is kN; A is cross-sectional area of the specimen, units is mm^2 ; l is original length of the specimen, units is mm; Δl is elongation of the specimen, units is mm.

As shown in Table 2, the average tensile strength of the epoxy resin adhesive was calculated to be 14.99 MPa and the modulus of elasticity was 1110 MPa.

Table 2
Test results of epoxy resin adhesive specimens

Specimen Number	Thickness (mm)	Breaking Load (kN)	Tensile Strength (MPa)	Average Tensile Strength (MPa)	Modulus Of Elasticity (MPa)
1	5.1	0.76	15.21		
2	4.9	0.55	11.22		
3	4.8	0.64	13.33		
4	4.6	0.93	20.22		
5	4.7	0.70	14.89	14.99	1110
6	5.0	0.75	15.00		
7	5.1	0.73	14.31		
8	4.9	0.72	14.69		
9	4.8	0.77	16.04		

2.3.2. Epoxy resin adhesive load-displacement curve

The load-displacement curve relationship of the epoxy resin adhesive specimen is shown in Fig. 3. From the load-displacement curve, it can be seen that the curve shows a linear relationship. The damage of the epoxy resin specimen is sudden brittle damage and the yield point before fracture is not obvious. After fracture, the bearing capacity will drop to 0. From the test, it can be seen that the epoxy resin adhesive belongs to the brittle material.

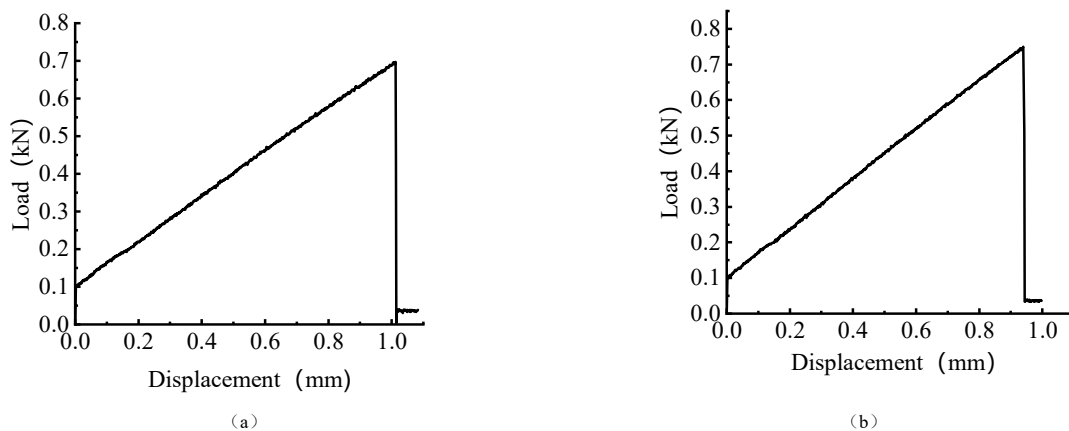


Fig. 3 Load-displacement graphs

2.4. Determination of material mechanical properties

2.4.1. Adjustment of wood parameters considering defects

Wood is an anisotropic material, and defects are not obvious in the small sizes of specimens used in wood properties tests, but are inevitable in full-size

specimens. Timber material defects will produce uncertainty in the use of structural safety, the need to reduce the timber parameters. The main factors affecting the discount factor are natural defects in the specimen (knots, insects, cracks, etc.), long-term loading, drying defects (drying inhomogeneity), dimensional effects. Reduction factor reference Eq. 3:

$$K_Q = K_{Q1}K_{Q2}K_{Q3}K_{Q4} \quad (3)$$

Where, K_{Q1} is influence coefficient of natural defects in wood; K_{Q2} is influence coefficient of drying defects of wood; K_{Q3} is influence coefficient of long-term loading strength of wood; K_{Q4} is influence coefficient of dimensions of wood. The reduction coefficient for different impact factors are shown in the table 3.

Table 3
Reduction coefficient for different impact factors

Stress State Of Wood	Compressive Strength Of Smooth Grain	Parallel Grain Tensile Strength	Bending Strength
Effects Of Natural Wood Defects K_{Q1}	0.66	0.80	0.75
Effects Of Wood Drying Defects K_{Q2}	0.90	—	0.85
Long-Term Load Strength Effects K_{Q3}	1.0	1.0	1.0
Wood Size Effects K_{Q4}	0.75	—	0.89
Discount Factor K_Q	0.446	0.80	0.567

Note: This factor is 1.0, because the wood used in this test was new and not subjected to long-term loading.

Due to the wood itself defects and volume effect will have an impact on the mechanical properties, wood damage belongs to the empirical judgment, the discount factor is taken as 0.6 for discounting. The test results of wood material properties after discounting are shown in Table 4:

Table 4
Mechanical parameters of wood

Wood	Parallel-To-Grain Compressive Strength /MPa	Tensile Strength Parallel to Grain /MPa	Flexure Strength /MPa	Elastic Modulus /MPa
Douglas Fir	34.18	50.96	36.08	10290

2.4.2. Mechanical parameters of thin-walled steel

The ultimate strength and yield strength of the specimen are calculated as shown in eq. 4. Where, σ is yield strength and ultimate strength of the specimen, units is MPa; F yield load and ultimate load of the specimen, units is kN; A is section area of the specimen, units is mm^2 .

$$\sigma = \frac{F}{A} \quad (4)$$

The modulus of elasticity for the design is shown in equ. 5. Where, E is modulus of elasticity of the specimen, units is MPa; F is the specimen is subjected to axial tension, units is kN; l is original scale distance of the specimen, units is mm; A is the cross-sectional area of the specimen, units is; Δl is elongation of the specimen, units is mm.

$$E = \frac{Fl}{A\Delta l} \quad (5)$$

According to the relevant data of the specimen automatically collected by the computer, the load-displacement curve of the specimen is drawn, as shown in Fig.4 and Fig.5. Then the obtained data are substituted into equ. 4 to calculate the strength of the specimen. The relevant data are substituted into equ. 5 to calculate the modulus of elasticity of the specimen. The calculation results are shown in Table 5.

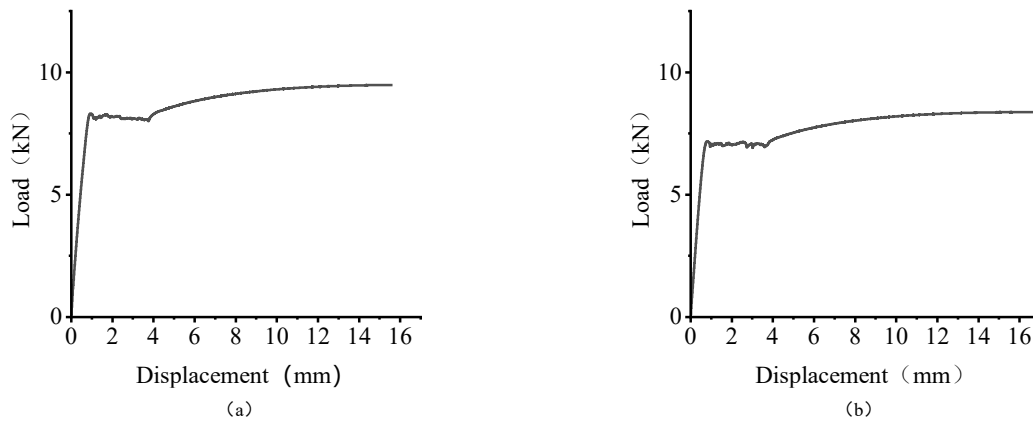


Fig. 4 Load-displacement curve of 1.5mm thick Q235 thin-walled steel section

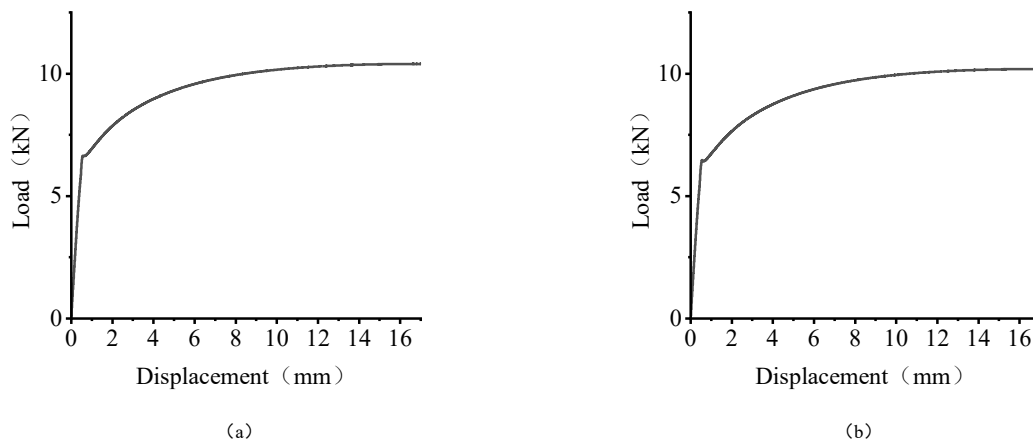


Fig. 5 Load-displacement curve of 2mm thick Q235 thin-walled steel section

Table 5
Mechanical parameters of thin-walled steel

Thicknesses (mm)	Serial Number	Yield Strength (MPa)	Average Yield Strength (MPa)	Ultimate Yensile Strength (MPa)	Average Limit Tensile Strength (MPa)	Modulus Of Elasticity (MPa)
1.5	1	278.67	272.00	318.24	311.64	2.03×10^5
1.5	2	283.00		321.16		
1.5	3	289.33		331.34		
1.5	4	265.33		303.09		
1.5	5	277.00		316.12		
1.5	6	238.67		279.86		
2	1	253.06	256.85	346.62	360.15	1.99×10^5
2	2	260.69		365.50		
2	3	254.87		357.45		
2	4	260.01		365.31		
2	5	247.43		361.34		
2	6	265.02		364.66		

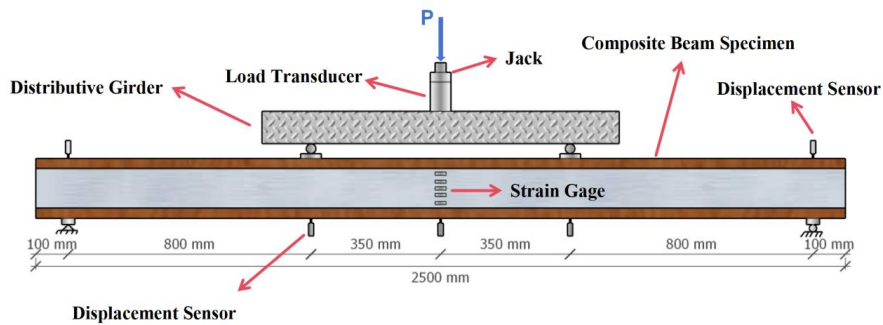
Materiality test data, the average yield strength of Q235 steel 1.5mm thick is 272.00 MPa, the average yield strength of 2mm thick steel is 256.85 MPa. 1.5mm thick average ultimate tensile strength is 311.64 MPa, the average ultimate tensile strength of 2mm thick is 360.15 MPa. The average elasticity modulus is 2.03×10^5 MPa.

2.5. Test loading and determination

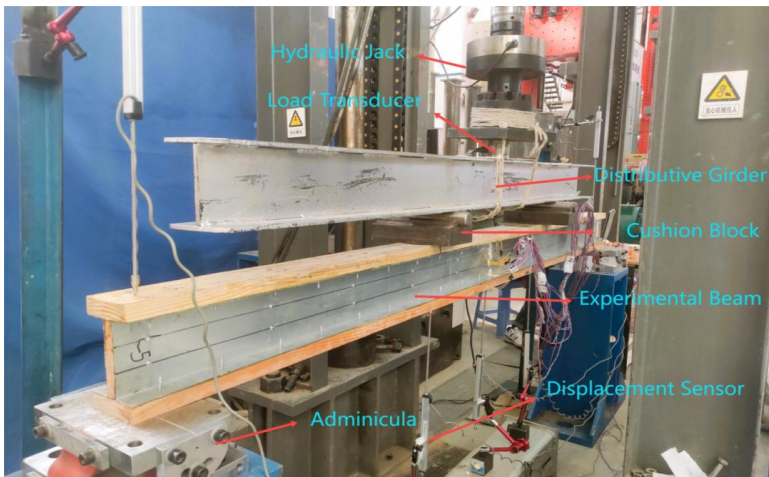
The thin-walled H-shaped steel-wood combination beam test belongs to the static loading test, and the bending loading test is performed on the supported beam specimen. The distribution beam support is 350mm in the span of the test beam. The combined beam test was carried out by displacement loading at a 1 mm/min speed. After loading a grade load, it was necessary to allow the load to act on the combined beam for about 3-5 minutes. Then the next load application after the value on the collector was stabilized, and the data collection was done by computer. However, it was necessary to

record the deformation state and the development of cracks in the test beams under different loads. During the loading process, pressure transducers are used to determine the load values, and displacement gauges are arranged in the span, crotch, and support of the combined beam to determine the vertical displacement of the beam. The load, displacement, and strain measurement points of the mid-span section are shown in Fig. 6. The combined beam test's loading program is divided into preloading and formal loading.

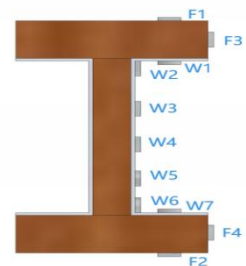
The devices and tools to be used in the combined beam test include: model YAW-2000 static hydraulic loading device to apply load to the member, model BZ1403 load cell to collect the load applied to the specimen, model 5G106 displacement transducer to collect the vertical deflection of the member, model DH3816N static collection system to collect the signal and output the data through the computer, computer to process the data, model 120-5AA and 120-3AA strain gauges, rulers, supports, reaction frame devices and so on. data, Model 120-5AA and 120-3AA strain gauges, rulers, supports, and reaction frame devices.



(a) Front elevation loading schematic



(b) Side elevation loading diagram



(c) Strain gauge arrangement

Fig. 6 Bending loading diagram of a combined beam

3. Test loading and damage process description

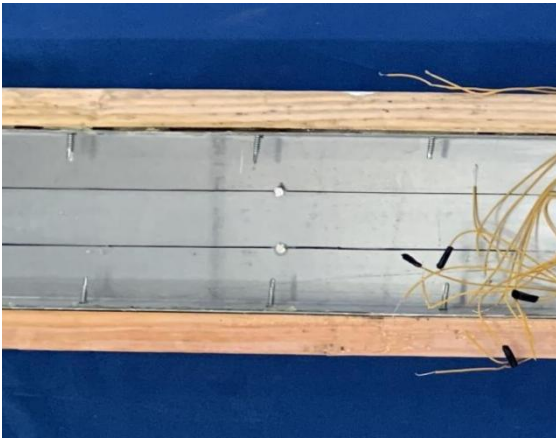
The damage process and damage form of the seven combined beams are similar. All of them are cracked by the structural adhesive between the steel and wood interface at the flange in the elastic stage. To the buckling of thin-walled steel at the flange in the elastic-plastic stage. Then the final destruction of wood at the lower flange to reach the destructive load of the damage process of cracking. The final damage pattern of the combined beam is a typical bending tensile damage. In this section, typical L-5 and L-6 specimens are selected as research objects to analyze the test phenomena.

3.1. L-5 combined beam

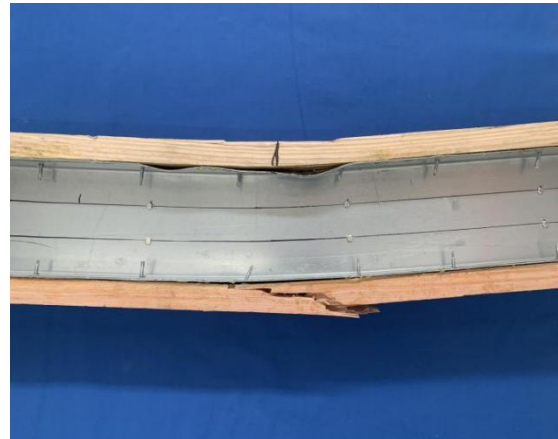
L-5 steel-wood beam specimen: Steel thickness specification is 2.0mm, the whole combination of beam cross-section dimensions of 100mm × 185mm × 100mm (width × height × width), and the wing self-tapping screws spacing is 120mm. The web bolts along the height of the web plate, three equal parts of the web plate along the length of the beam spacing of 240mm, the combination of the beam total length of 2500mm.

L-5 combination beam loading early, steel and wood are in the elastic stage. When the load increased to 17kN, the combination of beams occasionally issued a "click" the slight sound, observed and found that the

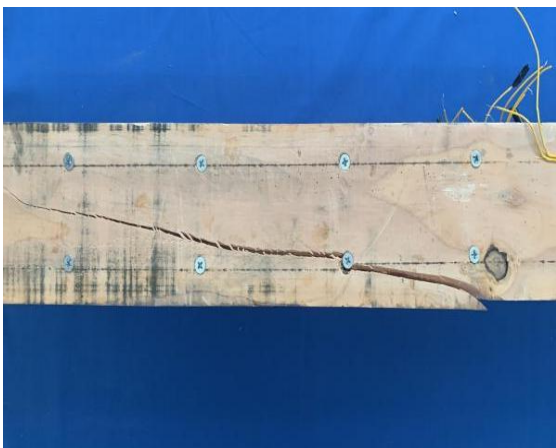
epoxy resin adhesive was not coated with a uniform cracking sound. With the increase in the load to 30 ~ 35kN, the occasional slight sound changes into a crunchy sound and becomes Intensive and increasingly large. Considering due to the force develops into large combined beam steel-wood connection glue cracking in large areas as shown in Fig. 7(a). When the load reaches 48kN, the combination of beams that appeared to the naked eye can be observed in the test phenomenon, spanning the upper and lower edge of the self-tapping screws by the shear tilt as shown in Fig. 7(b). The right side of the centralized loading point of the pressurized side of the thin-walled steel wing edge flexures outward bulge in the concentration of the loading point. Also accompanied by the pressurized area of the plank pressure deformation, planks, and steel sections have a greater separation. Load continues to increase to 54 ~ 63kN, the combination of beams spanning the three-point centralized load at the tensile side of the edge of the plank due to defects in its wood joints, first produced small cracks and then issued a "boom" sound, through the wood joints appear large cracks, and cracks along the beam width and length direction continue to extend, widening the formation of longer split cracks and transverse cracks as shown in Fig. 7(c) and Fig. 7(d). The transverse cracks are shown in Fig. 7(c) and Fig. 7(d). At this time, the load of the combined beam is no longer increased but can still withstand a certain load, and the damage test of the combined beam is declared to be finished.



(a) Adhesive mass cracking observed at the L-5 beam steel-to-wood connection



(b) Flange damage in the tensile zone of the L-5 beam and large separation of the planks and sections were observed



(c) Oblique shear damage of planks between self-tapping screws observed at L-5 beam webs



(d) Further destruction of the planks between the self-tapping screws along the smooth grain observed at the web of the L-5 beams

Fig. 7 L-5 Beam Failure Phenomenon

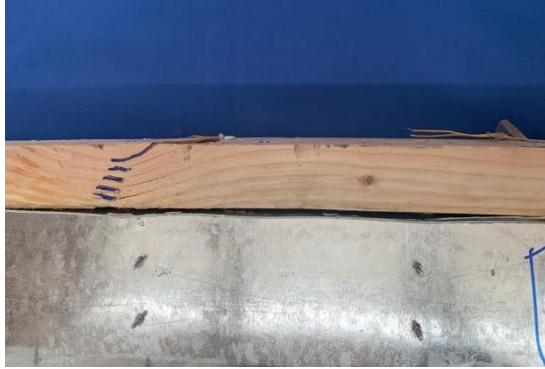
3.2. L-6 combined beam

L-6 steel-wood beam specimen: Steel thickness specification is 1.5mm, the whole combination of beam cross-section dimensions of 100mm × 205mm × 100mm (width × height × width). The wing self-tapping screw spacing is 120mm, the web bolts along the height of the web plate, three equal parts of the web plate along the length of the beam spacing of 240mm, and the combination of the beam total length of 2500mm.

L-6 combination beam loading initial, steel and wood are in the elastic

phase of the common force. When the load increased to 33 ~ 45kN, the combination of beams occasionally issued a "click" of the slight crunching sound and no traces of destruction. After observing the combination of beams for the steel and wood connection of the epoxy resin adhesive cracking ringing sound. With the increase in the load to 55kN, the combination of beams with the increase of load to 55kN. The combined beam made a continuous crunching sound and got bigger and bigger. At this time, due to the consideration of the force becomes a big combined beam steel-wood connection at the adhesive film layer peeling as shown in Fig. 8 (a). When the

load reached 72kN, the combined beam appeared obvious naked eye as observed in the test phenomenon. The upper and lower flange of the span of the self-tapping screws tilted in the shear. The middle of the span and the two concentrations of force loading point of the compression side of the adhesive layer peeling of thin-walled steel flanges in many places to the outward projection of the yielding of the flange as shown in Fig. 8 (b). Fig. 8 (b) showed that the three-point centralized loading point is also accompanied by the section steel web buckling outward buckling bulge as shown in Fig. 8 (c).



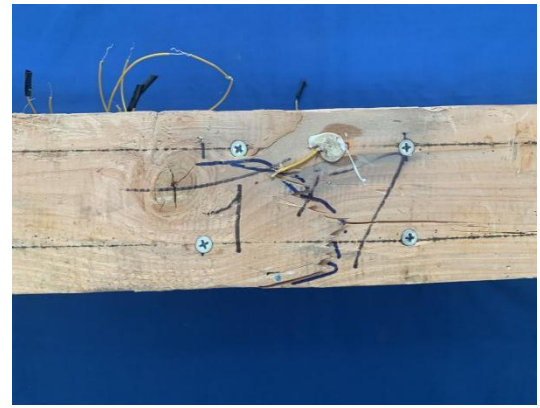
(a) Peeling of adhesive film layer observed at L-6 beams



(b) Buckling of the profile flange observed in the L-6 beam compression zone



(c) Buckling of the section web observed at the L-6 beam



(d) Cracking of planks along the width observed on the tension side of L-6 beams

Fig. 8 L-6 beam failure phenomenon

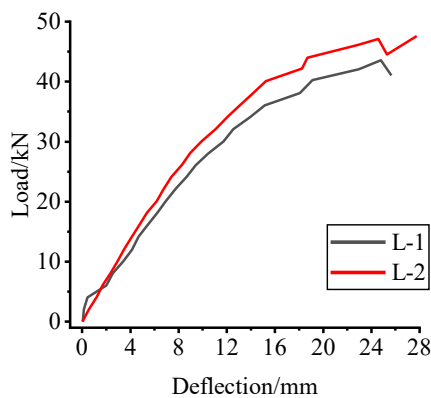


Fig. 9 Comparison of load-deflection curves

4. Results and analysis of test influencing factors

4.1. Influence of cross-section change of combined beam

4.1.1. Influence of flange width of combined beams

Member L-1 combined beam cross-section size of 80mm × 185mm × 80mm, L-2 combined beam cross-section size of 100mm × 185mm × 100mm. L-2 combined beam compared to the L-1 combined beam in other conditions are the same under the premise of the beam width changed to 100mm.

As shown in Fig. 9, by comparing the effect of different flange widths on

Load continues to increase to 88kN, the combination of beams on the right side of the loading point of the tensile side of the flange planks issued a "booming" loud sound, and crack along the width of the beam continues to extend. After widening to form a through crack, the crack extends along the length direction as shown in Fig. 8 (d). At this point, the load of the combined beam is no longer increased but still able to withstand a certain load. And the damage test of the combined beam is declared to be over.

the flexural capacity of the combined beams. From the load-deflection curve, it can be seen that when the flange width of the combined beams is changed from 80mm to 100mm. The slope of the load-deflection curve of the combined beams changes similarly to the flexural capacity from 43.57kN to 47.08kN. And the maximum flexural capacity is increased by 8.06%. With the increase in the width of the combined beams, the maximum flexural capacity is also increased, and the maximum bending capacity is increased. With the gradual increase of the flange width of the combined beam, the maximum bending capacity also increases but the increase is not large. So the flange width of the combined beam has a small effect on the bending capacity.

4.1.2. Influence of section height of combined beams

Component L-4 combination beam selection of steel section size 40mm × 125mm × 40mm flange plank thickness of 30mm. L-6 composite beam selection of steel section size 40mm × 125mm × 40mm flange plank thickness of 40mm. L-7 composite beam selection of steel section size 40mm × 165mm × 40mm flange plank thickness of 30mm. Combination beam L-4 and composite beam L-6 are compared for the composite beam section height from 185mm to 205mm. Combination beam L-4 and combination beam L-6 for the combination beam section height from 185mm to 205mm. Combination beam L-4 and composite beam L-6 for the composite beam section height from 185mm to 205mm. L-4 compared with the combination beam L-6 for the flange plank thickness changes in the combination beam section height from 185mm to 205mm. Combination beam L-4 compared with the built-up beam L-7 for the steel section size changes in the composite beam section height from 185mm to 225mm.

By comparing the effect of different section heights on the flexural load capacity of the combined beams, as shown in Fig. 10. Through the load-deflection the curve can be seen that the flexural load capacity of the

combined beams L-4 compared with the combined beams L-6 increased from 57.23kN to 89.13kN. The maximum flexural load capacity was increased by 55.74%. The flexural load capacity of the combined beams L-4 compared with the combined beams L-7 increased from 57.23kN to 83.34kN, the maximum bending capacity increased by 45.63%. The slope of the load-deflection curve of the two groups of specimens is almost the same at the beginning of loading. However, with the increase of the load, the stiffness of the specimen of the combined beam L-4 reaches the yielding load. And the slope of the curve starts to degrade and tends to flatten. In summary, due to the different heights of the combined beam section, the corresponding maximum flexural load capacity is different. Combined beam L-6 and combined beam L-7 for the specimen flexural load capacity increase are more obvious. Specimen L-6 and specimen L-7 damage process is similar. They are with the increase in load combination of the beam across the upper edge of the beam began to flex after the lower edge of the timber tensile rupture. But specimen L-6 than the corresponding cracking load L-7 is larger. However, the cracking load of specimen L-6 is larger than that of L-7. From the perspective of the overall load deflection of the specimen and the amount of steel used. It is relatively optimal to choose the combination of specimen L-6 and the load deflection of the combined beam.

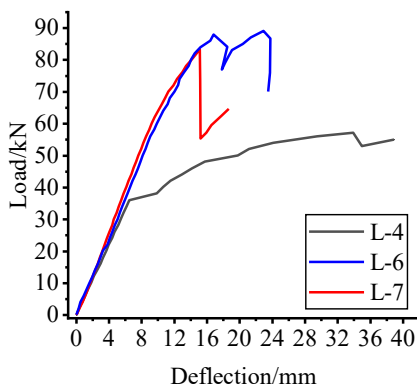


Fig. 10 Comparison of load-deflection curves

4.2. Combination of beams nail spacing change effect

Combined beam L-2, L-3, and L-4 cross-section dimensions are 100mm × 185mm × 100mm. In the case of other conditions are the same combination of the upper and lower flange of the beam into the self-tapping screw spacing is different, respectively, for 240mm, 180mm, and 120mm.

By comparing the effect of different self-tapping screw spacing on the flexural load capacity of the combined beam, as shown in Fig. 11. Combined beam L-2 flexural load capacity of 47.08kN, combined beam L-3 flexural load capacity of 52.19kN, combined beam L-4 flexural load capacity of 57.23kN. Combined beam L-3 than the maximum bending capacity of the L-2 increased by 10.08%. Combined beam L-4 than the maximum bending capacity of the L-3 increased by 10.08%, combined beam L-4 than the maximum bending capacity of the L-2 increased by 10.08%, combined beam L-4 than L-3 increased by 10.08%, combined beam L-4 than L-2 increased by 10.08%, combined beam L-4 than L-3 increased by 10.08%. 3. The maximum bending capacity of the combined beam L-3 was increased by 10.08%, and the maximum bending capacity of the combined beam L-4 was increased by 9.7%. From the specimen load-deflection curves, the overall load deformation of the three groups of specimens was similar. The change in the spacing of the self-tapping screws increased the bending capacity of the combined beam by a small amount. In summary, with the increase of load, the tapping screw spacing decreases, and the phenomenon of tapping screw shear damage gradually increases, which indicates that the interface shear force borne by the tapping screw increases. The combination of adhesive and shear-resistant connection of tapping screws is gradually reflected.

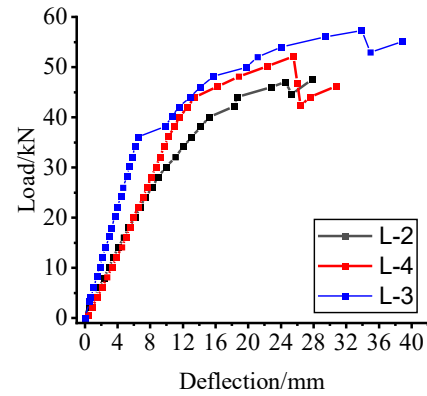


Fig. 11 Comparison of load-deflection curves

4.3. Influence of beam thickness

Combined beam L-4 and combined beam L-5 cross-section size of 80mm × 185mm × 80mm. The difference is that the combined beam L-4 selection of thin-walled steel thickness of 1.5mm. Combined beam L-5 selection of thin-walled steel thickness of 2mm and other conditions are the same.

As shown in Fig. 12, after comparing the steel-wood beam in the steel thickness of the different steel on the steel-wood beam bending capacity. When L-4 combined beams and L-5 combined beams are compared, the degree of thinness of the steel is thickened from the specification of 1.5mm to the degree of thinness of the steel 2mm specification. The bending capacity of L-5 steel-wood beams rises from 57.23kN of L-4 steel-wood beams to 64.09kN, and the peak load of the steel-wood beam specimens rises by about 12%. From the load-deflection curve and test phenomena, the beginning of the loading of the two groups of specimens' load deflection was linear growth. With the increase in load, adhesive peeling gradually increased after the combination of beams L-4 first reached the slope of the yield curve. With the increase in the thickness of the steel, the combination of beams compressed flange compression curvature phenomenon gradually became less obvious, which indicates that increasing the thickness of thin-walled steel can reduce the combination of beams thin-walled steel compression buckling generation. The damage phenomenon is also different when the bearing capacity is reduced. Through the above analysis, it can be seen that the steel thickness specification in the steel-wood beam specimen has a certain degree of influence on the peak load-carrying capacity of the steel-wood beam specimen. When the steel thickness specification of the steel-wood beam specimen is increased from 1.5 mm to 2 mm. The peak load carrying capacity of the steel-wood beam specimen is proportional to the thickness of the steel and the increase in peak load is not significant. However, the overall performance exhibited by the combined beam L-5 is better than that of the combined beam L-4. Therefore, it can be seen from the experimental analysis that the steel thickness specification of 2 mm in the steel-wood beam specimens is better for the overall performance of the steel-wood combination beam.

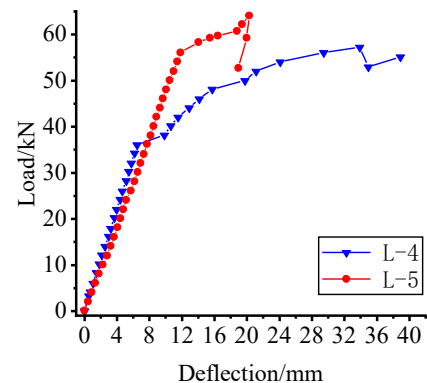


Fig. 12 Comparison of load-deflection curves

Yield point was a key factor in the design and research of engineering structures, and also a key factor in the measurement of structural ductility. Based on the method of P. Feng[33] for the definition of yield point. This

paper adopted the energy equivalent area method for the definition of yield displacement to determine the yield load P_y , the yield displacement Δ_y , and the ultimate load P_u , the ultimate displacement Δ_u are taken from the specimen to reach the peak load in the falling section of the curve with a load of 85% of the maximum load and the displacement value corresponding to this load (Fig. 13). The displacement value corresponding to this load (Fig. 13), and its deformation index ductility coefficient μ is calculated by using eq.6.

$$\mu = \frac{\Delta_u}{\Delta_y} \quad (6)$$

Where, Δ_u is ultimate displacement of the specimen; Δ_y is yield displacement of the specimen.

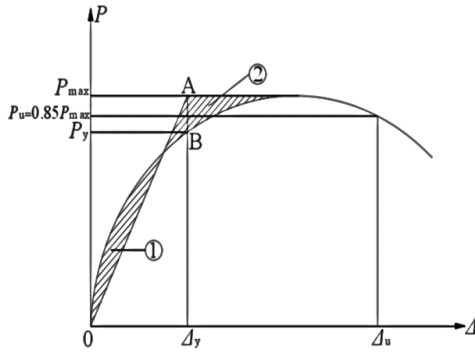


Fig. 13 Equal energy method

Table 6
Mechanical properties of combined beams

Specimen Number	Yield Load		Ultimate Load		Ductility Factor μ
	P_y /kN	Δ_y /mm	P_u /kN	Δ_u /mm	
L-1	34.06	13.93	41.04	25.67	1.84
L-2	40.07	15.23	44.51	25.28	1.66
L-3	44.05	13.44	42.29	26.43	1.97
L-4	48.01	15.73	52.97	34.96	2.22
L-5	56.16	11.86	52.67	18.98	1.60
L-6	72.18	12.47	70.04	23.51	1.89
L-7	62.08	9.57	55.32	15.21	1.59

From Table 6, it can be seen that the ductility coefficient of L-4 combination beam is the largest, and the ductility is better. The ductility coefficient of L-7 combination beam is the smallest. As a whole, all the steel-wood combination beam specimens have better ductility under bending.

According to the load-displacement relationship curves of thin-walled H-section steel-wood combination beams. It can be seen that all the combination beams are in the elastic stage of the load-displacement curves. It can be assumed that the thin-walled H-section steel-wood combination beams are in the elastic stress stage under the limit state of normal use. Therefore,

based on the deflection calculation equation for simply supported beams, the deflection calculation equation for thin-walled H-shaped cross-section steel-wood combination test beams can be given. Substituting the sectional flexural stiffness into the mid-span deflection calculation equation for single-span simply supported beams yields eq. 7:

$$f = \beta_s \frac{F a L^2}{48 E I} (3 - 4 \alpha^2) \quad (7)$$

Where: f is Beam mid-span deflection; β_s is deformation development factor; F is value of elastic phase load; a is distance of the point of action of the concentrated force from the support; $E I$ is total stiffness of the combined beam section; L is span of the combined beam; $\alpha = a/L$.

As the main bending load-bearing member in the building structure, the deformation development in the span of the beam needs to meet the limit values specified in the code under the normal use of the limit state when designing. In order to ensure the safety performance of the structure in use. In this paper, steel-wood combination beams should also meet the requirements. According to the relevant provisions of the Code for the Design of Steel Structures (GB 50017-2017)[34] and the Code for the Design of Wood Structures (GB/T 50005-2017)[35]. The combined beam specimens in the normal range of use, the control of deflection of the bending member of the maximum allowable deflection of $L/250$. 7 steel - wood combined beam specimens are 2.5 meters in length after removing the spacing of the supports, the length is 2.3 meters. The total length of the 7 steel-wood beam specimens is 2.5 meters after removing the spacing between the supports. The length is 2.3 meters, which can be calculated by the formula of the specification to obtain the deflection limit value corresponding to the limit state of normal use of the 7 steel-wood beam specimens as 9.2 mm. The 9.2 mm is substituted into the eq. 7 to calculate the 7 steel-wood beam specimens in the deflection of the specified value of 9.2 mm, when the corresponding loading force for the. The test deflections corresponding to the normal service limit states were found in the load-deflection curves of each specimen. Comparison of the theoretical and experimental values of the deflection of the combined beam under normal use limit state are analyzed as shown in Table 7. The error is within the permissible range and the theoretical calculated value is conservative enough to meet the needs of engineering use.

Table 7
Comparison of theoretical and experimental values of normal service limit state deflection

Specimen Number	Theoretical Deflection (mm)	Test deflection (mm)	Theoretical Deflection/ Test Deflection
L-1	9.20	8.65	1.06
L-2	9.20	9.67	0.95
L-3	9.20	9.11	1.01
L-4	9.20	9.04	1.02
L-5	9.20	8.85	1.04
L-6	9.20	8.16	1.13
L-7	9.20	8.01	1.15

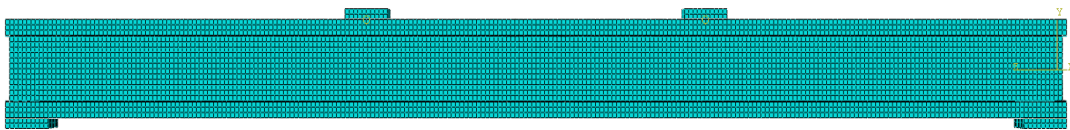


Fig. 14 Grid division

5. Finite element analysis

5.1. Establishment of finite element model

In the finite element modeling, the required two material parts as well as other components. They are established as solid models, and the 8-node hexahedral linear reduced integral C3D8R unit is selected as the unit. Among them, a simplified isotropic ideal elastic-plastic trilinear model is used for the steel principal structure. The anisotropic simulation of wood in the elastic and plastic phases is realized by using the "engineering constants" and Hill's yield criterion of the finite element software, respectively. The mesh size of the cells is 10 mm, and the cell division of the model is shown in Fig. 10. The loading mode is consistent with the experimental loading. The boundary conditions are consistent with the experimental boundary conditions, simply supported on one side and hinged on the other side.

Table 8
Finite element coordinate system and wood orthogonal triaxial correspondence

Input Value	Representative Value	Physical Meaning
E_1	E_L	Longitudinal modulus of elasticity of the smooth grain
E_2	E_R	Radial modulus of elasticity of cross-grain
E_3	E_T	Transverse tangential modulus of elasticity
ν_{12}	ν_{TL}	Transverse radial principal Poisson's ratio
ν_{13}	ν_{LR}	Transverse tangential principal Poisson's ratio
ν_{23}	ν_{RT}	
G_{12}	G_{LT}	Shear modulus on combined longitudinal and tangential surfaces
G_{13}	G_{LR}	Shear modulus on combined radial and longitudinal surfaces
G_{23}	G_{RT}	Shear modulus on combined radial and tangential surfaces

Table 9
Wood elasticity parameters

E_L	E_R	E_T	μ_{RT}	μ_{LR}	μ_{LT}	G_{LT}	G_{LR}	G_{RT}
(MPa)	(MPa)	(MPa)				(MPa)	(MPa)	(MPa)
11319	1131.9	565.95	0.63	0.27	0.43	679.14	849.93	203.74

The simulation of the mixed connection of epoxy resin glue and self-tapping screws between the thin-walled beam flange and the wood plate is the key to the simulation analysis of the thin-walled steel-wood beam. From the test phenomenon of the combined beam, it can be seen that there is a slip between the thin-walled beam flange and the wood plate in the descending section of the load-displacement curve of the combined beam. In the late loading period, a large separation between the two materials of the combined beam occurs, and the self-tapping screws show a shear tilt performance.

5.2. Finite element model validation

The simulation of the combined beams adopts the displacement loading method, which sets a collection of reference points in the span of the specimen. Then set the course outputs of the corresponding loads and displacements to

The physical significance of each parameter of wood material properties is shown in Table 8. The definition of each parameter is clarified in Table 9. The calculation method of the wood plastic yield strength coefficient is shown in Eq. (8):

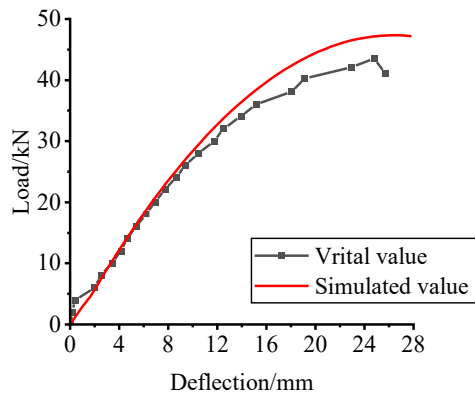
$$R_{ij} = \begin{cases} \sigma_{ij} / \sigma_0 (i = j) \\ \sigma_{ij} / \tau_0 (i \neq j) \end{cases} \quad (8)$$

Material plasticity is defined with reference to yield stress σ_0 , yield strength values for each material σ_{ij} . Moreover, the shear stress is τ^0 , which is shown in Eq. (2):

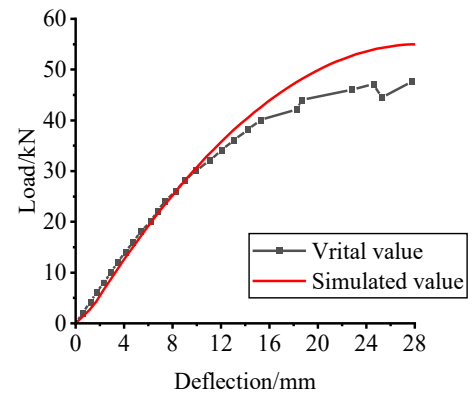
$$\tau^0 = \sigma^0 / \sqrt{3} \quad (9)$$

ultimately obtain the term load-deflection curves of each finite element model. Numerical simulation of seven combined beams is carried out by comparing the mid-span load-deflection curves of numerical analysis data and test information.

From the combined view of the curves as shown in Fig. 15 (The horizontal axis is the span-to-span displacement of the combined beam specimen, and the vertical axis is the load applied to the combined beam.) In the elastic phase, the slope of the test and simulated values is in a linearly increasing direction. In the elastoplastic phase, the growth of the slope of the curves starts to slow down. It can be seen in the graphs of the two curves that the overall error of the two data is small. It shows that the model unit selection, the definition of material parameters, cohesive contact model used for the interface connection can be used in the simulation of this model. The finite element can well simulate the whole process of steel-wood combination beam bending deformation. The maximum load values of the finite element simulations are a little higher compared to the tests. The reason for this is that from the numerical simulation point of view. The wood properties in the numerical simulation are different from the actual wood. Secondly, from the experimental point of view, the original defects and dimensional defects of the wood were not taken into account, and the processing of the specimens also had an influence. However, the errors are within the allowable limits.



(a) L-1



(b) L-2

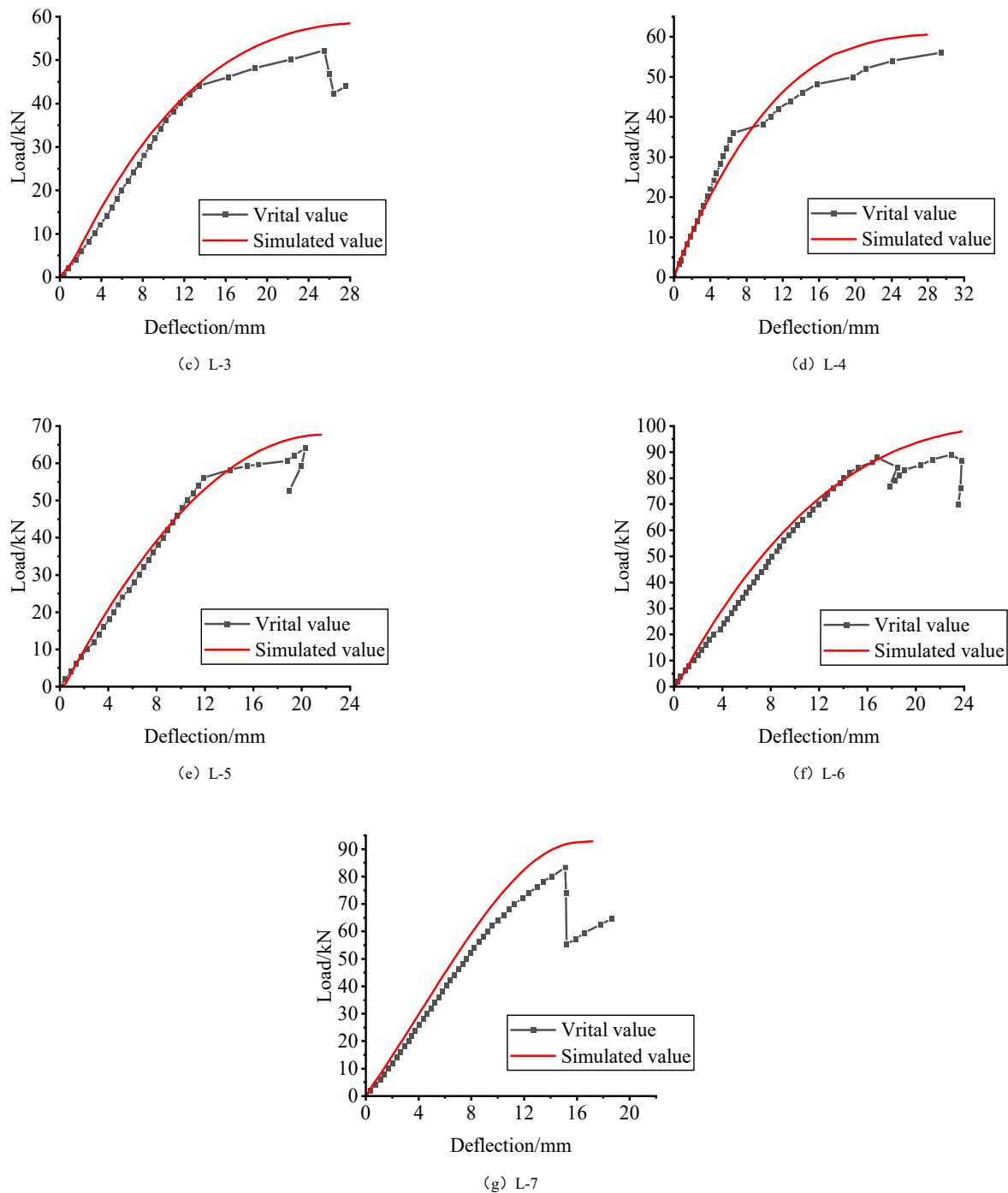


Fig. 15 Comparison of experimental and numerical simulation load-deflection curves

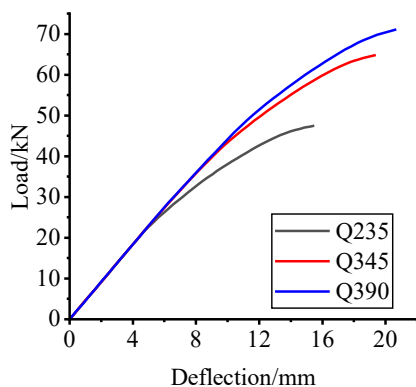


Fig. 16 Comparison of load-deflection curves at different yield strength spans

5.3. Parametric analysis of factors affecting the flexural performance of combined beams

5.3.1. Influence of steel yield strength

To study the effect of different yield strengths of steel on the bending performance of the combined beam. The Q235, Q345, and Q390 were selected as three kinds of steel with different yield strengths to simulate and analyze. Simulation of the three specifications of steel were taken as the yield strength of the yield strength value, modulus of elasticity, and Poisson's ratio are selected to take the value of the specification. As shown in Fig. 16, the load-displacement curves of the combined beams with different yield strengths of steel are compared.

As can be seen from the curve, the pre-loading period is characterized by an elastic trend of the three yield strengths of the combined beams in a line of linear development. The late loading of the combined beams to reach their respective yield strengths after the curve began showing non-linear development. With the increase of the yield strength, the load-carrying capacity of the combined beam also rises, when the steel specification changes

from Q235 to Q345. The load-carrying capacity of the specimen increases significantly, while when the steel specification changes from Q345 to Q390, the load-carrying capacity of the specimen increases by a small amount. Therefore, the increase in yield strength of steel is not obvious to improve the load-carrying capacity of the combined beam but will cause material waste.

5.3.2. Influence of the thickness of the combined beam flange planks

To study the influence of different thicknesses of flange planks on the bending performance of combined beams, Q235 specification, thickness of 1.5mm. And section size of 40mm×125mm×40mm were selected under the premise of the flange were 30mm, 35mm, and 40mm three plank thicknesses to simulate and analyze. As shown in Fig. 17, the load-displacement curves of the combined beams with different thicknesses of the flange planks are compared.

From the specimen load-deflection curves, it can be obtained that the maximum load-carrying capacity of the combined beam flange plank thickness increases from 30mm to 35mm and 40mm. Its maximum load-carrying capacity is also raised with the growth in the thickness of the flange plank. This is because of the increase in the thickness of the plank from 30mm to 35mm and 40mm when the specimen's cross-sectional stiffness changes, and there is a significant boost in the bending load-carrying capacity of the steel-wood beams.

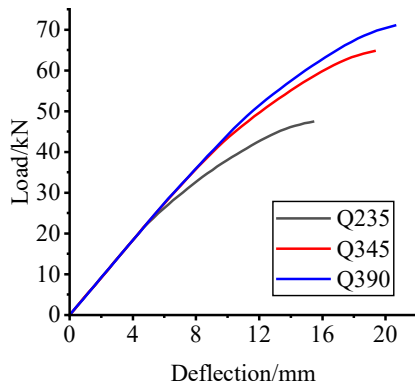


Fig. 17 Comparison of mid-span load-deflection curves for different thicknesses of wing planks

5.3.3. Combined beam thin-walled steel thickness effect

In order to study the combined beam, thin-walled steel thickness on the combined beam bending performance of the impact of different thicknesses. In the steel is selected Q235 specifications, the thickness of the wing edge board selection 30mm, and the steel size of 40mm × 125mm × 40mm under the premise of thin-walled steel thickness were selected 1.5mm, 2mm and 2.5mm thickness of the three kinds of simulation and analysis. As shown in Fig. 18, the load-displacement curves of combined beams with different thicknesses of thin-walled steel sections are compared. With the increase of the thickness of thin-walled steel sections in the combined beam, its flexural load capacity also has a large increase. The increase is about 10%.

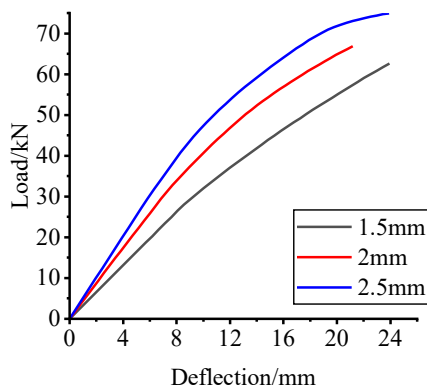


Fig. 18 Comparison of load-deflection curves at mid-span for different thicknesses of thin-walled sections

6. Conclusion

Since the strength of wood is much greater in the smooth grain than in the cross grain. The tensile strength is greater than the compressive strength. Steel has high strength, good plasticity and toughness properties, but thin-walled steel due to the thin wall thickness leads to its weak stability and other limitations of the material itself. A new thin wall H-section steel-wood composite beam member is proposed by combining the characteristics of the two materials, and seven different combination beams are tested for flexural performance. At the same time, ABAQUS finite element software is used to simulate the steel-wood combination beam and analyze its bending performance. The effects of the changes of the above factors on the bending capacity of steel-wood combination beams are analyzed. The following conclusions are obtained:

(1) The thin-walled steel profiles and wood are connected by epoxy resin glue and shear-resistant screws, which makes the combined beams have better integrity and give full play to the compressive and tensile properties of wood and thin-walled steel profiles. The stress process of the combined beam is mainly divided into three stages, i.e. elastic stage, elastic-plastic stage, and damage stage. In the elastic stage, the stiffness of the combined beam is large, and the steel and wood are jointly stressed. With the increase of load, when the combined beam reaches the elastic-plastic stage, the flange thin-walled steel appears local buckling; when the ultimate load is reached, the final damage phenomenon of the combined beam is the tensile bending damage of the lower flange board, and the combined beam damage mode is finally ductile damage.

(2) By analyzing the test data, it can be seen that under the same conditions. The change in the cross-section width of the combined beam has less influence on the bending capacity. The reduction of the shear screw spacing of the wing edge of the combined beam has no obvious effect on the load-carrying capacity but improves the connection performance of the interface. Changes in the height of the section of the combined beams had a significant effect on the load-carrying capacity. An increase in the thickness of the upper flange planks and an increase in the web height of the specimens resulting in a 52% and 45% increase in the load-carrying capacity, respectively. The change in the thickness of the flange planks had a greater effect on the load-carrying capacity than the change in the height of the webs. In the case where the thickness of the flange planks are 30mm, the increase in the thickness of the thin-walled steel sections results in a greater increase in the load-carrying capacity of the combined beams.

(3) A numerical simulation of seven combined beams was carried out using finite element software ABAQUS, and some factors affecting the bending performance of the combined beams, such as the yield strength of steel, thickness of the flange planks of the combined beams, and thickness of the thin-walled steel sections of the combined beams, were parametrically analyzed. The cohesive contact unit and modeling methods, such as load application and model boundary conditions are explored for simulation. The damage morphology and damage process of the steel-wood beams are verified more intuitively and the numerical simulation is compared with the test to verify its reasonableness.

Acknowledgments

This work is supported by the National Natural Science Foundation of China (Grant No.52268029) and the Open Fund of Shock and Vibration of Engineering Materials and Structures Key Laboratory of Sichuan Province (Grant No.20kfgk03).

Authorship contribution statement

Chang Wu: Conceptualization, Data curation, Methodology, Software, Visualization, Writing - original draft, Writing - review & editing.
Dongdong Ma: Investigation, Writing - review & editing, Validation.
Zhijiang Zhao: Writing - review & editing, Validation.
Yegong xu: Supervision, Investigation, Validation.
Renjun Fang: Software, Investigation, Methodology.

Conflict of interest statement

We declare that we have no financial and personal relationships with other people or organizations that can inappropriately influence our work.

References

- [1] T. Chen, Z. Chen, J. Liu, Bending properties of cold-formed thin-walled steel/fast-growing timber composite I-beams, *Forests*, 15(5), 2024.
- [2] Szewczak, Ilona, Rozylo, Influence of mechanical properties of steel and CFRP tapes on the

- effectiveness of strengthening thin-walled beams, *Materials*, 14(9), 2380, 2021.
- [3] A. M. Guzman, V. A. Roldan, Equivalent properties for analysis as beam-column of steel spatial lattices of rectangular cross-section, *Adv. Steel Constr.*, 17(2), 95-103, 2021.
- [4] S. Yan, Rasmussen Kim J. R., L. Jiang, Experimental evaluation of the full-range behaviour of steel beam-to-column connections, *Adv. Steel Constr.*, 16(1), 77-84, 2020.
- [5] L. Tian, Z. Li, M. Yang, Lateral torsional buckling strength of steel I-beams within preflexed beams in pre-bending stage, *Adv. Steel Constr.*, 16(1), 47-54, 2020.
- [6] H. Yang, H. Guo, Y. Wang, H. Jiang, Research on the shear performance of cold-formed thin-walled steel-glued laminated wood composite beams, *Buildings*, 13(12), 2023.
- [7] E. McConnell, D. McPolin, S. Taylor, Post-tensioning of glulam timber with steel tendons, *Constr. Build Mater.* 73, 426-433, 2014.
- [8] C. Marco, V. M. Chandra, E. Vikki, Local FRP reinforcement of existing timber beams, *Compos. Struct.* 258, 2021.
- [9] J. Aidas, V. Juozas, Analysis of the transfer, flexural bond and anchorage lengths of pretensioned FRP reinforcement based on Eurocode, *Compos. Struct.* 327, 2024.
- [10] H. Zhe, W. Yang, Y. Zhang, K. Zhao, Z. Dong, Flexural performance of FRP-SWSSC-steel composite beams: Experimental and analytical investigation, *Eng. Struct.* 306, 2024.
- [11] Szewczak, Ilona, Rozylo, Impact of adhesive layer thickness on the behavior of reinforcing thin-walled sigma-type steel beams with CFRP tapes, *Materials*, 15(3), 1250, 2022.
- [12] M. He, Y. Wang, Z. Li, An experimental and analytical study on the bending performance of CFRP-reinforced glulam beams, *Front. Mater.* 8, 2022.
- [13] A. Hassanieh, H. Valipour, M. Bradford, Composite connections between CLT slab and steel beam: Experiments and empirical models, *J. Constr. Steel Res.* 138, 823-836, 2017.
- [14] L. Wang, J. Lyu, J. Zhao, Experimental investigation of the shear characteristics of steel-to-timber composite joints with inclined self-tapping screws, *Eng. Struct.* 215, 2020.
- [15] A. A. Chiniforush, H. R. Valipour, A. Akbarnezhad, Long-term coupled analysis of steel-timber composite (STC) beams, *Constr. Build Mater.* 278, 2021.
- [16] Y. Zhao, Y. Yuan, C. Wang, Experimental and finite element analysis of flexural performance of steel-timber composite beams connected by hybrid-anchored screws, *Eng. Struct.* 292, 2023.
- [17] X. Song, L. Zhao, Y. Liu, Experimental and nonlinear analytical of the flexural performance of timber-filled steel tubular composite beam, *Eng. Struct.* 301, 2024.
- [18] G. Li, W. Zhang, X. Li, B. Yang, Flexural behavior of cold-formed thin-walled steel-glulam composite beams, *Wood Mater. Sci. Eng.* 18(1), 289-302, 2023.
- [19] S. Duan, W. Zhou, X. Liu, J. Yuan, Experimental study on the bending behavior of steel-wood composite beams, *Adv. Civ. Eng.* 2021, 2021.
- [20] R. Yang, H. Li, R. Lorenzo, Mechanical behavior of steel timber composite shear connections, *Constr. Build Mater.* 258, 2020.
- [21] T. Chen, Z. Chen, J. Liu, A. Zhang, Bending properties of cold-formed thin-wall steel/fast-growing timber composite I-beams, *Forests*, 15(5), 857, 2024.
- [22] S. Duan, W. Zhou, X. Liu, J. Yuan, Z. Wang, Experimental study on the bending behavior of steel-wood composite beams, *Adv. Civ. Eng.*, 2021(1), 2021.
- [23] Li, Y. Qiu, Young, Ben, Structural performance of cold-formed steel built-up section beams under non-uniform bending, *J. Constr. Steel Res.*, 189, 2022.
- [24] C. Wu, J. Duan, Z. Yang, Z. Zhao, Y. Xu, A novel rectangular-section combined beam of welded thin-walled H-shape steel/camphor pine wood: The bending performance study, *Sustainability*, 15(9), 7450-7450, 2023.
- [25] X. Zhao, L. Wei, D. Wen, Bending response and energy absorption of sandwich beams with novel auxetic honeycomb core, *Eng. Struct.*, 247, 2021.
- [26] W. Gu, H. Liu, Y. Dong, Experimental study on the flexural properties of concrete beams reinforced with Hybrid steel/Fiber-Belt-Bars, *Materials*, 15(10), 3505, 2022.
- [27] L. Zhang, J. Zhang, G. Chen, G. Lin, Flexural behavior of hybrid FRP-recycled aggregate concrete-steel hollow beams, *J. Constr. Steel Res.* 200, 2023.
- [28] U. Hilal, B. Agron, D. Nihat, I. H. Ozgur, S. Cevde, Modulus of elasticity and flexural behavior of glulam beams reinforced with steel mesh in different mesh openings, *Materials*, 16(12)4307, 2023.
- [29] B.C. Alberto, V. S. D. Brother, P. K. Augusto, Flexural and shear behavior of steel-UHPC composite beams: a review, *Eng. Struct.* 293, 2023.
- [30] S. Yuka, N. Yukihiro, U. Akikazu, Dissimilar materials bonding using epoxy monolith, *ACS omega* 3(7), 7532-7541, 2018.
- [31] Y. Li, C. Li, J. He, Y. Gao, Z. Hu, Effect of functionalized nano-SiO₂ addition on bond behavior of adhesively bonded CFRP-steel double-lap joint, *Constr. Build Mater.* 244, 2020.
- [32] B. J. A. Tadeu, G. F. J. F. Branco, Shear tests of steel plates epoxy-bonded to concrete under temperature, *J. Matre. Civil Eng.* 12(1), 74-80, 2000.
- [33] Feng, H. Qiang, L. Ye, Definition and discussion of "yield point" of materials, components and structures, *Engineering Mechanics*, 34(3), 36-46, 2017, [in Chinese].
- [34] Ministry of Construction of the People's Republic of China, Steel structure design code GB50017-2017, China Planning Press, 2017, [in Chinese].
- [35] Ministry of Construction of the People's Republic of China, Wood structure design code GB50005-2017, China Construction Industry Press, 2017, [in Chinese].

OPTIMAL DESIGN AND CONSTRUCTION OF A STEEL ARCHED PEDESTRIAN BRIDGE WITH STRUCTURAL ENHANCEMENT USING UHPC ENCASEMENT

Canh-Tuan Nguyen *

Faculty of Civil Engineering, Ho Chi Minh City University of Technology (HCMUT)-Vietnam National University Ho Chi Minh City (VNU-HCM)

** (Corresponding author: E-mail: ctnguyen@hcmut.edu.vn)*

ABSTRACT

This study focused on improving the structural design and reducing the costs of steel arched pedestrian bridges through detailed analysis and practical application. Optimization techniques were applied to identify the best sectional sizes and configurations for steel arch bridges, revealing that the arch ribs were sensitive to lateral buckling due to their high slenderness. To counter this and enhance the load-carrying capacity and stability, the arch ribs were proposed to be encased with Ultra-High-Performance Concrete (UHPC), especially near the bearings where the free length is substantial. Through non-linear finite element analysis, this study assessed the method's impact on buckling behavior, strength enhancement, and stress distribution within the arch ribs. The application of this solution in an actual construction project highlights its practicality and efficiency for pedestrian bridge development. Furthermore, the research contributes significantly to creating specialized manufacturing and construction methods for steel arched bridges, presenting an encouraging strategy for future applications.

ARTICLE HISTORY

Received: 25 April 2024
Revised: 4 February 2025
Accepted: 6 February 2025

KEYWORDS

Load-carrying capacity;
Stability enhancement;
Steel arched bridge;
Optimal design;
UHPC integration

Copyright © 2025 by The Hong Kong Institute of Steel Construction. All rights reserved.

1. Introduction

Steel arch constructions are highly preferred for pedestrian bridges, not only for their visual appeal but also for their structural effectiveness. The arch elements are crucial in bearing external forces, highlighting the importance of finding optimal designs that feature compact sections. This approach enhances the resistance to buckling and optimizes the structure's capacity to support loads. Addressing the risk of buckling in steel arch bridges is vital for maintaining structural integrity, safety, and overall functionality. Buckling, a frequent issue in such structures, occurs when slender arch components are subjected to compressive stress along their length. Maintaining stability to avert sudden and catastrophic failures is imperative. Extensive research has been dedicated to exploring the buckling behavior of steel arches, including studies on both in-plane and out-of-plane inelastic buckling. These efforts aim to refine predictive models for accurately determining the buckling strength of steel arches [1-5].

Buckling directly influences the load-carrying capacity of a steel arched bridge. Understanding the critical buckling modes and loads allows engineers to determine the maximum loads that the bridge can safely withstand without experiencing structural instability. This information is important for the design and assessment of the bridge's capacity to support various loads. Explorations into the impact of buckling on the load-carrying capacity of steel arches have been conducted. Pi et al. [6] explored the nonlinear in-plane buckling and post-buckling behavior to investigate influences of pre-buckling deformations on the overall behavior of steel arches. Multiple inquiries have examined the impact of bracings on the buckling strength of steel arches. Pi et al. [7] and Dou et al. [8, 9] focused on the influence of bracing stiffness from both lateral and rotational braces, on the elastic out-of-plane flexural-torsional buckling of steel circular arches. The research has revealed that enhancing bracing stiffness could effectively improve the strength of steel arches emphasizing that the slenderness of the arches is the pivotal factor in preventing buckling.

Optimization studies have been conducted to improve the structural performance of steel arched bridges, including the analysis of different arch geometries, support systems, and load distribution mechanisms. Finite element analysis (FEA) and computational tools effectively aid in assessing and refining these structures such as advanced analysis of inelastic buckling and post-buckling behavior. By understanding the buckling behavior, engineers can explore design modifications, such as adjusting the arch geometry, combining materials, or incorporating additional structural elements, to enhance the overall performance of the steel arched bridges. Nazmy [10] introduced an optimal methodology that comprehensively accounts for the impacts of diverse design parameters on both the strength and stability of steel arch bridges. Additionally, the optimal design of steel arch bridges has been addressed through the application of genetic algorithms, aiming to minimize the dimensions of the primary steel members [11, 12]. Numerous other investigations on optimization have been performed for various types of arched bridge, including arched trusses and funicular twin arches [13-15].

Extensive research has been dedicated to enhancing the materials used in steel arched bridges, with a focus on incorporating advanced materials such as high-strength steels, high-performance concrete, and fiber-reinforced composites. The aim is to improve the performance of steel arch bridges by achieving higher strength-to-weight ratios and enhancing their resistance and durability. This effort seeks to prolong the operational lifespan of bridges, addressing the critical need for sustained structural functionality. Researchers are exploring the optimal application of composite materials to boost the structural efficiency and carrying capacity of these bridges. This includes investigating various configurations, cross-sectional shapes, and combinations of materials to attain optimal performance under different loading scenarios. The study of composite arch members, which combine steel with materials like concrete or fiber-reinforced polymers, is particularly active. This research examines the structural behavior, load distribution, and longevity of composite arch elements versus traditional steel-only versions. Concrete-filled steel tubular arches, which blend steel's strength and durability with concrete's load-bearing capacity, represent a significant innovation in structural engineering. These arches feature a steel tube filled with concrete to create a composite structure that leverages the benefits of both materials. Additionally, this approach allows for efficient material use, leading to more sustainable and cost-effective construction practices [16-21]. The synergy of material properties in these arches enables them to cover large spans with few supports, offering an efficient and aesthetically pleasing solution for infrastructure projects. Discussions have also covered the advantages and limitations of Ultra-High-Performance Concrete (UHPC) in bridge construction. UHPC's exceptional mechanical properties and durability enhance the structural integrity of bridge connections, mitigate deformation and cracking in bridge pavements, and increase the load-bearing capacity of bridges [22].

The use of UHPC in structural design has been increasingly supported by life-cycle cost analysis (LCCA) to highlight its economic and sustainability benefits. A key study by Hossain and Chang [23] demonstrated that UHPC significantly reduces maintenance frequency and overall life-cycle costs in bridge retrofitting compared to conventional concrete alternatives. Their analysis showed that despite higher initial costs, UHPC's extended service life, up to 80 years compared to 30 years for conventional concrete, substantially decreases long-term expenditures. Similarly, Dong [24] evaluated UHPC's performance in terms of cost-effectiveness, environmental impacts, and durability. The study emphasized UHPC's ability to reduce CO₂ emissions and maintenance requirements over the lifecycle of structures, making it a sustainable alternative for infrastructure projects. The application of UHPC in precast girders demonstrated reductions in material volume and associated environmental impact. Furthermore, Stengel and Schießl [25] conducted an extensive LCCA to compare UHPC with traditional materials in various structural applications, including bridges. Their findings indicated that UHPC's higher strength and durability enable smaller cross-sections, reducing material consumption and long-term costs despite the energy-intensive production

process. These studies collectively support the economic and environmental viability of UHPC in modern construction, particularly for projects emphasizing durability and cost-efficiency in constrained environments. Such findings align with the methodology and outcomes of this study, reinforcing the relevance of UHPC in sustainable infrastructure development.

This study aims to address this gap by proposing a novel design and construction scheme that integrates Ultra-High-Performance Concrete (UHPC) with steel arches, optimizing both performance and cost for a specific project in a remote mountainous region. Unlike previous research, which primarily focuses on large-scale infrastructure or generalized design improvements, this study is tailored to the unique constraints of constructing pedestrian bridges in challenging environments. By leveraging finite element analysis and practical construction methods, we developed an optimized configuration for steel-UHPC composite arch structures. This approach not only enhances load-carrying capacity and stability but also minimizes costs, making it an accessible solution for underprivileged communities. Additionally, the research demonstrates the feasibility of implementing such designs under strict financial and temporal constraints, contributing to a broader understanding of how advanced materials like UHPC can be utilized in cost-sensitive applications. The project is distinguished by its focus on practical application, culminating in the successful construction of a pedestrian bridge that serves as a vital connection for a remote community. This achievement underscores the potential for replicating and scaling the proposed methodology in similar contexts, addressing a critical need for sustainable and affordable infrastructure.

2. Optimum design of the steel arched structure

2.1. Structural optimization approach

The collapse of an existing suspension bridge posed a significant divide between communities on either side of the spring, necessitating a new bridge for the local people. A steel tied arch bridge, chosen for its aesthetic appeal that enhances the local tourism landscape, was proposed. This new bridge, designed to be 39 meters long and 2.3 meters wide for walkway, could support a standard pedestrian load of 4.3 kN/m in accordance with the LRFD Guide Specifications for the Design of Pedestrian Bridges [26]. Owing to various constraints at the site of construction, the height of the steel arch should be restricted to 5.0 meters, resulting in a height-to-span ratio for the steel arch of only 0.128. The objective of this study was to identify a design solution that not only meets the criteria for cost efficiency but also ensures practicality in construction processes and strict compliance with project schedule within four months. To accommodate the transportation and erection requirements under local conditions, it was determined that the steel arch structure needs to be segmented into pieces no longer than 6.0 meters each. A thorough cost analysis, considering the fabrication expenses of the steel structures, the costs associated with structural connections, and the erection method, was conducted. The general alignment of the bridge is illustrated in Fig. 1.

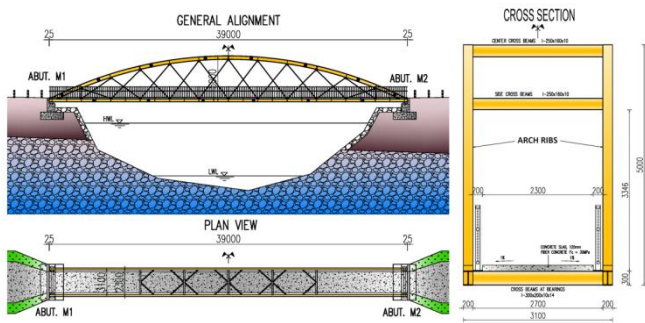


Fig. 1 General alignment of the steel arch bridge

The optimization of arch structures can be approached through various methods, each with its unique focus and application. These methods often aim at enhancing structural efficiency, reducing material usage, or improving the overall performance of the structure under different loading conditions. In the design of the steel arch structure, which comprises arch ribs, tie girders, floor beams, and hangers, structural analyses and partial optimization process was undertaken. This process was grounded in the principle of balancing construction costs while ensuring structural integrity and efficiency. The general process of the structural optimization process is described in Fig. 2.

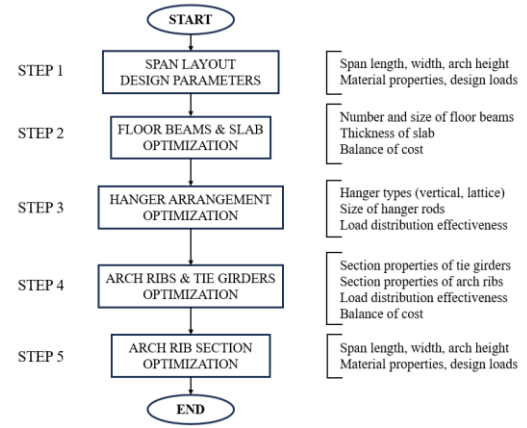


Fig. 2 Optimization process of the steel arch bridge

The optimization process was efficiently conducted with the aid of the finite element analysis program MIDAS CIVIL. To accurately simulate the structural components, beam elements were employed for arch ribs, tie girders and floor beams; tension-only truss elements for hangers; and truss elements for bracing components. Subsequently, internal forces were carefully obtained to facilitate the design of each section. The configuration of the simulation model is presented in Fig. 3.

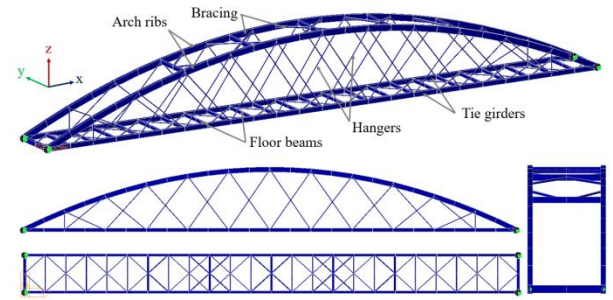


Fig. 3 Finite element model for optimization analysis

2.2. Results of optimal design

2.2.1. Floor beams and concrete slab

The parametric optimization method was conducted to find the best combination of the number and dimensions of floor beams, the thickness of the concrete slab, and the amount of reinforcing bar (rebar) within the slab. The number of floor beams was also found to have a significant impact on the alignment of the hanger system. The optimal design should be achieved not only to meet structural integrity and safety standards but also to minimize construction and material costs.

A target function for the optimal cost is defined from the total construction costs of floor beams and the concrete slab as follows:

$$C = \min(C_b + C_s) \quad (1)$$

Where $C_b = f(q_{PL}, N_b, L_b, A_b, S_{x,b}, f_y, c_b)$ is the cost of floor beams, and is a function of the pedestrian load q_{PL} , number of floor beams N_b , length of floor beams L_b , sectional area of floor beams A_b , section modulus $S_{x,b}$, yield strength $f_y = 250$ MPa, and unit cost for fabrication and construction of steel beams c_b ; $C_s = f(q_{PL}, S_b, b_s, t_s, A_r, f_y, f'_c, c_c, c_r)$ is the cost of the reinforced concrete slab, and is a function of the pedestrian load, floor beam spacing S_b , slab width b_s , slab thickness t_s , rebar area A_r , yield strength of rebar $f_y = 400$ MPa, compressive strength of concrete $f'_c = 28$ MPa, unit cost for concrete c_c and for rebar c_r .

To obtain the optimal design, strength constraints for floor beams and the slab should be defined. For the reinforced concrete slab, the factored bending moment in the slab $M_{str,s}$ at the Strength Limit State should satisfy:

$$M_{Str,s} \leq \phi A_r f_y \left(t_s - 0.59 \frac{A_r f_y}{f_c b_s} \right) \quad (2)$$

For floor beams, the factored bending moment in floor beams $M_{Str,b}$ at the Strength Limit State should satisfy:

$$M_{Str,b} \leq f_y S_{x,b} \quad (3)$$

Additional constraints for cross-section proportion limits including web and flange of floor beams should be considered in accordance with Clause 6.10.2 from AASHTO LRFD design code [27] for I-section flexural members.

In the process of parametric optimization, the characteristics of floor beams and slabs were directly influenced by a specific set of parameters which were optimized using an iteration method to satisfy the constraints from Eqs. (2) and (3) with minimum cost. This optimization could identify the minimum cost from these sets by using Eq. (1). The sequence of steps taken in this optimization process is clearly outlined in Fig. 4, and the results of the optimal design parameters for varying numbers of floor beams are detailed in Table 1.

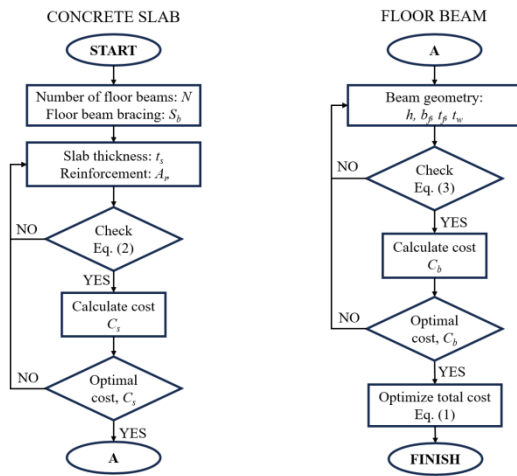


Fig. 4 Parametric optimization process for floor beams and slab

Table 1

Design data for cost optimization of floor beams and reinforced concrete slab

Variables	Optimal parameters for floor beams and slab								
N_b	40	33	29	25	23	21	19	17	16
S_b (m)	1	1.2	1.4	1.6	1.8	2	2.2	2.4	2.6
t_s (m)	0.08	0.08	0.1	0.12	0.12	0.15	0.15	0.18	0.18
A_r (mm ²)	159	230	236	253	321	320	388	396	464
h (mm)	100	100	100	125	125	150	150	150	175
b_f (mm)	51	63	80	71	82	77	86	103	91
t_f (mm)	8	8	8	8	8	8	8	8	8
t_w (mm)	5	5	5	5	5	5	5	5	5

It was observed that increasing the number of floor beams led to a reduction in the span length of the slab. This adjustment had a dual effect on the cost structure: while the cost associated with the floor beams increased due to the higher quantity required, there was a consequential decrease in the cost of the concrete slab. The reduction in slab cost can be attributed to the decreased span, which in turn reduces the slab thickness and the amount of rebar needed to meet structural demands. Through a detailed examination depicted in Fig. 5, the minimum total cost could be identified when the ideal number of floor beams is set to 25, with the slab spanning intervals of 1.6 meters and having a thickness of 120 mm.

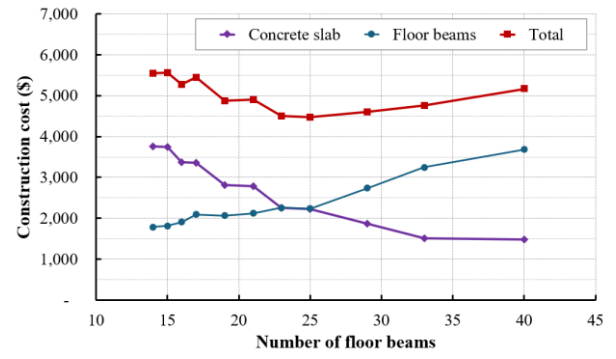


Fig. 5 Variation of optimal cost with different number of floor beams

2.2.2. Hanger members

The optimization of the hanger system in steel arch structures was evaluated by comparing the structural performance of lattice and vertical arrangements in the same loading condition. Two different finite element models were adopted to non-linear analyses to verify the structural performance using ABAQUS [28]. Fig. 6 reveals that the lattice configuration offers effective load distribution capabilities, with buckling confined to the arch ribs near the bearing locations after peak loads are applied. In contrast, the vertical hanger system fails to provide adequate load-carrying capacity, resulting in global buckling across the entire structure. Further comparative analysis, as shown in Fig. 7, demonstrates that the lattice system significantly outperforms the vertical system, with a load capacity of 1760 kN compared to the vertical system's 996 kN, showing a nearly 77% increase in capacity with a similar quantity of materials used. Based on these findings, the lattice system is identified as the optimal solution for steel arch structures, offering superior structural performance and efficiency.

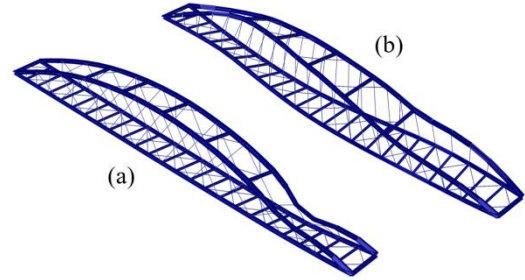


Fig. 6 Buckling of arch ribs with hanger arrangements: (a) lattice type; (b) vertical type

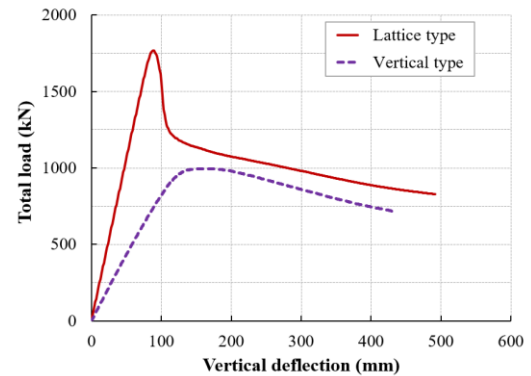


Fig. 7 Load-deflection curves of the steel arch bridge with different types of hangers

2.2.3. Arch ribs and tie girders

After successfully optimizing the floor beams, slab, and hanger system, the overall alignment of the structure was clearly established. It was assumed that cross beams of arch ribs and bracing components were excluded from the optimization process. The next step was to identify the ideal dimensions for arch ribs and tie girders. Critical analyses in the structural optimization of arch bridges revealed a significant correlation between tie girders and arch ribs concerning load distribution, particularly in relation to their rigidities.

Applying Clause 6.8.2.3 and Clause 6.9.2.2 from AASHTO LRFD Design Specification [27] for strength constraints, tie girders subjected to combined

tension and flexure and arch ribs subjected to combined axial compression and flexural shall satisfy:

$$k = \frac{P_u}{2P_r} + \left(\frac{M_{ux}}{M_{rx}} + \frac{M_{uy}}{M_{ry}} \right) \quad \text{if } \frac{P_u}{P_r} < 0.2 \quad (4-1)$$

$$k = \frac{P_u}{P_r} + \frac{8}{9} \left(\frac{M_{ux}}{M_{rx}} + \frac{M_{uy}}{M_{ry}} \right) \quad \text{if } \frac{P_u}{P_r} \geq 0.2 \quad (4-2)$$

Where k is the strength factor that should not exceed 1.0; P_u is the ultimate axial force (kN); P_r is the factored axial resistance (kN) which defined from Clause 6.8.2.1 for tension and Clause 6.9.4.1 for compression respectively [24]; M_{ux} and M_{uy} are the ultimate bending moments about x axis and y axis, respectively (kN.m); M_{rx} and M_{ry} are factored flexural resistances about x axis and y axis, respectively (kN.m). The calculations of M_{rx} and M_{ry} are detailed in the commentary C6.8.2.3 [27].

Local buckling of arch ribs in compression should be controlled through the limits of the slenderness in accordance with Clause 6.9.4.2 from AASHTO provision [27]. The slenderness of web plates shall satisfy:

$$\lambda_w = D / t_w \leq k_0 \sqrt{E_s / f_y} \quad (5)$$

Where D is web depth (mm); t_w is web thickness (mm); and k_0 is the plate buckling coefficient, $k_0 = 1.49$.

The slenderness of the half-width flanges of built-up I-sections shall satisfy:

$$\lambda_f = b_f / 2t_f \leq 0.64 \sqrt{k_c E_s / f_y} \quad (6)$$

Where b_f is flange width (mm); t_f is flange thickness (mm); and $0.35 \leq k_c \leq 0.76$ in which $k_c = 4 / \sqrt{D / t_w}$.

In addition, the structure should satisfy the constraint for the vertical deflection which is specified in Clause 2.5.2.6.2 [24] using load combination at the service limit state. The maximum deflection of the bridge shall not exceed 1/1000 of the span length. Vibrations shall be investigated as a service limit state. Vibration of the structure shall not cause discomfort or concern to users of a pedestrian bridge. The fundamental frequency in a vertical mode of the pedestrian bridge without live load shall be greater than 3.0 Hz to avoid the first harmonic [26].

A vector representing types of I-shaped sections is defined as follows:

$$\mathbf{I}^T = [\mathbf{I}_1, \mathbf{I}_2, \dots, \mathbf{I}_n] \quad (7)$$

Where $\mathbf{I}_i^T = [h_i, b_{f,i}, t_{f,i}, t_{w,i}]$ is a vector of the i th sectional dimensions; h_i is the height (mm); $b_{f,i}$ is the flange width (mm); $t_{f,i}$ is the flange thickness (mm); and $t_{w,i}$ is the web thickness (mm).

Vectors of internal forces, deflections, and natural frequencies corresponding to the i th combination of sections as input parameters for optimization process are defined as follows:

$$\mathbf{F}_i^T = [N_i^{rib}, M_i^{rib}, N_i^{tie}, M_i^{tie}, \delta_i, f_i] \quad (8)$$

Where N_i^{rib} is the maximum factored axial compression force in arch ribs (kN); M_i^{rib} is the maximum factored bending moment in arch ribs (kN.m); N_i^{tie} is the maximum factored axial compression force in tie girders (kN); M_i^{tie} is the maximum factored bending moment in tie girders (kN.m); δ_i is the maximum vertical deflection (mm); f_i is the natural frequency of the first vertical vibration mode. It is noted that internal forces, deflections, and natural frequencies are outputs of finite element analyses which can be automatically performed by a self-developed coding program including optimization algorithms using Matlab. However, developing such a program would be considered in another study.

Vectors of output results corresponding to the i th combination of sections including slenderness ratios, strength factors, deflections, and natural frequencies for checking violation condition are defined as follows:

$$\mathbf{K}_i^T = [\lambda_i^{w,rib}, \lambda_i^{f,rib}, \lambda_i^{w,tie}, \lambda_i^{f,tie}, k_i^{rib}, k_i^{tie}, \delta_i, f_i] \quad (9)$$

Where λ_i^{rib} and λ_i^{tie} are slenderness ratios of webs and flanges

corresponding to the i th combination of sections; k_i^{rib} and k_i^{tie} are strength factors of arch ribs and tie girders, respectively.

Fig. 8 describes the process of parametric optimization for tie girders and arch ribs. From given sets of sectional parameters, trial sections were assigned to tie and rib members in the finite element model. Factored axial compression forces and factored bending moments were extracted to calculate strength factors of tie girders and arch ribs. Variations in strength factors of tie girders and arch ribs according to Eq. (4) with different section properties were investigated. The optimization algorithm was developed to find a range of section geometries that could satisfy the strength, slenderness, and deflection constraints with minimum weight of steel material of arch ribs and tie girders.

In the analysis of arch rib and tie girder structures, a comprehensive investigation was conducted to find the most effective section combinations that would satisfy design constraints while optimizing strength and minimizing weight. From Table 2, a series of sectional dimensions were given as an initial source of data for optimization analyses to find ideal sections for tie girders and arch ribs. Utilizing finite element analysis, a total of 64 combinations of sections for the arch ribs and tie girders were evaluated. Key structural responses including deflections, natural frequencies, axial forces, and bending moments were subsequently extracted from the analysis. Strength factors were then calculated to assess the adequacy of each combination under applied loads.

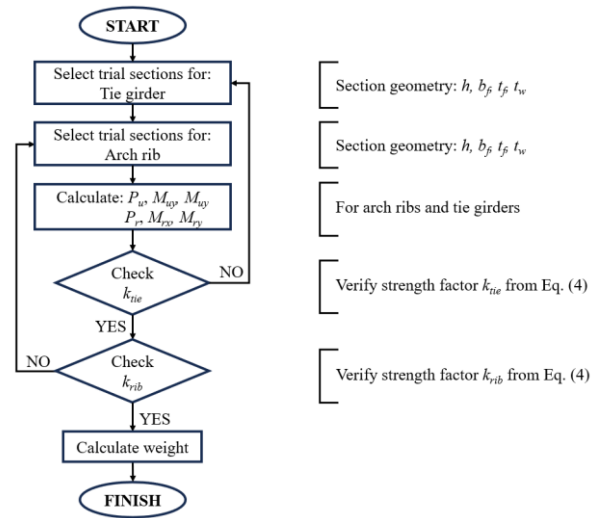


Fig. 8 Parametric optimization process for tie girders and arch ribs

Table 2

A source of sectional parameters for optimization

No.	h (mm)	b_f (mm)	t_w (mm)	t_f (mm)	A (mm ²)	I_x (mm ⁴)	I_y (mm ⁴)
1	150	125	8.5	14	4,537	17.5×10^6	4.56×10^6
2	200	150	9	16	6,312	44.3×10^6	9.01×10^6
3	250	125	10	19	6,870	71.4×10^6	6.20×10^6
4	300	150	10	18.5	8,180	125×10^6	10.4×10^6
5	350	150	9	15	7,380	151×10^6	8.45×10^6
6	400	150	10	18	9,040	237×10^6	10.1×10^6
7	450	175	11	20	11,510	387×10^6	17.2×10^6
8	600	190	13	25	16,650	966×10^6	28.7×10^6

The results, given in Fig. 9, present the distribution of strength factors corresponding to various section combinations, with the total weight of the arch ribs and tie girders plotted on the horizontal axis against the strength factors on the vertical axis. Particularly notable are the results highlighted by red dots for section numbers 6, 7, and 8, delineating combinations that not only provide sufficient strength factors but also comply with all design constraints, as shown in Fig. 9a. To identify a target efficient section combination, a search algorithm was applied to detect the most optimal configuration among 64 evaluated combinations. This optimal combination was found to consist of section number 6 for the arch ribs and section number 2 for the tie girders, achieving a minimum structural weight of 96.8 kN. The optimal dimensions and section properties for the arch ribs and tie girders were presented in Table 3 as a benchmark to select target sections for the detailed design.

Table 3
Optimal section properties for arch ribs and tie girders

Items	h (mm)	b_f (mm)	t_w (mm)	t_f (mm)	A (mm ²)	I_x (mm ⁴)	I_y (mm ⁴)
Tie girder	200	150	9	16	6,312	44.3×10^6	9.01×10^6
Arch rib	400	150	10	18	9,040	237×10^6	10.1×10^6

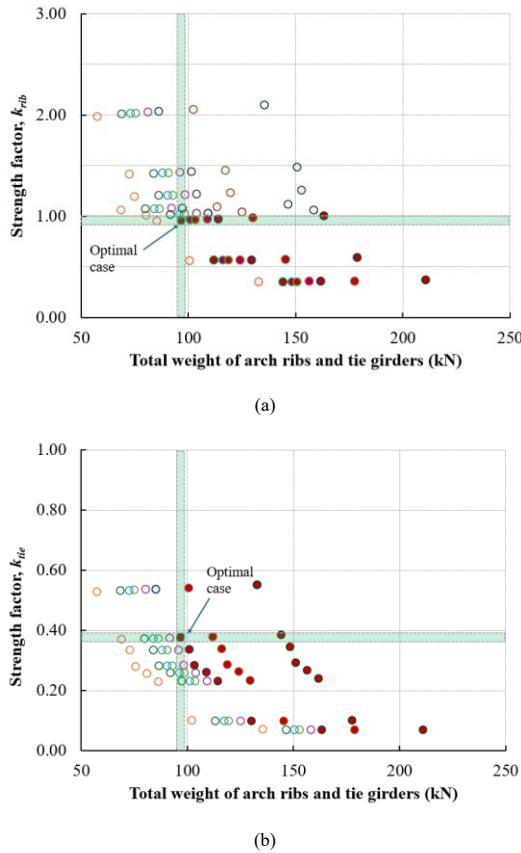


Fig. 9 Variation of strength factors in correlation with total weight: (a) for arch ribs; (b) for tie girders

2.2.4. Design of steel arch structures

The detailed design of the steel arch bridge progressed by finalizing sections that met the specified benchmarks for section properties as determined by optimization results. Table 4 provides a comprehensive overview of dimensions and section properties for all bridge components. Specifically, the section of the arch ribs was configured to have equal area and second moment of inertia compared to the optimal section, with an increased flange width aimed at enhancing out-of-plan bending stiffness. Furthermore, the design for tie girders exceeded the dimensions suggested by optimization results, driven by considerations of aesthetics and the need to mitigate deflection within the structure.

Table 4
Dimensions of structural components for detailed design

No.	h (mm)	b_f (mm)	t_w (mm)	t_f (mm)	A (mm ²)	I_x (mm ⁴)	I_y (mm ⁴)
Arch rib	390	200	10	14	9,220	237×10^6	18.7×10^6
Tie girder	300	200	10	14	8,320	131×10^6	18.7×10^6
Floor beam	200	100	5.5	8	2,612	17.6×10^6	1.33×10^6
Cross beam	250	160	10	10	5,500	56.2×10^6	6.84×10^6
Top brace	90	90	8	-	1,376	1.066×10^6	-
Bottom brace	60	60	6	-	684	0.233×10^6	-
Hanger rod	22	-	-	-	380	0.115×10^6	-

Fig. 10 illustrates the overarching configuration of the steel arch structure, which incorporates approximately 17 tons of steel material. The selection of this material not only conferred a lightweight attribute upon the structure but also simplified logistical management throughout the construction phase. The I-

shaped section of the arch rib was found to have a large slenderness which is sensitive to lateral buckling. Therefore, arch ribs, with large free length near bearings, were partially encased with UHPC to effectively improve the structure's stability and load-carrying capacity.

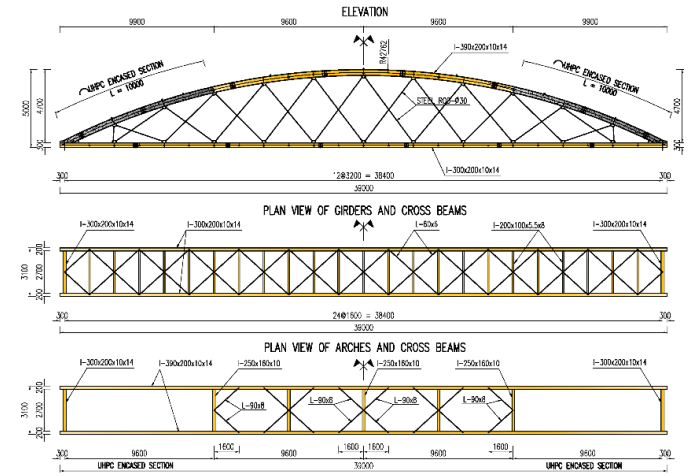


Fig. 10 General arrangement of steel structures: arches, girders, and cross beams

Fig. 11 shows the cross-sectional details of the steel arch ribs, illustrating both the steel section and the UHPC-encased section derived from the built-up I section design. The critical interaction between the UHPC and the steel section is achieved through the utilization of shear connectors positioned along the webs, ensuring an integrated structural behavior. The UHPC used in this design boasts a compressive strength of 100 MPa, providing exceptional durability and load-bearing capacity. This UHPC is made from a pre-mixed mortar and carefully cast in place to align precisely with the steel sections. This can improve the structural efficiency and strength of the arches.

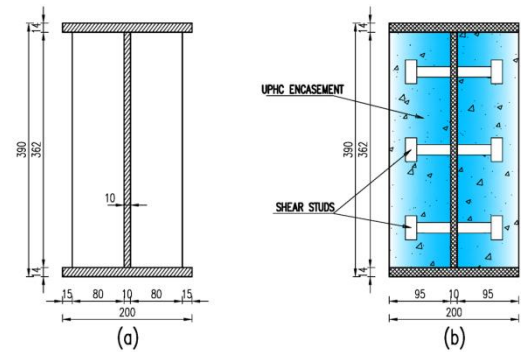


Fig. 11 Cross sections of arch ribs: (a) steel section; (b) UHPC encased section

3. Buckling analysis and verification

3.1. Finite element modeling

The steel arch structure, optimized in design, was analyzed using ABAQUS [28], to assess stability before construction. Models included steel sections and UHPC-encased sections to compare their instability behaviors. Steel arch members were modeled using 4-node quadrilateral stress/displacement shell elements (S4R) employing reduced integration and a large-strain formulation. The concrete parts were modeled using 8-node linear brick elements (C3D8R) with reduced integration and hourglass control. The hanger rods and bracing members of the vertical beams and arch were simplified using three-dimensional, 2-node truss elements (T3D2). For the UHPC encased parts, interaction between UHPC parts and arch ribs was controlled by using tie constraints along webs of arch ribs simulating shear connectors with the assumption that slip between the UHPC parts and steel web was negligible.

Fig. 12 illustrates the overall finite element model of the steel arch structure. The initial imperfection was considered as out-of-plan deformation $\delta_0 = 20$ mm (0.05% of total span length) in the z-axis direction at the middle of the arch ribs. Boundary conditions were modeled according to the actual design with

four bearing positions. The entire arch system was supported by one fixed bearing, two unidirectional movable bearings, and one bidirectional movable bearing to ensure a simple support condition. Concentrated loads applied in finite element analysis were imposed in the middle of the span. To facilitate nonlinear analysis, a displacement-based method was utilized instead of force application. The imposed displacement values were gradually increased until structural failure occurs. Reaction forces measured at the displacement-controlled locations represented the corresponding forces acting on the structure. Fig. 13 illustrates parts of the finite element models of the arch members simulating the steel section, UHPC encasement, and tie constraints to generate composite interactions between steel web and concrete parts.

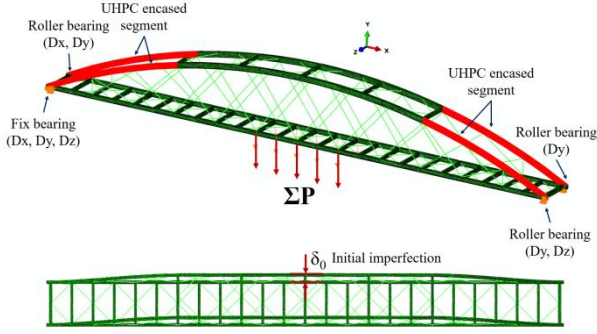


Fig. 12 General model of the steel arch with boundaries, loads, and imperfection

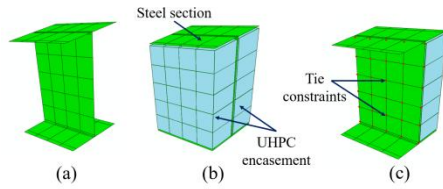


Fig. 13 Finite element models for steel arch members:
(a) steel section; (b) UHPC encased section; (c) tie constraints

Nonlinear analyses were conducted to investigate the steel arch's behavior considering nonlinear material modeling and applying large strain theory. The structural components, including the steel arch members and longitudinal beams, were constructed from SM490 steel plates, characterized by a yield strength of $f_y = 390$ MPa and a tensile strength of $f_u = 560$ MPa. The cross beams featured an I-shaped section and, along with the bracing members which are made of equal angle sections for both the arches and beam system, were fabricated from SS400 steel. This material was chosen for its yield strength of $f_y = 290$ MPa and ultimate strength of $f_u = 460$ MPa. Additionally, the hanger components were crafted from C45 steel bars, 22 mm in diameter, boasting a yield strength of $f_y = 360$ MPa and an ultimate strength of $f_u = 610$ MPa. The Young's modulus for all the steel materials used in the project was estimated to be 210,000 MPa, with a Poisson's ratio of 0.3. To ensure accuracy and reliability, stress-strain relationships for the verification models were derived from actual stress-strain curves obtained through material testing, whenever such data were available. Fig. 14 presents the stress-strain characteristic curves for the steel materials, utilizing a model that divides the curve into three linear segments. These curves, essential for the finite element analysis, were obtained from detailed studies on the steel materials' behavior. Initially, the material exhibits elastic behavior up to the yield strength and corresponding yield strain. Beyond this point, the material enters a yield plateau, maintaining the yield strength until the strain escalates to ten times the initial yield strain. Subsequently, the curve progresses to the tensile strength at an equivalent strain of 0.1. The Von-Mises yield criterion and isotropic hardening rule were used to model steel's behavior under different loads, providing a clear framework to predict its response to stress.

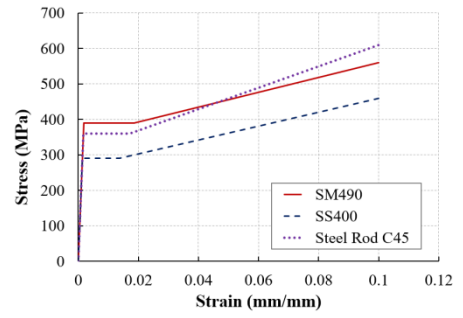


Fig. 14 Stress-strain relationship of steel materials for FEM analysis

In this study, UHPC was applied for composite interaction as encasement to improve the performance of steel arch members under compressive stresses. CEB-FIP Model Code [29] has proposed material models to simulate the behavior of the UHPC. The relation between stress σ_c and strain ϵ_c for short-term uniaxial compression is approximated by the following equation:

$$\frac{\sigma_c}{f_{cm}} = - \left(\frac{k\eta - \eta^2}{1 + (k-2)\eta} \right) \quad \text{for } |\epsilon_c| < |\epsilon_{c,lim}| \quad (10)$$

where, $\eta = \epsilon_c / \epsilon_{c1}$ and $k = E_{ci} / E_{c1}$; f_{cm} is the actual compressive strength of concrete at an age of 28 days, $f_{cm} = f_{ck} + 8$ (MPa); f_{ck} is a specific characteristic compressive strength (MPa); ϵ_{c1} is the strain at maximum compressive stress; E_{c1} is the secant modulus from the origin to the peak compressive stress.

Crack opening was assumed to be small and was not considered in the analysis. For the uncracked normal weight concrete subjected to tension, a bilinear stress-strain relation is given as follows:

$$\sigma_{ct} = E_{ci} \epsilon_{ct} \quad \text{for } \sigma_{ct} \leq 0.9 f_{ctm} \quad (11a)$$

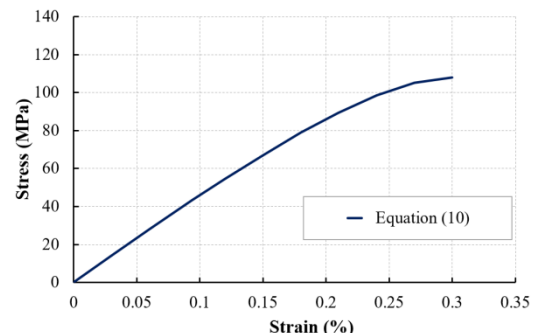
$$\sigma_{ct} = f_{ctm} \left(1 - 0.1 \frac{0.00015 - \epsilon_{ct}}{0.00015 - 0.9 f_{ctm} / E_{ci}} \right) \quad \text{for } 0.9 f_{ctm} < \sigma_{ct} \leq f_{ctm} \quad (11b)$$

Where, E_{ci} is the tangent modulus of elasticity (MPa); ϵ_{ct} is the tensile strain; σ_{ct} is the tensile stress (MPa); f_{ctm} is the tensile strength (MPa).

Table 5
Material parameters of UHPC grade C100 given by Model Code [29]

Concrete grade	f_{ck} (MPa)	f_{ctm} (MPa)	E_{ci} (GPa)	E_{c1} (GPa)	ϵ_{c1} (‰)	$\epsilon_{c,lim}$ (‰)
C100	100	5.2	47.5	36	3.0	3.0

The compressive strength of UHPC which was considered for the optimal design and finite element analyses was 100 MPa. Table 5 shows material parameters of UHPC grade C100 given by the Model Code [26] to construct the stress-strain diagrams in compression and tension. It is assumed that the maximum stress, $f_{cm} = 108$ MPa, was obtained at the proportional limit strain $\epsilon_{c,lim} = 0.003$. The value of tensile strength was approximated as $f_{ctm} = 5.2$ MPa to construct the stress-strain relation for UPHC in tension. Fig. 15 presents the approximated stress-strain diagrams of the UHPC derived from Eqs. (10) and (11) for the compressive strength and the tension strength, respectively.



(a)

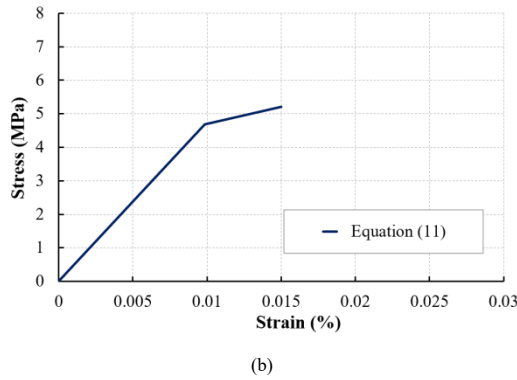


Fig. 15 Stress-strain diagrams of UHPC grade C100: (a) in compression; (b) in tension

3.2. Analysis results and verification

Fig. 16 illustrates the analytical outcomes derived from finite element analyses for two distinct scenarios involving arch ribs: one with a non-composite section and the other with a section encased in UHPC. The significance of points (a) and (c) lies in their representation of critical structural behaviors under peak loading conditions. Point (a) corresponds to the maximum load-carrying capacity of the non-composite section, recorded at 1,768.1 kN. This value indicates the limit at which the steel arch ribs begin to experience lateral buckling, leading to a rapid decrease in structural stability. Point (c), on the other hand, highlights the performance of the UHPC-encased section, with a maximum load-carrying capacity reaching 2,676.7 kN, an improvement of approximately 50% compared to the non-composite section. This significant increase is attributed to the UHPC encasement's ability to enhance the stiffness and reduce the susceptibility to lateral buckling, particularly in the critical regions near the bearings.

The comparison underscores the effectiveness of the UHPC encasement in mitigating lateral deformation and improving the overall structural resilience of the arch ribs. The inclusion of UHPC not only increases load-bearing capacity but also delays the onset of instability, thereby extending the operational safety margin of the structure. These findings validate the proposed design methodology and its potential applicability to similar projects requiring enhanced performance under constrained resources. By clearly indicating the importance of these points, Fig. 16 provides a visual representation of the substantial benefits achieved through UHPC integration in the design of steel arch bridges.

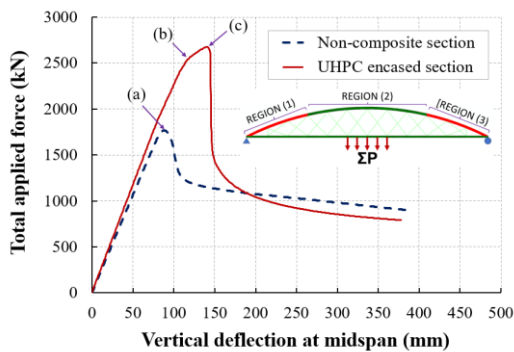


Fig. 16 Comparison of load-carrying capacity between steel section and UHPC encased section

In the study of a non-composite section under peak load conditions, Fig. 17 illustrates the progression of deformation in the steel arch alongside the corresponding loading states. Initially, it was observed that lateral buckling began to manifest subtly within the arch ribs. Specifically, the onset of yielding stress was identified at the edge regions of the top flange in designated areas (1) and (3), as depicted in Fig. 17a. This early sign of stress concentration was a precursor to more significant structural changes.

As the loading continued, these initial instances of lateral buckling evolved into pronounced out-of-plane deformations. These deformations were most notable in the middle sections of regions (1) and (3), where they expanded rapidly, as shown in Fig. 17b. This escalation in deformation led to a marked decrease in the structural integrity of the steel arch, culminating in an

approximate 30% reduction in its load-carrying capacity.

The culmination of these structural changes led to the eventual failure of the steel arch. The complete breakdown was attributed to the lateral deformations within the steel arch members, specifically in the regions with large effective lengths - regions (1) and (3). These sections were identified as particularly susceptible to lateral buckling due to their structural characteristics. The sequence of deformation and failure, captured in Fig. 17c, underscores the critical impact of lateral buckling on the stability and performance of steel arch structures under significant load conditions.

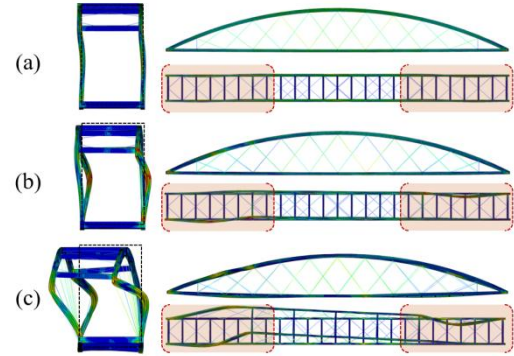


Fig. 17 Deformation and buckling behaviors of the steel arch: (a) at peak load; (b) after 30% drop; (c) at failure

In the case of the UHPC encased sections, the more vulnerable areas of the arch ribs were identified in region (2), where lateral buckling was a potential risk, particularly in unbraced sections of the arch. Observations from Fig. 18 indicate that the overall stiffness of the structure experienced a minor reduction starting from point (b), which corresponded to a total applied load of 2,535 kN. At this juncture, minor out-of-plane deformations began to manifest in the mid-sections of the arch ribs, accompanied by yielding of the top flanges because of maximum axial compression combined with bending, as illustrated in Fig. 18a.

As the stress continued to accumulate, it progressed toward the center of the web, peaking at point (c). This transition marks a critical phase where yielding stresses developed significantly between points (b) and (c), without the arch ribs undergoing instability, as depicted in Fig. 18b. Upon reaching peak load, out-of-plane deformations increased, especially in unbraced arch rib areas, reducing load capacity by 47% due to yielding and buckling effects (see Fig. 18c).

The most pronounced lateral deformations were observed in region (2), culminating in structural failure due to buckling in the sections comprised solely of steel, as evidenced in Fig. 18d. The analysis showed that encasing arch ribs in UHPC greatly improved stability and load-bearing capacity in regions (1) and (3), proving its effectiveness in strengthening these critical areas.

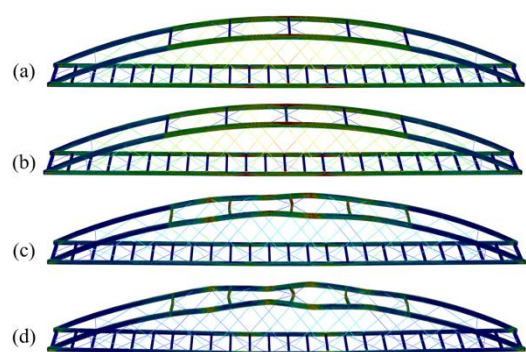


Fig. 18 Deformation of the steel arch with UHPC encased section: (a) at first yield; (b) at peak load; (c) after 47% drop of strength; (d) at failure

Figs. 19 and 20 illustrate the stress development and distribution within the steel arch under different scenarios: non-composite sections and UHPC-encased sections. These figures provide critical insights into how the integration of UHPC improves structural performance and mitigates vulnerabilities. To assess the impact of buckling in arch ribs, a critical location where buckling occurred was chosen for a comparative analysis of stress development between non-composite and UHPC encased sections. The analysis recorded stresses at seven points within these sections, correlating them with out-of-plane deflection.

In Fig. 19a, the stress distribution for the non-composite section shows significant disparities between the left and right sides of the arch ribs. This uneven stress distribution leads to pronounced in-plane and out-of-plane deformations, ultimately resulting in lateral buckling at peak load. Key stress concentrations are observed at points corresponding to the edges of the top flange, where instability initiates. The progression of stress and deformation underscores the limitations of the non-composite design in maintaining structural stability under high loads. Using the Von-Mises stress criterion, the stress in the non-composite section showed significant differences between the arch's sides as it approached 70 MPa, causing out-of-plane deformation and signs of instability. This instability was more pronounced with stresses reaching 90 MPa and 150 MPa at specific points, exacerbating the arch's in-plane and out-of-plane bending. At peak load, out-of-plane displacement reached 55 mm, and yielding started at around 150 mm, showing that arch instability was the main failure cause.

Fig. 19b shows the stress in the UHPC-encased section. UHPC reduces stress levels and distributes them more evenly, lowering bending effects and delaying buckling. At peak load, encased sections deflect about 20 mm, compared to 55 mm in the non-composite design, proving UHPC's effectiveness in improving structural strength. The results clearly demonstrate the effectiveness of UHPC encasement in reducing the stress experienced by the steel section. It was observed that the variation in stress levels between points 1 and 3, as opposed to points 2 and 4, attributable to transverse bending, was minimal. The peak load condition resulted in out-of-plane deformation of approximately 20 mm. Notably, the regions of the arch ribs reinforced with UHPC encasement showed no signs of instability, allowing the structure to reach its maximum load-bearing potential. Figure 20 shows the stress distribution at peak load for both scenarios. The non-composite section has high stress concentrations beyond the yield limit, causing rapid failure. In contrast, the UHPC-encased section keeps stress within safe limits, improving load capacity and stability. This highlights the benefits of UHPC encasement in enhancing the safety and durability of steel arches.

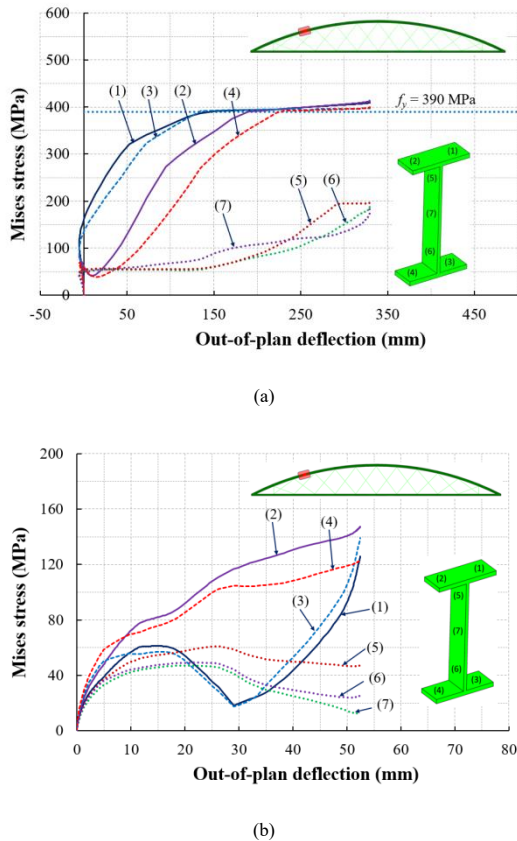


Fig. 19 Stress development: (a) Non-composite section with deformation; (b) UHPC-encased section with improved uniformity and reduced deformation

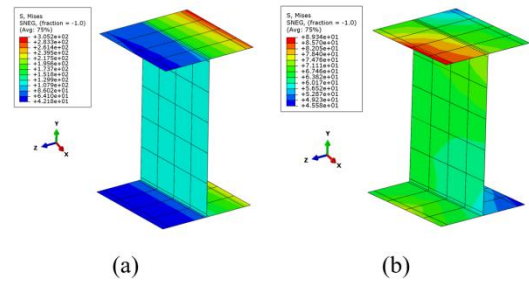


Fig. 20 Stress distribution at the peak load: (a) Non-composite section with high stress; (b) UHPC-encased section with improved stress

4. Application to a pilot construction project

4.1. Strength test for UHPC

The encasement process for the UHPC involved the use of a pre-mixed mortar that met the specified compressive strength requirements. This specific UHPC mix was developed through a prior study by Vinh et al. [30] and was selected for its robust characteristics for this pilot project. To ensure the material's strength met necessary standards, axial compression tests and tension tests were carried out before the UHPC was manufactured and transported to the site. The stress-strain relationships observed in these tests, as illustrated in Fig. 21, were then compared to theoretical predictions provided by the Model Code. The UHPC demonstrated a remarkable 28-day compressive strength of 118 MPa and a tensile strength of 6.8 MPa. The experimental results showed that the pre-mixed UHPC exceeded design standards and was approved for construction. A manually controlled intensive mixer ensured consistent quality and integrity during the mixing process.

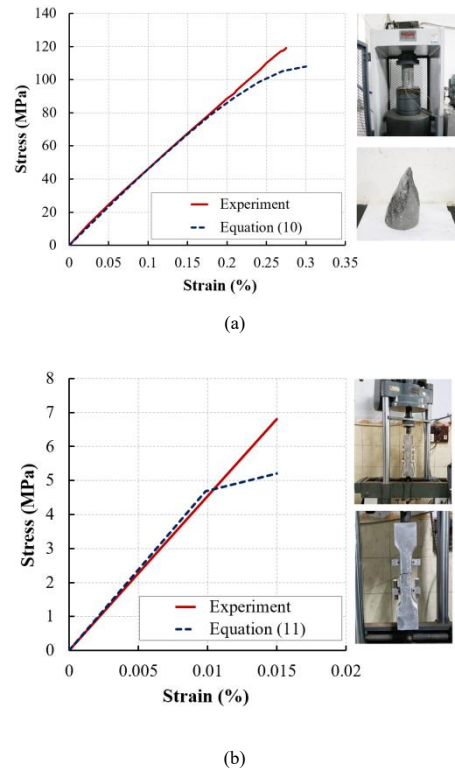


Fig. 21 Strength tests for pre-mixed UHPC: (a) compression test; (b) tension test

4.2. Fabrication of steel structures

Fig. 22 shows the steel structure manufacturing process in a factory. As this was the first use of the design, the process was carefully monitored, especially the welding. Non-destructive tests like ultrasonic testing (UT) and magnetic particle testing (MT) ensured the welds' quality. Furthermore, a trial assembly of the steel arch structure was carried out at the factory. This step was crucial for verifying the overall geometric accuracy and ensuring the compatibility of the various components that make up the steel arch. Considering the adoption of the incremental launching method for the structure's installation, a launching

nose equipped with a truss system was integrated with the steel arch during assembly. This procedure allowed for the testing of the structural launching process right at the factory, aiming to confirm both the feasibility of construction and the safety of the methodology.



Fig. 22 Fabrication and trial assembly of the steel structures at the factory

4.3. Construction implementation

Fig. 23 provides a visual guide to the steel arched bridge's erection sequence. Faced with several site-specific constraints, the construction team opted to assemble the steel structure entirely from one bank of the spring. This method effectively utilized the incremental launching technique, which was essential under the given conditions. A lightweight truss-equipped launching nose played a key role, while counterweights at the rear-maintained balance during construction. Pre-mixed UHPC mortar, produced in a factory, was intensively mixed to ensure quality and consistency before being delivered to the site. After assembling the steel framework, the UHPC encasement was carefully applied by hand, highlighting the precision and craftsmanship needed for this stage. Figure 23 shows the UHPC encasement in excellent condition at the end of construction, reflecting high-quality materials and workmanship. Load tests with actual service loads followed, ensuring the bridge's safety and functionality. These tests confirmed the structure's readiness for operation, marking a smooth transition from construction to service.



Fig. 23 Construction sequence of the pedestrian steel arched bridge

5. Conclusions

This study has presented an optimized design and construction scheme for steel arch pedestrian bridges enhanced with UHPC encasement, specifically developed to meet the demands of a resource-limited project in a remote area. By integrating UHPC with steel arches, the proposed method effectively mitigates lateral buckling and improves the load-carrying capacity and stability of the structure. Unlike prior studies, which often focus on large-scale or generic applications, this research uniquely addresses the practical challenges of constrained budgets and timelines, providing a tailored solution for underprivileged communities.

The successful implementation of the proposed design in an actual construction project highlights its practicality and impact. The bridge serves as a testament to the feasibility of advanced composite materials in addressing real-world challenges, offering a sustainable and cost-effective alternative to

traditional construction methods. Furthermore, the findings provide a foundation for preliminary design guidelines, enabling practitioners to apply similar techniques in analogous projects. These contributions pave the way for future research aimed at refining the methodology and expanding its applicability to a broader range of infrastructure needs.

Looking forward, we acknowledge the need for further experimental validation and expanded case studies to enhance the robustness of the proposed approach. The research offers a foundational reference for engineers and designers seeking to explore innovative solutions in bridge construction, highlighting the potential for cost-effective, stable, and durable pedestrian bridge designs.

Acknowledgments

The authors gratefully acknowledge the support provided by Nam Phuong Foundation in collaboration with 3E Steel Technology and Engineering Company. Their financial and technical assistance has been invaluable to the completion of this work for the local people.

References

- [1] Papangelis J.P., Trahair N.S., "Buckling of monosymmetric arches under point loads", *Engineering Structures*, 10(4), 257-264, 1988.
- [2] Pi Y.L., Trahair N.S., "Inelastic lateral buckling strength and design of steel arches", *Engineering Structures*, 22(8), 993-1005, 2000.
- [3] Pi Y.L., Trahair N.S., "Non-linear buckling and postbuckling of elastic arches", *Engineering Structures*, 20(7), 571-579, 1998.
- [4] Hu C.F., Li Z., Hu Q.S., "On non-linear behavior and buckling of arch-beam structures", *Engineering Structures*, 239, 112-214, 2021.
- [5] Han Q., Cheng Y., Lu Y., Li T., Lu P., "Nonlinear buckling analysis of shallow arches with elastic horizontal supports", *Thin-Walled Structures*, 109, 88-102, 2016.
- [6] Pi Y.L., Trahair N.S., "Non-linear buckling and postbuckling of elastic arches", *Engineering Structure*, 20(7), 571-579, 1998.
- [7] Pi Y.L., Bradford M.A., "Inelastic buckling and strengths of steel I-section arches with central torsional restraints", *Thin-Walled Structures*, 41(7), 663-689, 2003.
- [8] Dou C., Jiang Z.Q., Pi Y.L., Gao W., "Elastic buckling of steel arches with discrete lateral braces", *Engineering Structures*, 156, 12-20, 2018.
- [9] Dou C., Pi Y.L., "Flexural-torsional buckling resistance design of circular arches with elastic end restraints", *Journal of Structural Engineering*, 142(2), 04015104, 2016.
- [10] Nazmy A.S., "Stability and load-carrying capacity of three-dimensional long-span steel arch bridges", *Computers & Structures*, 65(6), 857-868, 1997.
- [11] Park J., Chun Y.H., Lee J., "Optimal design of an arch bridge with high performance steel for bridges using genetic algorithm", *International Journal of Steel Structures*, 16, 559-572, 2016.
- [12] Feng Y., Wang C., Briseghella B., Fenu L., Zordan T., "Structural optimization of a steel arch bridge with genetic algorithm", *Structural Engineering International*, 31(3), 347-356, 2021.
- [13] Latif M.A., Saka M.P., "Optimum design of tied-arch bridges under code requirements using enhanced artificial bee colony algorithm", *Advances in Engineering Software*, 135, 102685, 2019.
- [14] Pan W.H., Zhao C.H., Wang C.M., Luo Y.Z., "Optimal bracing system design for funicular twin arches against out-of-plane buckling", *Engineering Structures*, 301, 117250, 2024.
- [15] Zhang J.M., Wang C.M., Pan W.H., "Methodology for determining optimal design of funicular arches under point loads and selfweight against in-plane buckling", *Engineering Structures*, 300, 117255, 2024.
- [16] Bradford M.A., Pi Y.L., Qu W., "Time-dependent in-plane behaviour and buckling of concrete-filled steel tubular arches", *Engineering Structures*, 33(5), 1781-1795, 2011.
- [17] Jiang W., Lu D.G., "Reliability analysis for stability bearing capacity of CFST arches", *Proceedings of the 7th International Conference on Bridge Maintenance, Safety and Management*, Shanghai, China, 2014.
- [18] Huang F., Cui Y., Dong R., Wei J., Chen B., "Evaluation on ultimate load-carrying capacity of concrete-filled steel tubular arch structure with preload", *Advances in Structural Engineering*, 22(13), 2755-2770, 2019.
- [19] Sun J., Geng Y., Zhang H., Yin H., Wang Y., "Experimental and numerical study on slender concrete-filled steel tubular arches subjected to tilting loads", *Thin-Walled Structures*, 179, 109701, 2022.
- [20] Zhang Y., Liu A., Huang Y., Yang J., Fu J., Yu Y., Zeng X., "Experimental investigation of in-plane ultimate bearing capacity of parabolic high strength concrete-filled-steel-tubular arch", *Thin-Walled Structures*, 183, 110348, 2023.
- [21] Han X., Wei C., Hu Q., Liu C., Wang Y., "In-plane nonlinear buckling analysis and design method of concrete-filled steel tubular catenary arches", *Journal of Constructional Steel Research*, 214, 108485, 2024.
- [22] Zhou M., Lu W., Song J., Lee G.C., "Application of ultra-high-performance concrete in bridge engineering", *Construction and Building Materials*, 186, 1256-1267, 2018.
- [23] Chang C.M., Hossain A., "Life-Cycle Cost Analysis of Ultra High-Performance Concrete (UHPC) in Retrofitting Techniques for ABC projects", *Accelerated Bridge Construction University Transportation Center*, 3-5, 2022.
- [24] Dong Y., "Performance assessment and design of ultra-high performance concrete (UHPC) structures incorporating life-cycle cost and environmental impacts", *Construction and Building Materials*, 167, 414-425, 2018.
- [25] Stengel T., Schiebl P., "Life cycle assessment (LCA) of ultra high performance concrete (UHPC) structures", *Eco-efficient Construction and Building Materials*, 528-564. Woodhead Publishing, 2014.
- [26] AASHTO. LRFD Guide Specifications for the Design of Pedestrian Bridges. American Association of State Highway and Transportation Officials, Washington DC, 2009.
- [27] AASHTO. AASHTO LRFD bridge design specifications. American Association of State Highway and Transportation Officials, Washington DC, 2012.
- [28] ABAQUS. ABAQUS standard user's manual version 6.5. Hibbit, Karsson and Sorensen Inc., 2005.
- [29] Taerwe L., Matthys S., *Fib model code for concrete structures 2010*, Ernst & Sohn, Wiley, 2013.

- [30] Chu V.T.H., Bui V.D., Nguyen T.V., “Effect of aggregate grading and steel fiber on the properties of ultra-high performance fiber reinforced concrete”. Proceedings of the International Conference on Sustainable Civil Engineering and Architecture, Singapore, 2023.

DESIGN OF SINGLE POST-INSTALLED STEEL SCREW ANCHOR: A NOMOGRAM MODEL AND REASSESSMENT OF EUROCODE 2 PART 4

Ng Lieu Thai¹, Daniel Looi Ting Wee^{1,2,*}, Jessey Lee³, Adeline Ng Ling Ying¹ and S S Ajeesh⁴

¹ School of Engineering and Science, Swinburne University of Technology, Sarawak, Malaysia

² School of Engineering and Technology, Sunway University, Selangor, Malaysia

³ Department of Civil and Construction Engineering, Swinburne University of Technology, Melbourne, Australia

⁴ Department of Civil Engineering, National Institute of Technology Calicut, India

* (Corresponding author: E-mail: daniellooi@sunway.edu.my)

ABSTRACT

EN 1992-4:2018 covers the design of post-installed steel screw anchors considering the tensile failure modes such as concrete cone failure, pull-out failure, concrete splitting failure, and steel failure. However, recent findings from the literature have shown that the prediction from the Concrete Capacity Design method, which is the basis for EN 1992-4:2018, may overpredict the resistances of screw anchors due to unique mechanical characteristics and failure behaviour of the screw anchor. Given that screw anchors are widely used in structural and non-structural applications, a graphical tool is presented in this paper that aims to review the design for screw anchors in EN 1992-4:2018 in order to bridge the gap in research knowledge. A novel approach through the introduction of a graphical tool (called nomogram) is proposed by collecting 197 experimental data and verified with four models from product European Technical Assessment (ETA) to provide a rapid and reliable estimation of the resistances (i.e., tensile and shear) of screw anchors for concrete-related failures. The predicted resistances are corroborated with experimental results, and it was shown that approximately 48% to 69% of the predicted results exceeded the experimental results if the coefficient of variation is ranging from 10% to 15%. In the majority of cases, the Concrete Capacity Design method can be unconservative compared to the experimental results. The nomogram is foreseen to be useful for quick preliminary estimation of screw anchor capacities without the need to use detailed design software. It can also serve as an independent verification tool for senior engineers reviewing designs prepared by junior engineers in consulting offices.

ARTICLE HISTORY

Received: 30 October 2024
Revised: 18 February 2025
Accepted: 22 February 2025

KEYWORDS

Screw anchor;
Tensile resistance;
Shear resistance;
EC2-4 screw anchor verifications;
Nomograms

Copyright © 2025 by The Hong Kong Institute of Steel Construction. All rights reserved.

1. Introduction

Fasteners, also known as anchors, are used in steel-concrete connections to create robust joints that effectively transfer forces from steel elements to surrounding concrete [1, 2]. A steel screw anchor is a type of post-installed mechanical anchor in which the load is transferred through the mechanical interlock over the anchor threads and concrete. Screw anchors are relatively new compared to the more conventional expansion and undercut anchors. The use of screw anchors in concrete construction has gained popularity due to their advantages of reliable performance, convenience, and speed of installation [3]. Expansion anchors transfer the load to concrete through the expansion and friction forces at the interface between the anchor and the side wall of the drilled hole in the concrete [4]. On the contrary, undercut anchors transfer the load to concrete through the mechanical interlock at the tip of the anchor.

However, the load transfer mechanism of screw anchors is different from expansion or undercut anchors, and it can be complicated given that there will be multiple struts forming perpendicular to the surface of the screw threads, as compared to concentrated strut at the tip of common mechanical anchors. Kuenzlen and Eligehausen [5] pioneered experimental tests of 500 screw anchors of 8 mm to 18 mm diameter with embedment depth ranging from 30 mm to 110 mm installed in cracked and uncracked concrete of cube compressive strength of 30 MPa. It was observed that the failure modes of screw anchors are similar to bonded anchors, which are concrete cone failure (see Fig. 1(c)) and combined failure (see Fig. 1(e)), depending on the embedment depth of the anchors. Concrete cone failure is characterised by the formation of cone-shaped fractures in concrete, while combined failure is the combination of the pull-out of an anchor with a shallow cone-shaped concrete. The failure loads increased proportionally to $h_{ef}^{1.5}$ (where, h_{ef} is the effective embedment depth of the anchor), which is about 20% less than expansion and undercut anchors under the same embedment depth. Based on the Concrete Capacity Design (CCD) method, Kuenzlen [6] proposed an equation to calculate the reduced effective embedment depth for screw anchors (see Eq. (1)) and incorporated it into an equation developed by Fuchs et al. [7] for expansion and undercut anchors (see Eq. (2)), to predict the characteristic tensile resistance of screw anchors for concrete cone failure [3, 8].

$$h_{ef} = 0.85(h_{nom} - 0.5h_t - h_s) \quad (1)$$

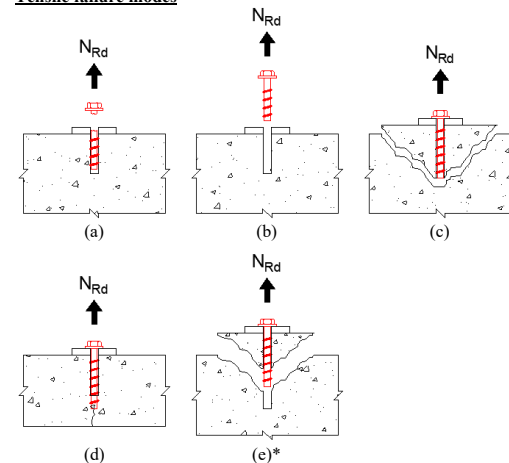
where, h_{nom} is the overall depth of the screw anchor embedded into the concrete, h_t is the distance of the thread pitch, and h_s is the distance between the tip of the screw anchor and first thread.

$$N_{u,c}^0 = k_c(\sqrt{f_{ck}})(h_{ef}^{1.5}) \quad (2)$$

where, k_c is taken as 14.64 for uncracked concrete in SI units, f_{ck} is the characteristic concrete cylinder compressive strength, and h_{ef} is the effective embedment depth of the anchor.

Olsen et al. [3] further expanded the database evaluated by Kuenzlen and Eligehausen [5] by considering another 353 tension tests. The diameter of screw anchors ranged from 6.35 mm to 19.05 mm with h_{ef} ranged from 25.4 mm to

Tensile failure modes



Shear failure modes

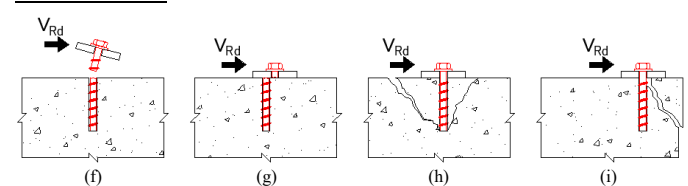


Fig. 1 The failure modes of post-installed screw anchors under tensile load: (a) steel failure, (b) pull-out failure, (c) concrete cone failure, (d) concrete splitting failure, (e) combined pull-out and concrete failure (*Note: This failure mode is not explicitly mentioned in EN 1992-4:2018), and under shear load: (f) steel failure with a lever arm, (g) steel failure without a lever arm, (h) concrete pry-out failure, (i) concrete edge failure

127 mm. It was concluded in the study that the modified CCD method proposed by Kuenzlen [6] fits their experimental results. Moreover, it was recommended to limit the design model for the spacing between two anchors (minimum spacing taken as the maximum of $0.6h_{ef}$ or $3.5D$) and the embedment depth ($40 \text{ mm} < h_{nom} < 11D$). Mohyeddin et al. [9] also concluded that the modified CCD method shows a good agreement with their experimental results based on 70 tension tests on screw anchors in early age concrete (24 hours, 36 hours, 48 hours, 72 hours, 7 days, 14 days and 28 days).

Mohyeddin et al. [8] stated that the modified CCD method by Kuenzlen [6] included the results from both concrete cone failure and combined failure. Hence, the tensile resistance of the anchor might be overestimated due to combined failure, and the resistance may be underestimated due to concrete cone failure. Mohyeddin et al. [8] further conducted 182 tension tests and proposed a prediction model based on individual failure modes (i.e., pull-out, combined, and concrete cone failures). The database consists of screw anchors with a diameter ranging from 6.5 mm to 16 mm and h_{ef} ranging from 38 mm to 115 mm. In their study, about 60% of the specimens failed in a combined failure followed by pull-out failure. Chen et al. [10] further proposed a prediction model on combined failure modes. The proposed model was based on the database of 144 tension tests on three types of screw anchors with a diameter ranging from 6.35 mm to 12.7 mm and h_{nom} ranging from 38.1 mm to 101.6 mm. The concrete strengths are between 31.4 MPa and 32.4 MPa. The combined failure dominated about 80% of the test results for both shallow and deep embedment depths.

These experimental works have led to the inclusion of screw anchors in design standards (e.g., EN 1992-4:2018 [11]) for use in normal concrete. The screw anchor design, in accordance with EN 1992-4:2018 [11], follows the post-installed mechanical anchor design. However, the screw anchor may exhibit a similar failure behaviour to bonded anchor, which is a combined pull-out and concrete failure. Even though the CCD method adopted in EN 1992-4:2018 [11] has accounted for combined pull-out and concrete failure, however, recent studies [8, 10] have shown that it may still overpredict the resistance of the screw anchors. The design process stipulated in EN 1992-4:2018 [11] appears to be complicated for engineers who are not familiar with the anchor design, particularly in countries where EN 1992-4 was recently adopted, such as Malaysia [12]. Consequently, Ng et al. [13, 14] developed two-dimensional graphical tools for quick estimation of tensile and shear resistances of post-installed mechanical and bonded anchors. The studies discovered that the controlling failure mechanisms were found varied according to the types of anchors (mechanical or bonded) and the embedment depth of the anchor. It was foreseen that the graphical tools would be useful for practicing engineers for quick estimation of anchor resistances; however, the graphical tools were limited to anchors installed in C30/37 cracked concrete with 125 mm thick concrete members. In addition, there is no reported study to provide generalized solutions for screw anchor design.

This paper reviews the design methodology for screw anchors outlined in EN 1992-4:2018 [11] and introduces a novel graphical tool, referred to as a nomogram, for estimating screw anchor resistances in tension and shear. The nomogram represents anchor resistance as a function of the normalised effective embedment depth and edge distance, with details provided in subsequent sections. While not intended to replace detailed design software (e.g., Hilti PROFIS Engineering [15] or C-Fix Online by Fischer [16]), the nomogram offers a rapid preliminary estimation tool for screw anchor resistances and serves as an independent verification method for completed designs.

2. Design philosophy in EN 1992-4:2018 for anchors

The design principles in accordance with EN 1992-4:2018 [11] involved the calculation of the characteristic resistance (i.e., tensile and shear) of the anchor for each of the potential failure modes that could occur. The failure mode with the lowest resistance will govern the anchor design. Fig. 1 shows the schematic diagrams of the relevant failure modes for screw anchors under tensile and shear loads. The tensile failure modes are steel failure, pull-out failure, concrete cone failure, concrete splitting failure, and combined pull-out and concrete failure. It should be noted that combined pull-out and concrete failure is not explicitly mentioned in EN 1992-4:2018 [11]. On the other hand, the shear failure modes are steel failure with or without a lever arm, concrete pry-out failure, and concrete edge failure. The characteristic resistance of steel failure (under tensile and shear loads) and pull-out failure (under tensile load) is dependent on the material and mechanical properties of the anchors, which can be acquired from the relevant European Technical Assessment (ETA) reports. This work focuses on anchors without a lever arm. Hence, the steel failure with a lever arm is omitted in the present investigation.

Eqs. (3 to 21) are the equations to calculate the characteristic tensile and shear resistances for relevant concrete-related failure modes adopted from EN

1992-4:2018 [11]. The design in EN 1992-4:2018 [11] caters for the concrete strength classes ranging from C12/15 to C90/105, where the first number with a prefix 'C' denotes the characteristic concrete cylinder compressive strength and the second number denotes the characteristic concrete cube compressive strength. However, the characteristic concrete cylinder compressive strength (f_{ck}) shall not exceed 60 MPa even if a higher concrete strength class is used.

2.1. Tensile failure modes

(a) Concrete cone failure ($N_{Rk,c}$)

The concrete cone failure ($N_{Rk,c}$) is calculated using Eq. (3).

$$N_{Rk,c} = N_{Rk,c}^0 \left(\frac{A_{c,N}}{A_{c,N}^0} \right) (\varphi_{s,N}) (\varphi_{re,N}) (\varphi_{ec,N}) (\varphi_{M,N}) \quad (3)$$

where, $N_{Rk,c}^0$ is calculated using Eq. (4).

$$N_{Rk,c}^0 = k_1 (\sqrt{f_{ck}}) (h_{ef})^{1.5} \quad (4)$$

where, k_1 is taken as 7.7 for cracked concrete and 11.0 for uncracked concrete. $A_{c,N}^0$ is calculated as $s_{cr,N}^2$, where $s_{cr,N}$ is considered as $3h_{ef}$ (where h_{ef} is the effective embedment depth of the anchor). $A_{c,N}$ is calculated using Eq. (5).

For single anchor,

$$A_{c,N} = (c_1 + 0.5s_{cr,N})(c_2 + 0.5s_{cr,N}) \quad (5)$$

$\varphi_{s,N}$ is calculated using Eq. (6).

$$\varphi_{s,N} = 0.7 + 0.3 \left(\frac{c}{c_{cr,N}} \right) \leq 1 \quad (6)$$

where, c is the smallest edge distance and $c_{cr,N}$ is considered as $1.5h_{ef}$.

$\varphi_{re,N}$ is calculated using Eq. (7).

$$\varphi_{re,N} = 0.5 + \frac{h_{ef}}{200} \leq 1 \quad (7)$$

$\varphi_{re,N}$ is taken as 1 if the provided spacing of the reinforcement is more than 150 mm for reinforcement size with any diameter or the provided spacing of the reinforcement is more than 100 mm for reinforcement size with diameter of 10 mm or smaller.

$\varphi_{ec,N}$ is taken as 1 if there is no tensile load eccentricity, otherwise it shall be calculated using Eq. (8).

$$\varphi_{ec,N} = \frac{1}{1 + 2(e_N / s_{cr,N})} \leq 1 \quad (8)$$

where, e_N is the eccentricity of resultant tensile force of anchors in respect to the centre of gravity of the anchors.

$\varphi_{M,N}$ is the factor to cater for the effect of a compression force between fixture and concrete in cases of bending moments with or without axial force. For single anchor, $\varphi_{M,N}$ can be taken as 1. The remaining symbols have been defined previously.

(b) Concrete splitting failure ($N_{Rk,sp}$)

The concrete splitting failure ($N_{Rk,sp}$) is calculated using Eq. (9).

$$N_{Rk,sp} = N_{Rk,sp}^0 \left(\frac{A_{c,N}}{A_{c,N}^0} \right) (\varphi_{s,N}) (\varphi_{re,N}) (\varphi_{ec,N}) (\varphi_{h,sp}) \quad (9)$$

where, $N_{Rk,sp}^0 = \min \{N_{Rk,p}^0, N_{Rk,c}^0\}$, $A_{c,N}$, $A_{c,N}^0$, $\varphi_{s,N}$, $\varphi_{re,N}$, and $\varphi_{ec,N}$ shall be calculated according to concrete cone failure (refer to Eqs. (5 to 8)), however the values $c_{cr,N}$ and $s_{cr,N}$ shall be replaced by $c_{cr,sp}$ and $s_{cr,sp}$, which is acquired from the relevant ETA reports.

$\varphi_{h,sp}$ is calculated using Eq. (10).

$$\varphi_{h,sp} = \left(\frac{h}{h_{min}} \right)^{2/3} \leq \max \left\{ 1; \left(\frac{h_{ef} + 1.5c_1}{h_{min}} \right)^{2/3} \right\} \leq 2 \quad (10)$$

where, h_{\min} is the minimum allowed thickness of the concrete member. The remaining symbols have been defined previously.

2.2. Shear failure modes

(a) Concrete pry-out failure ($V_{Rk,cp}$)

For anchor without supplementary reinforcement, the concrete pry-out failure ($V_{Rk,cp}$) is calculated using Eq. (11).

$$V_{Rk,cp} = k_8 (N_{Rk,c}) \quad (11)$$

where, k_8 is acquired from the relevant ETA reports. $N_{Rk,c}$ is calculated using Eq. (3).

(b) Concrete edge failure ($V_{Rk,c}$)

The concrete edge failure ($V_{Rk,c}$) is calculated using Eq. (12).

$$V_{Rk,c} = V_{Rk,c}^0 \left(\frac{A_{c,v}}{A_{c,v}^0} \right) (\varphi_{s,v}) (\varphi_{h,v}) (\varphi_{ec,v}) (\varphi_{\alpha,v}) (\varphi_{re,v}) \quad (12)$$

where, $V_{Rk,c}^0$ is calculated using Eq. (13).

$$V_{Rk,c}^0 = k_9 (d_{nom})^\alpha (l_f)^\beta (f_{ck})^{1/2} (c_1)^{1.5} \quad (13)$$

where, k_9 is taken as 1.7 for cracked concrete and 2.4 for uncracked concrete. α is calculated as $0.1(l_f/c_1)^{0.5}$, and β is calculated as $0.1(d_{nom}/c_1)^{0.2}$. d_{nom} and l_f are acquired from the relevant ETA reports; the limiting values of l_f is shown in Eqs. (14) and (15).

For case $d_{nom} \leq 24$ mm,

$$l_f = h_{ef} \leq 12d_{nom} \quad (14)$$

For case $d_{nom} > 24$ mm,

$$l_f = h_{ef} \leq \max \{8d_{nom}; 300 \text{ mm}\} \quad (15)$$

$A_{c,v}^0$ is calculated as $4.5c_1^2$ and $A_{c,v}$ is calculated using Eqs. (16) and (17). For single anchor,

$$\text{If } h \geq 1.5c_1; A_{c,v} = 1.5c_1(c_2 + 1.5c_1) \quad (16)$$

$$\text{If } h < 1.5c_1; A_{c,v} = h(c_2 + 1.5c_1) \quad (17)$$

$\varphi_{s,v}$ is calculated using Eq. (18).

$$\varphi_{s,v} = 0.7 + 0.3 \left(\frac{c_2}{1.5c_1} \right) \leq 1 \quad (18)$$

$\varphi_{h,v}$ is calculated using Eq. (19).

$$\varphi_{h,v} = \left(\frac{1.5c_1}{h} \right)^{0.5} \geq 1 \quad (19)$$

$\varphi_{ec,v}$ is taken as 1 if there is no shear load eccentricity, otherwise it shall be calculated using Eq. (20).

$$\varphi_{ec,v} = \frac{1}{1 + 2(e_v / 3c_1)} \leq 1 \quad (20)$$

where, e_v is the eccentricity of resultant shear force of anchors in respect to the centre of gravity of the anchors.

$\varphi_{\alpha,v}$ is calculated using Eq. (21).

$$\varphi_{\alpha,v} = \left(\frac{1}{(\cos \alpha_v)^2 + (0.5 \sin \alpha_v)^2} \right)^{1/2} \geq 1 \quad (21)$$

where, α_v is the angle between design shear load V_{Ed} and a line perpendicular to the verified edge ($0^\circ \leq \alpha_v \leq 90^\circ$).

$\varphi_{re,v}$ shall be taken as 1 for anchor in uncracked and cracked concrete without edge reinforcement or stirrups, and 1.4 for anchor in cracked concrete with edge reinforcement and closely spaced stirrups or wire mesh with spacing $a \leq 100$ mm and $a \leq 2c_1$. It is noted that a factor $\varphi_{re,v} > 1$ for applications in cracked concrete shall only be applied, if the h_{ef} of the anchor is at least 2.5 times the concrete cover of the edge reinforcement. The remaining symbols have been defined previously, in a consistent manner.

3. Nomogram for screw anchors design

The equations in EN 1992-4:2018 [11] can be complicated for many engineers, given that many parameters are required in the design. Hence, this work aims to develop a new graphical diagram (called nomogram) for a quick estimation of the preliminary design of screw anchors. The nomogram provides the resistances (i.e., tensile and shear) of the screw anchor encompassing all concrete-related failures based on the effective embedment depth of the anchor (h_{ef}), and edge distance (c), in a cracked concrete condition.

3.1. Parameters selection

Table 1 shows the range of parameters adopted from various ETA reports for post-installed screw anchors. Based on Table 1, typical anchor sizes of M6, M8, M10, M12, M14, and M16 are selected in this research. The effective embedment depth ratio (h_{ef}/D) ranges from 3 to 16. The minimum allowable thickness of the concrete member (h_{\min}) is taken as the maximum of 100 mm

Table 1
Range of parameters for post-installed screw anchors

ETA	Anchor size	h_{ef}/D	h_{\min} (mm)	$c_{cr,sp}$ (mm)	k_8	d_{nom} (mm)	l_f (mm)
ETA-08/0307 [17]	M6, M8, M10, M14	3.7 to 7.5	max (100 mm; 1.8 h_{ef} to 2.7 h_{ef})	1.5 h_{ef} to 1.8 h_{ef}	1.5 to 2	Equal to D	Equal to h_{ef}
ETA-13/1038 [18]	M6, M8, M10, M14	3.5 to 7	max (80 mm; 2.2 h_{ef} to 2.7 h_{ef})	1.5 h_{ef} to 2 h_{ef}	1 to 2	Equal to D	Equal to h_{ef}
ETA-19/0170 [19]	M8, M10	5.9 to 6.5	max (100 mm; 2.2 h_{ef})	1.3 h_{ef} to 1.5 h_{ef}	2	Equal to D	Equal to h_{ef}
ETA-20/0867 [20]	M8, M10, M12, M14, M16	3.5 to 8	max (80 mm; 1.8 h_{ef} to 2.7 h_{ef})	1.5 h_{ef} to 1.8 h_{ef}	1 to 2	Equal to D	Equal to h_{ef} or h_{nom}
ETA-15/0352 [21]	M6, M8, M10, M12, M14	3.5 to 7.3	max (80 mm; 1.8 h_{ef} to 2.5 h_{ef})	1.5 h_{ef}	1 to 2	Equal to D	Equal to h_{nom}
ETA-17/0740 [22]	M8, M10, M12	3.9 to 6.8	max (100 mm; 1.8 h_{ef} to 2.5 h_{ef})	1.5 h_{ef}	1 to 2	Equal to D	Equal to h_{nom}
ETA-16/0043 [23]	M6, M8, M10, M12, M14	4.1 to 7.3	max (80 mm; 1.5 h_{ef} to 2.6 h_{ef})	1.4 h_{ef} to 1.9 h_{ef}	1 to 2	Equal to D	Equal to h_{ef}
ETA-20/0731 [24]	M6, M8, M10, M12, M14	4.1 to 7.3	max (80 mm; 1.5 h_{ef} to 2.6 h_{ef})	1.4 h_{ef} to 1.9 h_{ef}	1 to 2	Equal to D	Equal to h_{ef}

Notes: D is the diameter of the anchor, d_{nom} is the outer diameter of the anchor, h_{ef} is the effective embedment depth of the anchor.

or two times the effective embedment depth of the anchor ($2h_{ef}$). The characteristic edge distance for concrete splitting failure ($c_{cr,sp}$) is taken as $1.5h_{ef}$. According to EAD 330232 [25], the resistance to pry-out failure test is optional, and default values of k_8 (i.e., k_8 equals 1 if the effective embedment depth (h_{ef}) is less than 60 mm, and k_8 equals 2 if the effective embedment depth (h_{ef}) is equal to or greater than 60 mm) can be used if the tests are not performed. It is noted that this assumption might give a lower bound of characteristic resistance of concrete pry-out failure. d_{nom} is taken as D (diameter of the anchor), and l_f is taken as h_{ef} with limitation as shown in Eqs. (14) and (15). Importantly, cracked concrete was assumed, given that it is challenging to ensure concrete will not crack in the actual construction and also throughout the service life of the connection. Also, dense reinforcement is assumed, as most concrete structures are provided with reinforcements. This assumption will give more conservative results.

3.2. Development of nomogram

The conceptual flowchart for creating the nomogram is shown in Fig. 2. As mentioned earlier, the characteristic resistance of steel failure (under tensile and shear loads) and pull-out failure (under tensile load) depends on the material and mechanical properties of the anchors, which can be acquired from the relevant ETA reports.

The graphs in the nomogram provide the characteristic resistances of the screw anchor for relevant concrete-related failures (i.e., concrete cone failure and concrete splitting failure under tensile load, and concrete pry-out failure and concrete edge failure under shear load) in terms of the effective embedment

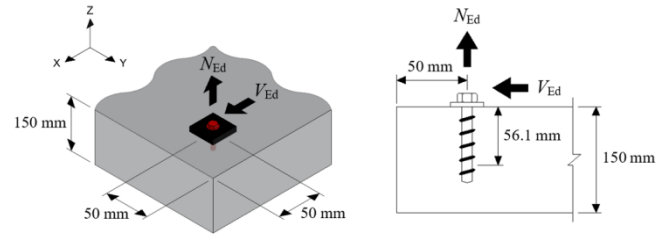


Fig. 3 Details of Model 1

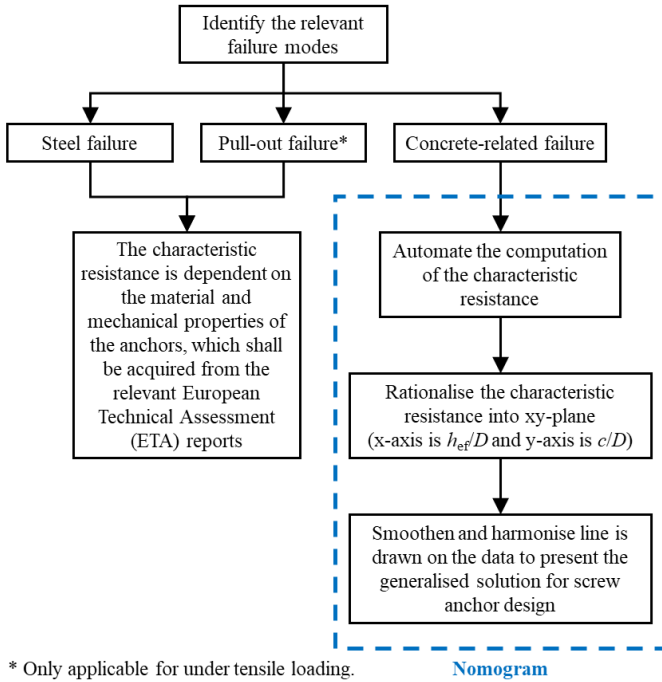
depth of the anchor (h_{ef}) and edge distance (c), in a cracked concrete condition with the material partial safety factor excluded. User of the nomogram is required to apply the safety factor after getting the characteristic values, to arrive at a design resistance. A design spreadsheet is first created to automate the computation of the characteristic resistance (i.e., tensile and shear) of screw anchors for each concrete-related failure. The design spreadsheet was verified using commercial software, e.g., Hilti PROFIS Engineering [15] or C-Fix Online by Fischer [16]. Then, the characteristic resistance is rationalised into xy-plane (x-axis is h_{ef}/D and y-axis is c/D). Lastly, a smoothened and harmonised line is drawn on the data to represent the generalised solution for screw anchor design. Nomograms for tensile and shear resistances for different anchor sizes are presented in Appendix A and Appendix B, respectively.

3.3. Verification of the nomogram

An explicit check on the screw anchor design that incorporates the nomogram is proposed and discussed here. Four models were verified using variables such as anchor size, concrete cylinder compressive strength (f_{ck}), effective embedment depth of the anchor (h_{ef}), edge distance (c), and concrete member thickness (h). An example of details for Model 1 is shown in Fig. 3. The edge distance for Models 1 and 3 is less than the characteristic edge distance ($c < c_{cr,N}$), while for Models 2 and 4, the edge distance is equal to or greater than the characteristic edge distance ($c \geq c_{cr,N}$). Table 2 shows a summary of the details and compares the results from the commercial software with those from the nomogram.

From Table 2, it can be seen that the results of the explicit checks concur well (within 7%) with the results obtained from the commercial software. The discrepancy in the results could be due to the smoothened line in producing the nomogram, as the round-off values for the reading were done manually. In subsequent discussions (see Section 5), the effect of the coefficient of variation (CV_F) was found to range from 10% to 15%. Therefore, the observed 7% discrepancy using the nomogram falls within the allowable variation range for anchor capacity and is deemed acceptable, making it suitable for preliminary estimation purposes. In the case of shear resistance for Model 2, the proposed nomogram underestimated the shear resistance for concrete pry-out failure. It is due to assumptions made for the k_8 values (k_8 value is equal to 1 for $h_{ef} < 60$ mm, and 2 for $h_{ef} \geq 60$ mm). A higher k_8 value is expected if the anchor product is tested for pry-out failure. Hence, readers are advised to obtain the tested k_8 value from the relevant ETA reports and incorporate it into Eqs. (22) and (23), if more accurate prediction is required.

$$\text{For } h_{ef} < 60 \text{ mm, } V_{Rk,cp}(\text{modified}) = V_{Rk,cp}(k_8(\text{ETA})) \quad (22)$$



* Only applicable for under tensile loading.

Fig. 2 Flowchart of the procedure for creating the nomogram

Table 2

Details for verification of nomograms

Model	Anchor size	f_{ck} (MPa)	h_{ef} (mm)	c (mm)	h (mm)	Tensile						Shear			
						Design resistance (kN)		$\frac{N_{sw}}{N_{nom}}$	Failure mode		Design resistance (kN)		$\frac{V_{sw}}{V_{nom}}$	Failure mode	
						N_{sw}	N_{nom}		Software	Nomogram	V_{sw}	V_{nom}		Software	Nomogram
						software	nomogram				software	nomogram			
1	M8	30	56.1	50	150	5.1	5.3	0.96	C or SP	C	2.7	2.7	1.00	CE	CE
2				200	250	9.2	9.3	0.99	C	C	16.6	9.2*	1.80	CE	CP*
												16.9+	0.98		CE+
3	M12	50	79.9	80	500	14.6	15.7	0.93	C	C	7.4	7.8	0.95	CE	CE
4				300	300	23.3	23.9	0.97	C	C	35.9	35.9	1.00	S	S

Notes:

The anchor size is equal to the diameter of the anchor (D); S is steel failure; C is concrete cone failure; SP is concrete splitting failure; CE is concrete edge failure; CP is concrete pry-out failure.

* The result is based on the default value of k_8 assumed in the nomogram.

* The result is based on the k_8 value obtained from ETA.

$$\text{For } h_{ef} \geq 60 \text{ mm, } V_{Rk,cp}(\text{modified}) = V_{Rk,cp} \left(\frac{k_8(ETA)}{2} \right) \quad (23)$$

where, $V_{Rk,cp}$ is the characteristic resistance of concrete pry-out failure obtained from the nomograms. $k_8(ETA)$ is acquired from the relevant ETA reports.

3.4. Applicable range and limitations of the nomogram

Some assumptions were made while developing the nomograms. The applicable range and limitations of the nomogram are highlighted below:

- applicable for the design of single screw anchor sizes of M6, M8, M10, M12, M14, and M16 in cracked concrete with no eccentricity;
- effective embedment depth ratio (h_{ef}/D) ranges from 3 to 16;
- edge distance (c) ranges from $2D$ to greater than $c_{cr,N}$. One edge distance in the x-direction and one edge distance in the y-direction, which are not less than $c_{cr,N}$ or $c_{cr,sp}$. Edge distance in the x-direction is equal to edge distance in the y-direction;
- dense reinforcement is assumed (i.e., spacing between reinforcements < 100 mm for reinforcement diameter ≤ 10 mm, or spacing between reinforcements < 150 mm for others reinforcement diameter);
- the minimum thickness of the concrete member allowed is assumed as $h_{min} = \max(100 \text{ mm}; 2h_{ef})$;
- characteristic edge distance for concrete splitting failure ($c_{cr,sp}$) is assumed equal to concrete cone failure, which is $1.5h_{ef}$;
- default values of k_8 were assumed. k_8 value is equal to 1 for $h_{ef} < 60$ mm, and 2 for $h_{ef} \geq 60$ mm; and
- applicable for concrete-related failures, i.e., concrete cone failure and concrete splitting failure for tensile, and concrete pry-out failure and concrete edge failure for shear.

4. Guide and a worked example of using the nomogram

The use of the proposed nomograms for screw anchor design is herein

demonstrated. Flowcharts are provided in Fig. 4 for tensile resistance and Fig. 5 for shear resistance to facilitate the explanation.

4.1. Tensile resistance for screw anchor

Refer to Fig. 4, the tensile resistance of screw anchors can be estimated in 6 steps.

Step 1: Select the type of screw anchor prior to calculating the anchor resistance.

Step 2: Define the anchor diameter (D), characteristic concrete cylinder compressive strength (f_{ck}), effective embedment depth (h_{ef}), edge distance (c), and concrete member thickness (h).

Step 3a: Obtain the characteristic resistance ($N_{Rk,s}$) and partial factor ($\gamma_{Ms,N}$) for steel failure.

$N_{Rk,s}$ is dependent on the material and mechanical properties of the anchors, which shall be acquired from the relevant ETA reports.

Step 3b: Calculate the design resistance of steel failure ($N_{Rd,s}$) using Eq. (24).

$$N_{Rd,s} = \frac{N_{Rk,s}}{\gamma_{Ms,N}} \quad (24)$$

Step 4a: Obtain the characteristic resistance ($N_{Rk,p}$) and installation factor (γ_{inst}) for pull-out failure.

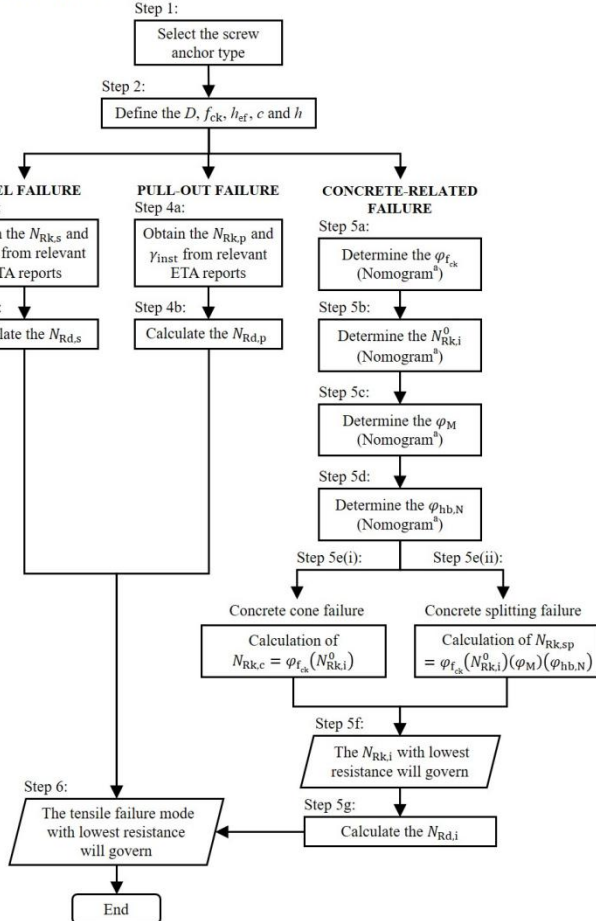
$N_{Rk,p}$ is dependent on the material and mechanical properties of the anchors, which shall be acquired from the relevant ETA reports. It should be noted that an influence factor of concrete strength (ϕ_{fck}) shall be multiplied, and as shown in Eq. (25).

$$N_{Rk,p} = \phi_{fck}(N_{Rk,p}(C20/25)) \quad (25)$$

Step 4b: Calculate the design resistance of pull-out failure ($N_{Rd,p}$) using Eq. (26).

$$N_{Rd,p} = \frac{N_{Rk,p}}{\gamma_{Mp}} \quad (26)$$

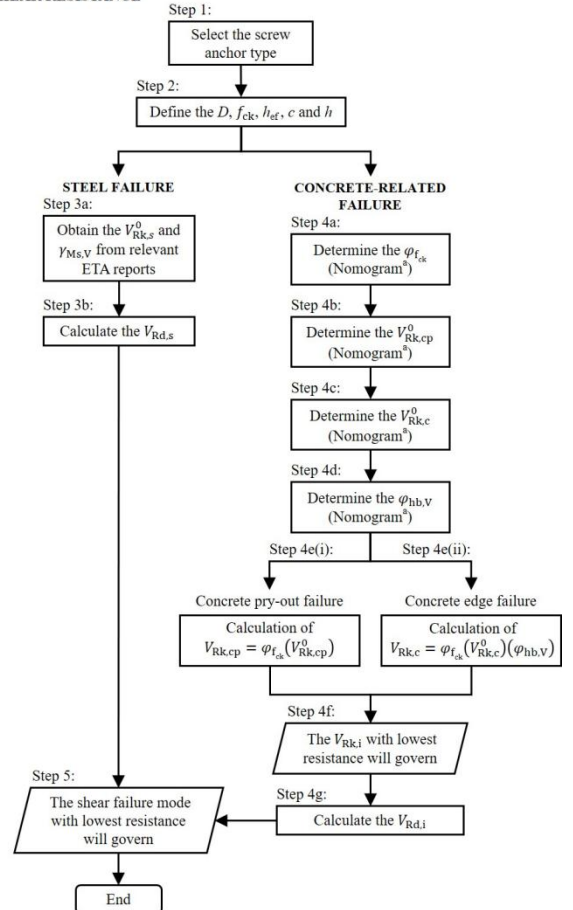
TENSILE RESISTANCE



Note: *The nomogram is referred to Figures A1 to A6.

Fig. 4 Flowchart of using the nomogram for tensile resistance

SHEAR RESISTANCE



Note: *The nomogram is referred to Figures B1 to B6.

Fig. 5 Flowchart of using the nomogram for shear resistance

where, $\gamma_{Mp} = \gamma_c(\gamma_{inst})$. The value γ_c can be taken as 1.5 in accordance with EN 1992-1-1.

Step 5a: Determine the influence factor of concrete strength (ϕ_{fck}).

ϕ_{fck} is determined using the nomogram proposed in Appendix A (refer to the bottom left diagram in Figs. A1(a) to A6(a), where the details for Figs. A1 to A6 will be demonstrated in a worked example later). As mentioned earlier, the characteristic concrete cylinder compressive strength (f_{ck}) shall not exceed 60 MPa even if a higher concrete strength class is used.

Step 5b: Determine the characteristic resistance for concrete-related failure ($N_{Rk,i}^0$).

$N_{Rk,i}^0$ is determined using the nomogram proposed in Appendix A (refer to the top right diagram in Figs. A1(b) to A6(b)). First, the normalised effective embedment depth (h_{ef}/D) and edge distance (c/D) are calculated. The identified point is the value of $N_{Rk,i}^0$.

Step 5c: Determine the modification factor (ϕ_M).

ϕ_M is determined using the nomogram proposed in Appendix A (refer to the middle right diagram in Figs. A1(c) to A6(c)). First, the $N_{Rk,sp}^0 (C20/25)$ and h_{ef}/D are located. The identified point is the value of ϕ_M .

Step 5d: Determine the influence factor of member thickness for the tensile load ($\phi_{hb,N}$).

$\phi_{hb,N}$ is determined using the nomogram proposed in Appendix A (refer to the bottom right diagram in Figs. A1(d) to A6(d)). Two identified points are positioned. The first identified point is based on h_{ef}/D and c/D , another identified point is based on h_{ef}/D and h . The identified point with the lowest value is taken as $\phi_{hb,N}$.

Step 5e(i): Calculate the characteristic resistance for concrete cone failure using Eq. (27).

$$N_{Rk,c} = \phi_{fck}(N_{Rk,i}^0) \quad (27)$$

Step 5e(ii): Calculate the characteristic resistance for concrete splitting failure using Eq. (28).

$$N_{Rk,sp} = \phi_{fck}(N_{Rk,i}^0)(\phi_M)(\phi_{hb,N}) \quad (28)$$

Step 5f: Obtain the $N_{Rk,i}$.

$N_{Rk,i}$ is obtained as the minimum of $N_{Rk,c}$ and $N_{Rk,sp}$ calculated in Eqs. (27) and (28), respectively. The lowest resistance is chosen and will govern the concrete-related failure.

Step 5g: Calculate the design resistance of concrete-related failure ($N_{Rd,i}$) using Eq. (29).

$$N_{Rd,i} = \frac{N_{Rk,i}}{\gamma_{Mc}} \quad (29)$$

where, $\gamma_{Mc} = \gamma_c(\gamma_{inst})$. The value γ_c can be taken as 1.5 in accordance with EN 1992-1-1.

Step 6: Compute the tensile resistance of the screw anchor.

The tensile resistance of the screw anchor is obtained by comparing the design resistance of steel failure, $N_{Rd,s}$ (Eq. 24), pull-out failure, $N_{Rd,p}$ (Eq. 26), and concrete-related failure, $N_{Rd,i}$ (Eq. 29). The tensile failure mode with the lowest resistance will govern the design.

4.2. Shear resistance for screw anchor

Refer to Fig. 5, the shear resistance of screw anchors can be estimated in 5 steps.

Step 1: Select the type of screw anchor prior to calculating the anchor resistance.

Step 2: Define the anchor diameter (D), characteristic concrete cylinder strength (f_{ck}), effective embedment depth (h_{ef}), edge distance (c), and concrete member thickness (h).

Step 3a: Obtain the characteristic resistance of a single anchor ($V_{Rk,s}^0$) and partial factor ($\gamma_{Ms,V}$) for steel failure.

It should be noted that the characteristic resistance for steel failure ($V_{Rk,s}$) is taken as $V_{Rk,s}^0$, as the ductility factor (k_7) for single anchor is taken as 1. $V_{Rk,s}^0$ is dependent on the material and mechanical properties of the anchors, which shall be acquired from the relevant ETA reports.

Step 3b: Calculate the design resistance of steel failure ($V_{Rd,s}$) using Eq. (30).

$$V_{Rd,s} = \frac{V_{Rk,s}}{\gamma_{Ms,V}} \quad (30)$$

Step 4a: Determine the influence factor of concrete strength (ϕ_{fck}).

ϕ_{fck} is determined using the nomogram proposed in Appendix B (refer to the top right diagram in Figs. B1(a) to B6(a), where the details for Figs. B1 to B6 will be demonstrated in a worked example in Section 4.3 in this paper). As mentioned earlier, the characteristic concrete cylinder compressive strength (f_{ck}) shall not exceed 60 MPa even if a higher concrete strength class is used.

Step 4b: Determine the characteristic resistance for concrete pry-out failure ($V_{Rk,cp}^0$).

$V_{Rk,cp}^0$ is determined using the nomogram proposed in Appendix B (refer to the bottom left diagram in Figs. B1(b) to B6(b)). First, the normalised effective embedment depth (h_{ef}/D) and edge distance (c/D) are calculated. The identified point is the value of $V_{Rk,cp}^0$.

Step 4c: Determine the characteristic resistance for concrete edge failure ($V_{Rk,c}^0$).

$V_{Rk,c}^0$ is determined using the nomogram proposed in Appendix B (refer to the bottom middle diagram in Figs. B1(c) to B6(c)). The h_{ef}/D and c/D are located, and the identified point is the value of $V_{Rk,c}^0$.

Step 4d: Determine the influence factor of member thickness for the shear load ($\phi_{hb,V}$).

$\phi_{hb,V}$ is determined using the nomogram proposed in Appendix B (refer to the bottom right diagram in Figs. B1(d) to B6(d)). The c/D and h are located, and the identified point is the value of $\phi_{hb,V}$.

Step 4e(i): Calculate the characteristic resistance for concrete pry-out failure using Eq. (31).

$$V_{Rk,cp} = \phi_{fck}(V_{Rk,cp}^0) \quad (31)$$

Step 4e(ii): Calculate the characteristic resistance for concrete edge failure using Eq. (32).

$$V_{Rk,c} = \phi_{fck}(V_{Rk,c}^0)(\phi_{hb,V}) \quad (32)$$

Step 4f: Obtain the $V_{Rk,i}$.

$V_{Rk,i}$ is obtained as the minimum of $V_{Rk,cp}$ and $V_{Rk,c}$, where they can be calculated in Eqs. (31) and (32), respectively. The lowest resistance governs the concrete-related failure.

Step 4g: Calculate the design resistance of concrete-related failure ($V_{Rd,i}$) using Eq. (33).

$$V_{Rd,i} = \frac{V_{Rk,i}}{\gamma_{Mc}} \quad (33)$$

where, $\gamma_{Mc} = \gamma_c(\gamma_{inst})$. The value γ_c can be taken as 1.5 in accordance with EN 1992-1-1.

Step 5: Compute the shear resistance of the screw anchor.

The shear resistance of the screw anchor is obtained by comparing the design resistance of steel failure, $V_{Rd,s}$ (Eq. 30), and concrete-related failure, $V_{Rd,i}$ (Eq. 33). The shear failure mode with the lowest resistance will govern the design.

4.3. Design example

Detailed calculations on the nomogram used to calculate the tensile and shear resistances of screw anchors are demonstrated in Appendix C. The design example refers to a single post-installed screw anchor used in a reinforced-concrete structure, as shown in Fig. 3. The details are based on Model 1, as shown in Table 2. The considered concrete grade is C30/37. The anchor size is M8 ($D = 8$ mm), with effective embedment depth, $h_{ef} = 56.1$ mm, and edge distance, $c = 50$ mm. The structure has a thickness, $h = 150$ mm.

5. Corroboration of predicted resistance in EN 1992-4:2018 with experimental results

A total of 197 test results were collected and used for further analysis in this study. The experimental test databases were collected from previous works of literature [8, 9, 10, 26, 27, 28, 29, 30, 31], and only the tensile resistance of the screw anchors have been compared with nomograms developed as a part of this study. It is known that shear failure of screw anchors is unlikely, except for situation where the anchors are located near the edge. Also, there are limited data available in the literature for shear tests of screw anchors. Table 3 shows the summary of the screw anchor database. The analysis focuses on concrete-related failures under tension, which include concrete cone failure, and combined pull-out and concrete failure. This is because the steel failure and pull-out failure due to the material and mechanical properties of anchors were excluded in the nomogram; hence is also excluded in the screw anchor database. The cracked or uncracked concrete conditions are also documented in Table 3.

Table 3

Summary of the screw anchor database

Data source	Diameter range (mm)	Embedment depth range (mm)	Concrete strength* (MPa)	State of concrete	Number of tests	Failure mode
Abdul-Hamid et al. [26]	6.4 to 12.7	49.3 to 75.9	33.7	Uncracked	14	CO
Chen et al. [10]	6.4 to 12.7	38.1 to 101.6	31.4 to 32.4	Uncracked	100	C/CO
Hoehler & Eligehausen [27]	12	76	21.8* to 26.8*	Cracked	5	C
Mohyeddin et al. [8]	6.5 to 12	38 to 98	33.5 to 35.4	Uncracked	20	CO
Mohyeddin et al. [9]	16	115	9.9 to 41.8	Uncracked	12	CO
Mohyeddin et al. [28]	10	53.8 to 74.2	37.5 to 49.5	Uncracked	29	C/CO
Mohyeddin et al. [29]	16	115	25 & 40	Uncracked	4	CO
Obayes et al. [30]	12	80	6.1 to 22	Uncracked	11	C
Ng et al. [31]	10	45 & 75	20.3 & 29.3	Uncracked	2	C/SP
Total	6.4 to 16	38 to 115	6.1 to 49.5	Cracked/Uncracked	197	C/CO/SP

Notes:

Pull-out failure has been excluded from the database as it is product-dependent.

C is concrete cone failure; CO is combined pull-out and concrete failure; SP is concrete splitting failure.

* The concrete strength refers to concrete cylinder compressive strength.

* The concrete cylinder compressive strength is taken as 0.85 of the concrete cube compressive strength.

The resistance obtained using EN 1992-4:2018 [11] is the characteristic value. Hence, a conversion from the characteristic to the mean value of resistance is required to corroborate with the experimental results. EAD 330232 [25] stipulated $F_{u,5\%} = F_{u,m}(1 - k_s CV_F)$. The ratio of mean resistance to characteristic resistance is very much dependent on the coefficient of variation (CV_F) of the failure load in the test. As stipulated in EAD 330232 [25], the CV_F value shall not exceed 30%. However, from the author's experience [8, 9, 28, 29], the CV_F value for screw anchor typically ranges from 10% to 15%. Fig. 6 shows the comparison of results between the nomogram and the experimental results. For a fair comparison, the characteristic values obtained from the nomogram for cracked concrete condition were converted to uncracked concrete condition using a linear conversion (i.e., Eq. (4) stipulated $k_1 = 7.7$ for uncracked concrete and $k_1 = 11$ for cracked concrete, then the linear conversion factor to get the uncracked concrete condition is $11/7.7 = 1.43$). Assuming a small variation of $CV_F = 10\%$ (see Fig. 6(a)), the mean resistance is about 1.2 times the characteristic resistance ($F_{u,m}/F_{u,5\%} = 1.197$). Comparing the nomogram results with the experimental results, the average is good, but approximately 48% of the nomogram results overestimated the resistance of the

screw anchor. The overestimation percentage is increased to approximately 69% if the $CV_F = 15\%$ (see Fig. 6(b)), and further increased to 83% if the $CV_F = 20\%$ (see Fig. 6(c)). If the failure load results are very scattered in the tests, i.e., $CV_F = 30\%$ (see Fig. 6(d)), the mean value is about two times the characteristic resistance ($F_{u,m}/F_{u,5\%} = 1.974$), which is unlikely to occur, with 100% of the results being unconservative. In general, the modified CCD method adopted in EN 1992-4:2018 [11] seemingly overestimated the resistance of the screw anchor, which may lead to unconservative results.

6. Conclusions

Screw anchors exhibit a different failure behaviour (i.e., combined pull-out and concrete failure) as compared to other post-installed mechanical anchors (e.g., undercut anchor and expansion anchor with steel failure, pull-out failure, concrete cone failure, and concrete splitting failure being the common failure modes). The screw anchor design following the post-installed mechanical anchor design in EN 1992-4:2018 may lead to unconservative resistance predictions. Hence, this paper has reviewed the screw anchor design in EN 1992-4:2018 and corroborated with experimental results.

A novel graphical tool (called nomogram) is proposed to facilitate the quick estimation of the characteristic resistances (tensile and shear) of screw anchors for concrete-related failures in EN 1992-4:2018, for cracked concrete condition. The effectiveness of the proposed nomograms was demonstrated and illustrated with an example. The authors anticipate that the proposed nomograms could serve as a useful tool for practising engineers to obtain a quick and reliable estimation of screw anchor resistance within the limitations of the nomograms. The readers are advised to obtain the tested k_8 value from the relevant ETA reports and incorporate it into Eqs. (22) and (23) for a more accurate prediction of shear resistance for concrete pry-out failure.

This study demonstrated that the modified CCD method adopted in EN 1992-4:2018 seemingly overestimated the resistance of the screw anchor. Approximately 48% to 69% of the predicted results exceeded the experimental results if CV_F is ranging from 10% to 15%. Hence, further research is required for a better method to design the screw anchors; for example, a mechanical model can be developed. In addition, the proposed nomogram can be further extended to group anchors or other specific conditions, such as anchors with a lever arm, different reinforcement configurations or more complex loading conditions.

Acknowledgement

The authors would like to thank Hilti Malaysia for providing their technical input and supplying the engineering software. Also, the contribution of AEFAC in various technical discussions is gratefully acknowledged.

References

- [1] Yan J., Liew R.J.Y. and Zhang M., "Shear-tension interaction strength of J-hook connectors in steel-concrete-steel sandwich structure", *Advanced Steel Construction*, 11(1), 73-94, 2015.
- [2] Shan Z., Su R.K.L., Looi, D.T.W. and Chen L., "A review of direct fastening steel jacket for

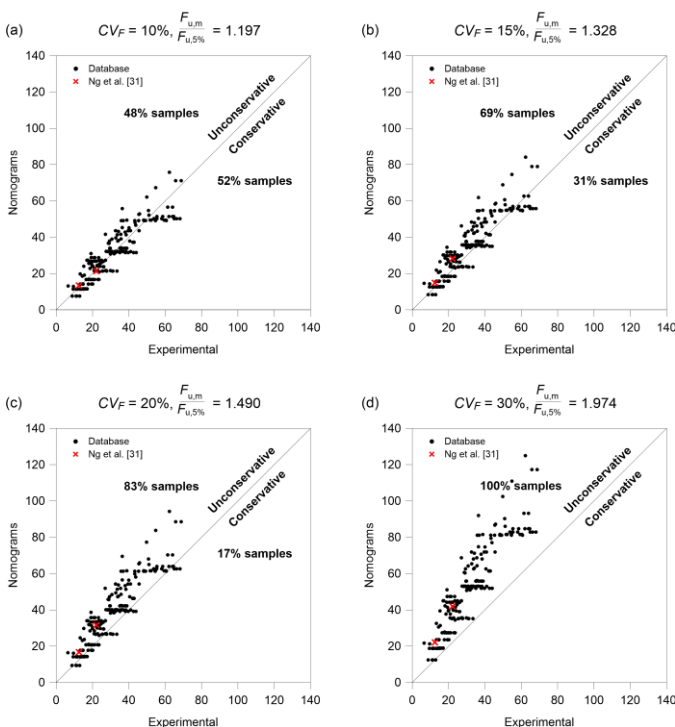
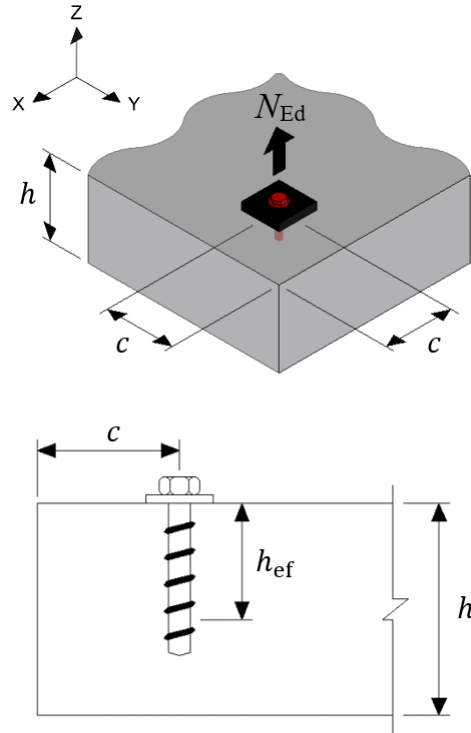


Fig. 6 Comparison of nomogram results and experimental results: (a) $CV_F = 10\%$, (b) $CV_F = 15\%$, (c) $CV_F = 20\%$, and (d) $CV_F = 30\%$

- strengthening of reinforced concrete columns", *Advanced Steel Construction*, 19(4), 383-388, 2023.
- [3] Olsen J., Pregartner T. and Lamanna A.J., "Basis for design of screw anchors in concrete", *ACI Structural Journal*, 109(4), 559-567, 2012.
- [4] Karmazinová M., Melcher J. and Kala Z., "Design of expansion anchors to concrete based on results of experimental verification", *Advanced Steel Construction*, 5(4), 390-405, 2009.
- [5] Kuenzlen J.H.R. and Eligehausen R., "Load bearing behaviour of fastenings with concrete screws", *Otto-Graf Journal*, 13, 27-51, 2002.
- [6] Kuenzlen J.H.R., Load-bearing behaviour of screw anchors under axial tension [dissertation], University of Stuttgart, Stuttgart, 2005. (in German)
- [7] Fuchs W., Eligehausen R. and Breen J.E., "Concrete capacity design (CCD) approach for fastening to concrete", *ACI Structural Journal*, 92(1), 73-94, 1995.
- [8] Mohyeddin A., Gad E.F. and Lee J., "Failure modes and tensile strength of screw anchors in non-cracked concrete", *Construction and Building Materials*, 221, 501-513, 2019.
- [9] Mohyeddin A., Gad E.F., Yangdon K., Khandu R. and Lee J., "Tensile load capacity of screw anchors in early age concrete", *Construction and Building Materials*, 127, 702-711, 2016.
- [10] Chen Z., Nassiri S. and Lamanna A., "Investigation of a combined failure mode for screw anchors under tension", *Advances in Structural Engineering*, 23(13), 2803-2812, 2020.
- [11] EN 1992-4, European Standard: Design of concrete structures - Part 4 Design of fastenings for use in concrete, British Standard Institution, 2018.
- [12] MS EN 1992-4, Malaysia Standard: Design of concrete structures - Part 4 Design of fastenings for use in concrete, Department of Standards Malaysia, 2023.
- [13] Ng L.T., Wong E.S.W. and Looi D.T.W., "Feasible design tensile capacity of post-installed anchors based on the new Eurocode 2: Part 4 (2018)", In: Belayutham S., Che Ibrahim C.K.I., Alisibramulisi A., Mansor H. and Billah M., editors, *Proceedings of the 5th International Conference on Sustainable Civil Engineering Structures and Construction Materials (SCESCM 2020)*, Lecture Notes in Civil Engineering, Springer, Singapore, 819-836, 2022.
- [14] Ng L.T., Looi D.T.W., Lee J. and Ng A.L.Y., "A simplified design solution for shear capacity of post-installed anchors encompassing all failure modes in EC2-4 (2018)", In: Kwong K.Z., Alengaram U.J., Raman S.N., Jumaat Z., Ng S.C., Chua Y.S. and Alisibramulisi A., editors, *Proceedings of the 15th International Conference on Concrete Engineering and Technology (CONCET2022)*, Journal of Physics: Conference Series, IOP Publishing, 2521, 012014, 2023.
- [15] Hilti, PROFIS Engineering [Internet], Malaysia: Hilti, 2024 [cited 2024 April 3], Available from: <https://www.hilti.com.my/content/hilti/A2/MY/en/engineering/software/profis-engineering1.html>
- [16] Fischer, FiXperience Online [Internet], Singapore: Fischer, 2024 [cited 2024 April 17], Available from: <https://www.fischer.sg/en-sg/service/planning-aids/fixperience>
- [17] European Organisation for Technical Approvals (EOTA), ETA-08/0307, Hilti HUS-HR/HUS-CR screw anchor, 2018.
- [18] European Organisation for Technical Approvals (EOTA), ETA-13/1038, Hilti HUS3 screw anchor, 2020.
- [19] European Organisation for Technical Approvals (EOTA), ETA-19/0170, Hilti HUS2-H screw anchor, 2019.
- [20] European Organisation for Technical Approvals (EOTA), ETA-20/0867, Hilti HUS4 screw anchor, 2022.
- [21] European Organisation for Technical Approvals (EOTA), ETA-15/0352, fischer screw anchor ULTRACUT FBS II, 2020.
- [22] European Organisation for Technical Approvals (EOTA), ETA-17/0740, fischer screw anchor ULTRACUT FBS II A4, 2018.
- [23] European Organisation for Technical Approvals (EOTA), ETA-16/0043, Würth concrete screw W-BS/S, W-BS/A4, W-BS/HCR, 2021.
- [24] European Organisation for Technical Approvals (EOTA), ETA-20/0731, AnkaScrew Xtrem, 2020.
- [25] European Organisation for Technical Approvals (EOTA), EAD 330232-01-0601, Mechanical fasteners for use in concrete, 2021.
- [26] Abdul-Hamid A., Braimah A. and Tai F., "Impact load effects on screw anchors in concrete", *Engineering Structures*, 251(5), 113491, 2022.
- [27] Hoehler M.S. and Eligehausen R., "Behavior and testing of anchors in simulated seismic cracks", *ACI Structural Journal*, 105(3), 348-357, 2008.
- [28] Mohyeddin A., Gad E.F., Aria S. and Lee J., "Effect of thread profile on tensile performance of screw anchors in non-cracked concrete", *Construction and Building Materials*, 237, 117565, 2020.
- [29] Mohyeddin A., Gad E.F., Lee J., Hafsia M. and Saremi M., "Adverse effect of too-small edge distances on tensile capacity of screw anchors", *Australian Journal of Structural Engineering*, 21(1), 94-106, 2020.
- [30] Obayes O., Gad E.F., Pokharel T., Lee J. and Abdouka K., "Assessment of the tensile behaviour of post-installed screw anchors in early age concrete", *Construction and Building Materials*, 331, 127350, 2022.
- [31] Ng L.T., Lau L.C., Looi D.T.W., Lee J. and Ng A.L.Y., "Tensile test of screw anchor in thin uncracked concrete", 16th International Conference on Concrete Engineering and Technology, CONCET2024, Selangor, Malaysia, 9-12 July 2024.

Appendix A

In this section, six nomograms for screw anchors design under tensile load are reported by varying the anchor size (i.e., M6, M8, M10, M12, M14, and M16).

Tensile resistance - 6 mm

$$N_{Rd,i} = \frac{N_{Rk,i}}{\gamma_{Mc}}$$

where, $N_{Rk,i} = \min \{N_{Rk,c}; N_{Rk,sp}\}$

(i) Concrete cone failure

$$N_{Rk,c} = \varphi_{fck}(N_{Rk,i}^0)$$

(ii) Concrete splitting failure

$$N_{Rk,sp} = \varphi_{fck}(N_{Rk,i}^0)(\varphi_M)(\varphi_{hb,N})$$

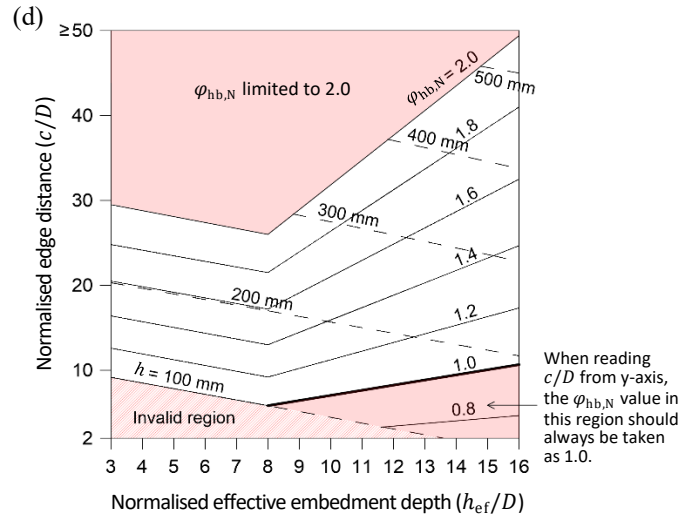
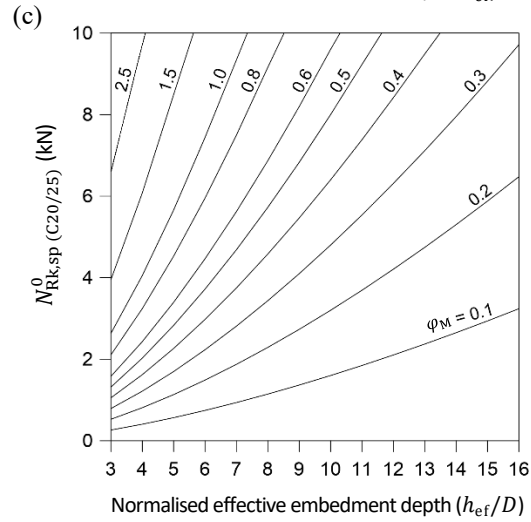
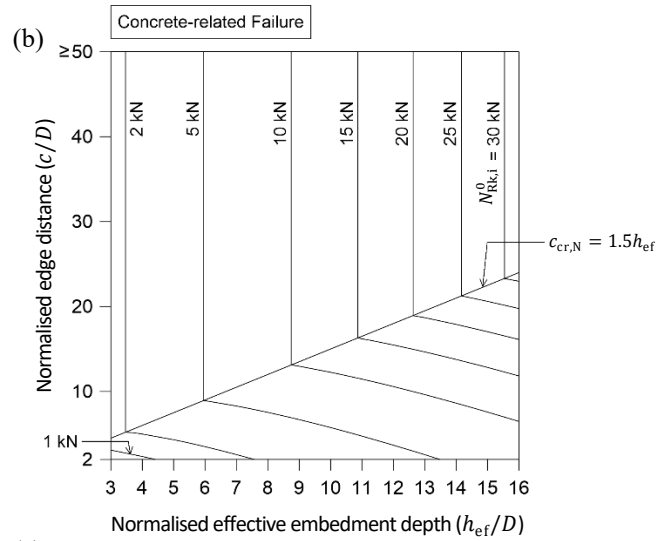
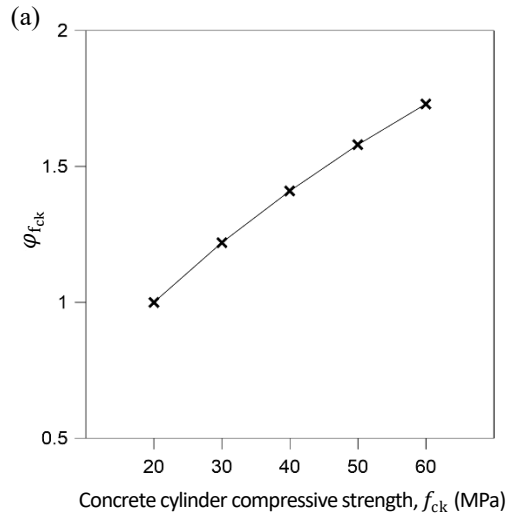
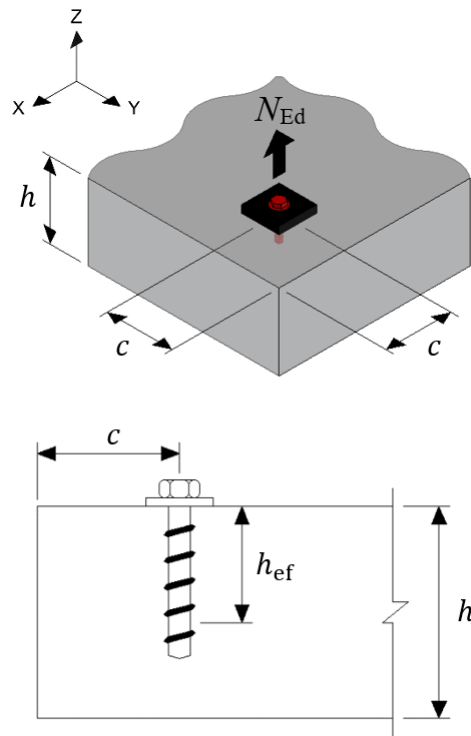


Fig. A1 Nomogram for tensile resistance for anchor size M6

Tensile resistance - 8 mm



$$N_{Rd,i} = \frac{N_{Rk,i}}{\gamma_{Mc}}$$

where, $N_{Rk,i} = \min \{N_{Rk,c}; N_{Rk,sp}\}$

(i) Concrete cone failure
 $N_{Rk,c} = \varphi_{fck}(N_{Rk,i}^0)$

(ii) Concrete splitting failure
 $N_{Rk,sp} = \varphi_{fck}(N_{Rk,i}^0)(\varphi_M)(\varphi_{hb,N})$

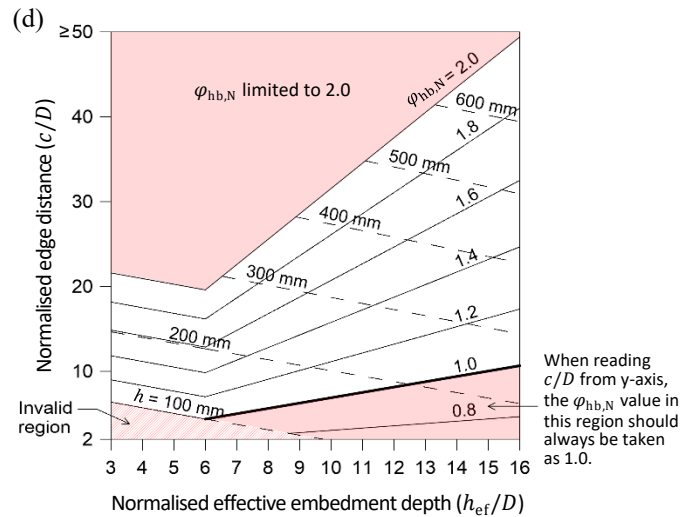
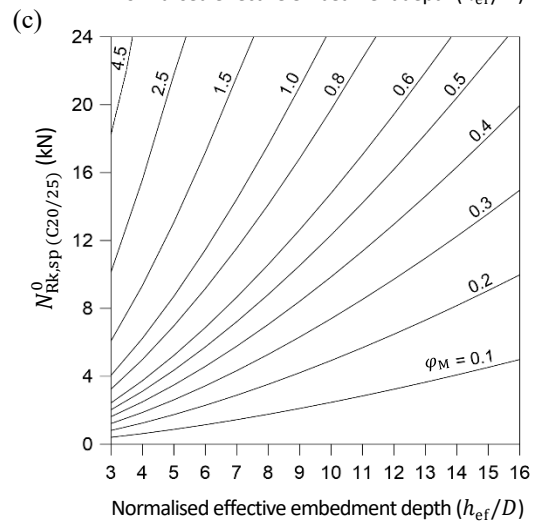
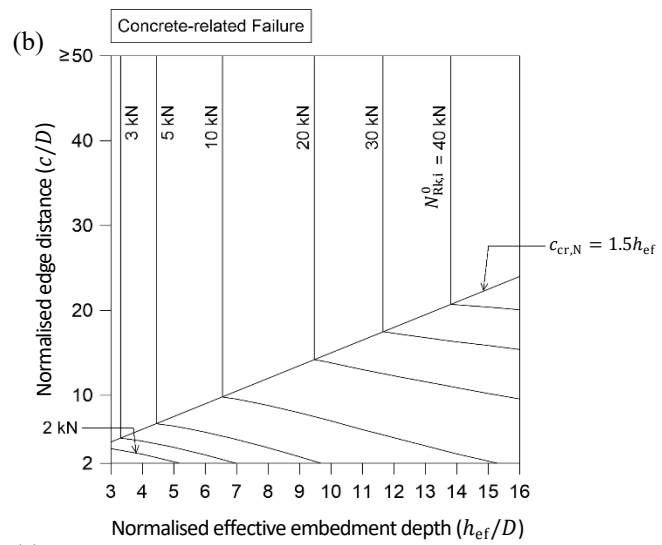
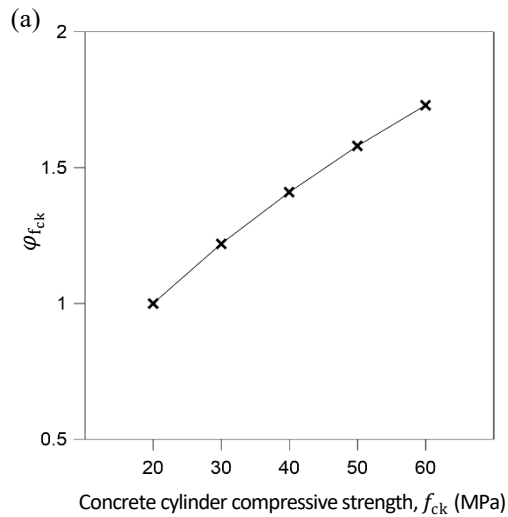
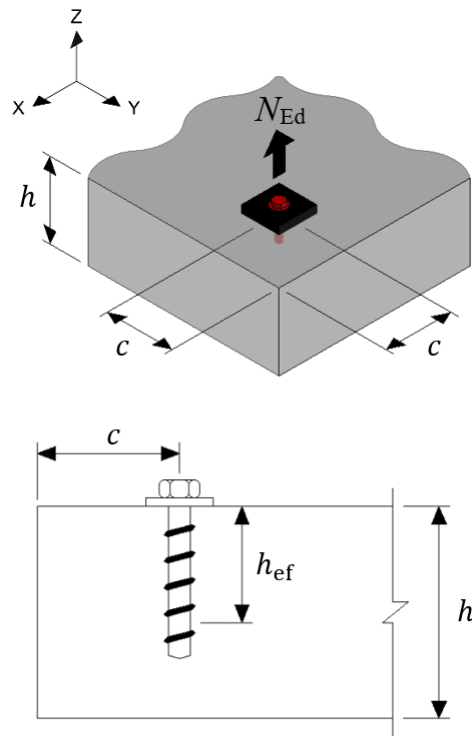


Fig. A2 Nomogram for tensile resistance for anchor size M8

Tensile resistance - 10 mm



$$N_{Rd,i} = \frac{N_{Rk,i}}{\gamma_{Mc}}$$

where, $N_{Rk,i} = \min \{N_{Rk,c}; N_{Rk,sp}\}$

(i) Concrete cone failure
 $N_{Rk,c} = \varphi_{f_{ck}}(N_{Rk,i}^0)$

(ii) Concrete splitting failure
 $N_{Rk,sp} = \varphi_{f_{ck}}(N_{Rk,i}^0)(\varphi_M)(\varphi_{hb,N})$

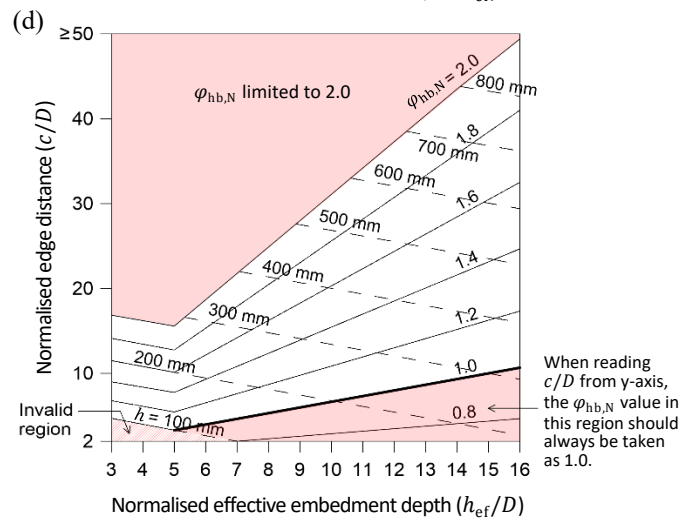
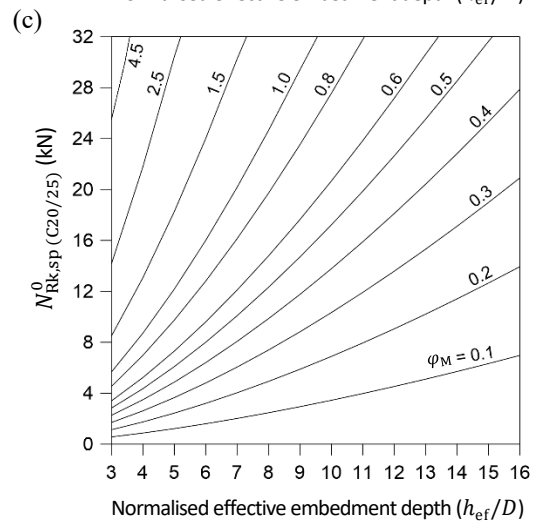
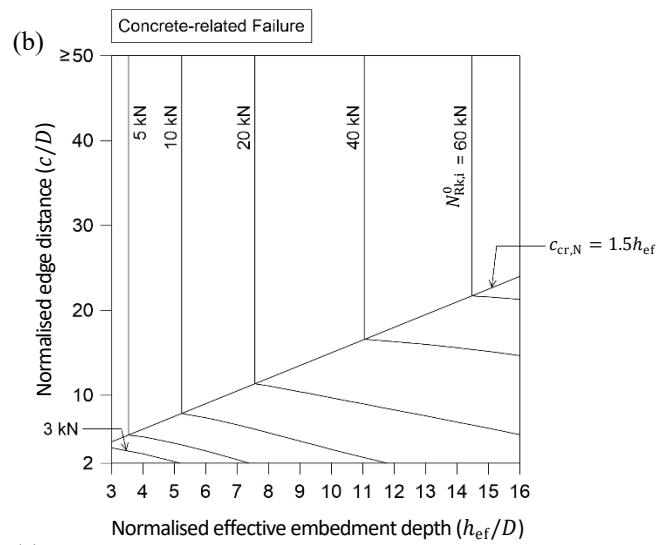
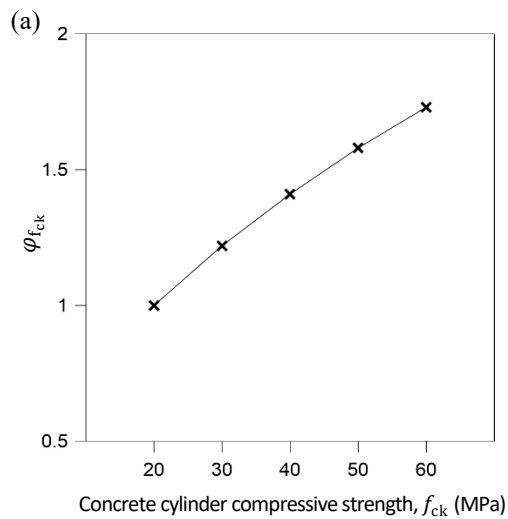
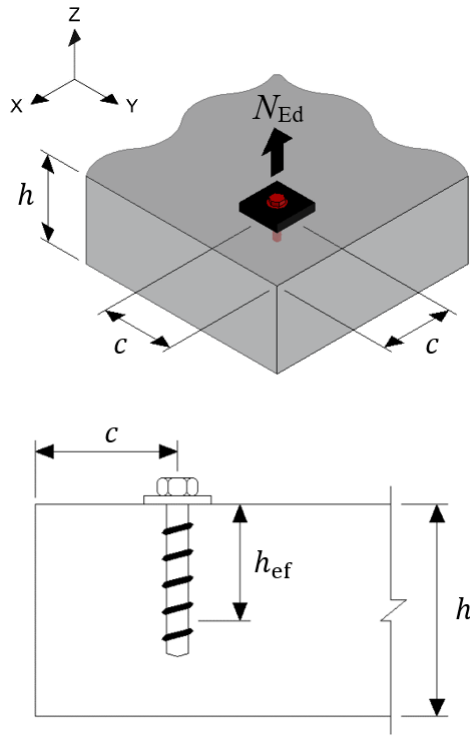


Fig. A3 Nomogram for tensile resistance for anchor size M10

Tensile resistance - 12 mm



$$N_{Rd,i} = \frac{N_{Rk,i}}{\gamma_{Mc}}$$

where, $N_{Rk,i} = \min \{N_{Rk,c}; N_{Rk,sp}\}$

(i) Concrete cone failure

$$N_{Rk,c} = \varphi_{fck}(N_{Rk,i}^0)$$

(ii) Concrete splitting failure

$$N_{Rk,sp} = \varphi_{fck}(N_{Rk,i}^0)(\varphi_M)(\varphi_{hb,N})$$

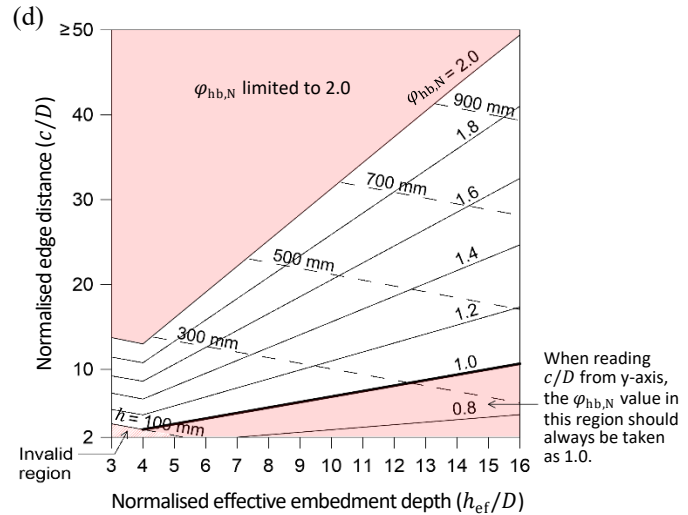
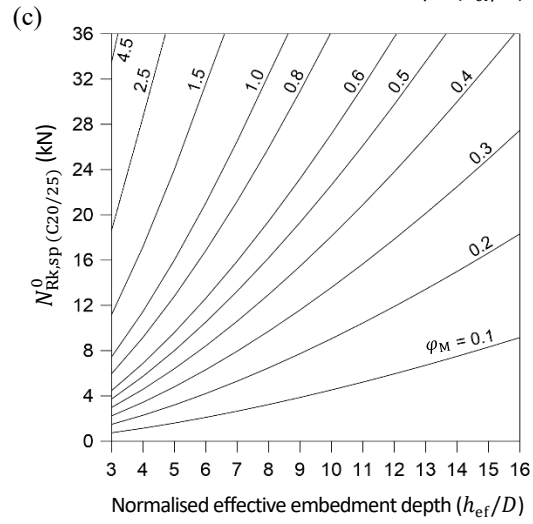
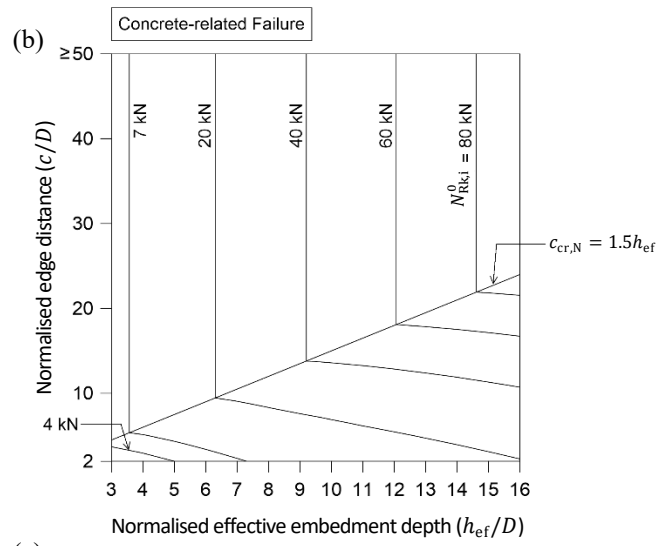
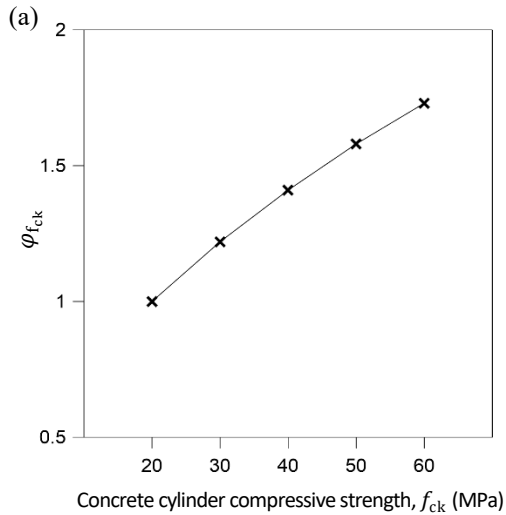
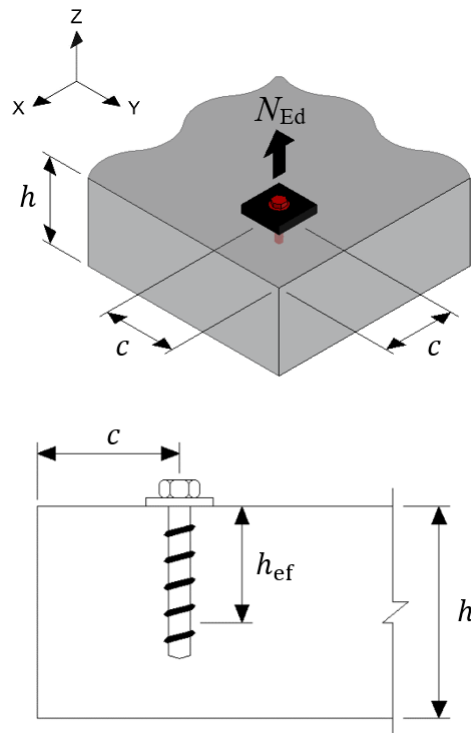


Fig. A4 Nomogram for tensile resistance for anchor size M12

Tensile resistance - 14 mm



$$N_{Rd,i} = \frac{N_{Rk,i}}{\gamma_{Mc}}$$

where, $N_{Rk,i} = \min \{N_{Rk,c}; N_{Rk,sp}\}$

(i) Concrete cone failure

$$N_{Rk,c} = \varphi_{fck}(N_{Rk,i}^0)$$

(ii) Concrete splitting failure

$$N_{Rk,sp} = \varphi_{fck}(N_{Rk,i}^0)(\varphi_M)(\varphi_{hb,N})$$

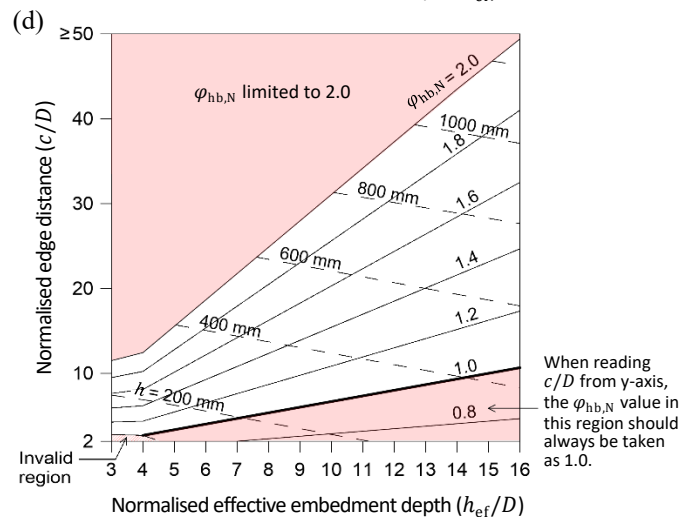
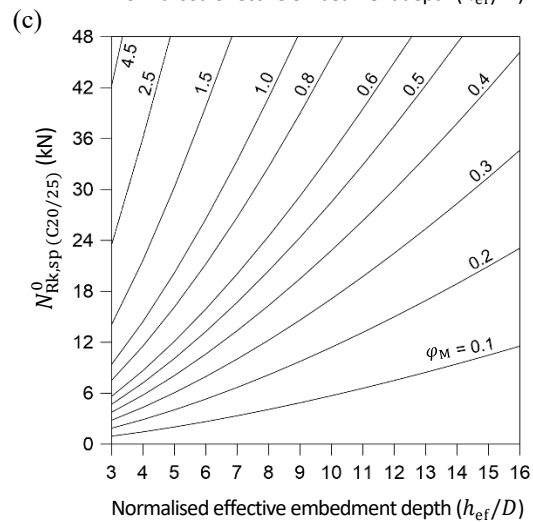
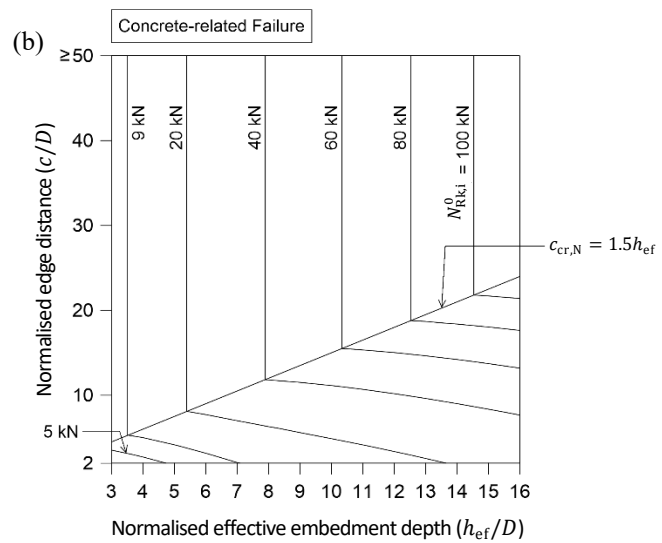
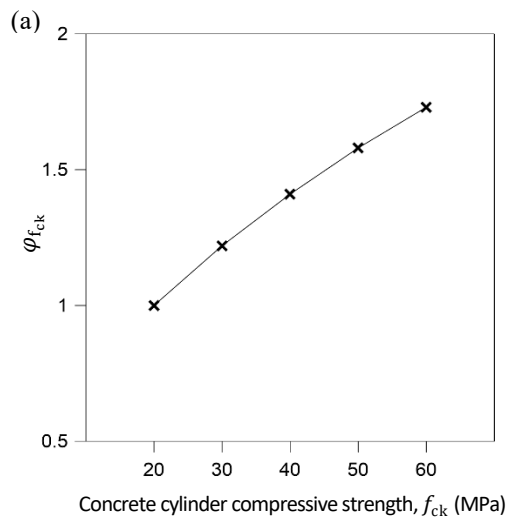
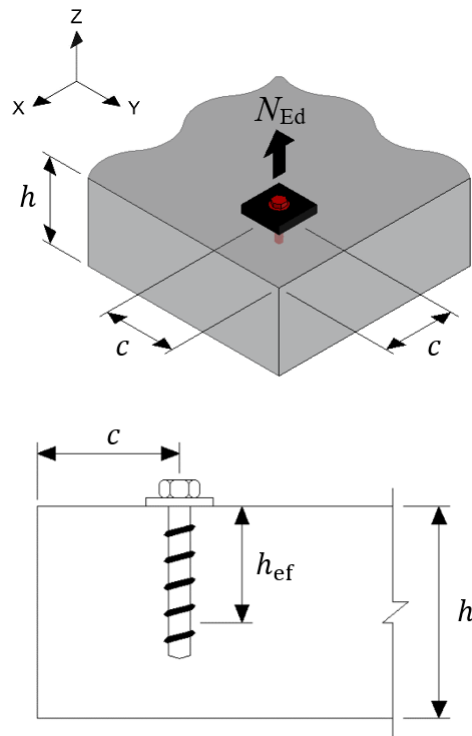


Fig. A5 Nomogram for tensile resistance for anchor size M14

Tensile resistance - 16 mm



$$N_{Rd,i} = \frac{N_{Rk,i}}{\gamma_{Mc}}$$

where, $N_{Rk,i} = \min \{N_{Rk,c}; N_{Rk,sp}\}$

(i) Concrete cone failure

$$N_{Rk,c} = \varphi_{fck}(N_{Rk,i}^0)$$

(ii) Concrete splitting failure

$$N_{Rk,sp} = \varphi_{fck}(N_{Rk,i}^0)(\varphi_M)(\varphi_{hb,N})$$

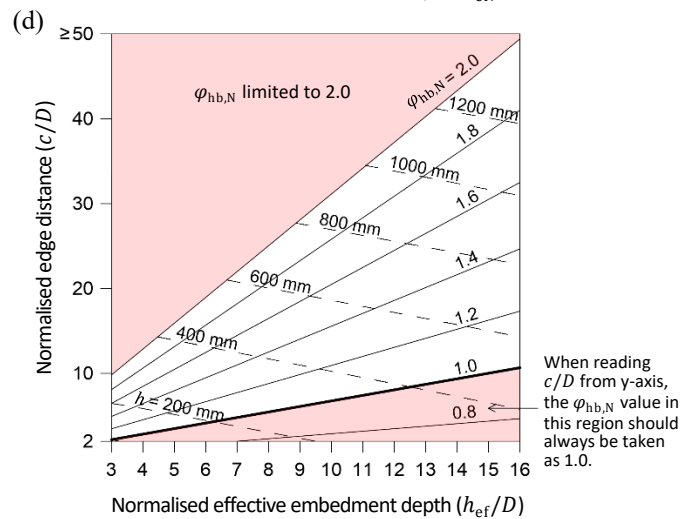
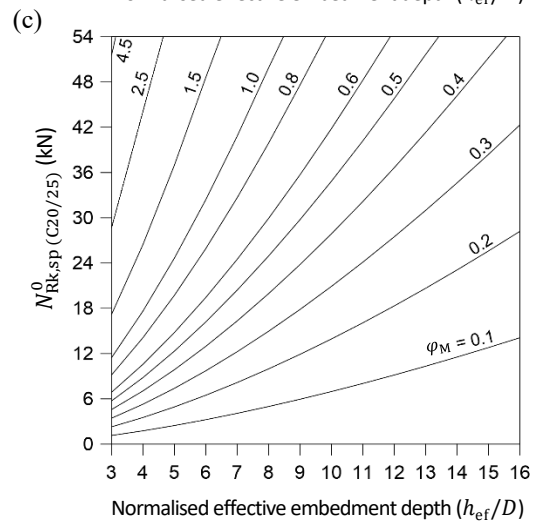
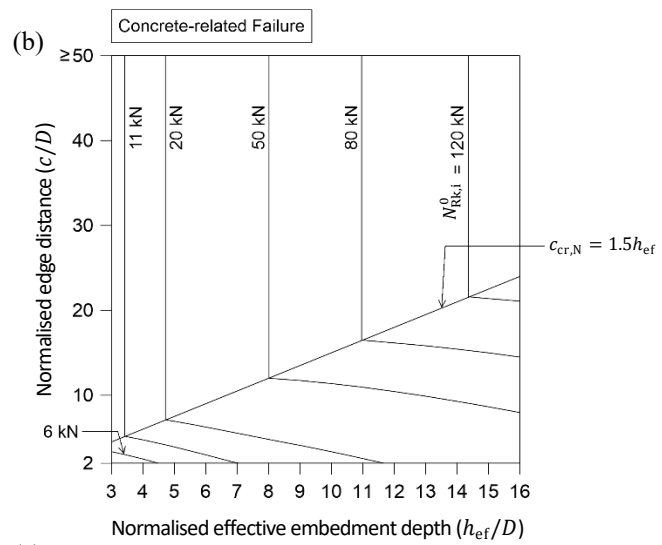
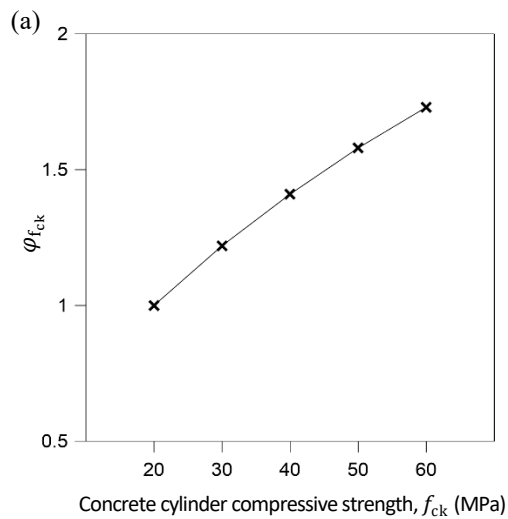


Fig. A6 Nomogram for tensile resistance for anchor size M16

Appendix B

In this section, six nomograms for screw anchors design under shear load are reported by varying the anchor size (i.e., M6, M8, M10, M12, M14, and M16).

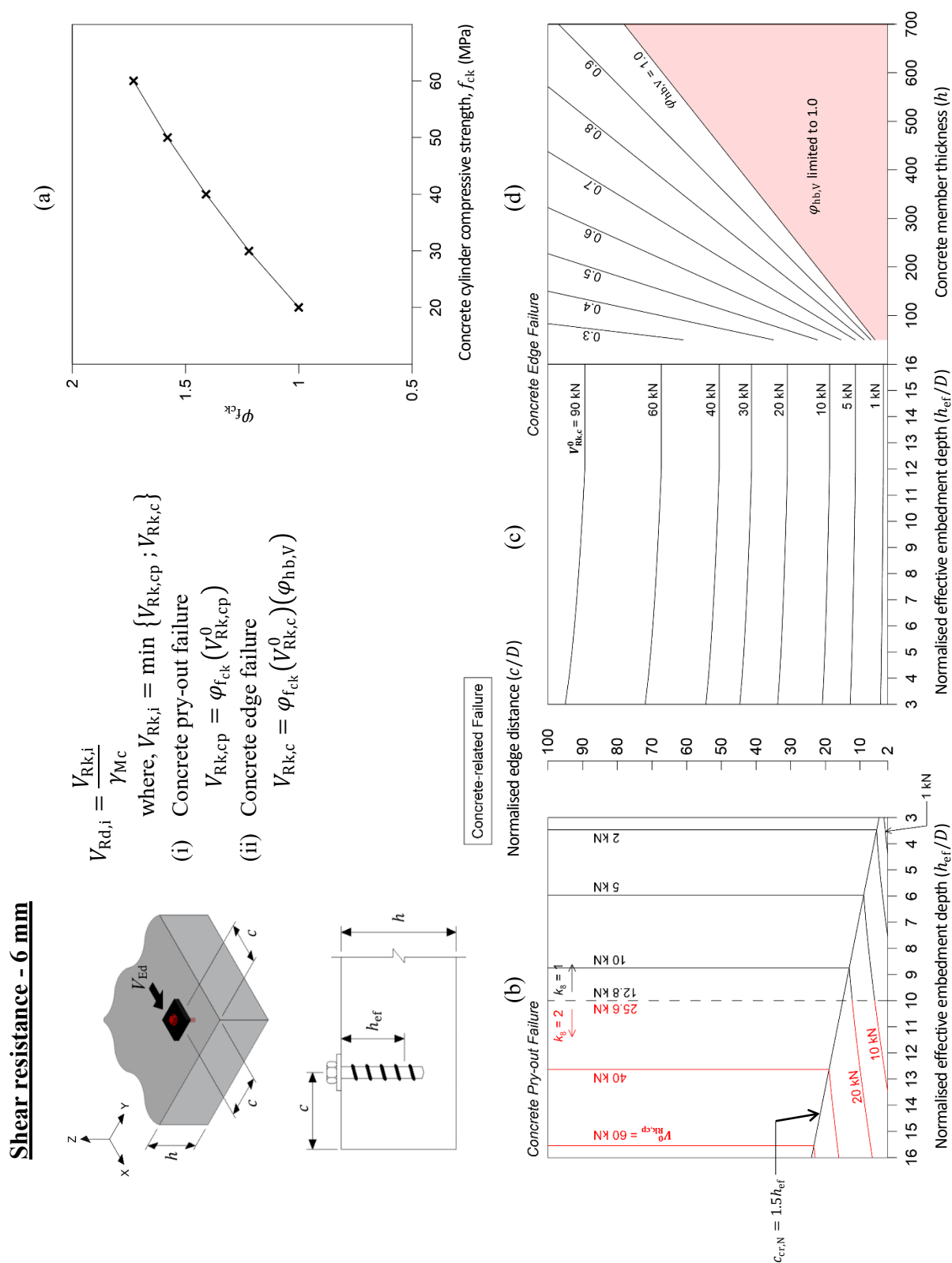
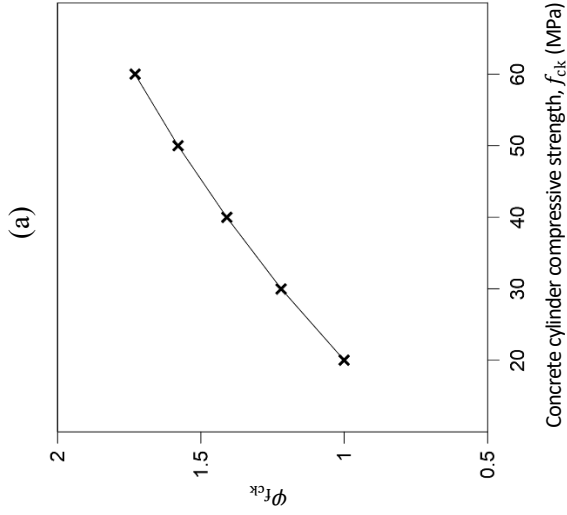
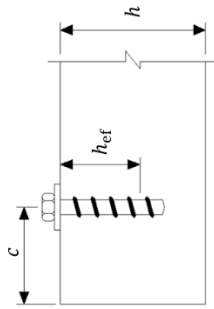
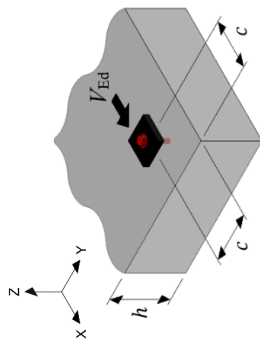


Fig. B1 Nomogram for shear resistance for anchor size M6

Shear resistance - 8 mm



$$V_{Rd,i} = \frac{V_{Rk,i}}{\gamma_{Mc}}$$

where, $V_{Rk,i} = \min \{V_{Rk,cp}; V_{Rk,c}\}$

(i) Concrete pry-out failure

$$V_{Rk,cp} = \phi_{fck} (V_{Rk,cp}^0)$$

(ii) Concrete edge failure

$$V_{Rk,c} = \phi_{fck} (V_{Rk,c}^0) (\phi_{hb,v})$$

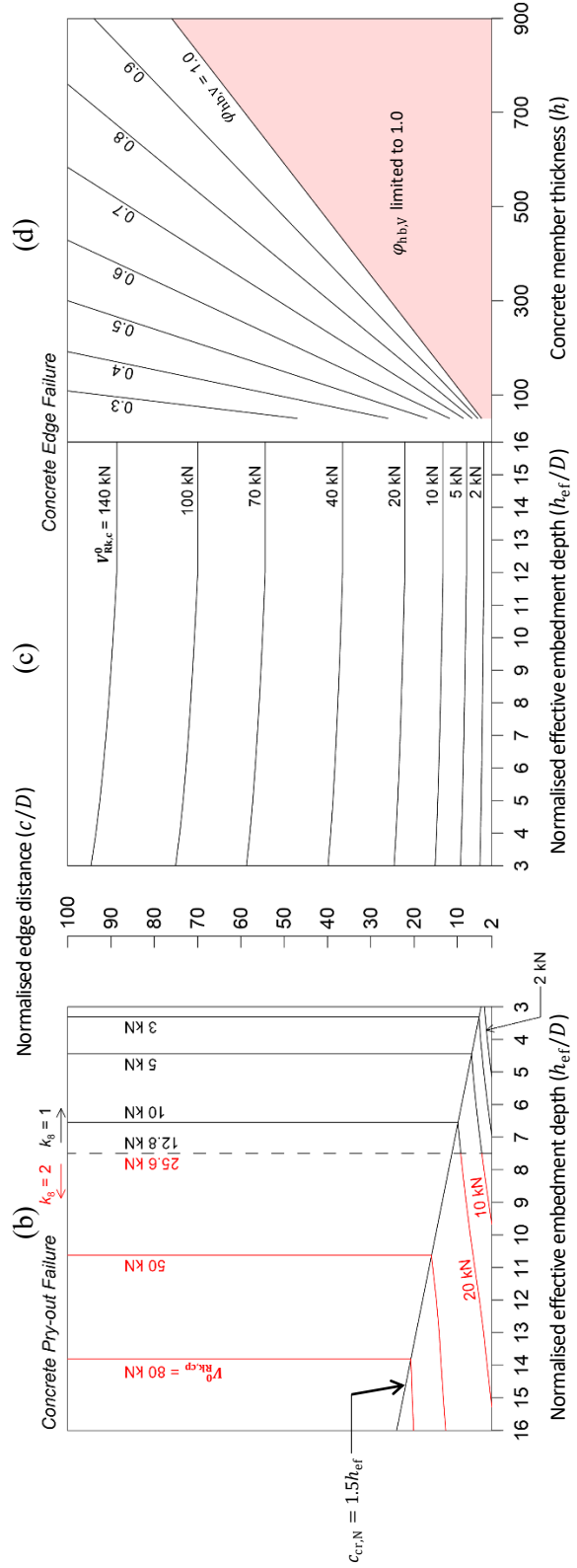
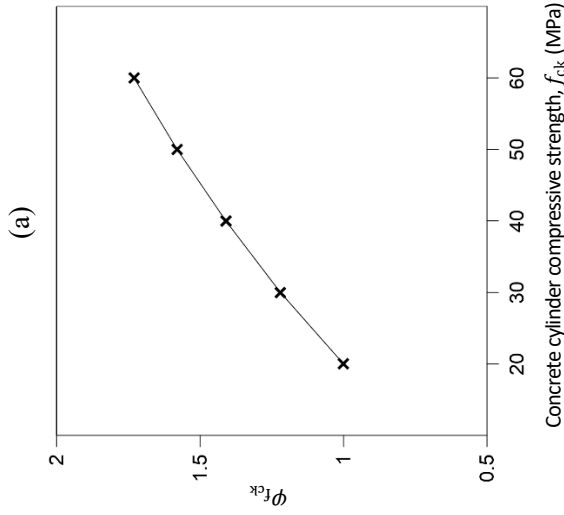
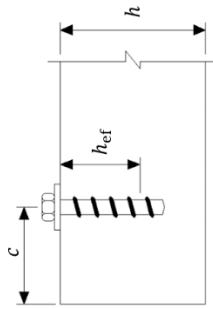
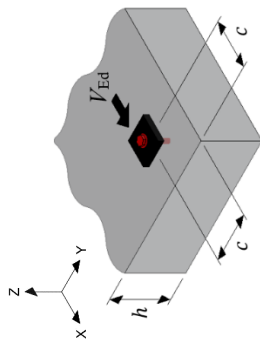


Fig. B2 Nomogram for shear resistance for anchor size M8

Shear resistance - 14 mm



$$V_{Rd,i} = \frac{V_{Rk,i}}{\gamma_{Mc}}$$

where, $V_{Rk,i} = \min \{V_{Rk,cp}; V_{Rk,c}\}$

(i) Concrete pry-out failure

$$V_{Rk,cp} = \varphi_{fck} (V_{Rk,cp}^0)$$

(ii) Concrete edge failure

$$V_{Rk,c} = \varphi_{fck} (V_{Rk,c}^0) (\varphi_{hb,v})$$

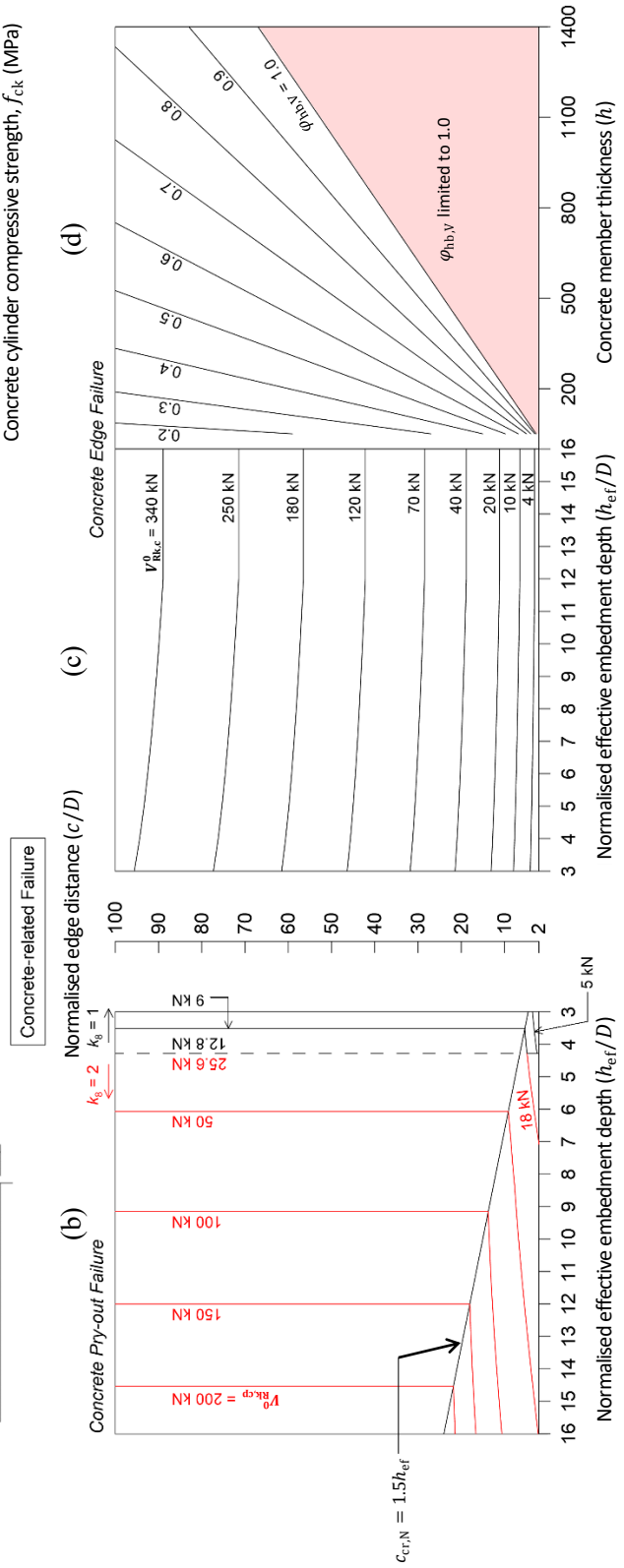
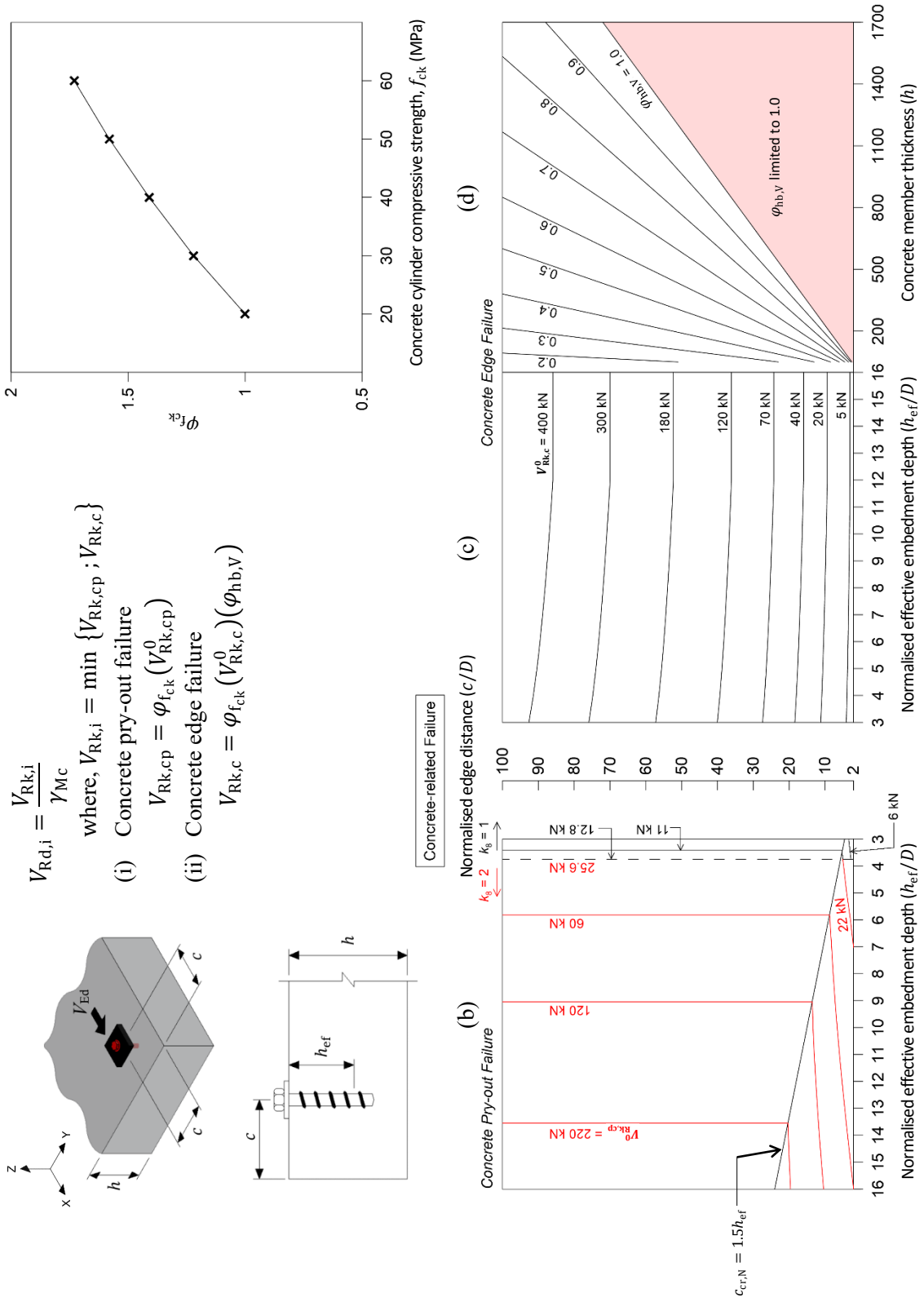


Fig. B5 Nomogram for shear resistance for anchor size M14

Shear resistance - 16 mm



Appendix C

An example of calculating the tensile and shear resistances using the proposed nomogram is presented here. The example refers to the details of Model 1, as shown in Table 2.

Dimensions and details

Anchor size = M8 ($D = 8$ mm); $f_{ck} = 30$ MPa; $h_{ef} = 56.1$ mm; $c = 50$ mm; and $h = 150$ mm

Tensile resistance of screw anchor

Step 1: Product A prequalified as per EAD 330232 [25] and designed to EN 1992-4:2018 [11] is selected as an example.

Step 2: $D = 8$ mm; $f_{ck} = 30$ MPa; $h_{ef} = 56.1$ mm; $c = 50$ mm; $h = 150$ mm

Step 3a: From the ETA of Product A, $N_{Rk,s} = 36.0$ kN; $\gamma_{Ms,N} = 1.5$

Step 3b: $N_{Rd,s} = \frac{N_{Rk,s}}{\gamma_{Ms,N}} = \frac{36.0}{1.5} = 24.0$ kN

Step 4a: From the ETA of Product A, $N_{Rk,p(C20/25)} \geq N_{Rk,c}^0$, so it is conservatively taken as equal to $N_{Rk,c}^0 = 14.5$ kN; $\gamma_{inst} = 1.0$

$$N_{Rk,p} = \varphi_{f_{ck}}(N_{Rk,p(C20/25)}) = 1.22(14.5) = 17.7 \text{ kN}$$

Step 4b: $N_{Rd,p} = \frac{N_{Rk,p}}{\gamma_{Mp}} = \frac{17.7}{1.5(1.0)} = 11.8$ kN

Note: For Steps 5a to 5d, an example of using the nomogram is shown in Fig. C1.

Step 5a: $\varphi_{f_{ck}} = 1.22$

Step 5b: $h_{ef}/D = 7$; $c/D = 6.3$, $N_{Rk,i}^0 = 6.5$ kN

Step 5c: $N_{Rk,sp(C20/25)}^0 = 14.5$ kN, $\varphi_M = 1.0$

Step 5d:

For $h_{ef}/D = 7$; $c/D = 6.3$, $\varphi_{hb,N} = 1.09$

For $h_{ef}/D = 7$; $h = 150$ mm, $\varphi_{hb,N} = 1.20$

Hence, $\varphi_{hb,N} = 1.09$ (lowest value is chosen)

Step 5e(i): $N_{Rk,c} = \varphi_{f_{ck}}(N_{Rk,i}^0) = 1.22(6.5) = 7.9$ kN

Step 5e(ii): $N_{Rk,sp} = \varphi_{f_{ck}}(N_{Rk,i}^0)(\varphi_M)(\varphi_{hb,N}) = 1.22(6.5)(1.0)(1.09) = 8.6$ kN

Step 5f: $N_{Rk,i} = \min \{N_{Rk,c}; N_{Rk,sp}\} = \min \{7.9; 8.6\} = 7.9$ kN (Governed by concrete cone failure)

Step 5g: $N_{Rd,i} = \frac{N_{Rk,i}}{\gamma_{Mc}} = \frac{7.9}{1.5(1.0)} = 5.3$ kN

Step 6: The tensile resistance of the screw anchor = $\min \{N_{Rd,s}; N_{Rd,p}; N_{Rd,i}\} = \min \{24.0; 11.8; 5.3\} = 5.3$ kN (Governed by concrete cone failure)

Shear resistance of screw anchor

Step 1: Product A prequalified as per EAD 330232 [25] and designed to EN 1992-4:2018 [11] is selected as an example.

Step 2: $D = 8$ mm; $f_{ck} = 30$ MPa; $h_{ef} = 56.1$ mm; $c = 50$ mm; $h = 150$ mm

Step 3a: From the ETA of Product A, $V_{Rk,s}^0 = 21.9$ kN, hence $V_{Rk,s} = 21.9$ kN; $\gamma_{Ms,V} = 1.25$

Step 3b: $V_{Rd,s} = \frac{V_{Rk,s}}{\gamma_{Ms,V}} = \frac{21.9}{1.25} = 17.5$ kN

Note: For Steps 4a to 4d, an example of using the nomogram is shown in Fig. C2.

Step 4a: $\varphi_{f_{ck}} = 1.22$

Step 4b: $h_{ef}/D = 7$; $c/D = 6.3$; $V_{Rk,cp}^0 = 6.7$ kN

Step 4c: $V_{Rk,c}^0 = 3.4$ kN

Step 4d: $\varphi_{hb,V} = 1.0$

Step 4e(i): $V_{Rk,cp} = \varphi_{f_{ck}}(V_{Rk,cp}^0) = 1.22(6.7) = 8.2$ kN

Step 4e(ii): $V_{Rk,c} = \varphi_{f_{ck}}(V_{Rk,c}^0)(\varphi_{hb,V}) = 1.22(3.4)(1.0) = 4.1$ kN

Step 4f: $V_{Rk,i} = \min \{V_{Rk,cp}; V_{Rk,c}\} = \min \{8.2; 4.1\} = 4.1$ kN (Governed by concrete edge failure)

Step 4g: $V_{Rd,i} = \frac{V_{Rk,i}}{\gamma_{Mc}} = \frac{4.1}{1.5(1.0)} = 2.7$ kN

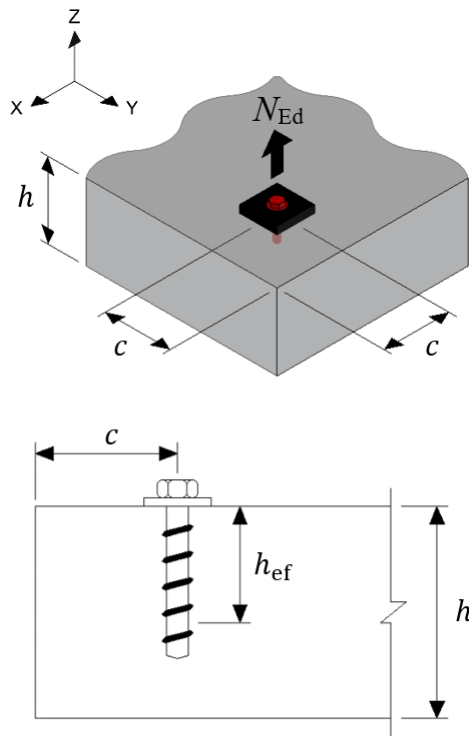
Step 5: The shear resistance of the screw anchor = $\min \{V_{Rd,s}; V_{Rd,i}\} = \min \{17.5; 2.7\} = 2.7$ kN (Governed by concrete edge failure)

Summary of screw anchor design

The design tensile resistance = 5.3 kN (Governed by concrete cone failure)

The design shear resistance = 2.7 kN (Governed by concrete edge failure)

Tensile resistance - 8 mm



$$N_{Rd,i} = \frac{N_{Rk,i}}{\gamma_{Mc}} \quad \text{Step 5g}$$

$$\text{where, } N_{Rk,i} = \min \{N_{Rk,c}; N_{Rk,sp}\} \quad \text{Step 5f}$$

(i) Concrete cone failure

$$N_{Rk,c} = \varphi_{f_{ck}}(N_{Rk,i}^0) \quad \text{Step 5e(i)}$$

(ii) Concrete splitting failure

$$N_{Rk,sp} = \varphi_{f_{ck}}(N_{Rk,i}^0)(\varphi_M)(\varphi_{hb,N}) \quad \text{Step 5e(ii)}$$

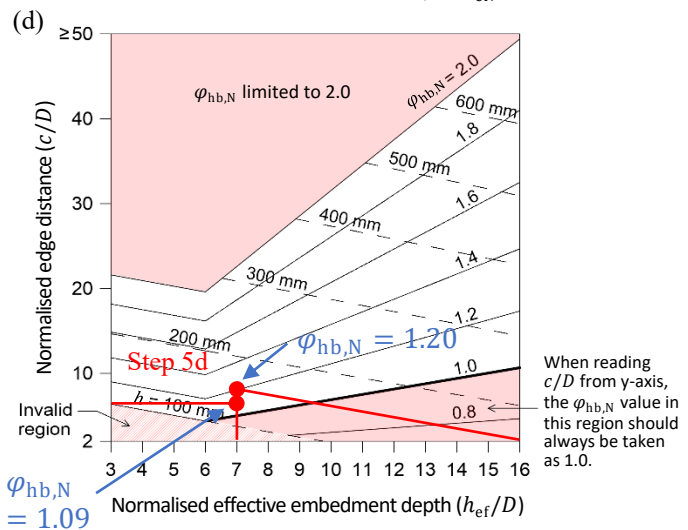
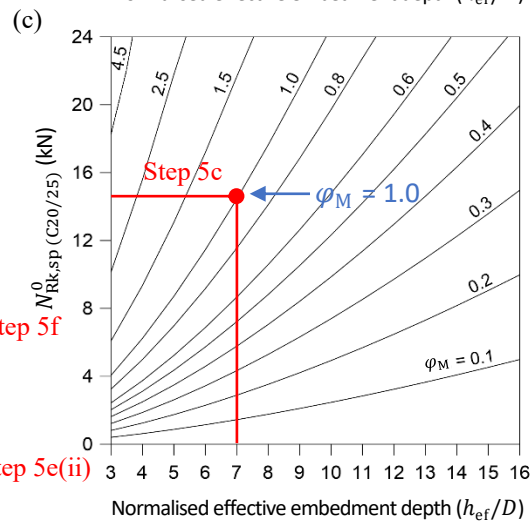
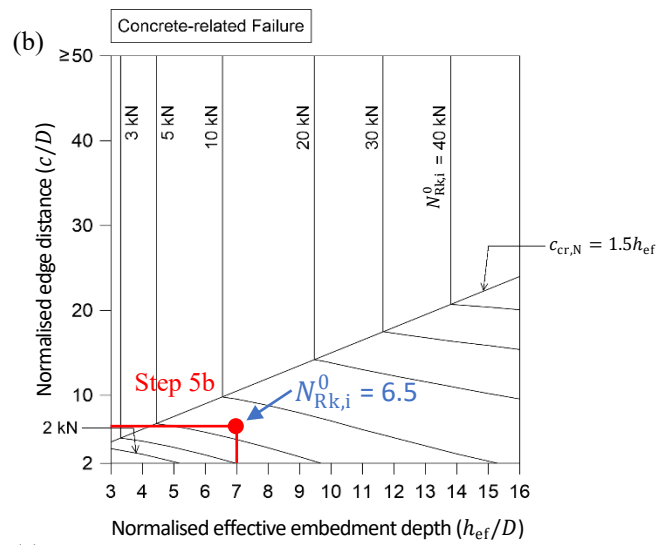
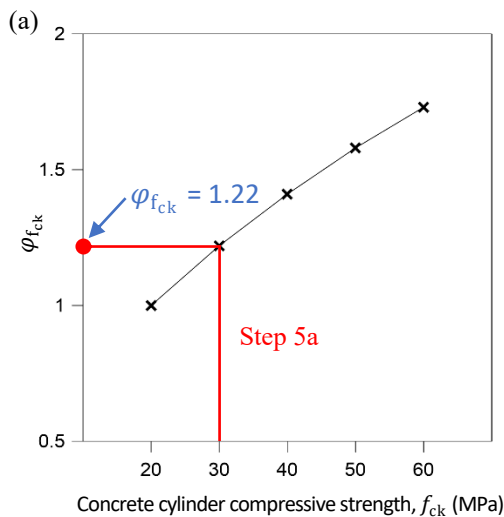
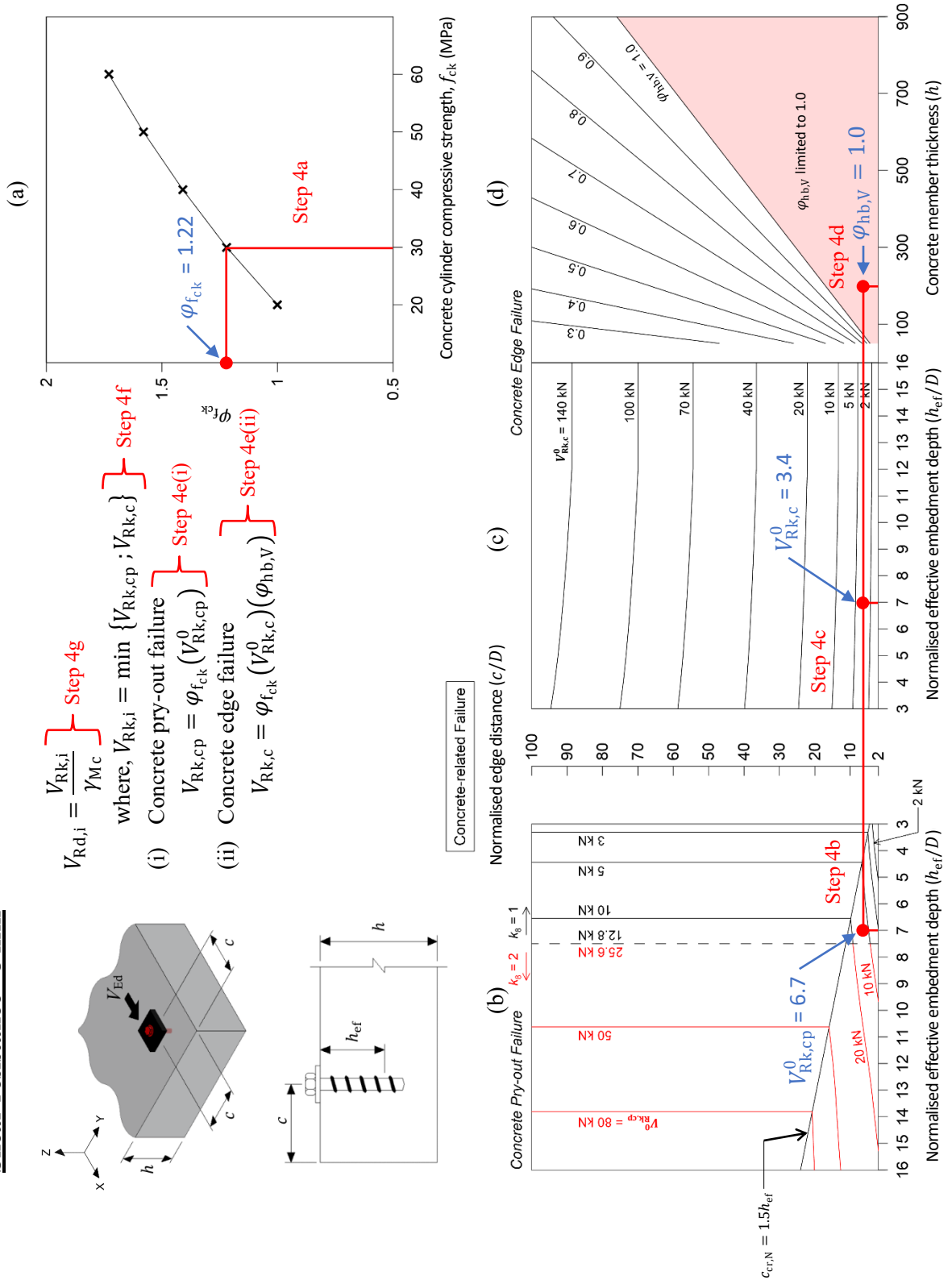


Fig. C1 An example of using the nomogram under tensile load

Shear resistance - 8 mm



STUDY ON THE AXIAL COMPRESSION PERFORMANCE OF CONCRETE FILLED CIRCULAR ALUMINUM ALLOY TUBULAR COLUMN WITH BUILT-IN HOLLOW STEEL TUBE

Zheng-Tao Zhang, Bing Li and Zhou Bo*

School of Civil Engineering, Shenyang Jianzhu University, 25 Hunnan Rd., Liaoning, Shenyang, 110168, China

* (Corresponding author: E-mail: wys20020816@163.com)

ABSTRACT

In this paper, longitudinal compression tests were conducted on 8 concrete filled aluminum alloy tubular (CFAT) columns with built-in hollow steel tube, and their failure modes, load-strain curve, transverse deformation coefficient, load-displacement curve, axial compressive stiffness and strength coefficient were analyzed. The results show that each component of the specimens have a good deformation coordination. The type of concrete has a notable impact on the bearing capacity and stiffness of member, when the hollow ratio is 0.72, 0.61, and 0.39, the bearing capacity of specimens with ordinary concrete as the sandwich concrete is 43.4%, 37.0%, 39.7% larger than specimens with lightweight concrete as the sandwich concrete, and the axial compression stiffness is 4.8%, 11.3%, and 25% greater than them. The strength coefficients SI of 8 specimens were greater than 1, which indicate a good composite effect between the components. A full-scale finite element model was set up through using ABAQUS software, through numerical simulation, it is found that the load will be mainly borne by the sandwich concrete and aluminum alloy tube, in addition, the analysis of contact stress indicates that there is minimal interaction between the sandwich concrete and the steel tube. To quantify the effects of factors such as the nominal aluminum ratio, compressive strength of the concrete cubes, hollow ratio, and yield strength of the internal tube on axial compressive performance indicators, parametric analyses were conducted. The method suggested for assessing bearing capacity demonstrates good applicability to CFAT column with built-in hollow steel tube.

ARTICLE HISTORY

Received: 16 June 2024
Revised: 8 January 2025
Accepted: 6 February 2025

KEYWORDS

Concrete filled aluminum alloy tubular (CFAT) column;
Built-in hollow steel tube;
Axial compression performance;
Composite effect;
Analysis of the whole stressing process;
Parametric analysis

Copyright © 2025 by The Hong Kong Institute of Steel Construction. All rights reserved.

1. Introduction

The Concrete Filled Double-Skin Steel Tube (CFDST) member represents an innovative structural configuration that entails the substitution of the solid concrete core in a traditional Concrete Filled Steel Tube (CFST) with a hollow steel tube, thereby enhancing the overall structural efficiency and design versatility. The special hollow structure inside not only make the member itself lighter in weight, but also reduce the dosage of concrete, and it has the feature of good ductility, high stiffness, high bearing capacity, and good seismic performance, so it is widely used in piers of viaduct, transmission towers as well as some towering structures or buildings [1-4]. However, in practical engineering applications, due to the influence of external environment, especially in moist environment, the exterior surface of the steel tube is easily corroded owing to long-term contact with moisture in the air, if improper operation and maintenance are not carried out or corresponding measures are not taken in a timely manner, it will have a specific level of detrimental impact on the structure, thereby affecting the service life of the building or structure. Therefore, under the premise of not affecting the mechanical indicators of the member, the selection of materials with strong corrosion resistance to replace external steel tube needs to be given priority consideration.

Aluminum alloy is currently one of the most widely used metal materials, the amount of usage is second only to steel. It was found that its surface has a dense Al_2O_3 protective layer by tracing its chemical essence, which can effectively block the further reaction between air and internal aluminum, therefore, its corrosion resistance is strong, meanwhile, its weight is relatively light. With the support of the above advantages, it ultimately became the preferred choice among numerous corrosion-resistant materials. This composite component composed of aluminum alloy pipes, concrete, and steel is called CFAT member with built-in hollow steel tube. Due to the good corrosion resistance and small self-weight of aluminum alloy, they not only meet the durability performance of the structure or components, but also satisfy the demands of lightweight design of the structure, meanwhile, the application of aluminum alloy materials greatly reduces the incremental costs caused by frequent replacement of accessories, while also reducing the consumption of steel.

Researchers in the relevant discipline have undertaken exhaustive research on the behavior under single or multiple load conditions and the design principle of aluminum-concrete composite structural systems. Zeng et al [5] examined the mechanical characteristics of aluminum alloy tube-encased concrete short columns subjected to axial compression, their findings indicate that the aluminum alloy tube and concrete interact synergistically throughout the stress process, and the proposed method for calculating bearing capacity provides a reasonable estimation of the specimen's relevant mechanical properties. Li et al [6] utilized finite element simulations to analyze the axial compression mechanical properties of 7075 high-strength aluminum alloy tubular concrete

columns, and introduced a practical calculation method for bearing capacity based on pertinent steel tube structural specifications. Chen et al. [7] performed axial compression tests on 16 seawater sea-sand concrete-filled aluminum alloy circular tubular columns, exploring their compressive working mechanism and synergistic behavior. Additionally, references [8-13] offer detailed analyses of the related properties of aluminum alloy tube-concrete composite members, with the resulting research contributions serving as valuable references for future studies.

Nowadays, the Investigations into the axial compression mechanical properties of CFAT columns has been relatively mature, however, there have been no reports on the research of CFAT with built-in hollow steel tube proposed in this article, therefore, this paper designed a total of 8 specimens for axial compression testing research, analyzed the failure modes of specimens, and further studied the mechanical performance indicators such as load-strain curve, load-displacement curve, stiffness, and bearing capacity. Due to constrained by test conditions and number of specimens, this paper conducted finite element simulation calculations on the basis of experimental research, analyzed the working mechanism of the specimens, include analysis of the whole stressing process and contact stress analysis. Furthermore, the influence of diverse parameters, including nominal aluminum ratio, concrete cube compressive strength, hollow ratio, and yield strength of internal steel tube on the bearing capacity, axial compressive stiffness, and ductility of specimens has been investigated. Eventually, a streamlined approach for assessing bearing capacity was suggested based upon relevant technical regulations and parameter analysis.

2. Basic situation of the experiment

2.1. Design and processing of specimens

Before the experiment is conducted, a total of 8 CFAT column with built-in hollow steel tube were designed. The components that make up the specimen are aluminum alloy tube, sandwich concrete, and steel tube from the outside to the inside in sequence. In the diagram presented in Fig.1. All specimens have been designed with a height of 720mm. ($H=720\text{mm}$), the cross-sectional diameter is 240mm ($D_o=240\text{mm}$), and the wall thickness of aluminum alloy tube is 5.5mm ($t_o=5.5\text{mm}$). The experimental parameters include hollow ratio χ , the wall thickness t_i of internal steel tube, and concrete type. Table1 provides a comprehensive overview of the parameter specifications and significant outcomes obtained from the conducted tests.

Depending on the type of sandwich concrete, two series of specimens were designed in this test, they are respectively the HACSC series with ordinary concrete as sandwich concrete and the HALCSC series with lightweight concrete as sandwich concrete. The processing steps of the specimen need to be implemented in the following sequence: (1) Placing the rolled steel tube on the

bottom end plate and continuously adjusting its position until the centerline of the steel tube aligns with the centroid of the bottom end plate, and ensuring that the steel tube is perpendicular to the bottom end plate, then, welding the steel tube and bottom end plate together. (2) Concentrically place the aluminum alloy tube on the outside of the steel tube, and angle steel and self-tapping nails are used to achieve the effective connection between the aluminum alloy tube and bottom end plate, the connection form is shown in Fig.2(a). (3) The concrete is poured into sandwich area of aluminum alloy tube and steel tube by using a layered pouring method and vibrates continuously to guarantee the compactness of concrete (In order to prevent concrete from shrinkage due to chemical reactions during the curing stage, the final batch of poured concrete is slightly higher), subsequently, it is cured for 28 days under specific conditions. (4) The excess slurry accumulated on the top of the specimen is chiseled to achieve a level surface that aligns with the aluminum alloy tube and steel tube, then polish the specimen's surface. The polished specimen is depicted in Fig.2(b).

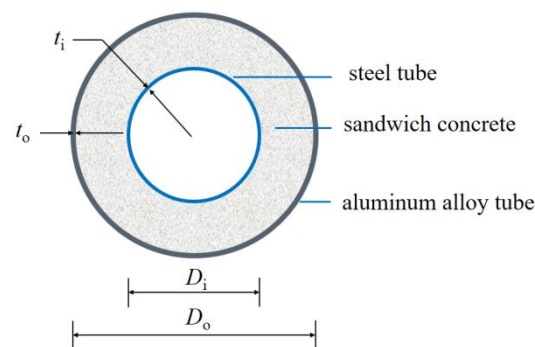


Fig. 1 Internal cavity structure of the specimen and detailed schematic of each part

Table 1

Specimen parameter information and test results (finite element results)

Specimen number	D_o/mm	t_o/mm	D_i/mm	t_i/mm	H/mm	χ	Concrete type	Test and finite element calculation results		
								$N_{ue\ test}\ (kN)$	$N_{ue\ FEM}(kN)$	$N_{ue\ FEM}/N_{ue\ test}$
HACSC1-1	240	5.5	165	4	720	0.72	Ordinary concrete	2782.6	2693.7	0.97
HACSC2-1	240	5.5	140	4	720	0.61	Ordinary concrete	2863.2	2775.6	0.97
HACSC3-1	240	5.5	89	4	720	0.39	Ordinary concrete	3115.2	3066.6	0.98
HACSC3-2	240	5.5	89	3	720	0.39	Ordinary concrete	3023.2	3001.4	0.99
HALCSC1-1	240	5.5	165	4	720	0.72	Lightweight concrete	1939.8	2039	1.05
HALCSC2-1	240	5.5	140	4	720	0.61	Lightweight concrete	2089.6	2121.4	1.02
HALCSC3-1	240	5.5	89	4	720	0.39	Lightweight concrete	2229.9	2214.6	0.99
HALCSC3-2	240	5.5	89	3	720	0.39	Lightweight concrete	2184.2	2132.9	0.98
Average value										0.99
Standard deviation										0.04



(a) Connection between aluminum alloy and end plate



(b) Polished specimens

Fig. 2 Sketch map of the key processes during specimen processing

2.2. Properties of materials

2.2.1. The aluminum alloy

The aluminum alloy tube type for making the specimens is 6061-T6. Pursuant to the Chinese standard GB/T 228.1-2010 regulation, the tensile coupon tests will be implemented, 4 tensile coupons are cut from the raw materials used to make the specimen. Within a period of time after starting the tensile test, there is no change in the appearance of the tensile coupon. As the force applied by the tensile testing machine gradually increases, when the tensile force reaches a certain value, the middle of the tensile coupon suddenly fractures without any signs, and the elongation is small. From the failure of the specimen, it can be seen that the fracture section is perpendicular to the length direction of the coupon, and the size of the fracture section remains almost unchanged. After the experiment is completed, the data collected from 4 sets of samples will be processed, the relevant mechanical properties indicators of aluminum alloy tube are shown in Table 2, which involves nominal yield strength (the point of conditional yield at which residual strain reaches 0.2%),

ultimate strength, elastic modulus and Poisson's ratio.

Table 2

Mechanical property index of aluminum alloy tube

Material type	Nominal yield strength/MPa	Ultimate strength/MPa	Elastic modulus/MPa	Poisson's ratio
Aluminum alloy	210.9	252	69645	0.35

2.2.2. Sandwich concrete

Two types of sandwich concrete were used during the specimen fabrication process, which includes ordinary concrete and lightweight concrete, the mixture proportions of the above two types of sandwich concrete are shown in Table 3. Based on the guidance of the Chinese standard GB/T50081-2019, the real strength of the above two types of concrete has been determined, common concrete and lightweight concrete is 43.8Mpa and 22.1Mpa respectively

Table 3

Mixture proportions of different types of sandwich concrete

The type of concrete	cement	sand	fly ash	Cobble	large particle ceramsite	Medium size ceramic particles	Small particle ceramsite	tail mineral fly-ash	Water reducer	water
Ordinary concrete	284	795	72	1124	--	--	--	--	5	150
Lightweight concrete	486	389	--	--	83	122	122	85	5.8	170

2.2.3. Steel tube

The steel type with built-in steel tube is Q235B. Based on the Chinese standard GB/T 228.1-2010 regulation [14], the mechanical properties of steel tube are obtained by pull-out Test, the tensile coupon are taken from steel tubes of different sizes, the mechanical properties indicators pertaining to steel tubes of differing sizes are detailed in Table 4, f_y and f_u represent the yield strength and ultimate strength of steel tube respectively in Table 4.

Table 4

Mechanical properties indicators of steel tube

Material	f_y /MPa	f_u /MPa	Poisson's ratio
Steel plate ($t_i=4\text{mm}$)	327.7	460.3	0.297
Steel plate ($t_i=3\text{mm}$)	321.4	440.5	0.301

2.3. Test preparation

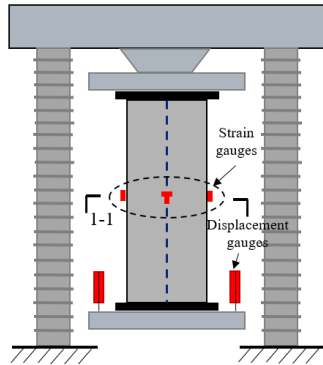
2.3.1. Layout of data collection points

To analyze the deformation law of the aluminum alloy tube, strain gauges were positioned in the midsection of aluminum alloy tube, both transverse and

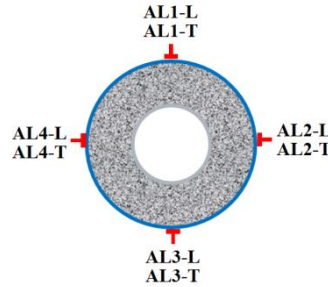
longitudinal. The setup of the gauges is portrayed in Fig.3(a) and (b), where AL1-L ~ AL4-L denote the longitudinal gauges, and AL1-T ~ AL4-T represent the transverse gauges affixed to the exterior of the aluminum alloy tube.

2.3.2. Experimental loading scheme and loading system

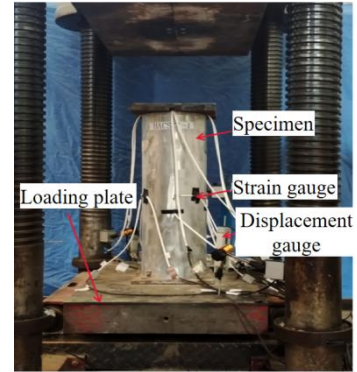
The experiment was executed in the structural laboratory of Liaoning provincial transportation planning and design institute, 500T hydraulic testing machine was used for graded loading. Four displacement gauges are arranged perpendicular to specimen to measure the transverse displacement, which are arranged in a ring with an interval angle of 90° , and the longitudinal displacement is measured by two displacement gauges arranged on the diagonal of the loading plate. Pre-loading is recommended to be done before formal loading to ensure good contact between the components of the specimens and the normal operation of the machine. In this experiment, the load value of pre-loading was approximately 10% of the estimated ultimate bearing capacity (The result of Numerical simulation calculation), after verifying that there were no other issues, the pre-loading was unloaded and then formally loaded. During the formal loading stage, a graded loading system was implemented, incrementally applying a load that is roughly 10% of the estimate ultimate load-bearing capacity at each stage, and the load of each level was sustained for a period of 2 to 3 minutes.



(a) Schematic diagram of the test device



(b) Strain gauge placement



(b) the test device

Fig. 3 Measurement point arrangement and test loading device

3. Analysis of experiment results

3.1. Failure mode of the specimen

Axial compression tests were conducted on 8 CFAT columns with built-in hollow steel tube. Through observation, it was found that the test phenomena and final failure modes of the 8 specimens from the beginning of loading to the end of the test were basically similar. This paper introduces two specimens numbered HACSC1-1 and HALCSC1-1 as examples.

During the inception phase of the loading, because of the small load, all components of the specimen are in a uniaxial compression state, and the specimen will make a slight sound under axial compression, and the specimen's exterior exhibits no apparent alterations; As the load progressively rises, reaching approximately $0.7N_{uc}$, the specimen produces audible cracking sounds, aluminum alloy tube begin to occur local bulging phenomenon, which is mostly appears near the height of $H/2$, the root cause for this destructive phenomenon primarily hinge on two aspects, on the one hand, under axial compressive loading, the middle section of the member typically bears the maximum compressive stress, due to the effect of stress concentration, the aluminum alloy tube and concrete in this area are more prone to deformation. On the other hand, when the concrete is compressed, the aluminum alloy tube provides lateral confinement to prevent lateral expansion of the concrete. However, when the

compressive stress exceeds a certain limit, the lateral deformation of the concrete increases, leading to buckling of the aluminum alloy tube; As the load increases from $0.7N_{uc}$ to N_{uc} , the outward deformation of the aluminum alloy tube becomes more noticeable, with the concrete at the deformed position being crushed simultaneously; The load gradually decreases after exceeding the ultimate bearing capacity N_{uc} , however, the axial deformation and section transversal deformation of the specimen continue to increase, eventually, the aluminum alloy at $H/2$ height is torn, which marks the complete destruction of the specimen, the final destruction phenomenon is shown in Fig. 5 (a). For the purpose of further observing the failure mode of the sandwich concrete and the internal steel pipe, the specimen is dissected, it is found that the concrete corresponding to the bulging position of the aluminum alloy tube is crushed, and the inner wall of steel tube in the corresponding position will also be sunken inward.

Moreover, an assessment was performed on the failure behavior of specimen HALCSC1-1, with Fig.5(c) and 5(d) illustrating the failure mode of the specimen and its constituent component. Upon close examination, it was determined that the failure modes of specimens HACSC1-1 and HALCSC1-1 showed a high degree of consistency. The experimental phenomena of specimen HACSC1-1 and HALCSC1-1 show that aluminum alloy tube and sandwich concrete have a good deformation coordination under axial compression, which exhibit a good composite effect.

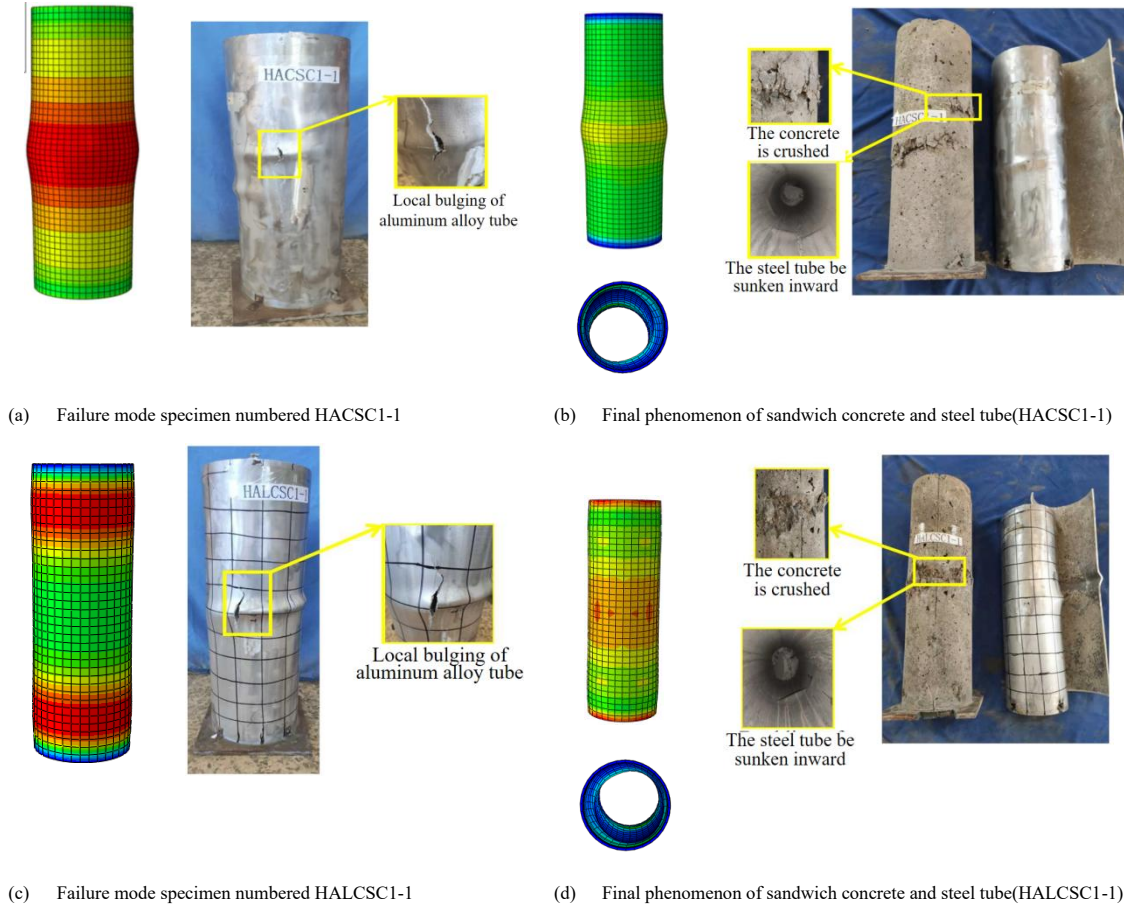


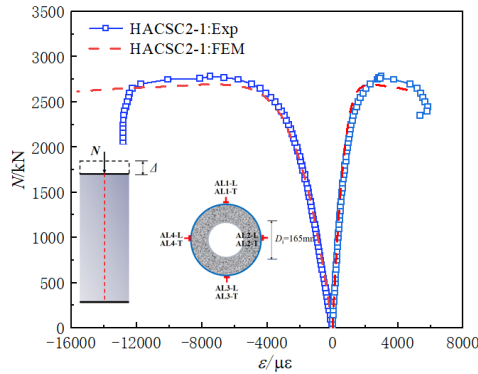
Fig. 5 Failure mode of typical specimen

3.2. Strain analysis

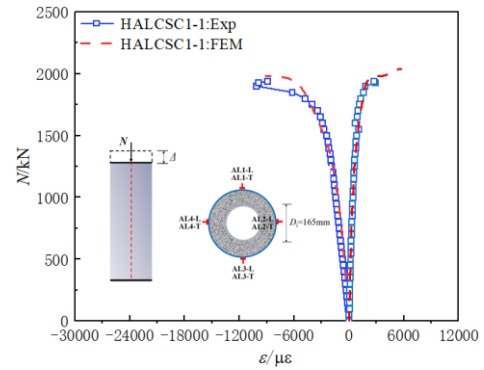
3.2.1. Load-strain curve

The Fig.6 illustrates the rule of longitudinal and transverse strain variations in specimens featuring ordinary and lightweight concrete as sandwich materials under axial loading. These strain measurements are derived by averaging the data collected by strain gauges AL1-L to AL4-L and AL1-T to AL4-T, which are symmetrically positioned at a height of $H/2$. By examining the load-strain curves depicted in figure 6 for the eight specimens, the following concise summary of the observed rules can be provided: (1) Early on in the loading process, the strain is approximately linear with the load, following the attainment of peak bearing capacity, the longitudinal and transverse strains

increase rapidly, this is because when the load approaches the ultimate bearing capacity, the sandwich concrete in the middle of the column expands laterally, causing the aluminum alloy tube to be compressed by the sandwich concrete, accelerating its lateral deformation, and the lateral deformation will have a certain impact on the longitudinal strain; (2) With the decrease of the hollow ratio, the buckling longitudinal strain of the aluminum alloy tubes of the HACSC series and HALCSC series gradually increases; (3) When other conditions remain constant, the transverse deformation of the specimen using lightweight concrete as sandwich concrete is faster than the specimen using ordinary concrete, the slope of the load-strain curve is reduced, and the stiffness is smaller.



(a) HACSC1-1



(b) HALCSC1-1

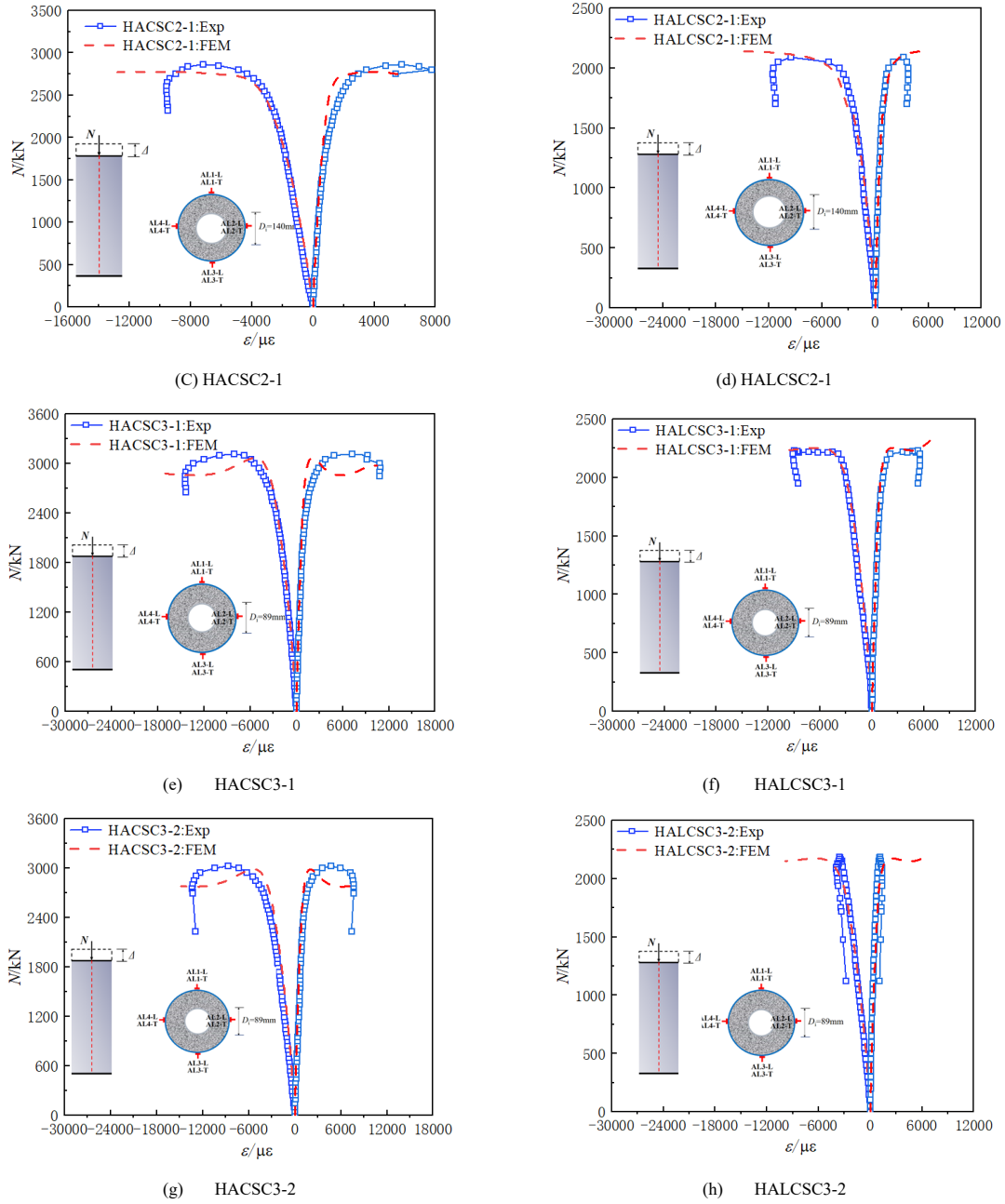


Fig. 6 Load-strain curve

3.2.2. Transverse deformation coefficient

Continuously increase the load until reaching a specific characteristic point, aluminum alloy tube has just begun to exert a progressive restraining influence on the sandwich concrete. For the further study of confinement mechanism of aluminum alloy tube on sandwich concrete at different stress stage, the transverse deformation coefficient is introduced [16-17], it is the ratio of the transverse strain (ε_{AL-T}) and the longitudinal strain (ε_{AL-L}) of the aluminum alloy tube. The relationship curves of the transverse deformation coefficient ($\varepsilon_{AL-T}/\varepsilon_{AL-L}$) with the load of the HACSC series and HALCSC series specimens are exhibited in Fig. 7(a) and (b).

The diagram in Fig. 7(a) illustrates that at the inception phase of loading, the transverse deformation coefficient rises and gradually converges towards the Poisson's ratio of aluminum alloy materials. During this phase, the interaction between the aluminum alloy tube and the sandwich concrete is negligible, and the entire specimen undergoes uniaxial compression. As loading progresses to later stages, the transverse deformation coefficient surpasses the

intrinsic Poisson's ratio of the aluminum alloy tube and continues to climb. This is due to the progressive increase in plastic deformation of the sandwich concrete with rising loads, resulting in greater transverse deformation of the concrete at the column's center compared to the aluminum alloy tube. Upon reaching the ultimate bearing capacity, the transverse deformation coefficient decreases, which is attributed to internal buckling of the steel tube, causing the specimen's transverse deformation to develop inwardly.

When Fig. 7(a) is compared with Fig. 7(b), it becomes apparent that the HALCSC series specimens exhibit a lower transverse deformation coefficient compared to the HACSC series, this is because the transverse and longitudinal deformation of the specimen using lightweight concrete as sandwich concrete is faster than the specimen using ordinary concrete, however, the longitudinal strain exhibits a quicker rate of increasing than the transverse strain.

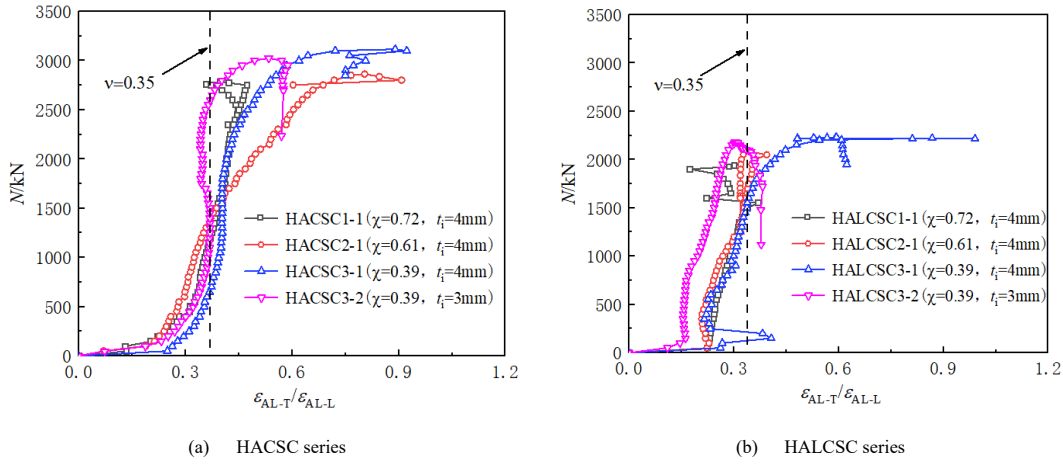


Fig. 7 Load- transverse deformation coefficient curve

3.3. Representative axial compression mechanical performance indicators

3.3.1. Load-displacement curve

Fig.8 displays the load-displacement profiles for specimens, while Table 1 outlines the ultimate bearing capacities derived from these profiles. The graphical representation in Fig.8 clearly indicates that eight specimens exhibit a largely similar trend in their load-displacement curves, progressing sequentially through a linear increase, a nonlinear increase, and a descent or stabilization phase. These phases are classified as the elastic stage, the elastic-plastic stage, and the plastic stage, respectively.

The rules drawn from comparing the ultimate bearing capacities of specimens across various parameters listed in Table 1 are as follows. (1) Upon decreasing the hollow ratio from 0.72 to 0.61 and further to 0.39, the HACSC series (and HALCSC series) specimens showed an increase in their ultimate bearing capacities by 3.28% and 12.38% (7.72% and 14.95%), respectively. This suggests that, while reducing the hollow ratio does enhance the bearing

capacity somewhat, its impact is relatively modest when the geometric dimensions and material strength of the specimens remain unchanged. (2) When the wall thickness t_i of the steel tube was incremented from 3mm to 4mm, the ultimate bearing capacity of the HACSC series (and HALCSC series) specimens rose by 3.04% (2.09%). This is because the interaction between the steel tube and the sandwich concrete remains limited throughout the loading process, and the steel tube experiences inward local buckling during the later stages of loading. Consequently, augmenting the wall thickness of the steel tube contributes only marginally to the bearing capacity of the specimens. (3) In comparison to the HALCSC series specimens, the HACSC series specimens with hollow ratios of 0.72, 0.61, and 0.39 demonstrated significant increases in their bearing capacities by 43.4%, 37.0%, and 39.7% respectively. This is due to the superior composite strength exhibited by the aluminum alloy tube and sandwich concrete in the HACSC series specimens, which surpasses that of the HALCSC series specimens.

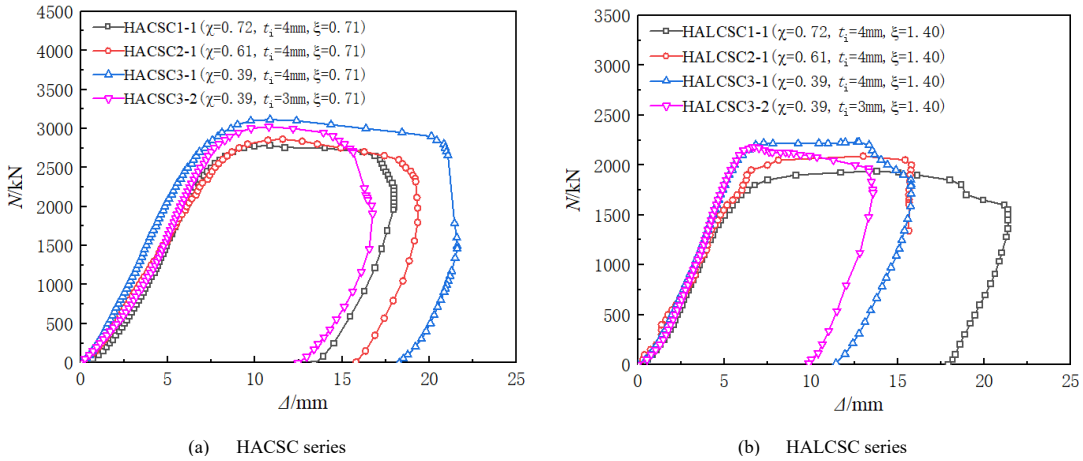


Fig. 8 Load-displacement curve

3.3.2. Axial compressive stiffness

Axial compression stiffness is a key indicator reflecting the ability of specimens to resist axial deformation, it can be calculated based on Ref. [18], the calculation formula can be expressed as follows:

$$EA = 0.4N_{uc} \cdot H / \Delta_{0.4} \quad (1)$$

Where EA represents the axial compression stiffness, N_{uc} is the ultimate bearing capacity, H represents the height of the column, $\Delta_{0.4}$ represents the longitudinal displacement when the bearing capacity reaches $0.4 N_{uc}$.

Fig.9 illustrates the axial compressive stiffness of specimens with varying parameters, Fig. 9(a) reveals a negative correlation between the hollow ratio and the axial compressive stiffness of the specimen. Specifically, as the hollow ratio rose from 0.39 to 0.61 and then to 0.72, the axial compressive stiffness of the HACSC series decreased by 20% and 27.7%, respectively, while the HALCSC series exhibited reductions of 10.2% and 13.9%. The underlying reason for this is that, during the elastic stage, the components of the specimen undergo

uniaxial compression without significant interaction among them, consequently, the axial compressive stiffness of the specimen can be approximated by summing the stiffness of its individual components, an increase in the hollow ratio leads to a reduction in the sandwich concrete's area and a corresponding increase in the internal steel tube's area. Calculations indicate that the stiffness loss due to the decreased cross-section of the sandwich concrete outweighs the stiffness gain from the expanded steel tube area. Fig.9(b) displays the axial compressive stiffness of specimens with different wall thicknesses. It is apparent from Fig.9(b) that an increment in the steel tube's wall thickness from 3 mm to 4 mm results in a 21.6% increase in the axial compressive stiffness of the HACSC series and a 4.3% increase in the HALCSC series. This occurs because augmenting the wall thickness of the steel tube expands its cross-sectional area, subsequently boosting the specimen's capacity to withstand axial deformation.

In conclusion, the axial compressive stiffness is significantly influenced by the cross-sectional area, making it imperative to thoroughly consider the cross-sectional area ratio of each component during the structural design phase to guarantee that both strength and stiffness meet the required safety standards.

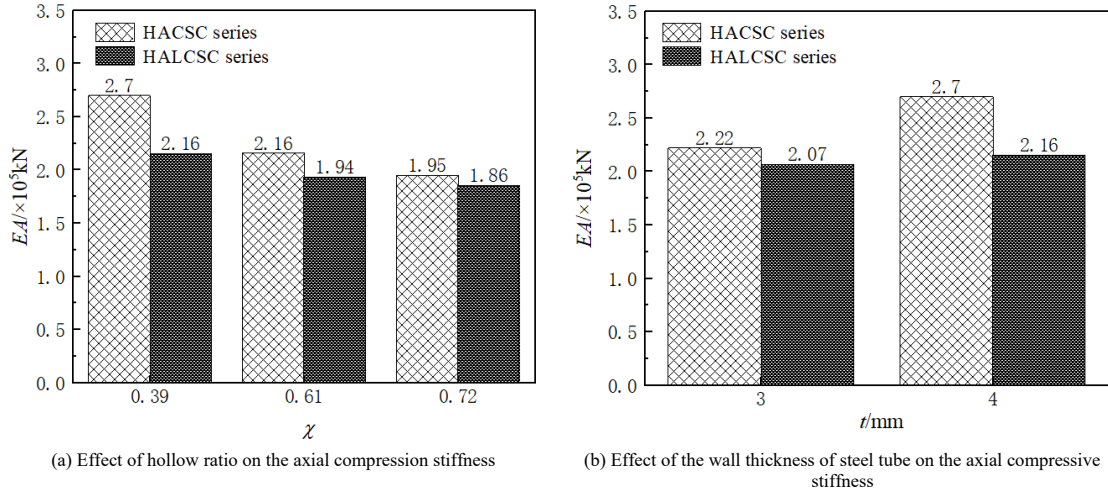


Fig. 9 axial compressive stiffness

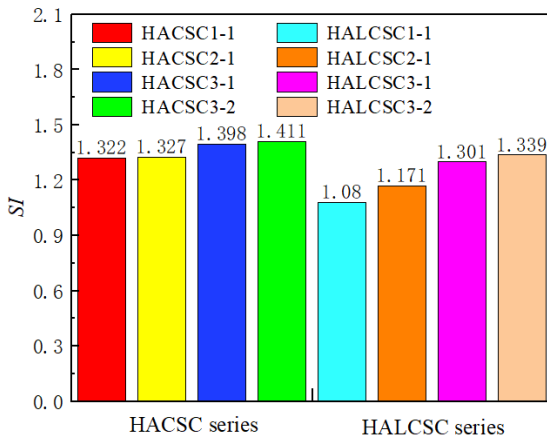
3.3.3. Strength coefficient

The strength coefficient SI can reflect the composite effect of the specimens, the paper adopts the method recommended in Ref. [19] for calculation, the representation of SI is outlined below:

$$SI = \frac{N_{ue}}{f_{A-0.2}A_a + f_{ck}A_c + f_{yi}A_s} \quad (2)$$

Where $f_{A-0.2}$ is the nominal yield strength of the aluminum alloy tube, A_a is the area of the aluminum alloy tube's cross-section, f_{ck} is the axial compressive strength of the concrete, A_c is the area of sandwich concrete's cross-section, f_{yi} is the yield strength of the internal steel tube, A_s is the area of the internal steel tube's cross-section.

Fig.10 presents the strength coefficients SI of the specimens under different parameters. As illustrated in Fig.10, the SI of the HACSC series (HALCSC series) specimens is in the range of 1.322 ~ 1.411 (1.080 ~ 1.339), which indicates that the specimen has a good composite effect. In addition, it can also be found from Fig.10 that the SI of the HACSC series (HALCSC series) specimens increases by 0.38% and 5.75% (8.4% and 20.5%) when the hollow ratio decreases from 0.72 to 0.61 and 0.39 respectively, the SI increase rate of the HALCSC series specimens is faster than the HACSC series specimens, this is because the confinement effect coefficient ξ ($\xi = \alpha_n f_{A-0.2} / f_{ck}$, $\alpha_n = A_a / A_{ce}$, α_n is the nominal aluminum ratio, A_{ce} is the nominal cross-sectional area of sandwich concrete) increased from 0.71 to 1.40 when the ordinary concrete in the sandwich area is replaced by lightweight concrete, therefore, the aluminum alloy tube of the HALCSC series specimens has a stronger confinement effect on the sandwich concrete.

Fig. 10 the strength coefficients SI

4. Numerical simulation analysis

4.1. Establish finite model

4.1.1. The stress-strain relationship of each component material

4.1.1.1. Aluminum alloy

The distinctive mechanical features of aluminum alloys set them apart from steel produced through hot-rolling of low-carbon and standard low-alloy steel, as they exhibit no pronounced yield point. On that account, the stress-strain characteristics of aluminum alloys are captured using the isotropic elastoplastic constitutive model outlined in Reference [20], and this model can be mathematically expressed through Equ (3):

$$\varepsilon_a = \frac{\sigma_a}{E_a} + 0.002 \left(\frac{\sigma_a}{f_{A-0.2}} \right)^n \quad (3)$$

where σ_a and ε_a represent the stress and strain of the aluminum alloy respectively, and E_a is the modulus of elasticity of the aluminum alloy ($E_a = 70000 \text{ MPa}$), n is the parameter describing strain hardening, Eq.(4) is applied to calculate it.

$$10n = f_{A-0.2} (\text{MPa}) \quad (4)$$

4.1.1.2. Sandwich concrete

Sandwich concrete is primarily constrained by aluminum alloy tubes, which have the difference constraining effect compared to steel tubes on concrete, therefore, the constitutive relationship of sandwich concrete adopts the equivalent compressive stress-strain model proposed in Ref. [5], which can be expressed by Eq. (4), and Fig. 11 depicts the stress-strain curve.

$$\sigma = \begin{cases} \left[\frac{2\varepsilon}{\varepsilon_{c0}} - \left(\frac{\varepsilon}{\varepsilon_{c0}} \right)^2 \right] f'_c & \varepsilon \leq \varepsilon_{c0} \\ f'_c & \varepsilon_{c0} < \varepsilon \leq \varepsilon_{cc} \\ f_r + (f'_c - f_r) \exp \left[- \left(\frac{\varepsilon - \varepsilon_{cc}}{\alpha} \right)^{1.2} \right] & \varepsilon > \varepsilon_{cc} \end{cases} \quad (5)$$

where f'_c represents the compressive strength of the concrete cylinder, the other indicators (f_r , ε_{c0} , ε_{cc} , f_{rp} , k , α) included in equation (5) can be calculated by equation (6)~(11).

$$f_r = 0.25 f'_c \quad (6)$$

$$\varepsilon_{c0} = f'_c \times 10^{-5} + 0.0022 \quad (7)$$

$$\varepsilon_{cc} = \varepsilon_{c0} \times \frac{t_o}{D_o} \times (611k^2 - 956k + 608) \quad (8)$$

$$k = f'_c \times \left(\frac{f_{rp}}{f'_c} \right)^{0.3124+0.002f'_c} \quad (9)$$

$$f_{rp} = \frac{1+0.027f_{A-0.2}e^{-0.02\frac{D_o}{t_o}}}{1+1.6e^{-10}(f'_c)^{4.8}} \quad (10)$$

$$\alpha = 0.04 - \frac{0.036}{1+e^{6.08\xi-3.49}} \quad (11)$$

In the Equ(6)-(11), f_r represents the compressive strength of concrete after considering strength reduction, ε_{co} denotes the strain at which peak compressive stress occurs, ε_{cc} is the strain corresponding to the confined axial compressive strength of concrete, and α stands for the strain adjustment coefficient, which is primarily related to the confinement effect coefficient.

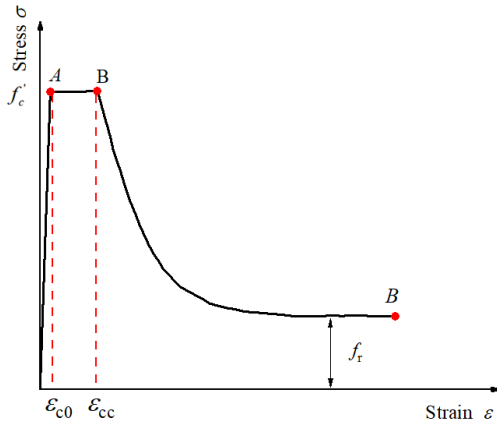


Fig.11 Stress-strain relationship curve of sandwich concrete

4.1.1.3. Steel

The constitutive model chosen for the embedded hollow steel tube is the five-stage stress-strain model introduced by Han et al. [21], and its formulation is detailed as follows.

$$\sigma_s = \begin{cases} E_s \varepsilon_s & \varepsilon_s \leq \varepsilon_e \\ -A\varepsilon_s^2 + B\varepsilon_s + C & \varepsilon_e < \varepsilon_s \leq \varepsilon_{e1} \\ f_y & \varepsilon_{e1} < \varepsilon_s \leq \varepsilon_{e2} \\ f_y \left[1 + 0.6 \frac{\varepsilon_s - \varepsilon_{e2}}{\varepsilon_{e3} - \varepsilon_{e2}} \right] & \varepsilon_{e2} < \varepsilon_s \leq \varepsilon_{e3} \\ 1.6f_y & \varepsilon_s > \varepsilon_{e3} \end{cases} \quad (12)$$

The indicators involved in formula (12) can be calculated using the following formula : $\varepsilon_e = 0.8f_y / E_s$, $\varepsilon_{e1} = 1.5\varepsilon_e$, $\varepsilon_{e2} = 10\varepsilon_{e1}$, $\varepsilon_{e3} = 100\varepsilon_{e1}$, $A = 0.2f_y / (\varepsilon_{e1} - \varepsilon_e)^2$, $B = 2A\varepsilon_{e1}$, $C = 0.8f_y + A\varepsilon_e^2 - B\varepsilon_e$.

4.1.2. Element type, mesh division, constraints and boundary conditions

In Fig.12, the finite element model constructed through the use of ABAQUS is displayed, featuring a specimen that is made up of four distinct parts: the upper and lower end plates, an aluminum alloy tube, sandwich concrete, and an internal steel tube. During the process of establishing this model, 8-node solid elements (C3D8R) were utilized for modeling all four of these components.

The interface model between component surface include tangential and normal behaviors, tangential behavior adopts "hard" contact, normal behavior adopts "penalty" friction, the friction coefficient is 0.25 [9]. To avoid relative slip between the end plate and the end face of the member, "tie" is used between the end plates and the specimen end. Mesh segmentation is vital to ensuring calculation precision, the size of the mesh is 1/20 of the diameter of each component itself.

To simulate the boundary conditions under test conditions with realism, we place reference points RP1 and RP2 at the central points of the upper and lower

end plates, respectively. We then couple the surfaces of these end plates to RP1 and RP2, respectively, where RP2 is constrained while an axial displacement is imposed on RP1.

Considering the initial defects caused by the fabrication and modeling assumptions of each material constituting the specimen, the initial defects will be taken as 1/1000 of the column length and defined in the finite element software in the form of low-order global buckling modes during the finite element calculation.

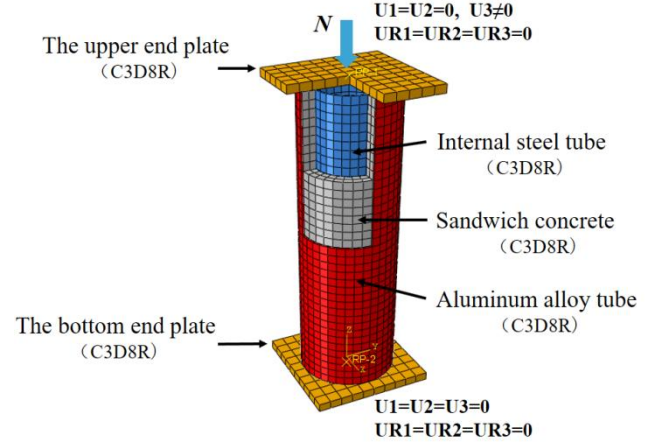


Fig.12 Schematic diagrams of model

4.2. Finite element verification

The load-strain curves of each specimen obtained through experimental and numerical simulation methods are presented in Fig.6 (a) ~ (h). Through comparison, it was found that the change trend of the load-strain curves obtained by the above two methods is basically consistent, and the ultimate bearing capacity attained through the experiment and the finite element calculation is listed in Table 1, The mean value and standard deviation $N_{u,FEM} / N_{u,e}$ are 0.99 and 0.04.

The failure mode using the experiment and finite element calculations are exhibited in Fig.5. By observing the failure modes of specimen adopting finite element calculation, it is found that the specimen was mainly manifested as bulging of the aluminum alloy tube at the middle and end of the column, the sandwich concrete at the corresponding position is crushed, and the internal steel tube was locally concave inward, which is generally consistent with the experimental phenomenon described in chapter 2.1.

In conclusion, the constitutive model and boundary conditions employed in the finite element analysis conducted in this study are dependable, enabling the finite element model to provide a more accurate assessment of the specimen's various mechanical performance indicators throughout the entire stressing process.

4.3. Analysis of working mechanism

According to the technical specification for CADST structures, a full-scale finite element model was designed as typical specimen, and the whole stressing process analysis and contact stress analysis of typical specimens were carried out. The parameter information of a typical specimen is summarized as follows: $D_o=400\text{mm}$, $H=1200\text{mm}$, $D_i=195\text{mm}$, $t_i=4\text{mm}$, $\chi=0.5$, $f_{cu}=40\text{MPa}$, $f_{A-0.2}=210\text{MPa}$, $f_{y1}=345\text{MPa}$.

4.3.1. Analysis of the whole stressing process

The figure depicted in Fig. 13 displays the load-displacement curves for a typical specimen and its constituent parts. Analyzing the trend of these curves reveals three distinct and identifiable characteristic points: Feature point A marks the yielding of the internal steel tube and the attainment of ultimate bearing capacity by the sandwich concrete; Feature point B signifies the achievement of ultimate bearing capacity by the typical specimen; and Feature point C indicates that the aluminum alloy tube has reached its ultimate bearing capacity.

The three aforementioned feature points segment the load-displacement curve into three distinct phases: the elastic phase (OA), the elastoplastic phase (AB), and the strengthening phase (BC). Figure 14 illustrates the distribution of longitudinal stresses at each of these feature points.

During the elastic stage (OA), as the displacement increases, the load rises linearly. At feature point A, the longitudinal stress within the sandwich concrete exhibits a gradual decline from the outer regions towards the center.:

Elastoplastic Stage (AB): Once the feature point A is surpassed, the load

begins to rise in a nonlinear fashion as displacement increases. When the specimen reaches feature point B, it attains its peak bearing capacity, with the loads carried by the aluminum alloy tube, sandwich concrete, and steel tube making up 31.1%, 53.5%, and 15.9% of the total axial compressive capacity of the specimen, respectively. An examination of the stress contour diagram during the elastoplastic stage reveals a gradual escalation in the average longitudinal stress of the sandwich concrete. The peak longitudinal stress, which occurs on the inner surface of the aluminum alloy tube at feature point A, amounts to 1.74 times the axial compressive strength of the concrete ($1.74f_{ck}$). This is owing to the aluminum alloy tube providing the utmost restraint to the sandwich concrete in this particular area.

Strengthening stage (BC): After the feature point B is exceeded, the bearing capacity of the specimen gradually decreases, sandwich concrete is constrained by aluminum alloy tubes, so its longitudinal stress variation is small; Upon attaining feature point C, the maximum longitudinal stress of the sandwich concrete is 1.76 times of the axial compressive strength, and the load-bearing capacity of the sandwich concrete reaches its peak.

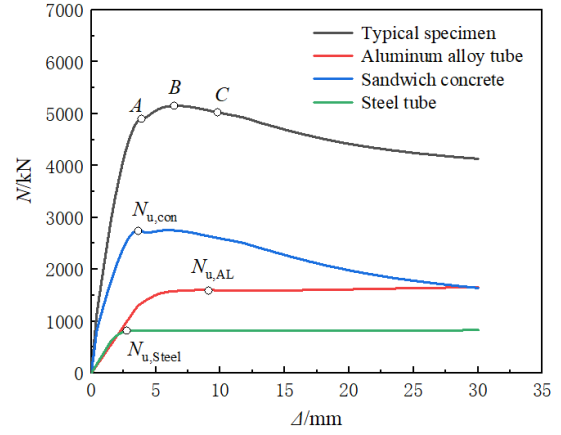


Fig. 13 Load-displacement curves of typical specimen and its components

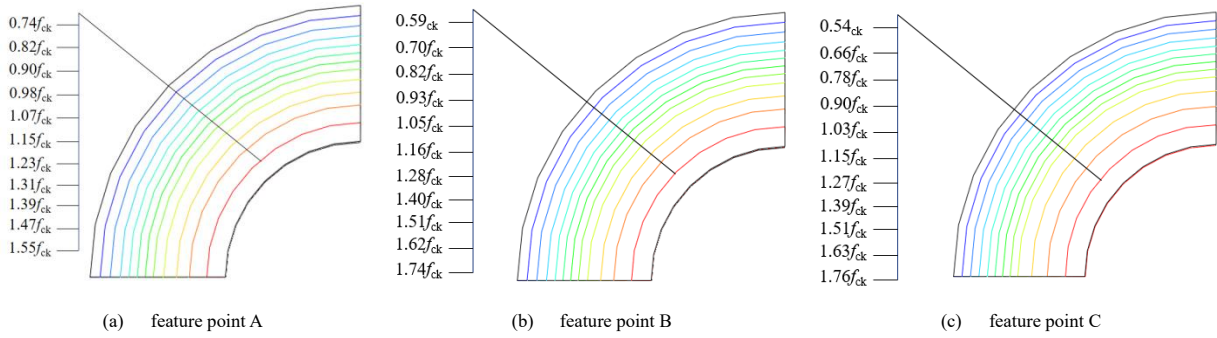


Fig. 14 Longitudinal stress distribution of sandwich concrete at each feature point

4.3.2. Contact stress analysis

The contact stress-displacement curves of each component at different height cross-sections of the typical specimen are shown in the Fig.15, P_1 represents the contact stress between aluminum alloy tube and sandwich concrete, and P_2 represents the contact stress between steel tube and sandwich concrete. As shown in the Fig.15, the contact stress between the steel tube and the sandwich concrete is always small throughout the whole stressing process, so its contact stress can be ignored, which illustrates that the internal steel tube work independently under axial compression; The contact stress value of aluminum alloy tube and sandwich concrete in the elastic stage at different height cross-sections is 0 ($P_1=0$), and each part of the specimen is in a uniaxial compression state, after exceeding the feature point A, the interaction between the aluminum alloy tube and the sandwich concrete is gradually obvious, and the contact stress between the two increases, when the load of the typical specimen reaches the ultimate bearing capacity (At feature point B), the average value of the contact stresses $P_{1H/4}$ and $P_{1H/2}$ of aluminum alloy tube and sandwich concrete are 0.77MPa and 0.99MPa respectively, the contact stress distribution is shown in Fig.16 ; After the feature point B is exceeded, the contact stress $P_{1H/4}$ and $P_{1H/2}$ still continue to increase.

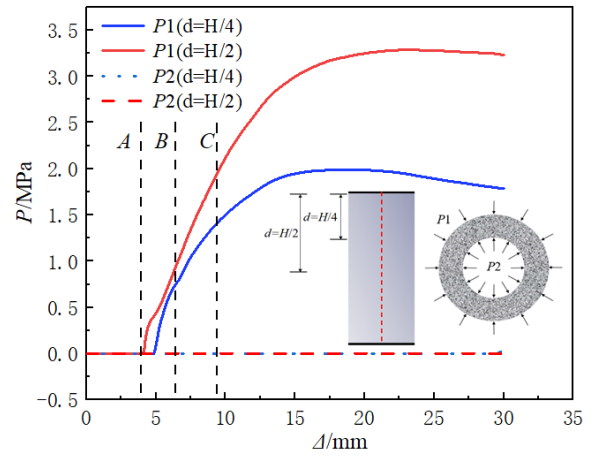


Fig. 15 The contact stress-displacement curves of each component

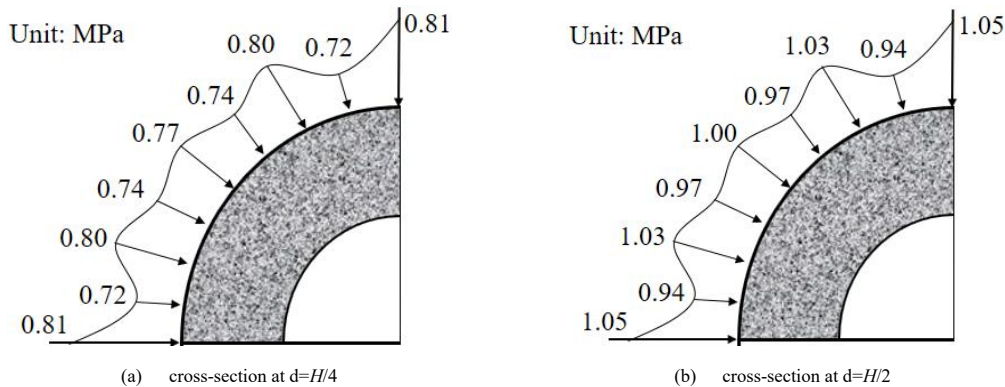


Fig. 16 Cross-section contact stress distribution at different heights under peak loads

5. Parametric analysis

Due to the limitations of current experimental conditions and the number of specimens, a lot of parameters cannot be fully covered, for the purpose of exploring the law of influence of parameters on the relevant performance of specimens, based on the typical specimens mentioned in chapter 3.3, the effects of nominal aluminum ratio, hollow ratio, concrete cube compressive strength and internal steel tube yield strength on the bearing capacity, axial compressive stiffness and ductility of specimens were subjected to detailed analysis.

5.1. Nominal aluminum ratio

When the wall thickness of the aluminum alloy tube is 3mm, 5mm, 7mm

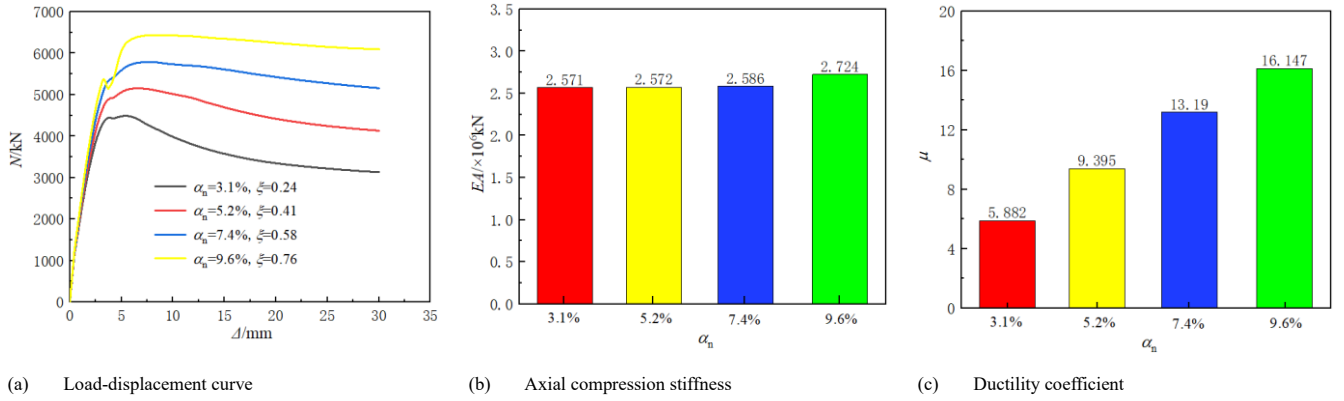


Fig. 17 The influence of nominal aluminum ratio on axial compression performance indicators

5.2. Hollow ratio

By adjusting the diameter of the internal steel tube, we can achieve variations in the hollow ratio of the specimens. Specifically, when the internal steel tube's diameter is set to 0mm, 117mm, 195mm, and 273mm, the corresponding hollow ratios of the specimens are 0, 0.3, 0.5, and 0.7, respectively. Fig.18 illustrates the impacts of these hollow ratios on the specimens' bearing capacity, axial compressive stiffness, and ductility. As depicted in Fig.18, as the hollow ratio increases from 0 to 0.3, 0.5, and 0.7, the

ultimate bearing capacity of the specimens decreases by 9.4%, 13.8%, and 21.8%, respectively, while the axial compressive stiffness decreases by 6.5%, 8.4%, and 20.2%. Conversely, the ductility increases by 32.9%, 40.3%, and 97.1%, respectively. This is attributed to the reduction in the sandwich concrete's cross-sectional area as the hollow ratio increases, which subsequently decreases the bearing capacity and axial compressive stiffness. Simultaneously as well, the increase in the hollow ratio enlarges the cross-sectional area of the internal steel tube, leading to an increase in the specimen's steel ratio and ultimately enhancing its ductility.

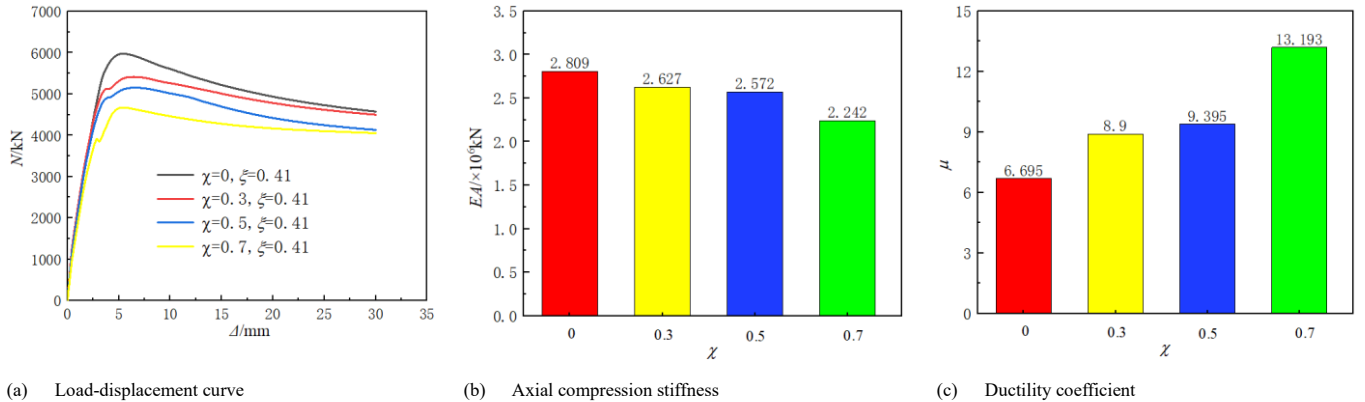


Fig. 18 The influence of hollow ratio on axial compression performance indicators

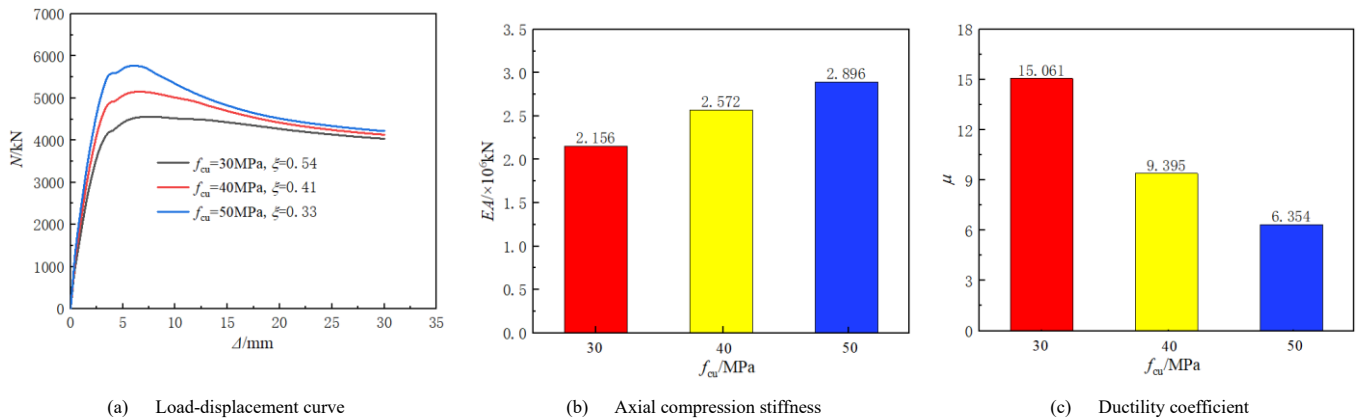


Fig. 19 The influence of concrete cube compressive strength on axial compression performance indicators

5.3. Concrete cube compressive strength

The graphical representation in Fig.19 illustrates how the compressive strength of concrete cubes influences the specimen's load-bearing capacity, stiffness in axial compression, and ductility. According to Fig.19, as the concrete cube compressive strength f_{cu} rose from 30MPa to 40MPa and then to 50MPa, the ultimate load-bearing capacity augmented by 12.9% and 26.5% respectively. Similarly, the stiffness in axial compression increased by 19.3% and 34.3%. Conversely, the ductility coefficient decreased by 37.6% and 57.8% respectively. This is because, with the cross-sectional area of the components remaining constant, an elevation in the compressive strength of the concrete cubes results in an increase in load-bearing capacity. Furthermore, an increase in the compressive strength of the concrete cubes leads to a corresponding rise in the concrete's elastic modulus, thereby directly enhancing its stiffness in axial compression. However, the higher the compressive strength of the concrete, the more pronounced its brittle nature becomes, causing a gradual decrease in the specimen's ductility.

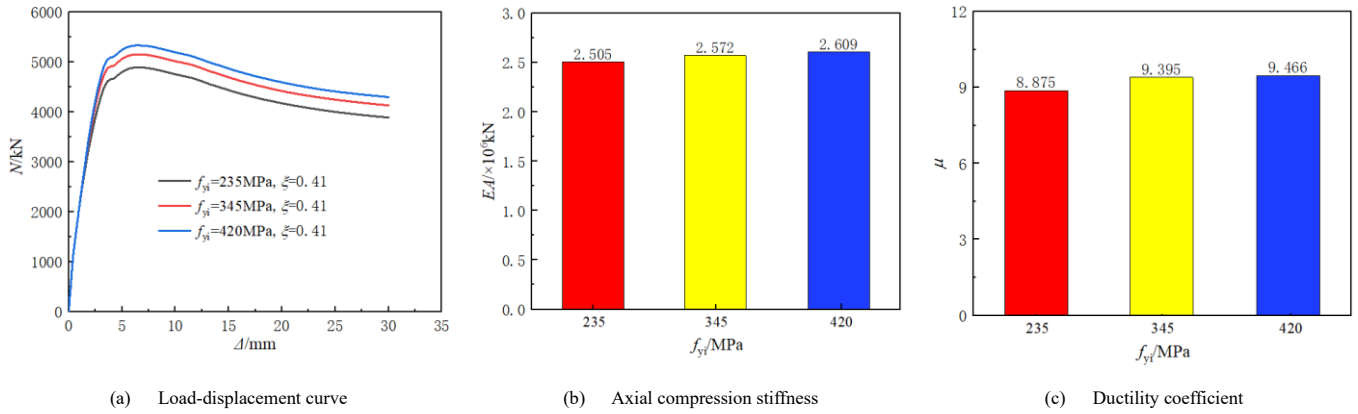


Fig. 20 The influence of internal steel tube yield strength on axial compression performance indicators

6. Practical bearing capacity calculation method

Drawing upon the insights from section 3.3.2, it is possible to conclude that there is insignificant interaction between the internal steel tube and the sandwich concrete. Therefore, the bearing capacity of the specimen can be approximated by summing the bearing capacity contributed by the aluminum alloy tube and sandwich concrete composite action, and the bearing capacity provided by the internal steel tube. Guided by the superposition principle outlined in the Technical Specification for CFST Structures (T/CCES7-2020) [22], we propose an equation to determine the axial compressive load-bearing capacity of concrete filled circular aluminum alloy tubular column with built-in hollow steel tube.

$$N_{u,acs} = N_{u,ac} + N_{is}$$

$$N_{u,ac} = f_{oac} \cdot (A_a + A_c)$$

$$N_{is} = f_{yt} A_s$$

Where $N_{u,acs}$ is the bearing capacity of CFAT column with built-in hollow steel tube, $N_{u,ac}$ represents the bearing capacity of the aluminum alloy tube and sandwich concrete composite action, $N_{u,is}$ represents the bearing capacity of the internal steel tube, f_{oac} is design values for the composite strength of aluminum alloy tube and sandwich concrete.

Considering that the CFAT column with built-in hollow steel tube is a structural design refined from the CFAT column, therefore, it is necessary to first assess the composite axial compressive strength f'_{oac} of CFAT column, then calculating the design value of the composite strength of aluminum alloy tube and sandwich concrete f_{oac} . References [5,23-24] conducted experimental analysis and theoretical research on CFAT column under different parameters, the relationship between the confinement effect coefficient ξ and f'_{oac}/f_{ck} was obtained by collecting and processing relevant data, through Origin fitting, it was found that there is a good linear relationship between ξ and f'_{oac}/f_{ck} , the correlation between the composite axial compressive strength f'_{oac} of CFAT

5.4. Internal steel tube yield strength

Fig.20 demonstrates the influence of the yield strength of the internal steel tube on the specimen's bearing capacity, axial compressive stiffness, and ductility. According to the data presented in Fig.20, as the yield strength of the internal steel tube rose from 235MPa to 345MPa and subsequently to 420MPa, the ultimate bearing capacity increased by 5.3% and 9.0%, respectively. Similarly, the axial compressive stiffness augmented by 2.7% and 4.2%, and the ductility coefficient also rose by 5.6% and 6.7%. The aforementioned research findings reveal that the yield strength of the internal steel tube exerts a relatively minor influence on the bearing capacity, axial compressive stiffness, and ductility coefficient. This is attributed to the lack of substantial interaction between the internal steel tube and the sandwich concrete during axial compression, as well as the occurrence of concave buckling in the steel tube during the later stages of loading. Consequently, enhancing the yield strength of the internal steel tube contributes less significantly to improving the bearing capacity, axial compressive stiffness, and ductility.

column and the confinement effect coefficient ξ is expressed as follows:

$$f'_{oac} = (1.1967\xi + 1.3631)f_{ck}$$

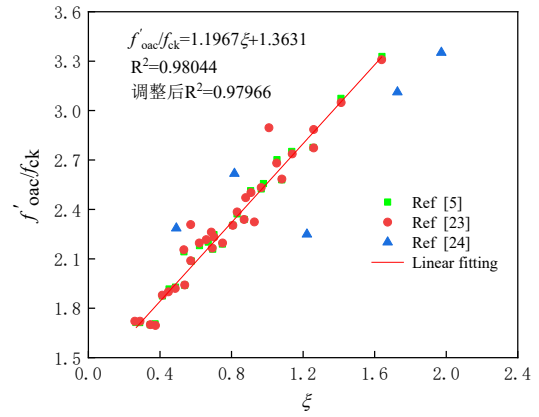


Fig.21 The relationship of $f'_{oac}/f_{ck} - \xi$

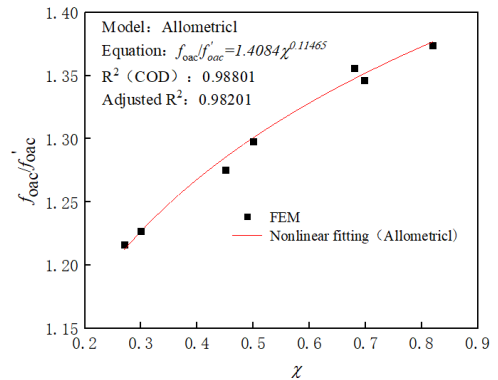


Fig. 22 f_{oac}/f'_{oac} and λ fitting results

Furthermore, taking a typical specimen as an example to study the correlation between hollow ratio χ and f_{oac} / f'_{oac} , the hollow ratio χ is taken as 0.27, 0.3, 0.45, 0.5, 0.68, 0.7, and 0.82 respectively, the correlation between hollow ratio χ and f_{oac} / f'_{oac} of the specimen was obtained by nonlinear fitting as follows:

$$f_{oac} / f'_{oac} = 1.4084\chi^{0.11465}$$

To summarize, the load-bearing capacity $N_{u,ac}$ of the aluminum alloy tube and sandwich concrete, when subjected to composite action, can be formulated as outlined below.

$$N_{u,ac} = 1.4084\chi^{0.11465} (1.1967\xi + 1.3631) f_{ck} (A_a + A_c)$$

Utilizing the superposition principle, the equation for assessing the load-bearing capacity of a circular aluminum alloy tube column filled with concrete and featuring an integral hollow steel tube is presented below:

$$N_{u,acs} = 1.4084\chi^{0.11465} (1.1967\xi + 1.3631) f_{ck} (A_a + A_c) + f_{yt} A_s$$

The bearing capacity $N_{u,acs}^c$ of 8 specimens was calculated using the proposed bearing capacity formula, and compared with the test measured and finite element simulation results $N_{u,acs}^{t+FEM}$. The comparison results are shown in Fig.23, between the above two have a deviation of 9.9% to -19.4%, this indicates that the proposed bearing capacity calculation formula can effectively predict the axial compressive bearing capacity of CFAT column with built-in hollow steel tube.

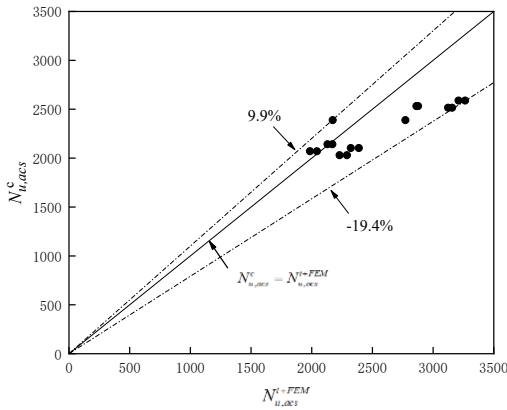


Fig. 23 Comparison between calculation results and test (finite element) results

7. Conclusions

Through experiments and numerical simulations, a thorough and systematic evaluation has been conducted on the performance indicators of the innovative component presented in this paper. Drawing from current research findings, the conclusions can be derived are listed as follows.

The failure mode of CFAT column with built-in hollow steel tube under axial compression is manifested as local bulging at the middle or top of the column, aluminum alloy tube exhibit local bulging and even cracking, the concrete located at the corresponding area has been fractured, and the internal steel tube presents concave buckling, each component demonstrates good deformation coordination.

The type of concrete is pivotal in determining both the load-bearing capacity and stiffness of the specimens. When the hollow ratio is 0.72, 0.61, and 0.39, the bearing capacity of specimens with ordinary concrete as the sandwich concrete is 43.4%, 37.0%, 39.7% larger than specimens with lightweight concrete as the sandwich concrete, and the axial compression stiffness is 4.8%, 11.3%, and 25% greater than them. Increasing the wall thickness of the internal steel tube has a relatively small impact on the bearing capacity and stiffness of the specimen. Through calculation, it was found that the strength coefficients S_f of two types of specimens (HACSC series and HALCSC series) were greater than 1, which indicate a good composite effect between the components

Through numerical simulation analysis methods, the working mechanism

of the specimen was studied, including the analysis of the entire stress process and contact stress. The study found that most of the load was shared by the sandwich concrete during the entire stress process, and The failure sequence of the specimen unfolds as follows: The yield of internal steel tube and the ultimate bearing capacity of sandwich concrete almost occur simultaneously→ the load of the specimen reaches its ultimate bearing capacity→ aluminum alloy tube reach their ultimate bearing capacity. Meanwhile, the findings from the contact stress analysis demonstrate a nearly absent level of interaction at the interface between the inner steel tube and the sandwich concrete.

The results of parameter analysis reveal that the aluminum ratio exerts the most prominent influence on the specimen's load-bearing capacity and ductility. Specifically, as the aluminum ratio escalated from 3.1% to 5.2%, 7.4%, and 9.6%, the specimen's load-bearing capacity augmented by 14.8%, 28.9%, and 43.4%, respectively, while its ductility coefficient soared by 59.7%, 124.2%, and 174.5%. Conversely, fluctuations in the yield strength of the internal steel tube had a comparatively minor effect on the specimen's load-bearing capacity, axial compression stiffness, and ductility.

Following a comparison of the results derived from the formula calculation, rooted in pertinent technical specifications and parameter evaluations, with the experimental (finite element modeling) data for concrete filled circular aluminum alloy tubular column with built-in hollow steel tube, it was evident that the proposed method for calculating bearing capacity exhibited good practical utility, with deviations within a range of -19.4% to 9.9%.

Reference

- [1] L.H. Han, Y.F. Yang, Technology of concrete with tubular structures. Beijing: China Architecture & Building Press, 2004.
- [2] X.H. Zhou, Y.H. Wang, G.B. Lu, et al. Mechanical behavior of concrete filled double skin steel tubular columns under cyclic pure torsion. Journal of Building Structures 38. S1(2017):266-271.
- [3] H.Y. Xu, Z.W. Yu. Behavior analysis of concrete-filled double skin steel tubular columns under axial loading. Journal of Huazhong University of Science and Technology (Natural Science Edition), 39.12(2011):123-127.
- [4] Z.B. Wang, H.Y. Gao, S. Y. Chi, et al. Behavior of concrete-filled double-skin thin-walled steel tubular columns under eccentric compression. Journal of Building Structures (2018).
- [5] X. Zeng, W.B. Wu, J.S. Huo, et al. The axial strength of concrete-filled aluminum alloy circular tubular stub columns. Engineering Mechanics, 38.2(2021):52-60.
- [6] X.Y. Li, G.H. Xing, P.Y. Zhang, et al. Calculation on bearing capacity of 7075 high-strength aluminum alloy tubular confined concrete column under axial compression. Industrial Construction, 50.11(2020):162-167.
- [7] D. Chen, H. Qu, W. Li, et al. Mechanical Property of Seawater Sea-sand Concrete-filled Aluminum Alloy Circular Tubular Columns under Axial Load. Journal of Yantai University (Natural Science and Engineering Edition), 35.04(2022):467-475.
- [8] Y. Shi, J.G. Zhang, T. Wang, et al. Experimental study on the axial compression performance of a new type of metal tube concrete short column. Building Structure, 52.03(2022):110-115.
- [9] F. Zhou, B. Young. Concrete-filled double-skin aluminum circular hollow section stub columns. Thin-Walled Structures 133.12(2018):141-152.
- [10] X.X. Zha, Y.L. Gong. Behavior study of new type concrete filled metal tubular (CFMT) I: Columns strength capacity of axially compressed short columns. Progress in Steel Building Structures, 14.03(2012):12-18+35.
- [11] F. Zhou, B. Young. Numerical analysis and design of concrete-filled aluminum circular hollow section columns. Thin-Walled Structures, 50.1(2012):45-55.
- [12] F.C. Wang, H.Y. Zhao, L.H. Han. Analytical behavior of concrete-filled aluminum tubular stub columns under axial compression. Proceedings of the 12th International Conference on Advances in Steel-Concrete Composite Structures. ASCCS 2018.
- [13] Patel V I, Liang Q Q, Hadi M N S. Numerical simulations of circular high strength concrete-filled aluminum tubular short columns incorporating new concrete confinement model. Thin-Walled Structures 147.
- [14] GB/T 228.1. Metallic materials-tensile testing-part 1: method of test at room temperature. Standards Press of China, Beijing, 2010.
- [15] Standard for test methods of concrete physical and mechanical properties: GB/T 50081-2019. Beijing: China Architecture & Building Press, 2019.
- [16] F. X. Ding, Z. Li, S. S. Cheng, et al. Composite action of hexagonal concrete-filled steel tubular stub columns under axial loading. Thin Walled Structures 107(2016):502-513.
- [17] Q. Rong, Y.S. Zeng, X.M. Hou, et al. Experimental study on mechanical behavior of RPC-filled circular steel tube columns under axial compression. Journal of Building Structures (2019).
- [18] H. Zhao, Y. Zhang, R Wang. Study on mechanical behavior of square hollow concrete-encased CFST columns with inner steel plate under axial compression. Journal of Building Structures, 43.06(2022):53-62+141.
- [19] Li Y J, Han L H, Xu W, et al. Circular concrete encased concrete-filled steel tube (CFST) stub columns subjected to axial compression. Magazine of Concrete Research 68.19(2016):995-1010.
- [20] Ramberg W, Osgood W R. Description of stress-strain curve by three parameters [R]. Washington DC, USA: National Advisory Committee for Aeronautics, 1943.
- [21] Han L H, An Y F. Performance of concrete-encased CFST stub columns under axial compression. Journal of constructional steel research. 93.7(2014):62-76.
- [22] Chinese Code, Technical specification for concrete-filled double skin steel tubular structures: T/CES 7-2020, Beijing, China, 2020.
- [23] T Hu . Study on concentric compressive behavior of concrete-filled Aluminum Alloy Circular Tubular Stub Columns. Hainan University, 2019.
- [24] Y Q LIU. Experimental study on axial compression of concrete stub column with round Aluminium alloy tube . Shenyang Jianzhu University, 2020 .

LOAD-SLIP BEHAVIOR OF PERFOBOND SHEAR CONNECTORS POST HYDROCHLORIC ACID CORROSION ON BEARING CAPACITY

Fan Yang¹, Wen-Jing Qiao^{1,*}, Ting-Kun Zhou¹, Yun-Long Li¹, Zhi-Dan Ruan¹ and Shou-Fu Li²

¹ Dept. of Civil and Architecture Engineering, Xi'an Technological Univ., Xuefuzhonglu Ave., Weiyang District, Xi'an City, Shaanxi Province 710021, China

² China Construction Third Bureau Group Northwest Limited company, Jinyelu Ave., Yanta District, Xi'an City, Shaanxi Province 710076, China

* (Corresponding author: E-mail: qiaowenjing@xatu.edu.cn)

ABSTRACT

The study conducted push-out tests on seven specimen groups to investigate the load-slip behavior of PBL shear connectors affected by hydrochloric acid corrosion. Among them, the corrosion time of PBL shear connectors in specimens was 0, 1, 4, 12, 24, 48 and 72 h, respectively. Based on the test verification, 147 refined finite element models with varying corrosion durations were developed to examine factors such as concrete strength grade, end bearing conditions, penetrated steel bar diameter, and hole size in the steel plate. The load-slip characteristics decrease gradually with increased corrosion time. When the concrete grade, penetrated steel bar diameter, and steel plate hole size were increased to C60, 25 mm, and 65 mm, the slippage decreased by 17.13%, 9.49%, and 11.77%, respectively. Additionally, the slip amount under end pressure was 8.26% lower compared to that without end pressure. The load-slip formula is proposed by comparing the test findings.

ARTICLE HISTORY

Received: 22 July 2024
Revised: 15 January 2025
Accepted: 6 February 2025

KEYWORDS

Perfobond shear connectors;
Hydrochloric acid corrosion;
Push-out experiment;
Load-slip characteristics

Copyright © 2025 by The Hong Kong Institute of Steel Construction. All rights reserved.

1. Introduction

PBL shear connectors enable the concrete to constrain the steel beam's compression flange, thereby improving its stability [1-4]. Meanwhile, tanks carrying dangerous chemicals are increasing day by day. When the corrosive liquid in the vehicle overturns and penetrates penetrated steel bar. This action can lead to the corrosion of shear connectors to diminish their load-slip behaviour. Therefore, ductility and durability of the bridge decrease. Hence, it is urgent for PBL shear connectors to study the load-slip behaviour with hydrochloric acid corrosion.

At present, load slip properties and fatigue properties of PBL shear connectors have been studied extensively [5-6]. Yang took the numerical regression analysis method to establish the load-slip curve [7]. Xiao analyzed the load transfer characteristics, load slip law and mechanical properties [8]. Aguiar failure mode, controlled by transverse reinforcement, proposed an innovative model to forecast the entire load-slip curve [9]. Le proposed an efficient long short-term memory-based model for prediction of the load-displacement curve of concrete-filled double-skin steel tubular columns [10]. While the experimental and numerical investigations provide the load-slip curve [11-13], a calculation formula still needs to be established.

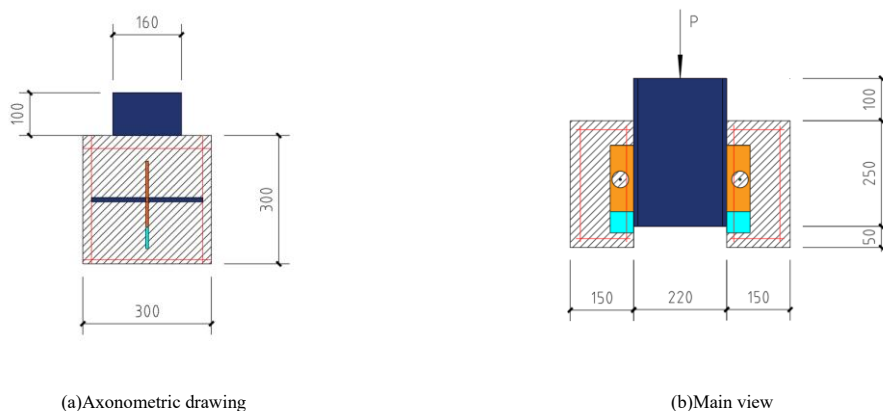
It is well known that different stages of load-slip curves are in various forms. Li put forward linear and power law models of elastic and elastoplastic stages [14]; Wang also raised linear and log models of the same stages [15]. Cao JX predicted the nonlinear behaviour based on load-slip curves of composite materials and used a Bayesian method to quantify model parameters [16]. Huang selected two introduced position functions to establish the relative slip constitutive model [17]. Cao YM posed a descriptive model of shear slip

characteristics taking into the stiffness of elastic connectors of connectors account [18]. In view of the above mathematical models of the load-slip formula, scholars also studied the effects of various factors on load-slip, including ultra-high performance, ordinary, lightweight, high-strength and lightweight high-strength concrete; bond friction between transverse reinforcement and elliptical holes; round and long holes of the connectors [19-23]. However, the load-slip behavior of shear link components in a hydrochloric acid environment was not considered in the above research.

To summarize, prior research has been dedicated to investigating the impact of atmospheric exposure on the mechanical performance of PBL shear connectors, with a focus on developing formulas specific to atmospheric corrosion conditions. The research primarily concentrated on the mechanical behavior of PBL shear connectors and the influence of parameters such as the thickness of perforated steel plates, the size of the openings, the strength grade of the concrete, and the diameter of the through-reinforcement. When 36% industrial hydrochloric acid contact penetrates the steel bar in a short time, the strong-corrosion will affect the overall durability of the composite structure. This paper examines the load-slip behavior and formula of PBL shear link components corroded by industrial hydrochloric acid, based on push-out tests and finite element modeling (FEM). The findings establish a foundation for analyzing the structural and mechanical properties following strong acid corrosion.

2. Experimental setup

2.1. Design of test specimens



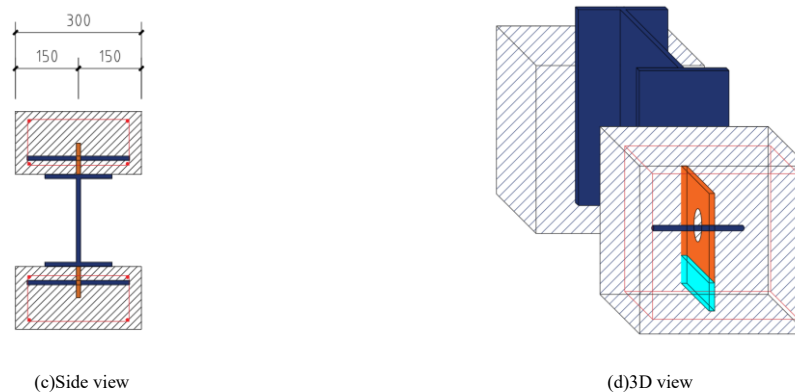


Fig. 1 Specimen structure (Units: mm)

The design included fourteen specimens arranged into seven groups. The main parameter sizes are shown in Fig. 1. The specimen mainly comprises C50 concrete, $\phi 10$ mm HPB300 light round steel bar of ordinary steel bars, and $\phi 14$ HRB400 screwed reinforcement. According to the above data, the reinforcement rate of the specimen is 0.60% transverse and 0.69% longitudinal. In addition, both I-steel and perforated steel plate are Q345q; the size is I-steel 220mm \times 160mm \times 16mm \times 16mm, and perforated steel plate 160mm \times 80mm \times 16mm.

The penetrated steel bar was corroded 0, 1, 4, 12, 24, 48 and 72 h, respectively. Then, the loss rate with different corrosion times was measured. The tensile test, conducted using the CSS-44000 series electronic universal testing machine, determined the mechanical properties, including elongation and strength. The rate of loading is elastic stage 0.75 mm/min, and yield stage 5 mm/min. The test procedure strictly adhered to the stipulations of GB/T 228.1-2021, "Test Method for Metal Tensile Properties"[24]. Table 1 indicated the penetrated steel bars' material mechanical indexes.

Table 1
The penetrated steel bars' material mechanics index with different corrosion time

Corrosion time/h	Corrosion rate/%	Ultimate strength/MPa	Yield strength/MPa	Elasticity modulus/Gpa
0	0.00	573.78	423.44	218.58
	0.00	578.47	390.67	220.91
	0.00	586.02	388.97	217.61
	0.54	571.69	396.00	217.34
1	0.49	578.94	402.72	218.43
	0.46	578.68	402.56	213.34
	1.75	601.03	391.00	208.96
4	1.83	555.53	396.00	211.89
	1.80	556.60	403.00	210.83
	3.28	548.57	393.00	206.76
12	3.28	546.35	390.00	203.78
	3.35	597.25	392.00	200.74
	6.67	552.82	385.99	202.55
24	5.98	556.11	389.39	198.77
	4.36	560.40	392.73	200.69
	5.55	552.82	387.00	198.79
48	6.22	556.11	383.00	197.63
	7.80	560.40	381.00	191.97
	9.10	553.20	382.00	190.68
72	9.25	552.49	382.00	193.47
	9.47	551.67	383.00	193.14

2.2. Test procedure

The test adopted a 2000 kN hydraulic four-column pressure testing machine (see Fig. 2). The loading method was firstly preloading the specimen at 80 kN for 3 times. The formal loading rate was adjusted to 1kN/s, and then the

specimens were yielded at 10% the estimated ultimate load. During the 2 min load holding stage of each stage, the load displacement of equipment and the cracks of the specimens were needed to record. Subsequently, the loading was stopped when the bearing capacity decreased to 70% of the ultimate load, with increments of 1 mm.

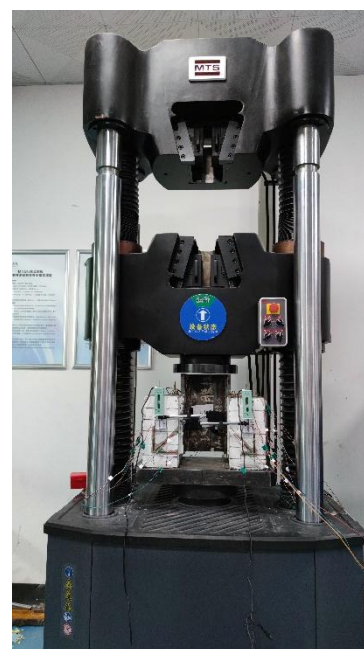


Fig. 2 Test arrangement and instrumentation

3. Experimental results

3.1. Test phenomena

The load on the I-steel transferred to the concrete plate at the beginning of loading. It can be seen that the bottom of the concrete plate has a small part of the concrete to produce many tiny cracks. At 0.69 Pu (ultimate load), the concrete on the contact surface between the concrete slab and the I-beam starts to detach, accompanied by a faint sound. As the loading reaches 0.82 Pu, small cracks begin to form in the center and along the bottom edge of the concrete slab, indicating that the sample is approaching the yield stage. The cracks are about 0.05 mm in width and 4–5 cm in length. After that, if the specimen arrived at peak bearing capacity, the sound inside makes a rattling sound, and 45° oblique cracks appear inside the concrete slab, extending to the periphery with a length of up to 6–7 cm. The cracks of the specimen mainly appear on the outside and inside surfaces of the concrete. Fig. 3 explains failure forms of specimens.

After corroded PBL shear link components are shear, the bending angles of the penetrated steel bar are 7.8°, 9.5°, 13.0°, 14.9°, 18.5°, 19.7°, and 21.1°, respectively (Fig. 4). At the same time, concrete cracks are deepened and lengthened. The initial crack load at corrosion time is 306.16, 287.22, 270.35, 268.33, 264.08, 251.67, and 231.26 kN, respectively. Additionally, The maximum bearing capacity with a 45° inclined crack decreases to 332.30, 311.74, 293.42, 291.24, 286.62, 273.16, 251.00 kN in turn.

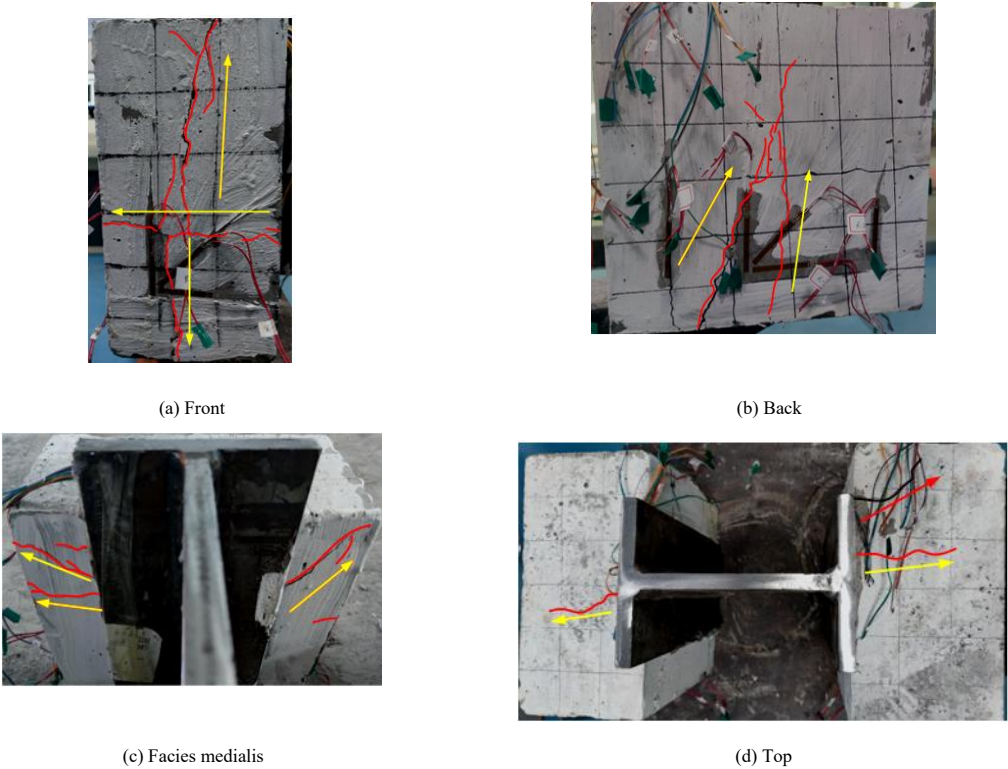
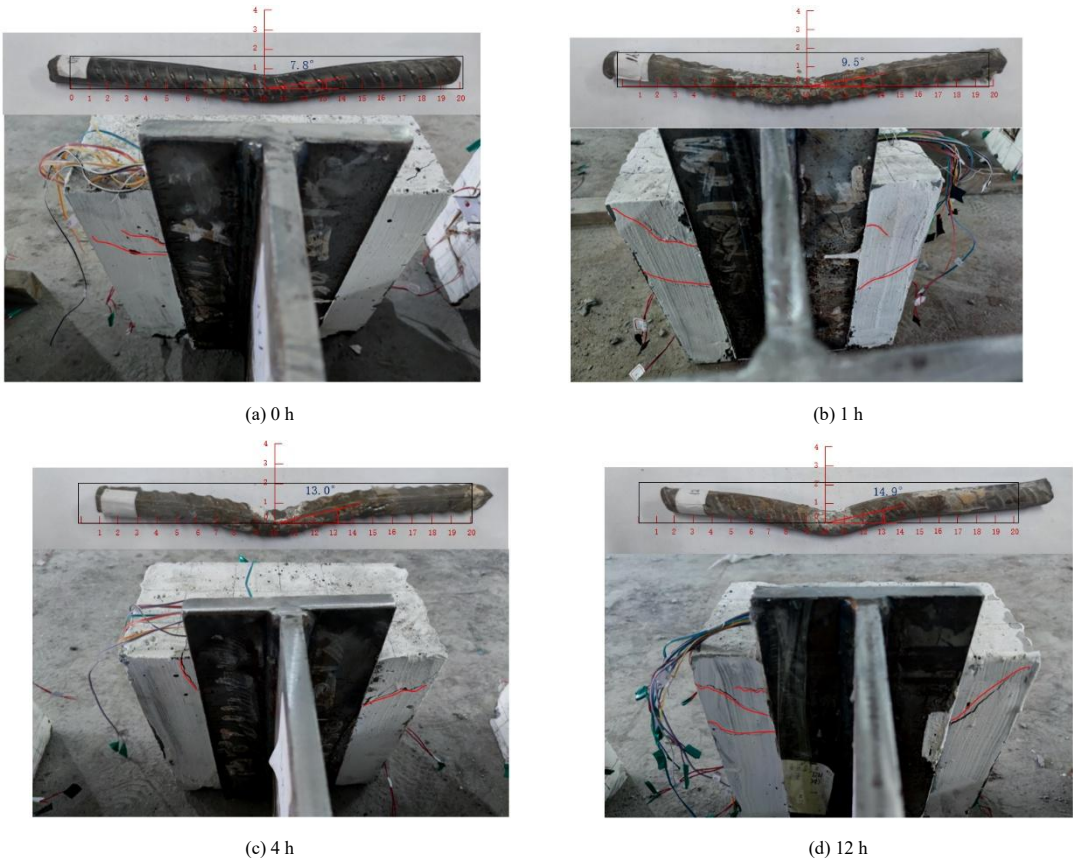


Fig. 3 Failure mode



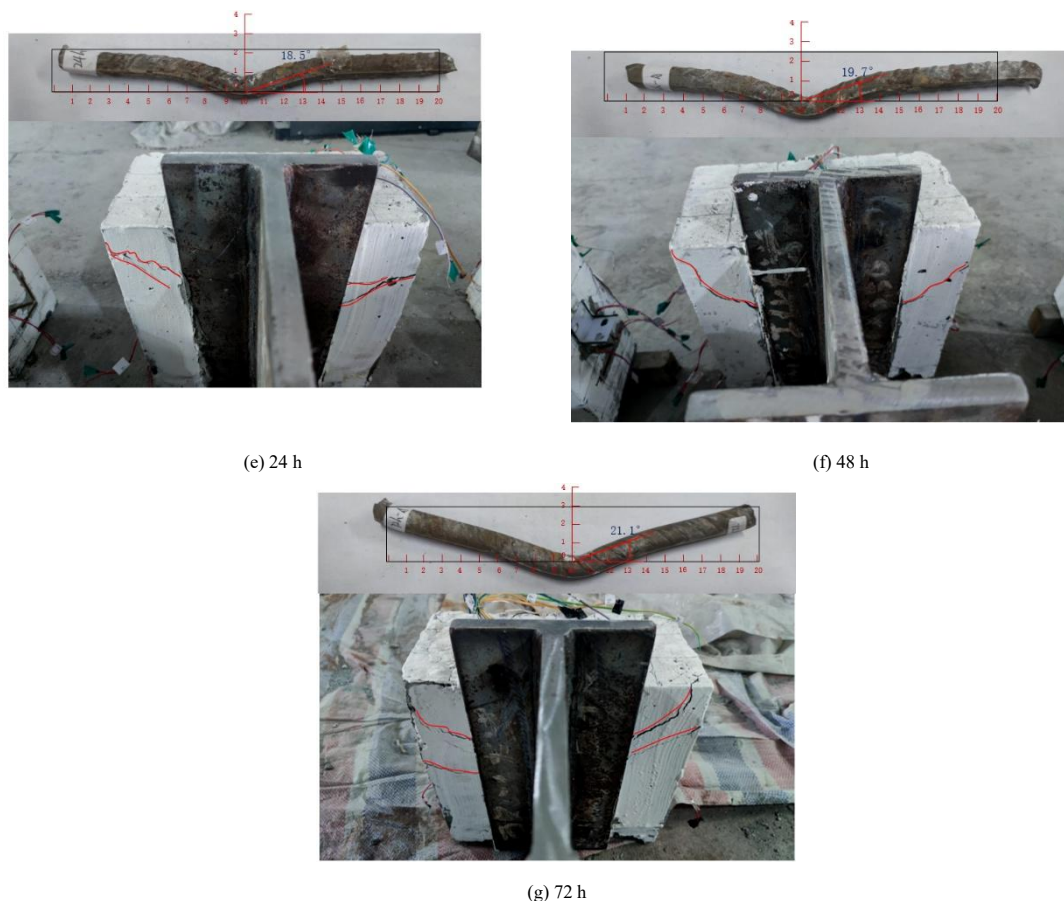


Fig. 4 Failure modes of corroded specimens

3.2. Load-slip curves

In evaluating the mechanical properties, the load-slip curve in Fig. 5 illustrates the relative deformation of steel and concrete as the load varies. It highlights the three key mechanical characteristics: ultimate bearing capacity, shear stiffness, and deformability of the shear link components. The data characteristic points of the curve are demonstrated in Table 2.

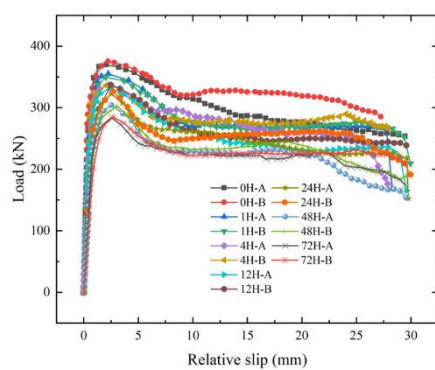


Fig. 5 Load-slip curves

In table 2, the maximum bearing capacity P_u decreases by 0%, 3.76%, 6.33%, 9.54%, 13.86%, 17.91%, and 24.57%, respectively; the relative slip amount δ_u increased by 0%, 4.43%, 14.78%, 19.21%, 23.64%, 32.02%, and 34.48%, respectively; the ultimate slip amount δ_{uk} decreased by 0%, 4.75%, 8.86%, 10.82%, 35.43%, 42.14%, and 59.25%, respectively; shear stiffness k_s decreased by 0%, 1.56%, 2.69%, 3.77%, 5.22%, 6.37%, and 9.17%, respectively; ductility coefficient δ_{uk}/δ_{rk} decreased by 0%, 29.55%, 39.92%, 46.65%, 63.46%, 70.03%, and 77.41%, respectively. A contributing factor to the decline in mechanical properties is the decrease in the diameter of the penetrated steel bar.

Table 2

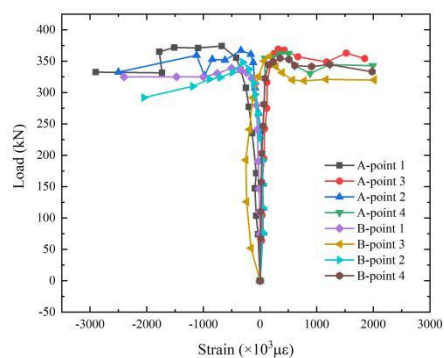
The data characteristic points of the curve in the test

Corrosion time/h	Bearing capacity P_u /kN	Peak slip δ_u /mm	$P_{rk}=0.9P_u/k$ N	δ_{rk}/m m	Ultimate slip δ_{uk}	Shear stiffness $K_s/kN \cdot mm$	Ductility factor δ_{uk}/δ_{rk}
0	378.83	1.96	341.23	1.24	8.74	494.23	6.42
	367.93	2.1	330.85	0.88	8.46	483.99	6.24
1	363.84	2.09	323.67	1.43	8.44	486.34	5.14
	336.7	2.15	306.81	1.39	7.98	476.58	3.78
4	340.53	2.24	304.67	1.57	8.13	479.82	3.91
	318.85	2.42	288.77	1.65	7.67	472.08	3.69
12	332.87	2.38	299.85	1.64	7.91	472.98	3.65
	321.61	2.46	289.17	1.78	7.61	468.4	3.11
24	327.65	2.46	292.32	1.94	6.52	466.53	2.42
	316.45	2.56	287.38	1.84	6.18	460.61	2.2
48	313.76	2.59	282.54	1.98	6.34	460.54	2.29
	300.08	2.77	269.92	2.3	5.76	455.38	1.51
72	298.64	2.66	270.45	2.43	5.54	447.32	1.89
	265.4	2.8	237.19	2.33	5.26	441.16	0.97

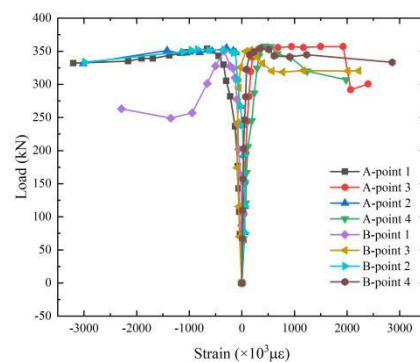
Note: δ_{rk} is the slip amount of the load rising to P_{rk} ; δ_{uk} is the slip amount of the maximum load descending to P_{rk} .

3.3. Load-strain curve

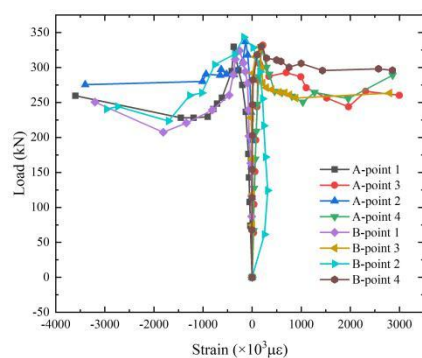
Load-strain curves in Fig. 6 shows the internal stress state and yield of shear link components. These data in Fig. 6 was collected by the upper and lower of penetrated steel bars.



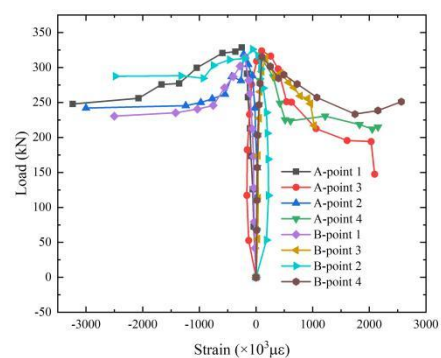
(a) 0 h



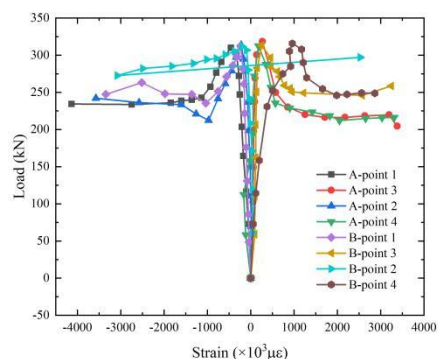
(b) 1 h



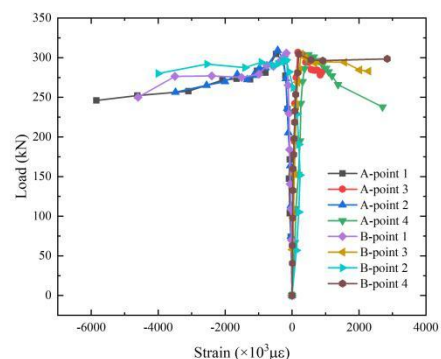
(c) 4 h



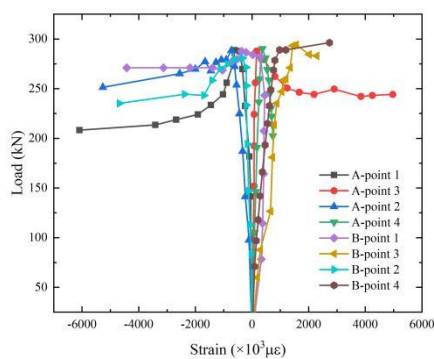
(d) 12 h



(e) 24 h



(f) 48 h



(g) 72 h

Fig. 6 Load-strain curves

As shown in Fig. 6, the compressive strain increases from $-2200 \mu\epsilon$ to $-5300 \mu\epsilon$, while the tensile strain increases from $2000 \mu\epsilon$ to $4232 \mu\epsilon$. Furthermore, at the beginning of loading stage, the strain rises slowly with the load increase. Once the steel bar reaches its yield point, the load starts to decrease, and the strain rises rapidly. The strain law is basically the same. Furthermore, the compressive strain of measuring points 1 and 2 is negative, and the tensile strain of points 3 and 4 is positive. The steel bar is in a compression-bending stress state, as its compressive strain is always greater than the tensile strain. The one-side strain value obtained from the penetrated steel bar on both sides of A and B is always greater than the other. The main reason is that the specimen will produce eccentricity with compression, resulting in a large force on one side and a small one on the other.

4. Finite element models

4.1. Finite element simulation

In order to further study the internal failure mechanism of PBL connectors during loading, the software ABAQUS was especially used to simulate tests. C3D8R reduced solid element could simulate I-steel, perforated steel plate, concrete, and penetrated steel bar. The T3D2 was used to simulate a stirrup. Constraints were applied to bind the concrete tenon with the slab, the concrete tenon with the penetrated steel bar, and the perforated steel plate with the I-beam. The tangent line adopted the function of friction coefficient 0.904. The stirrup and concrete were linked with embedding constraints, symmetric constraints were applied at the center of the steel beam web, and fully fixed constraints were used for the concrete bottom plate. The displacement was imposed on the coupling point to simulate the loading state in Fig. 7.

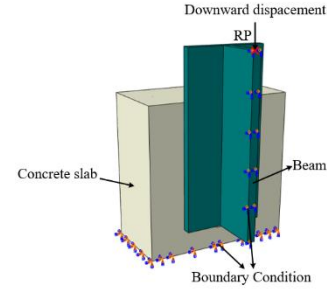


Fig. 7 1/2 model

The mesh of the FEM is fitted with 5 mm concrete tenons, 3 mm penetrating steel and 15 mm stirrups (see Fig. 8). C50 concrete use the plastic damage model with an expansion angle 30° , an eccentricity rate 0.1, and the viscosity coefficient 0.0005. Additionally, the biaxial compressive strength is 1.16 times the uniaxial compressive strength, and the constant stress ratio of the tensile meridian to the compressive meridian (K) is $2/3$. The elastic modulus is 34.523 GPa, and compressive strength is 53.35 MPa, respectively. The steel exhibits a yield strength of 476.26 MPa, an ultimate strength of 613.61 MPa, an elastic modulus of 234.96 GPa, and an elongation of 43.30%.

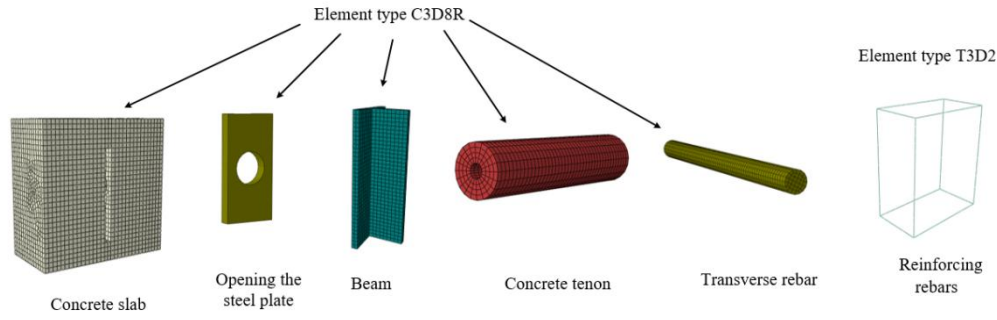
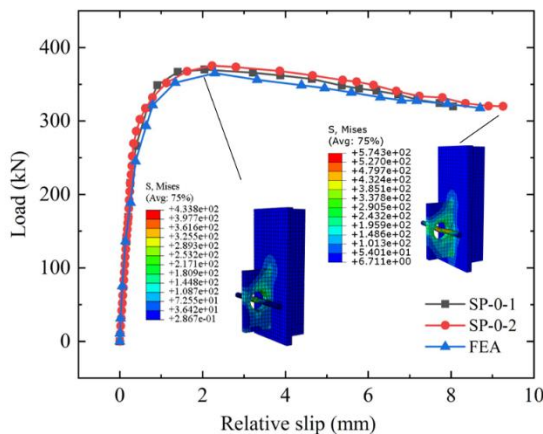


Fig. 8 Mesh generation

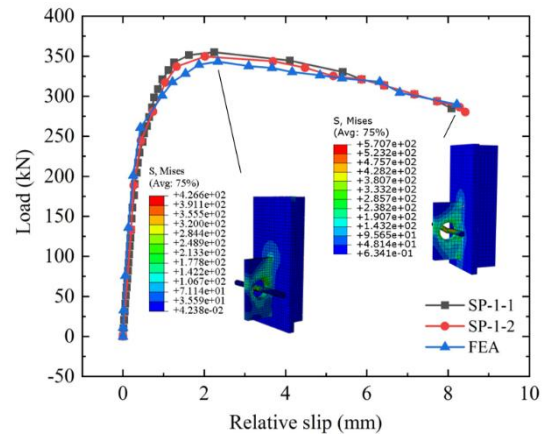
4.2. Finite element results and analysis

Fig. 9 shows that the test values are largely consistent with the finite element values in both the linear elastic and nonlinear stages. At ultimate shear capacity, the steel reaches its yield strength, and then the load-slip curve slip velocity increases with the increasing load. At this stage, there is a slight

difference between the test and the FEM. The error is less than 10%, mainly caused by the construction error. It can be concluded from Fig. 11 that the maximum stress position is welding joint between the I-beam and perforated steel plate, so does the concrete tenon. Fig. 11 indicates that the FEM can accurately simulate the load-slip curve.



(a) 0 h



(b) 1 h

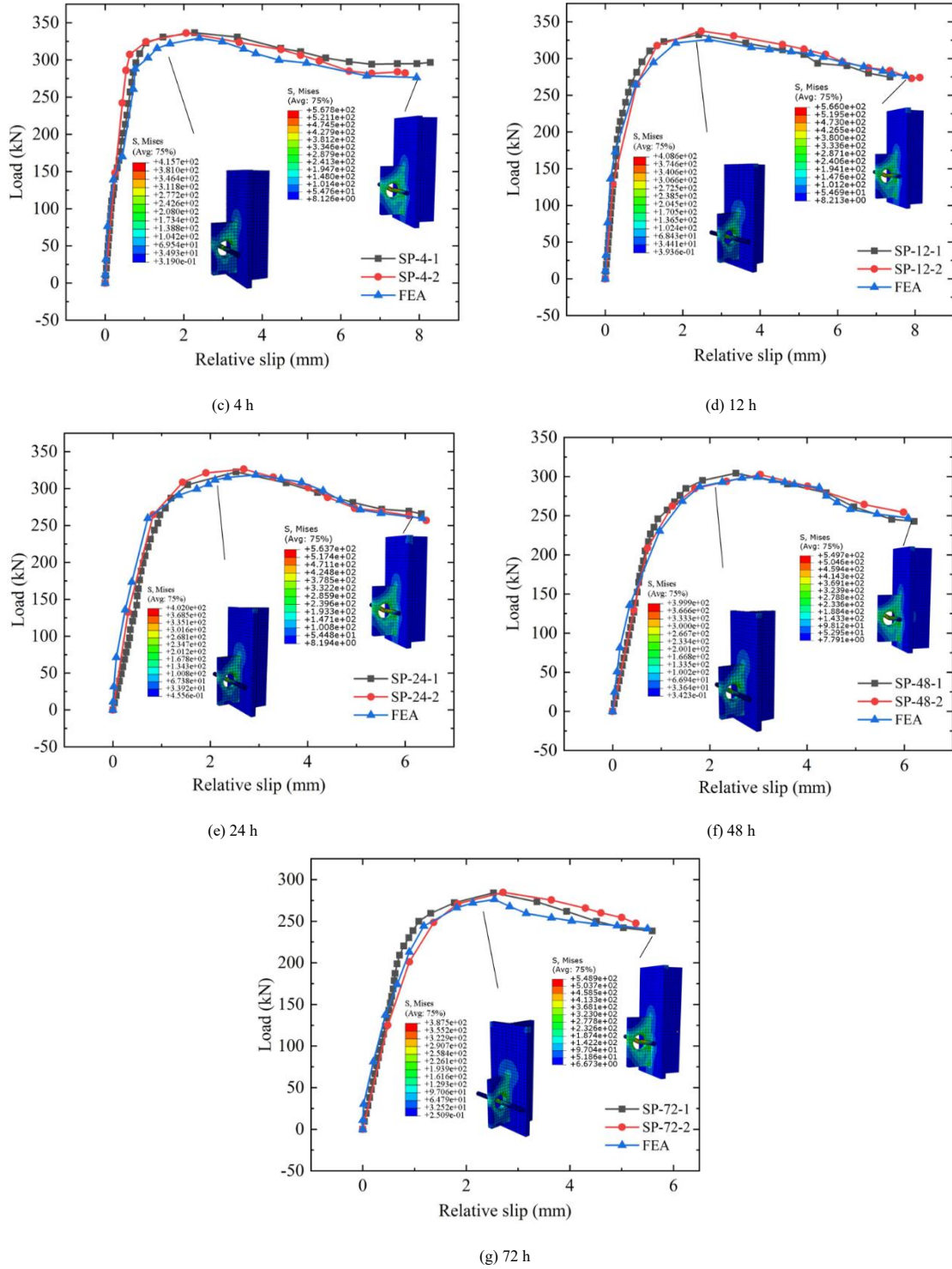


Fig. 9 Load-strain curves

4.2.1. Parametrical investigations

This paper employs software to investigate how various factors affect the shear strength and deformation under hydrochloric acid corrosion.

(1) Concrete strength. For concrete grades C30, C35, C40, C45, C50, C55, and C60, the shear bearing capacity decreased by 28.11%, 27.47%, 27.56%, 25.23%, 24.52%, 23.66%, and 22.92% as the corrosion time increased, respectively (Fig. 10(a)). Meanwhile, the slip amount decreased by 41.91%, 39.64%, 38.20%, 37.85%, 35.67%, 30.24%, and 24.78%, respectively (Fig. 11(a)).

(2) The diameter of Penetrated steel bar. For steel bars with diameters of 12mm, 14mm, 16mm, 20mm, and 25mm, the shear capacity decreased by 22.35%, 24.46%, 17.97%, 14.40%, and 12.76%, respectively (Fig. 10(b)), while

the slippage reduced by 34.75%, 33.72%, 31.46%, 30.11%, and 25.26%, respectively (Fig. 11(b)).

(3) End-bearing mode. Of the non-endbearing structure, the shear capacity and the slippage are reduced by 24.47% and 33.72%. The end-bearing structure exhibited reductions of 11.16% in shear capacity and 25.46% in slippage (Fig. 10(c) and Fig. 11(c)), indicating superior anti-corrosion performance compared to the non-end bearing structure.

(4) The diameter of the steel plate holes. With an increase in diameter, the shear capacity experienced reductions of 20.35%, 20.70%, 19.75%, 19.28%, 18.44%, 17.57%, and 17.87%, respectively (Fig. 10(d)). Correspondingly, the slippage decreased by 39.80%, 35.23%, 34.35%, 33.57%, 33.72%, 32.50%, 29.28%, and 28.03%, respectively (Fig. 11(d)).

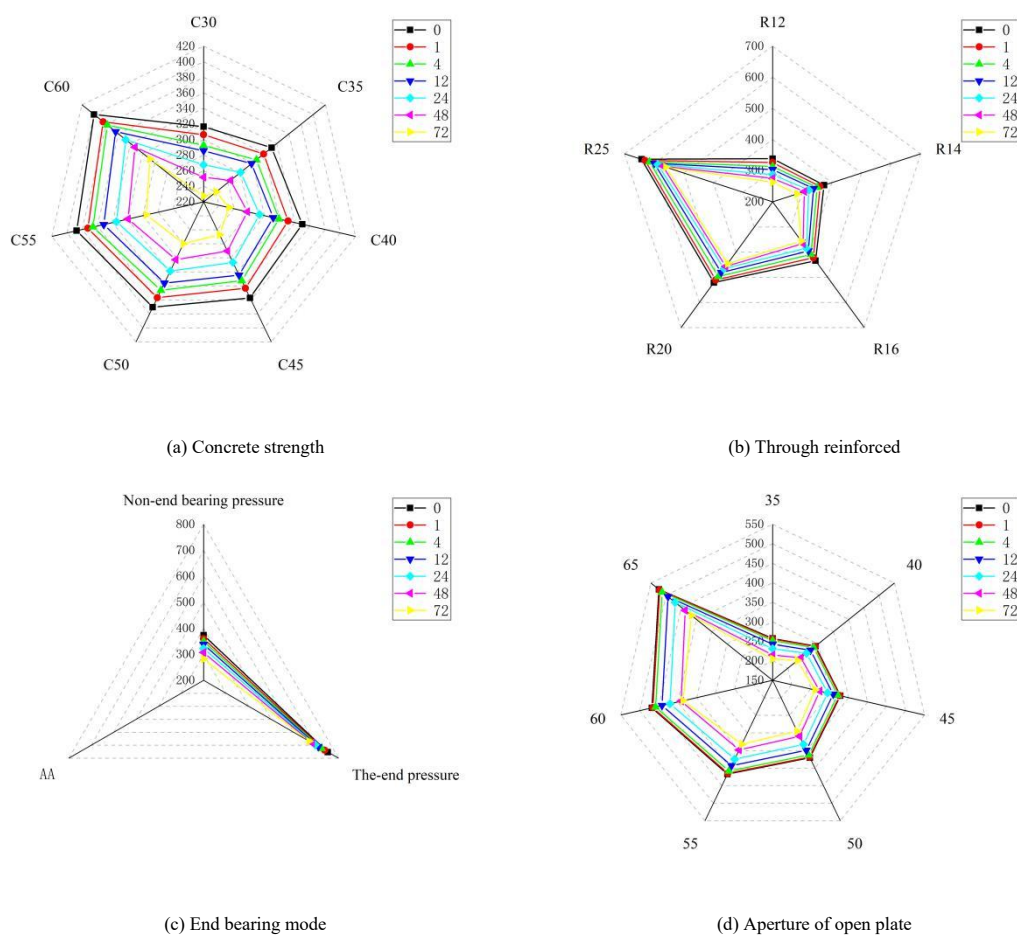


Fig. 10 Influence factors of the shear capacity

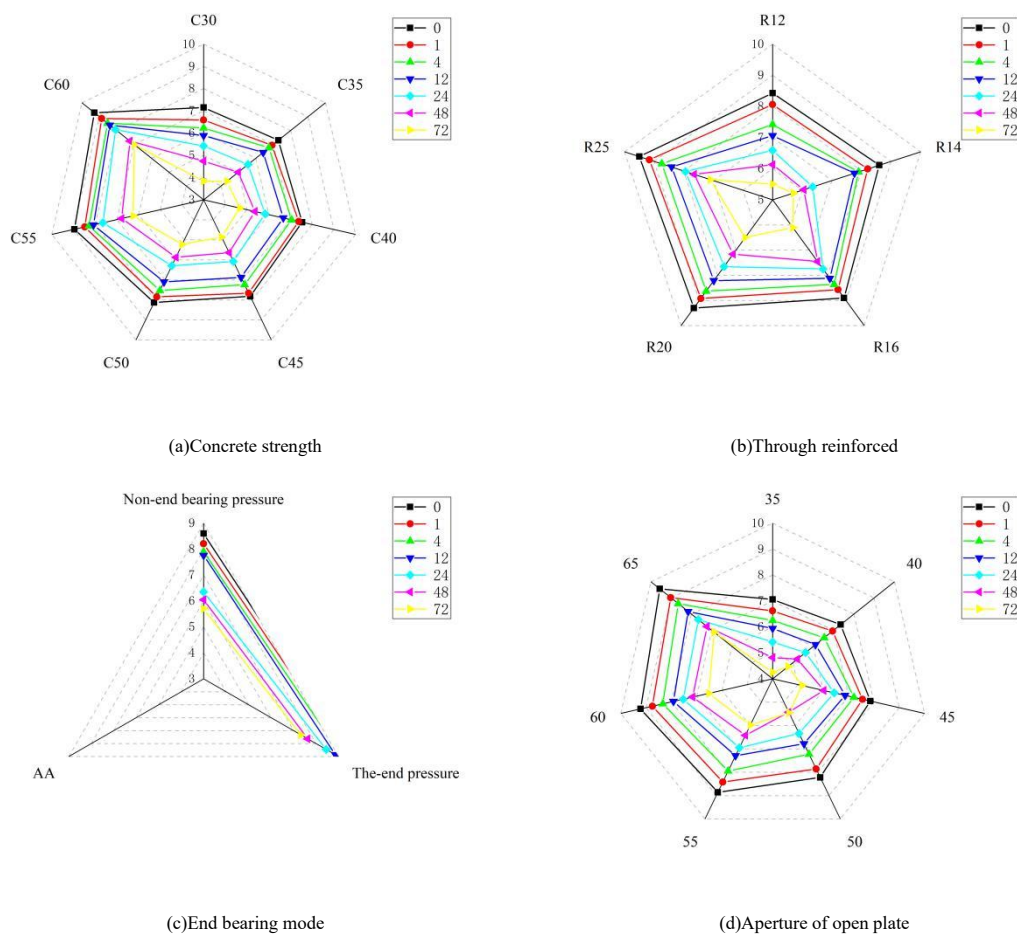


Fig. 11 Influence factors of the amount of slip of the connector

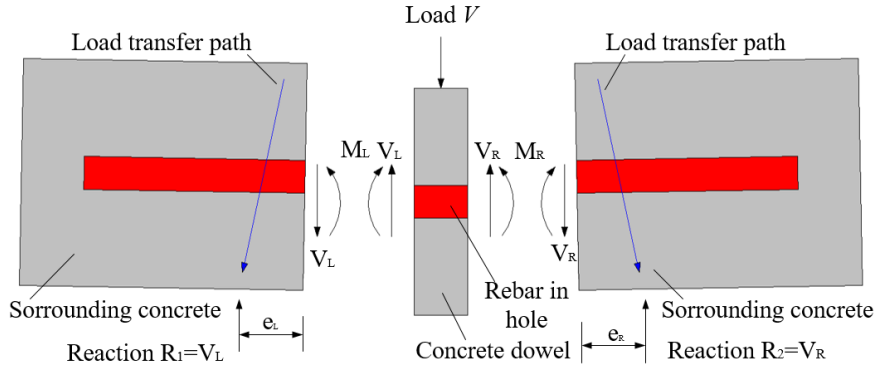


Fig. 12 The connectors' shear mechanism

5. Stud load-slip curve calculation method

5.1. Perforbond shear connector force mechanism

The shear mechanism of connectors is studied according to the test, as shown in Fig. 12. The load transfer mode at the concrete transfer bar was described, and the shear mechanism of the perforated steel bar shear connector was discussed. When Load V was applied to I-beams, I-beams transmitted shear to perforated steel plates, which in turn transmitted shear to concrete tenons and perforated steel bars. The shear and bending deformations increased the slippage S between the tenon and the surrounding concrete, producing shear V_L , V_R and moment M_L , M_R . The resistance of M_L and M_R was increased by the steel bar in the hole, leading to more shear and bending deformation, which in turn resulted in greater slippage between the steel bar and concrete. In Fig. 12, the load transfer extends outwards at a certain angle. As corrosion time increases, the shear link components V_L , V_R , M_L , and M_R , along with the yield strength of the steel bars, decrease, resulting in a reduction in the shear capacity of the composite structure.

5.2. Load-slip curve calculation formula

To sum up, the load-slip trend of each steel-concrete composite structure was roughly the same, including three stages: linear elastic, non-linear elastic development, and load decline stages. This paper analyzed the curves of the plastic and the descending sections. It was found that the load-slip curves could be described theoretically by a logarithmic function. Hence, the curves of the plastic and descending stages are fitted as Eq. (1):

$$\frac{P}{P_u} = a \ln(s) + b \quad (1)$$

Where, both a and b are parameters, P_u stands for the ultimate bearing capacity, and S represents the relative slip.

The origin software was used to fit the plastic and descending sections of Eq. (1) to obtain the plastic section $a=0.250$, $b=0.915$, and $R^2=0.96$, descending section $a=-0.071$, $b=1.057$, and $R^2=0.92$. Eq. (2) can be received by putting the fitting parameters a and b into Eq. (1):

$$\frac{P}{P_u} = \begin{cases} 0.250 \ln(S) + 0.915 & S_i \leq S \leq S_p \\ -0.071 \ln(S) + 1.057 & S_p \leq S \end{cases} \quad (2)$$

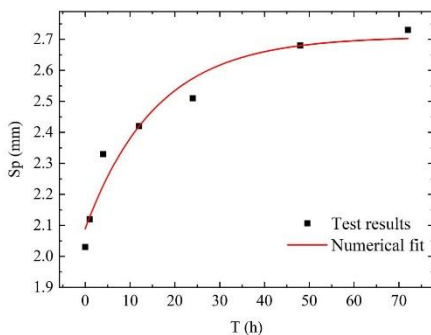


Fig. 13 Fitting curve of peak slip

Where, S_i denotes the initial sliding value, roughly 0.2 mm; S_p refers to the peak slip amount, and S_u represents the ultimate slip value.

The test model of linear elasticity stiffness K_s in the rising stage is formula (3).

$$K_s = \frac{P}{S} \quad (3)$$

The load-slip is shown as Eq. (4).

$$\frac{P}{P_u} = \begin{cases} \frac{K_s S}{P_u} & 0 \leq S \leq S_i \\ 0.250 \ln(S) + 0.915 & S_i \leq S \leq S_p \\ -0.071 \ln(S) + 1.057 & S_p \leq S \end{cases} \quad (4)$$

5.3. Calculation formula of perforbond shear connector load-slip curve

The hydrochloric acid corrosion time t of PBL shear link components is introduced into the formula (4) to obtain the calculation model, as shown in Formula (5).

$$\frac{P}{P_u(t)} = \begin{cases} \frac{K_s(t) S}{P_u(t)} & 0 \leq S \leq S_i \\ 0.250 \ln(S) + 0.915 & S_i \leq S \leq S_p(t) \\ -0.071 \ln(S) + 1.057 & S \leq S_u(t) \end{cases} \quad (5)$$

Where,

$$\begin{aligned} K_s(t) &= (0.90 - 0.09 \times 0.96^t) (0.27 + 0.14 n_E n_d^2) E_c d & R^2 &= 0.94 \\ P_u(t) &= (0.719 + 0.26 \times 0.98^t) \times 1.4 (d^2 - d_s^2) f_{cd} + 1.2 d_s^2 f_{sd} & R^2 &= 0.94 \\ S_p(t) &= 2.71 - 0.62 \times 0.94^t & R^2 &= 0.94 \\ S_u(t) &= 0.000587 t^2 - 0.08 t + 8.39 & R^2 &= 0.95 \end{aligned}$$

Fig. 13 and Fig. 14 shows the fitting curves of $S_p(t)$ and $S_u(t)$ with different corrosion times.

The comparison of theoretical and test curves is shown in Fig. 15.

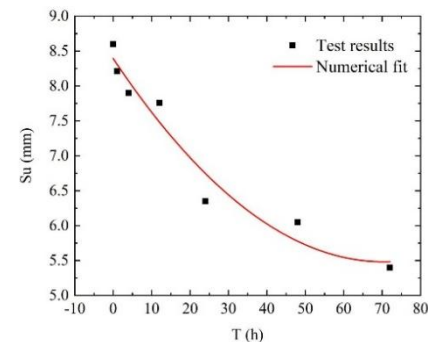


Fig. 14 Fitting curve of limit slip

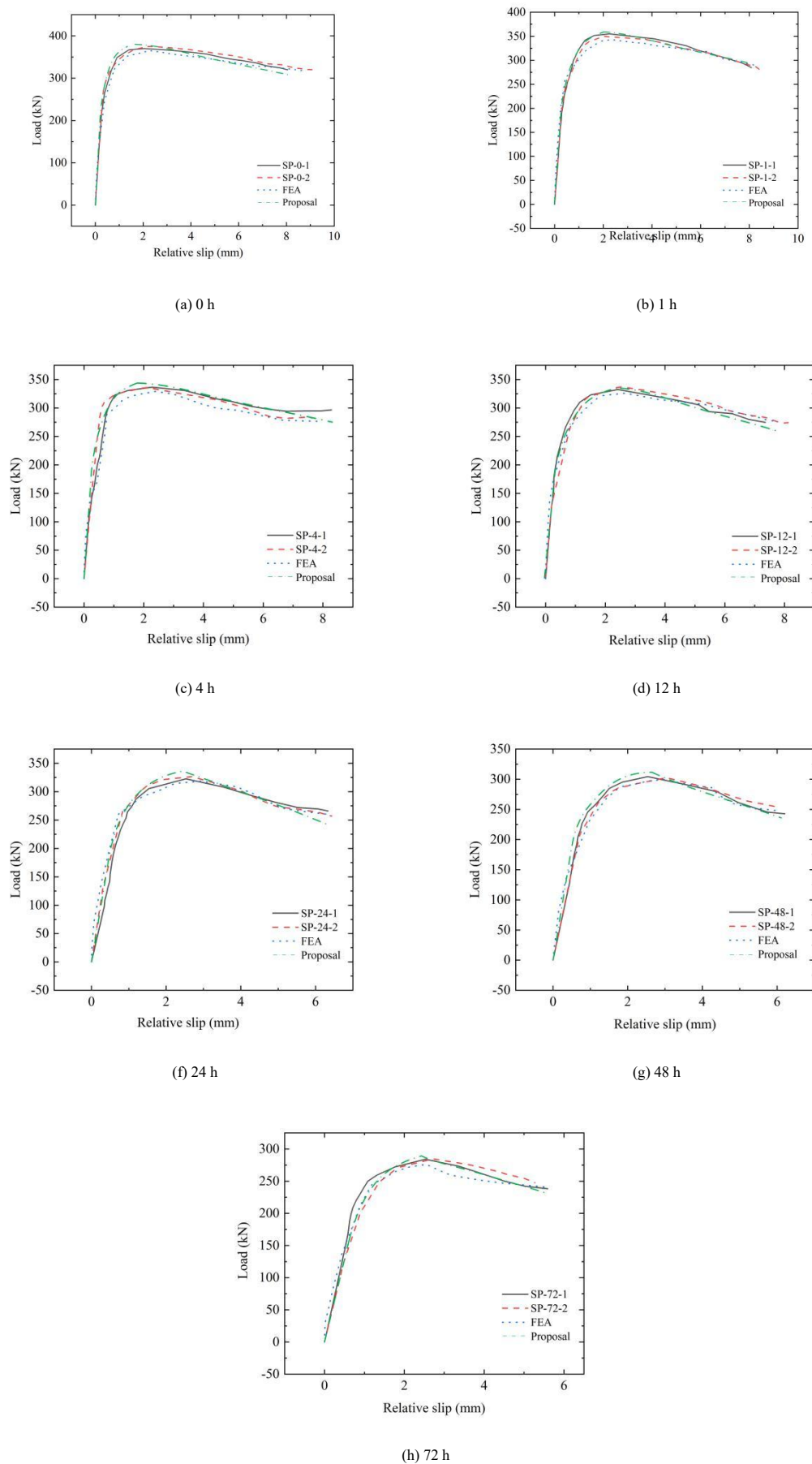


Fig. 15 Load-slip curve comparison for varying corrosion times

The consistency of the load-slip curve is evident, as the results from the formula calculation, testing, and finite element simulation match closely. Hence, formula (5) effectively represents the load-slip calculation model for PBL connectors subjected to hydrochloric acid corrosion.

6. Conclusions

Combined with the experimental research, theoretical analysis and finite element method, the following conclusions are drawn from 14 test specimens

and 147 finite element models.

(1) In push-out tests with varying corrosion times, the failure of shear link components is directly caused by the bending of steel bars and the cracking of concrete. After failure, the bending angle of the penetrated steel bar increases by 13.3°, while the cracking load and the load at the 45° inclined crack decrease by 74.9 kN and 81.3 kN, respectively.

(2) The load-slip curve of the PBL shear connector from 0 h to 72 h shows a 34.48% increase in the relative slip at maximum load, while the ultimate slip, shear stiffness, and ductility coefficient decrease by 59.25%, 8.22%, and 77.41%, respectively.

(3) An FEM model from 0 h to 72 h was established to compare with the test results. The slip decreased by 17.13% as the concrete strength increased from C30 to C60, and by 9.49% when the diameter of the penetrated steel bar increased from 12 mm to 25 mm. The slip under end pressure was reduced by 8.26% compared to non-end pressure, while an increase in the steel plate hole diameter from 35 mm to 65 mm led to an 11.77% reduction in slip.

(4) The failure modes of the shear link components are analyzed to understand their failure mechanism, and the load-slip curve is derived from the test data. The load-slip formula for the PBL shear connector corroded by hydrochloric acid is then developed based on the observed trends.

Author Contributions

Conceptualization, Yang, F.; methodology, Qiao, W.J.; software, Zhou, T.K.; writing—review and editing, Li, Y.L., Ruan, Z.D. and Li, S.F.. All authors have read and agreed to the published version of the manuscript.

Funding

This research was funded by the Natural Science Foundation of Shaanxi Province, grant number“ 2024JC-YBMS-427 , 2024JC-YBMS-446”. This research was funded by the Natural Science Foundation of Shaanxi Province, grant number“ 2024SF-YBXM-618”.

Conflicts of Interest

The authors declare no conflict of interest.

References

- [1] Zhan YL, ASCE M, Yin Chao, et al. Pushout Tests on Headed Studs and PBL Shear Connectors Considering External Pressure[J]. *Journal of Bridge Engineering*, 2020,25(1): 04019125.
- [2] Kong FL, Huang PM, Han B, et al. Experimental Study on Behavior of Corrugated Steel-concrete Composite Bridge Decks with MCL Shape Composite Dowels[J]. *Engineering Structures*, 2021,227: 111399.
- [3] Gu YW, Nie X, Liu YF, et al. Experimental and Numerical Study of Steel-to-concrete Joint Section in Hybrid Cable-stayed Bridges[J]. *Journal of Constructional Steel Research*, 2021,187, 106982.
- [4] Hu WG, Zhang JL. Study on Static Lateral Load-slip Behavior of Single-shear Stapled Connections in Plywood for Upholstered Furniture Frame Construction[J]. *Journal of Wood Science*, 2021, 67:40.
- [5] Zhang QH, Jia DL, Bao Y, et al. Internal Force Transfer Effect-based Fatigue Damage Evaluation for PBL Shear Connector Groups[J]. *Journal of Constructional Steel Research*, 2018, 148: 469-478.
- [6] Wang BING, LIU Xiaoling, YI Xian. Load-slip calculation model of bolted connection under fatigue load. *Journal of Harbin Institute of Technology*, 2023,55 (11): 91-98.
- [7] Yan LB, Han B, Fan L, et al. Fatigue Damage of PBH Shear Connector of Steel-concrete Composite Structure[J]. *Engineering Structures*, 2020,213: 110540.
- [8] Xiao L, Qiang SZ, Xu X. Experimental Research on PBL Shear Connector for Steel-Concrete Composite Structures[J]. *Advanced Materials Research*, 2010, 163-167: 2137-2141.
- [9] Aguiar OP, Caldas RB. Circular Openings with Transverse Rebar as Steel-concrete Shear Connection (part 1/2): Analytical model for strength and slip capacity[J]. *Engineering Failure Analysis*, 2022,133: 106007.
- [10] Le N D, Pham H T, Pham D T, et al. An efficient long short-term memory-based model for prediction of the load-displacement curve of concrete-filled double-skin steel tubular columns [J]. *Construction and Building Materials*, 2024, 449 138122-138122.
- [11] Tan XY, Fang Z, Xiong XW. Experimental Study on Group Effect of Perfobond Strip Connectors Encased in UHPC[J]. *Engineering Structures*, 2022,250: 113424.
- [12] Zhao Y, Song C, Jinglai S, et al. Bar load-displacement curve model based on statistical damage mechanics [J]. *Frontiers in Earth Science*, 2022, 10
- [13] Hao M, Wei W, Rongqiao X. Analytical model for the Load-Slip behavior of headed stud shear connectors [J]. *Engineering Structures*, 2022, 252
- [14] Li SQ, Su LC, Sun ZB. Research on the Load-slip Properties of Corrugated Rib Connectors' Push-out Test[J]. *KSCCE Journal of Civil Engineering*, 2018, 22(4), 12205.
- [15] Wang WA, Zhao CZ, Li Q, Zhuang WL. Study on Load-Slip Characteristic Curves of Perfobond Shear Connectors in Hrbid Structures[J]. *Journal of Advanced Concrete Technology*, 2014, 12: 413-424.
- [16] Cao JX, Liu YY, Wang YX, et al. Load-slip Performance of Timber-to-concrete Connections with U-steel Connectors under Push-out test[J]. *Journal of Building Engineering*, 2022, 45, 103527.
- [17] Huang PM, He JL, Kong FL, et al. Experimental Study on the Bearing Capacity of PZ Shape Composite Dowel Shear Connectors with Elliptical Holes[J]. *Scientific Reports*, 2022, 12(1):2457.
- [18] Gao YM, Li CJ, Wang XF, et al. Shear-slip Behaviour of Prefabricated Composite Shear Stud Connectors in Composite Bridges[J]. *Engineering Structures*, 2021,240: 112148.
- [19] Li ZX, Zhao CH, Deng KL, et al. Load Sharing and Slip Distribution in Multiple Holes of a Perfobond Rib Shear Connector[J]. *Journal of Structural Engineering*, 2018, 144(9): 04018147.
- [20] Zhang J, Hu XM, Kou LY, et al. Experimental Study of the Short-term and Long-term Behavior of Perfobond Connectors[J]. *Journal of Constructional Steel Research*, 2018, 150: 462-474.
- [21] Yu ZL, Zhu B, Dou ST, et al. 3D FEM Simulation Analysis for PBL Shear Connectors[J]. *Applied Mechanics and Materials*, 2012,170-173:3449-3453.
- [22] Tan XY, Fang Z, Xiong XW. Experimental Study on Group Effect of Perfobond Strip Connectors Encased in UHPC[J]. *Engineering Structures*, 2022,250: 113424.
- [23] Jiang HB, Fang HZ, Liu J, Fang ZC, Zhang JF. Experimental Investigation on Shear Performance of Transverse Angle Shear Connectors[J]. *Structures*, 2021, 33:2050-2060.
- [24] GB/T 228.1-2021, *Metallic Materials-Tensile Testing-Part 1: Method of Test at Room Temperature*, Chinese Standard, 2021.

EXPERIMENTAL RESEARCH ON MECHANICAL PERFORMANCE OF COLD-FORMED THIN-WALL FABRICATED RACK COLUMNS

Yan-Bo Qu¹, Gan Tang^{1,*}, Ling-Feng Yin² and Ren-Yi Shi¹

¹ Department of Civil and Airport Engineering, Nanjing University of Aeronautics and Astronautics, Nanjing, 211106, China

² School of Civil Engineering, Southeast University, SiPaiLou 2, Nanjing 210096, China

* (Corresponding author: E-mail: tanggan@sina.com)

ABSTRACT

The increasing prevalence of thin-wall fabricated rack has heightened demands on the load-bearing capabilities of structural components, particularly columns. Traditional cold-formed thin-wall single-limb columns are now often inadequate for safety standards, prompting the need for innovative column designs and reinforcement techniques. A prevalent reinforcement strategy involves transforming single-limb columns into double-limb configurations. This study employs experimental and theoretical analyses to evaluate the mechanical properties of both single-limb and double-limb columns, proposing reinforcement methods such as force transfer plates. The research includes: (1) designing load-bearing tests for both column types to determine load-displacement curves and ultimate capacities; (2) developing an enhanced finite element model to validate mechanical performance against experimental data; and (3) conducting a parametric study on factors influencing the mechanical behavior of double-limb columns, providing guidelines for their practical application.

ARTICLE HISTORY

Received: 4 August 2024
Revised: 16 January 2025
Accepted: 6 February 2025

KEYWORDS

Steel storage rack;
Cold-formed thin-walled;
Coupled composite column;
The simulation of the finite element model;
Parametric analysis

Copyright © 2025 by The Hong Kong Institute of Steel Construction. All rights reserved.

1. Introduction

In the past, the storage industry was dominated by ordinary warehouses, with a single structure and a simple function. With the rapid development of other upstream industries, the storage industry has also developed from the original single to the diversified, from a simple enclosure stacking to a modern material access and invocation, and the utilization efficiency of space has greatly improved. Shelves now fall into three main categories: assembled, integral, and integrated.

A cold-formed thin-wall opening multi-rolled edge ohmic column is the typical design of a steel shelf construction (Fig.1a), which maximizes material performance and improves local buckling bearing capacity. However, continual alterations to the steel structural system of storage shelves, such as multi-high-rise shelves, double-deep shelves, and integrated stereoscopic storage shelves have created new demands on the classic single-leg ohmic column form.^{[1][2][3][4]} Simply increasing the thickness of the column members can improve the

structure's bearing performance, but it cannot fundamentally fix the problem, and it will cause the size of the column members and other elements to vary, resulting in intricate operations. And the columns that need to be improved frequently have only a percentage of the area or height, so merely raising the thickness of all columns will increase the cost burden.

There are now engineering efforts in the industry to improve the shelf's column shape and innovatively change the single-leg ohmic column into a double-leg composite column form consisting of two long and short ohmic columns, resulting a novel column section (Fig.1b). The advantage of this arrangement is that it allows for full use of the column space perpendicular to the direction of the roadway while not taking up shelf storage space. At the same time, improve the shelf column's bearing capability. However, this portion has not been thoroughly tested or studied theoretically, and experts and academics at home and abroad are currently focusing mostly on the typical cold-formed thin-wall multi-wound ohm column, with minimal research on the two-limb superimposed column.^{[5][6][7]}

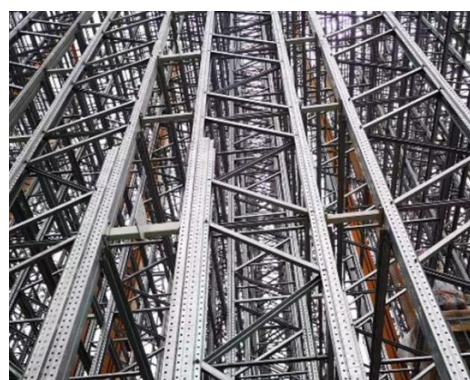
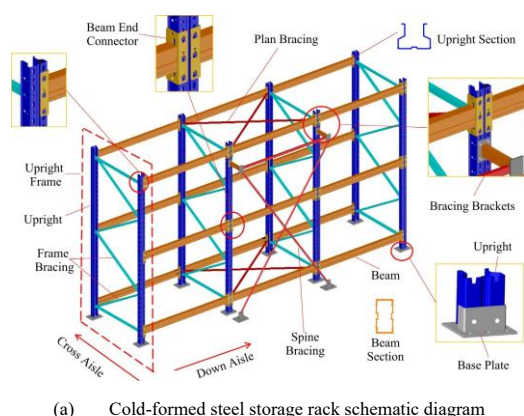


Fig. 1 Cold-formed thin-wall fabricated rack

Yasar Pala^[8] explored the structural performance of cold-formed thin-wall steel rack columns, focusing on enhancing their buckling resistance. The study involved testing and finite element analysis of columns with varying heights to determine critical buckling loads and section sizes. Michael Davies et al.^[9] assessed column performance using both finite element analysis and ordinary beam theory (GBT), introducing the "equivalent thickness method" to simplify the modeling of column openings. This approach provides a more accurate representation of the column's behavior under load. Shanmugam et al.^[10] developed formulas to assess the impact of different opening shapes (square,

circular, and proprietary) on column capacity. Their finite element model considered web slenderness, opening geometry, and proposed that web slenderness and opening area ratio are key variables affecting column performance. Freitas et al.^[11] conducted short column tests to establish the bearing capacity of open-hole columns, aligning with standards set by the American Shelf Manufacturing Association and the American Iron and Steel Institute. ANSYS software was used to analyze material and geometric nonlinearities, with results compared to empirical data. Moen et al.^[12] presented a simplified method for estimating buckling loads in open-hole columns and

beams of cold-formed thin-wall steel shelves. The study investigated the mechanical properties of columns with variable web openings, considering local, distortional, and global buckling modes, as well as ultimate and failure strengths. Baldassino et al. [13] performed extensive tests (48 axial compression and 24 bidirectional bending) on both perforated and solid sections. They proposed schemes to evaluate the effective second moment of area, addressing gaps in standard specifications and highlighting the influence of opening geometry on column performance. Talebian et al. [14] proposed a finite element model to determine the biaxial bending capacity of cold-formed steel shelf columns. The model accurately replicated published test data and was used for parametric analysis, providing insights into design optimization. Ren et al. [15] used computational methods to investigate the deformation-global buckling interactions in cold-formed steel porous columns under axial compression. The finite element analysis was validated against the direct strength method (DSM), offering a robust framework for design and analysis.

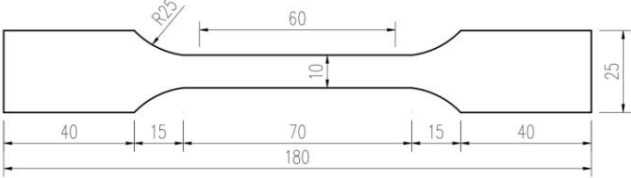
A new sort of column construction is currently being used in real projects, but it has not been extensively analyzed and assessed using numerical simulation, and it is merely installed and welded empirically, with uncertain ramifications for structural safety. Furthermore, the household shelf structure was started late, research on the mechanical performance of the new steel shelf column is still in its early phases, and the theory and standards that can be utilized in practical engineering are still developing. The absence of standardized and appropriate design and processing will also result in a waste

of economic and time resources for businesses. As a result, this paper will conduct experimental research on the mechanical properties of commonly used cold-formed thin-wall multi-rolled edge ohm columns and improved two-legged superimposed columns in order to gain a better understanding of their properties and mechanical conditions, as well as provide guidance for engineering applications.

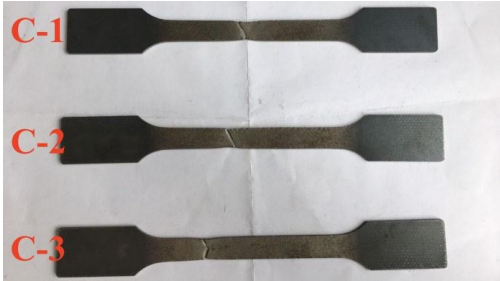
2. Experimental research

2.1. Material properties

This test employed Q345B steel that had been cold bent at the factory. The steel was bent repeatedly to form different corners and stiffeners. The cross-sectional shape was complex, and the bearing capacity was large. The column material used for the material test must be from the same batch of steel as the bearing capacity test. It should be cut during the rolling process of the steel plate, with the direction perpendicular to the rolling direction. The specimen material is processed into a plate-shaped lead specimen in accordance with the provisions of standard GB/T 228.1-2021 [16]. Three identically sized standard plates were given to each group of specimens (Fig.2), and each specimen was subjected to uniaxial tensile testing at room temperature in compliance with EN 15512-2022 [17] standard. Table.1 displays the test results.



(a) Size diagram of material performance test specimen



(b) The final failure mode of the material performance test specimen

Fig. 2 Schematic diagram of material performance test specimen

Table 1
Results of material performance test

Specimen	Specimen Number	Yield Strength $f_y(MPa)$	Average Value $f_y(MPa)$	Plastic Stress ϵ_{pl}	Tension Strength $f_t(MPa)$	Average Value $f_t(MPa)$	Plastic Stress ϵ_{pl}
Column	C-1	352			447		
	C-2	365	363	0	453	453	0.016
	C-3	371			460		

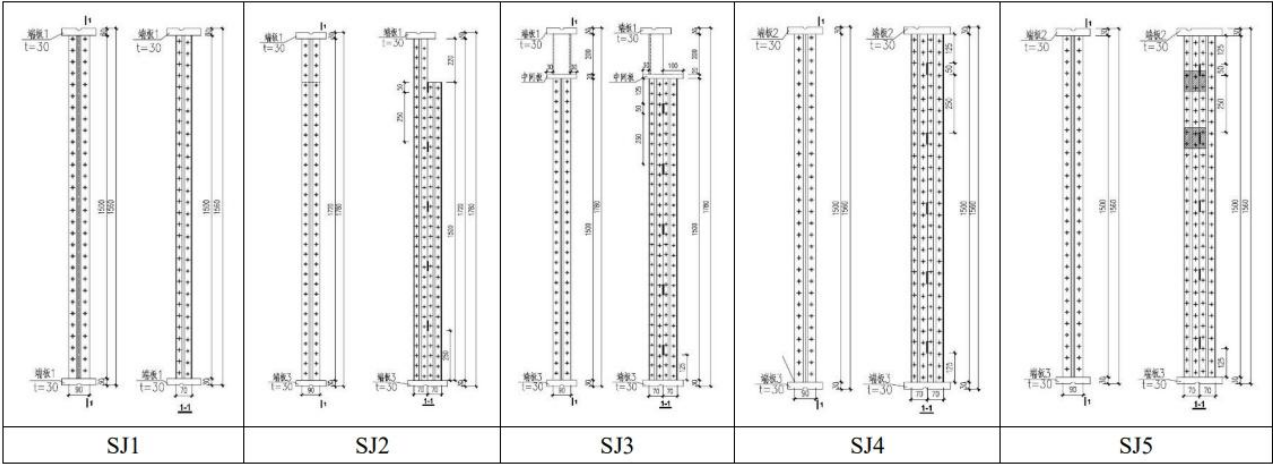


Fig. 3 Specimen diagram

2.2. Specimen design

The column specimens (Fig.3) are divided into five types. The first type

of SJ1 column is a single-limb ohmic column. The N90 segment, which is extensively utilized in the market today, is used. The specimen is 1500 mm long and has 150 × 150 × 30 mm end plates welded at the upper and lower ends to

accommodate the test device's height and space limits.

The second type of SJ2 column is a double-limb laminated column, which was employed in the project. The single-limb ohmic column is converted into a double-limb laminated column by immediately splicing a long (1720mm) and a short (1500mm) ohmic column, resulting in a closed superposition of an open cross-section column. There is no force plate between the long and short transition zone. The upper end is welded with a $150 \times 150 \times 30$ mm end plate, while the lower end is welded with a $200 \times 150 \times 30$ mm end plate.

The third specimen, SJ3, is an optimized version of SJ2. The preliminary test demonstrated that the ohm column on the upper half of the transition portion of the SJ2 column is susceptible to distortional buckling, resulting in a reduction in ultimate bearing capacity. To prevent distortional buckling of the upper portion, the SJ3 column is divided into two sections: upper and lower. The upper part consists of three 6 mm composite plates enclosed by a 200-mm-high short column. The centroid position is same to that of the single limb ohm column. The central transition part has a $200 \times 150 \times 20$ mm thick force transmission plate. The lower part is a double-limb composite column joined by two 1500 mm single-limb ohm columns. The splicing component is welded discontinuously, causing the top short column and outer limb column of the lower double-limb composite column to overlap. The upper end is welded with $150 \times 150 \times 30$ mm end plate, while the lower end is welded with $200 \times 150 \times 30$ mm plate.

The fourth specimen SJ4 simplifies the specimen JS3 by removing the upper short column and replacing the middle force transmission plate with a 30mm thick force transmission end plate. The upper and lower ends are welded with plates measuring $200 \times 150 \times 30$ mm.

The fifth specimen, SJ5, has a batten plate attached to both sides of specimen SJ4. The batten plate measures $96 \times 90 \times 5$ mm. Two layers are welded together, with one layer consisting of the batten plate's two sides that have the same height. The center of the first batten plate layer is 150 mm from the bottom of the top end plate, and the second layer's center is 400 mm from

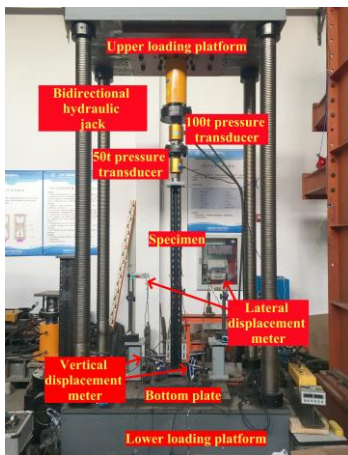
the same place. Welding secures the batten plate to the column.

2.3. Test setup and process

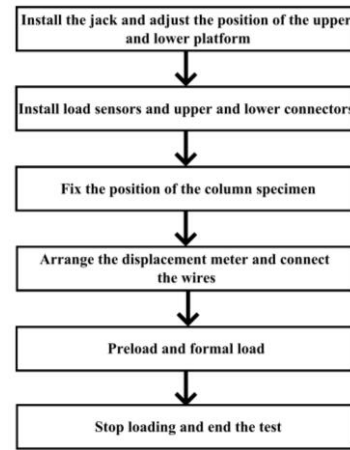
The mechanical performance of the cold-formed thin-walled constructed shelf column was assessed at the structural laboratory at Nanjing University of Aeronautics and Astronautics. The test platform is a 200t bidirectional loading test bench capable of withstanding loads ranging from 0 to 200 t. By reviewing the research methodologies of researchers at home and abroad, [18][19][20] it is discovered that the use of hinged ends can eliminate the majority of the end limitations, allowing the test to more closely imitate the true stress of the column in the real project.

Given the stress situation of cold-formed thin-walled assembly shelf columns in engineering practice, the specimen SJ1 column's bearing capacity test uses the column's axial compression test technique. The remaining parts are double-limb stacked columns. In engineering practice, the compression test scheme is used with the upper loading point as the center of the outer limb column and the lower connection point as the center of the double limb superimposed column. The column compression test loading device is basically made up of a two-way hydraulic jack, a pressure sensor, end spherical hinge support, a support platform, and other components. The bottom support of the column loading device is made up of the end spherical hinge support, steel ball, and support platform, which are bolted together. Fig.4(a) displays the schematic diagram of the loading device and the support.

The bearing capacity test primarily uses the load and displacement of the two primary mechanical parameters to determine the column's mechanical qualities. The vertical displacement primarily measures the displacement of the upper and lower end plates, but it also determines the column's vertical compression displacement and the end plate's rotation angle. The horizontal displacement primarily measures the deformation of the column section.



(a) Loading device of load test



(b) Flow diagram of test loading

Fig. 4 Loading device and flow diagram

During the test, the jack must be installed and the upper and lower platforms' positions adjusted. The column specimen is then put in position, the displacement meter is set up, and the wire is connected, followed by the loading test and data collection. The specific test process is shown in the Fig.4(b). The DH3816 static strain test system automatically collects and summarizes data from the load sensor and displacement meter in all directions.

2.4. Analysis of test failure results

The test involved loading five different types of columns and six specimens. (Because the first test column may contain test mistakes such as misalignment and measurement problems, two SJ1 specimens with the same cross-section size were created, designated SJ1-1 and SJ1-2). Because the test conditions for each column varies, this section discusses the test phenomena for each specimen separately. The test data is collated and calculated to generate several load curves, and the variations in each curve are examined.

2.4.1. Single limb Ohm column SJ1

Fig. 5 shows the failure modes and load-displacement curves for specimens SJ1-1 and SJ1-2. The vertical compression displacement of the upper and lower end plates is measured at four corner points to provide more precise data; the

average value is selected as the final value. When the load is first applied to the column, it is proportional to the axial displacement, which rises with the load. Nevertheless, the displacement rises and the load growth rate falls when the load approaches the ultimate load range, or when the load approaches 70% of the ultimate bearing capacity. The two are disproportionately huge. The column begins to plasticize, and the plastic hinge appears on the failure portion. Local bending occurs at the claw hole in the center of the SJ1-1 web, causing the specimen to shift to one side. The distortional buckling starts at the central flange of SJ1-2 and moves slightly to the exterior. When the load exceeds the ultimate bearing capacity range, the load and axial displacement rapidly decrease until they approach the critical value or failure condition. The central section of the specimen SJ1-1 was noticeably twisted, and there was noticeable local buckling at the web claw hole. The test was finished after the central part of specimen SJ1-2 demonstrated evident distortional buckling.

The two single-limb ohm columns SJ1-1 and SJ1-2 rotate in both the X and Y axes, but the Y axis rotation is modest, while the X axis rotation is very noticeable. The load-rotation curve is given in Fig.6. During the initial loading stage, the upper and lower end plates rotate minimally, with no visible difference. The specimen's angle remains rather consistent across the range of final bearing capacity, with no discernible rotation at the upper and lower ends. The angle around the X axis gradually increases after exiting the range of

ultimate bearing capacity, and it is evident that the upper and lower end plates rotate. The rotation angle varies between 1.0° and 3.0° , and the total angle around the X axis, which is the sum of the angles of the upper and lower end plates, is 5.0° .

The column's load-lateral displacement curve describes the change in cross section at maximum deformation. The two single-leg ohm columns distort most significantly around the middle. When setting the lateral tie rod type displacement time, a positive value on the displacement meter indicates that the tie rod is pushed back, implying that the plate of the column section is bulging

or bending outward; a negative value indicates that the tie rod is extended. The plate of the column section is concave, meaning it curves inward. Depending on the location of the measurement point, the displacement meter at each position shows the deformation of various regions. The single limb ohm column's flange deformation is measured by displacement meters Nos. 9 and 14. While Nos. 11 and 12 displacement gauges show section web deformation in the center of the column, Nos. 10 and 13 show flange distortion at the web surface in the middle of the column (Fig.7).

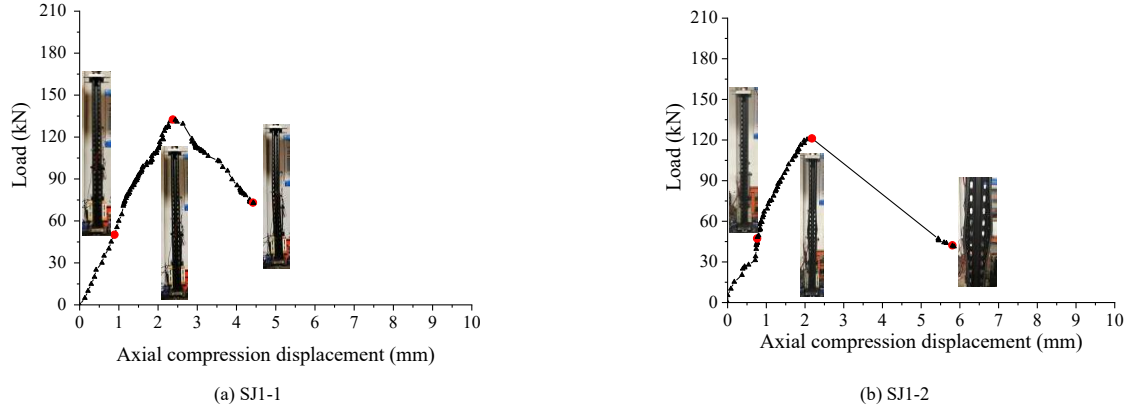


Fig. 5 Load-axial compression displacement curve of specimen SJ1

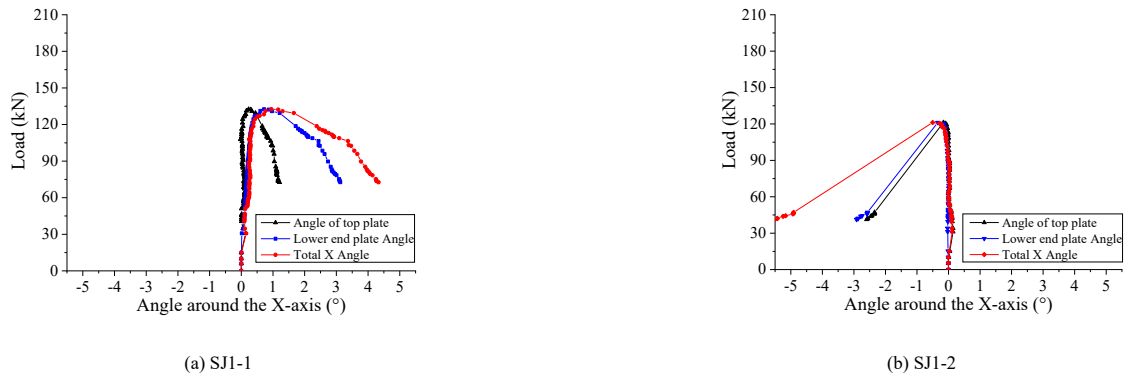


Fig. 6 Load-angle curve of axial compression specimen

The distortion and buckling of the center half of the two single-limb ohm columns happened first, followed by the appearance of the specimens' plastic hinges and, to some extent, overall instability. The load's lateral displacement. The angle curves of the two single-limb ohm columns are generally compatible

with the test findings, indicating the columns' overall instability. When the load exceeds the column's maximum bearing capacity, the deformation speed of the central component accelerates, emphasizing the column's overall instability.

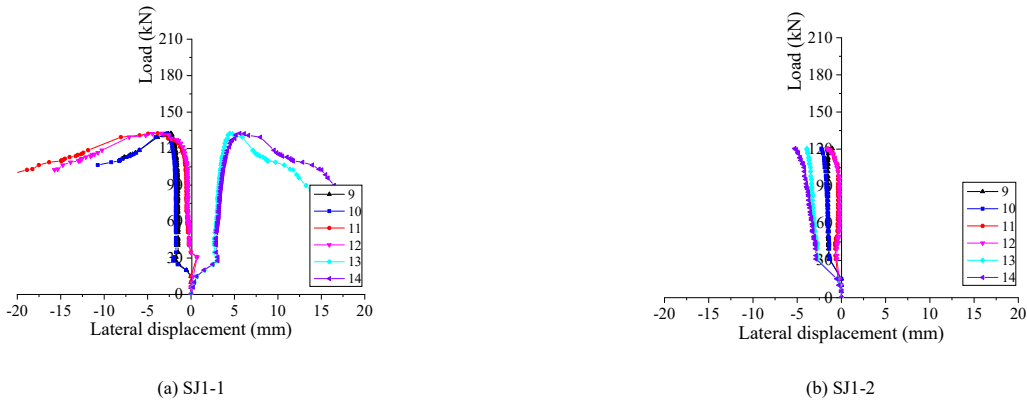


Fig. 7 Load-lateral displacement angle curve of axial compression specimen

2.4.2. Double limb ohm column SJ2-SJ5

Fig.8 shows the load-vertical displacement curve for SJ2-SJ5. The double-limb composite column has significantly more bearing capacity than the single-limb column. At the start of loading, the load is proportional to the axial displacement, which increases as the load increases. But when the load approaches 80% of the ultimate bearing capacity or enters the zone of ultimate

load, the displacement rises while the load growth rate falls, and the two are not equal. The plastic hinge appears on the failure area as the column starts to plasticize. The load and axial displacement rapidly decrease and swiftly reach the critical value or failure situation when the load is outside the range of ultimate bearing capacity. This marks the end of the test.

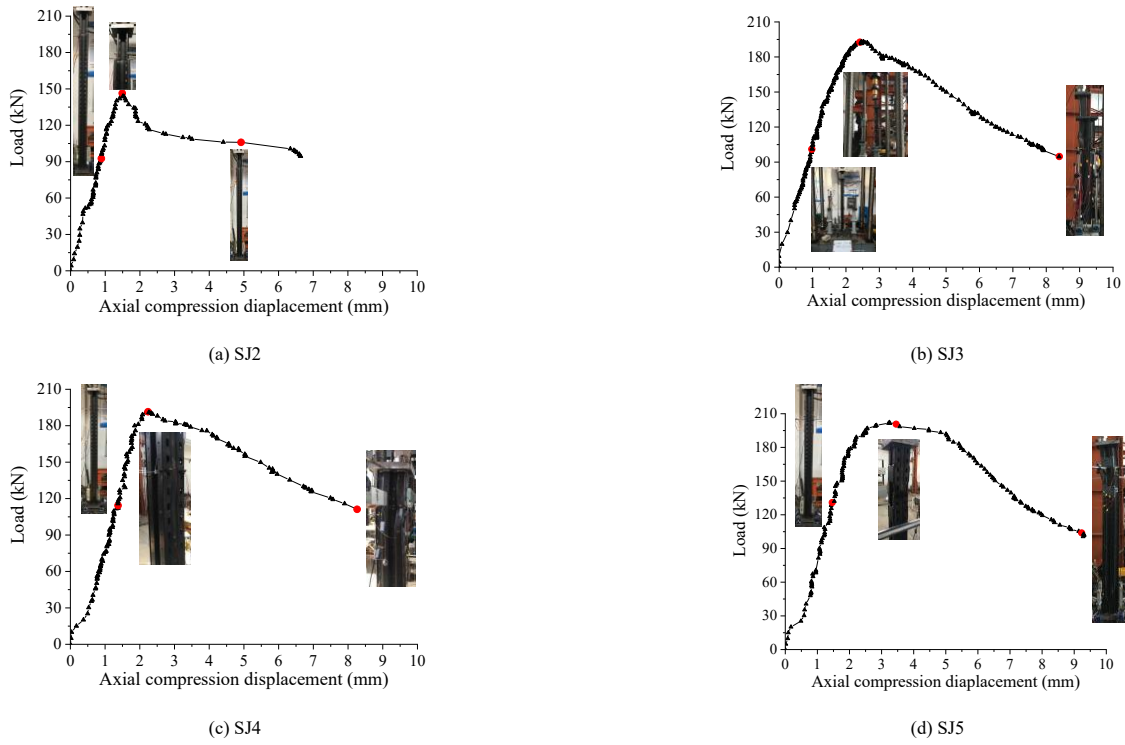


Fig. 8 Load-axial compression displacement curve of double-limb composite column

The mechanical performance of the outer limb ohm column has the greatest influence on the bearing capacity of the SJ2 column used in this project. Its bearing capacity is not considerably higher than that of a standard single-limb cold-formed thin-walled column, and it is reduced due to the eccentricity. With an intermediate transition plate, the SJ3 column's bearing capacity has significantly enhanced. When the column height, position, and direction of the loading point on the upper end plate are all the same, the SJ3 section's bearing capacity is 31.4% greater than that of the SJ2 section.

During the bearing capacity test, all of the double-limb composite columns were rotated to varying degrees around the X/Y axis, with the X axis being the most visible. As a result, the system's data will be calculated and processed to generate the load-rotation curve of the four double-limb composite columns

around the X axis (Fig.9). Column SJ2's total rotation angle around the X-axis is opposite that of the other three columns. The SJ2 column end plate rotates around the X-axis at a negative angle, whereas the SJ3, SJ4, and SJ5 end plates rotate positively. The bottom end plate of the column rotates at a small angle ($\pm 0.5^\circ$), whereas the higher end plate rotates the most. When the specimen reaches the ultimate load and is destroyed, the one with the SJ4 section has the greatest angle of rotation. The SJ4 and SJ5 sections' rotation angle changes very little in the first stage, suggesting that the displacement meter's sensitivity is low at the beginning of the loading stage and that the section's rotation angle does not change significantly. The lower end plate rotates along the X-axis in the opposite direction before turning in the positive direction when the load hits 20kN, causing a significant shift in rotation angle.

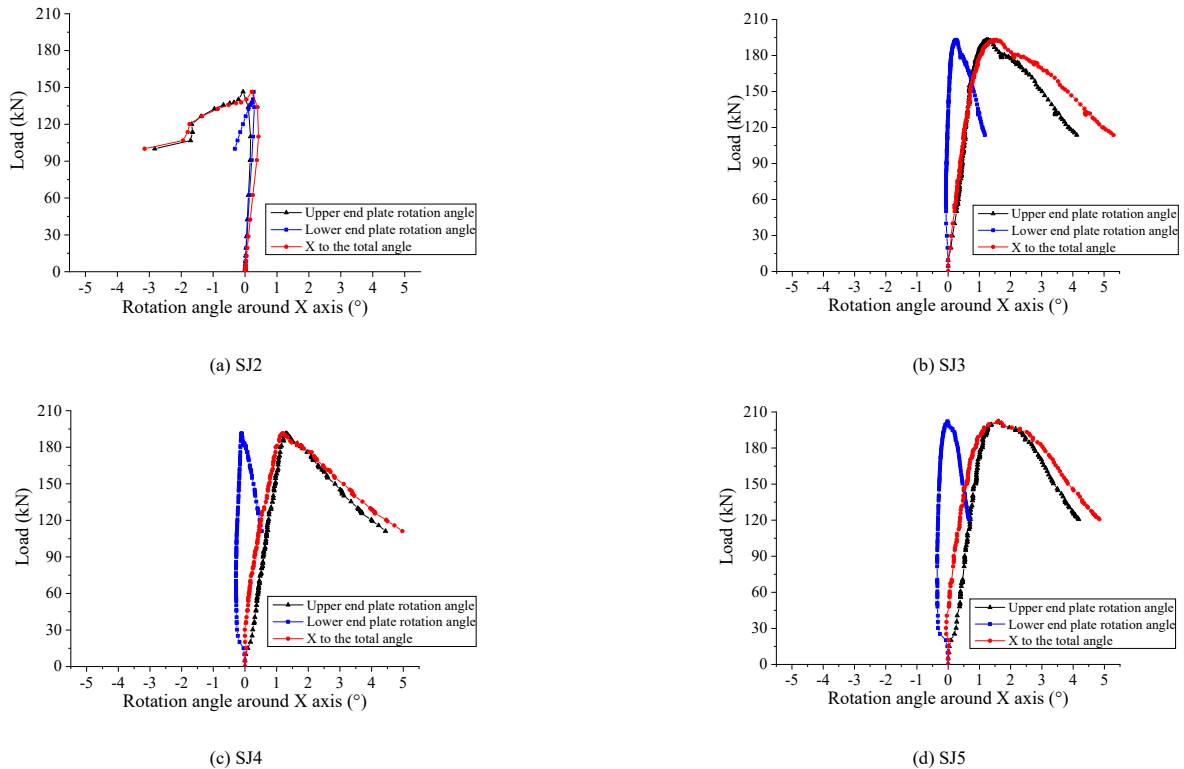


Fig. 9 Load-rotation curve of double-limb composite column under compression

The load-lateral displacement curve for the four column specimens is shown in Fig. 10. The variation law of the curve in the figure is broadly consistent with the test procedure: the column SJ2 does not change appreciably before the load is applied to the final bearing capacity. The displacement at the deformation increases quickly after reaching the maximum bearing capacity, which is broadly consistent with the test's findings. The displacement values obtained by symmetrical measuring locations in the other three columns' load-

lateral displacement curves are essentially the same, implying that the shapes and changes of No.9 and No.14, No.10 and No.13, and No.11 and No.12 curves are all consistent. The local buckling failure deformation of the column is also symmetric around the symmetry axis. Consistent with the field test results, the displacement range of the No. 11 and No. 12 curves is significantly larger than that of the other four displacement meters, indicating that the outer column web is more severely deformed than the flange.

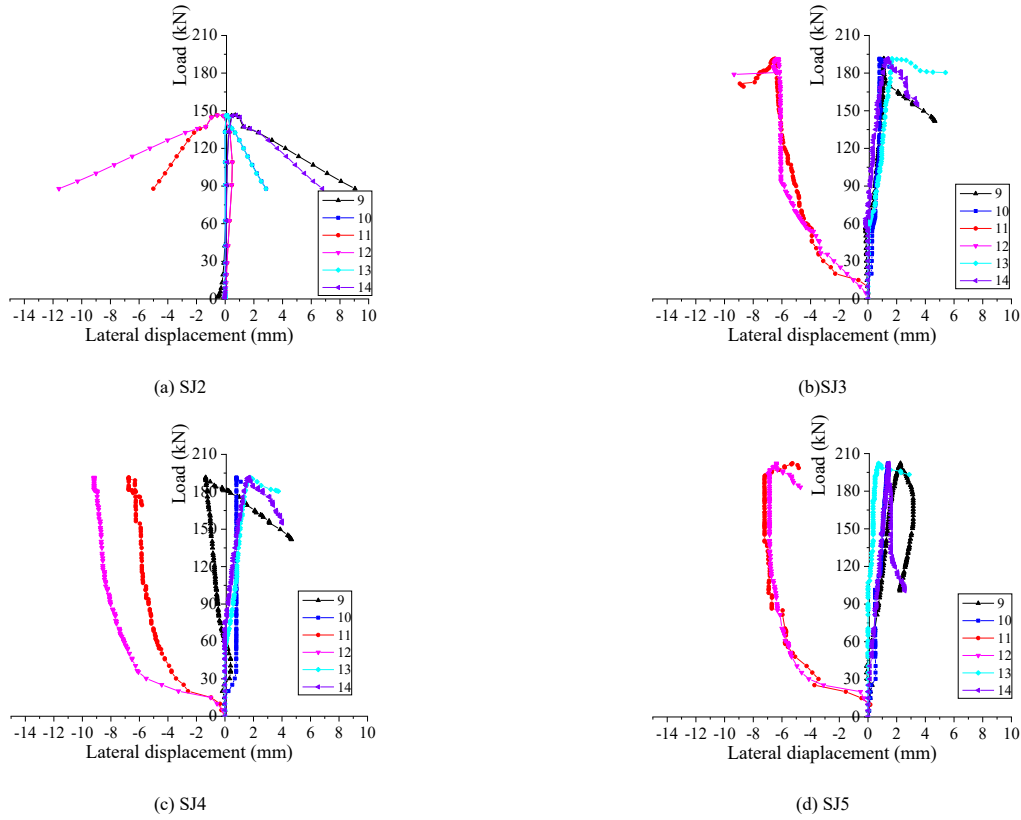


Fig. 10 Load-lateral displacement curve of double-limb composite column under compression

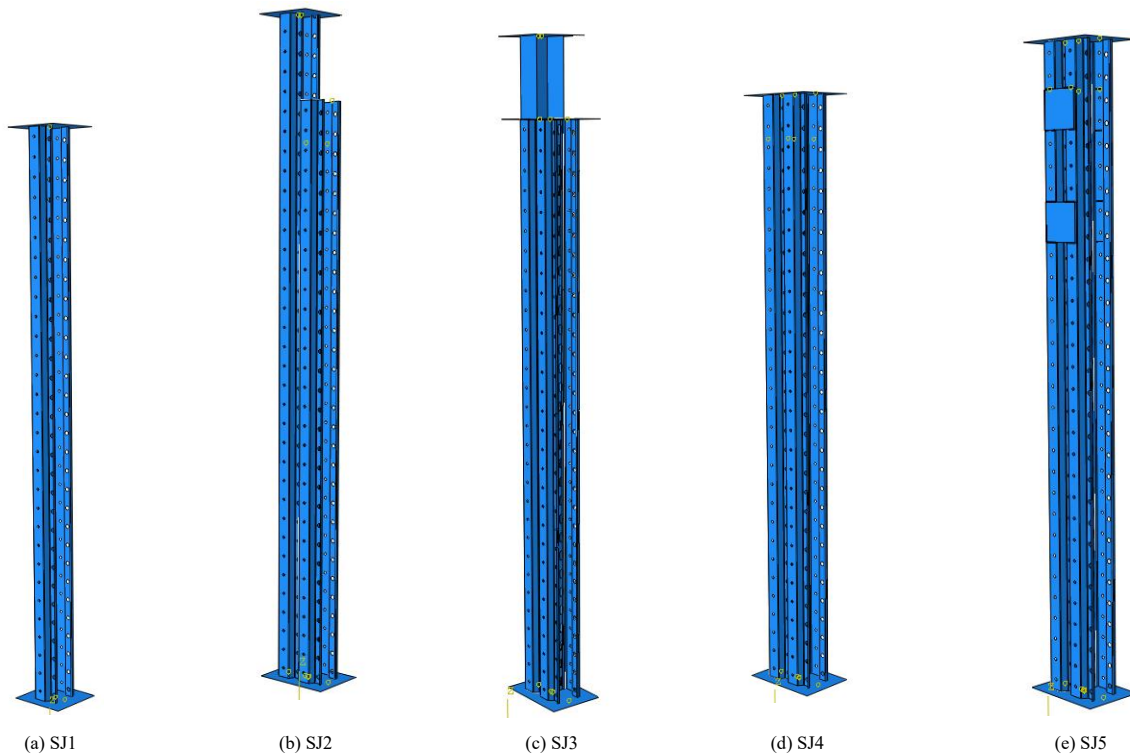


Fig. 11 Finite element model of column specimen

3. Finite element analysis

This chapter uses the finite element program ABAQUS to examine the mechanical properties of a cold-formed thin-walled assembled shelf column. The software compares numerical simulation results to the experimental results and investigates stress distribution and column deformation during the stress process are examined [25]–[30]. The model's perspective is used to explain the fundamental notion of column force change, as well as the essential aspects that may affect the mechanical performance of the cold-formed thin-walled constructed shelf column.

3.1. Finite element model

This research focuses on cold-formed thin-walled steel members. In this paper, the columns, end plates, and batten plates are modeled and analyzed using the general shell element S4R (4-node quadrilateral finite film strain linear reduction integral shell element), which has the best performance and is extensively used in the ABAQUS software element library.

Because the cross-section curling of the commonly used cold-formed thin-walled steel shelf column is difficult, the drawing function in AutoCAD must be utilized to create the cross-section of the ohm column. The software's stretching function transforms the cross-section into a three-dimensional entity, after which the column is opened with a Boolean operation. When the column member is completed, the component module is imported using the ABAQUS software's import system, and the whole column component is received. The remaining components, such as the batten plate and end plate, are imported in the same way. Fig.11 shows the finite element model for the five column specimens under test.

The nominal stress and strain of elastoplastic materials are determined directly from the material performance test. However, the material's actual stress and plastic strain must be mentioned in the ABAQUS material definition. As a result, the nominal stress and strain received from the material property test must be converted into real stress and plastic strain (Table.1). In ABAQUS,

section characteristics with containing material attributes are first established and then assigned to each area of the overall model to describe component material properties.

The component's initial geometric defects are introduced utilizing the consistent defect mode [21][22] technique in conjunction with the buckling form of the test findings, as investigated in this study. Scholars, both domestic and international, use the technique's relatively simple and workable approach. In the simulation study of this article, the amplitude value of various starting defects may be used to derive the load displacement curve and ultimate load of the specimen when combined with GB50017-2017 [23] and EN1993-1-5 [24]. A minor amount of residual stress will be created during the specimen processing, however the effect of taking residual stress into account is more complicated, hence the effect is not taken into account in the finite element model used in this work.

Each node in the ABAQUS program has six matching degrees of freedom that can be controlled. The real state of the node can be duplicated by defining or limiting the degrees of freedom associated with it. The hinge point in this simulation initially situated on the end plate, and its six degrees of freedom are controlled and restricted. The higher end of the column can be used to simulate a test jack by limiting UX and UY's degrees of freedom at the upper end plate's loading location. The specimen's flat east in the Z direction and the column's rotation in the X, Y, and Z directions. The four degrees of freedom of UX, UY, UZ, and ROTZ are thus limited at the lower end plate's hinge point, allowing the lower end plate to rotate solely in the X and Y planes.

When changing the grid control properties, the unit shape is changed to quadrilateral to reduce grid distortion and improve simulation computation convergence. The neutral axis algorithm is then utilized to choose the minimum grid transition to divide the grid freely. The grid is divided according to the norm that the approximate global size of the column member is 8 mm, and the approximate global size of the end plate and batten plate member is 5 mm, when the grid size is established in accordance with the empirical law of the research group's previous simulation. Fig.12 shows the divided mesh model.

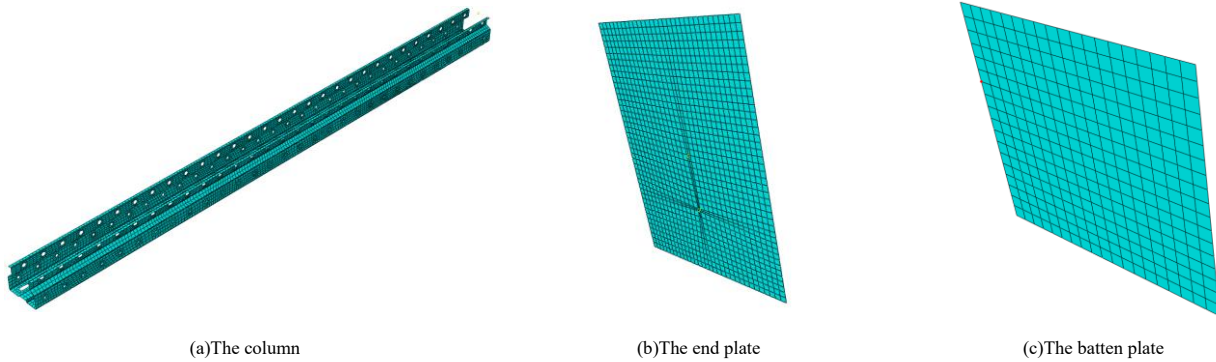
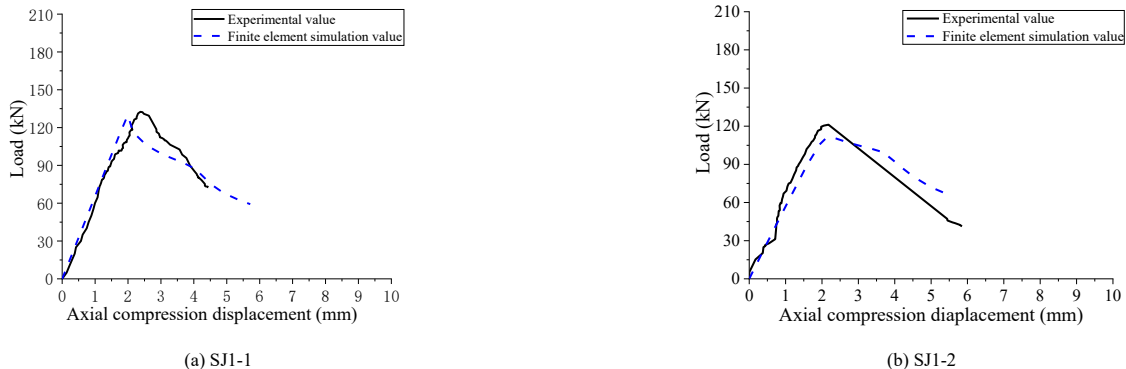


Fig. 12 Meshing Shape of Column Components

3.2. Finite element simulation analysis

The finite element simulation in this study employs nonlinear buckling analysis, allowing the deformation of the section entering the post-buckling stage to be calculated. In the finite element simulation, 60% of the ultimate load is used as the critical value, and the calculation is terminated when the load

surpasses the ultimate load and reaches the critical value. The simulation result represents the final deformation. The load-displacement curve generated from the simulation calculation is compared to the experimental result (Fig. 13). The overall trend is relatively constant, and the slope of the initial stage is nearly identical.



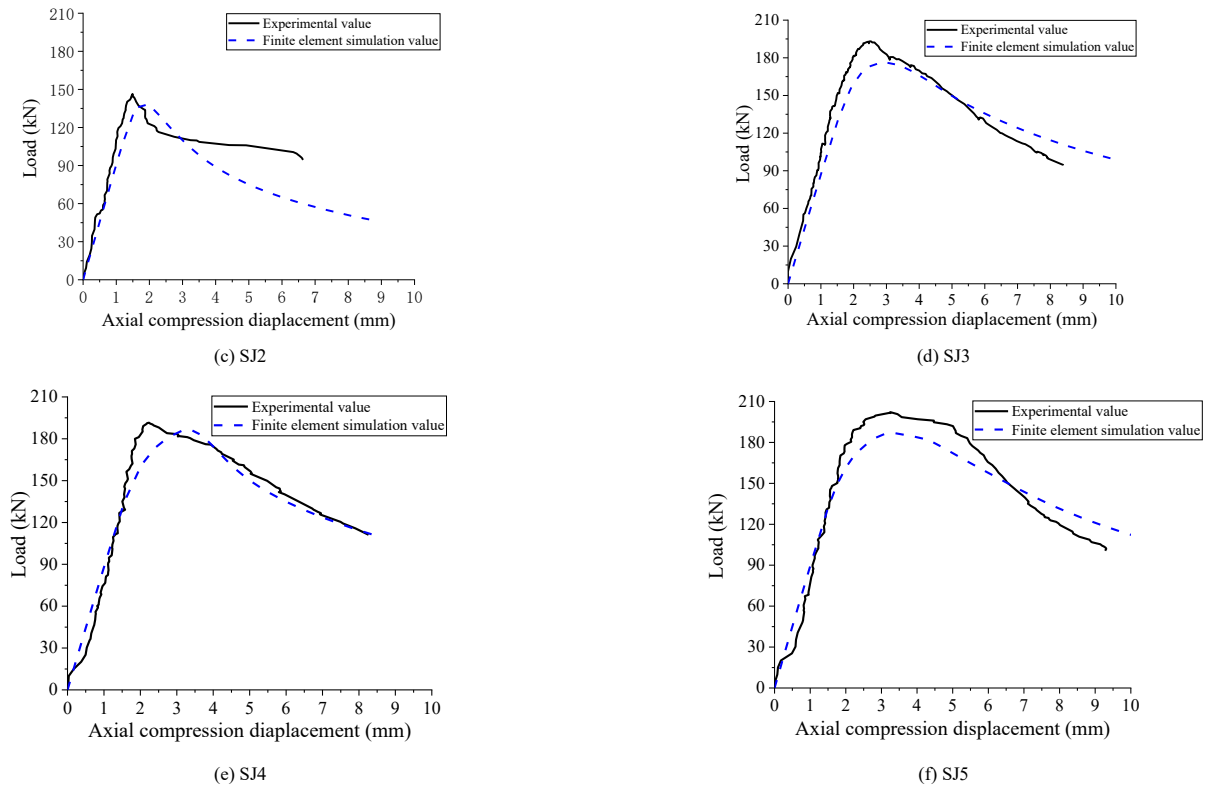
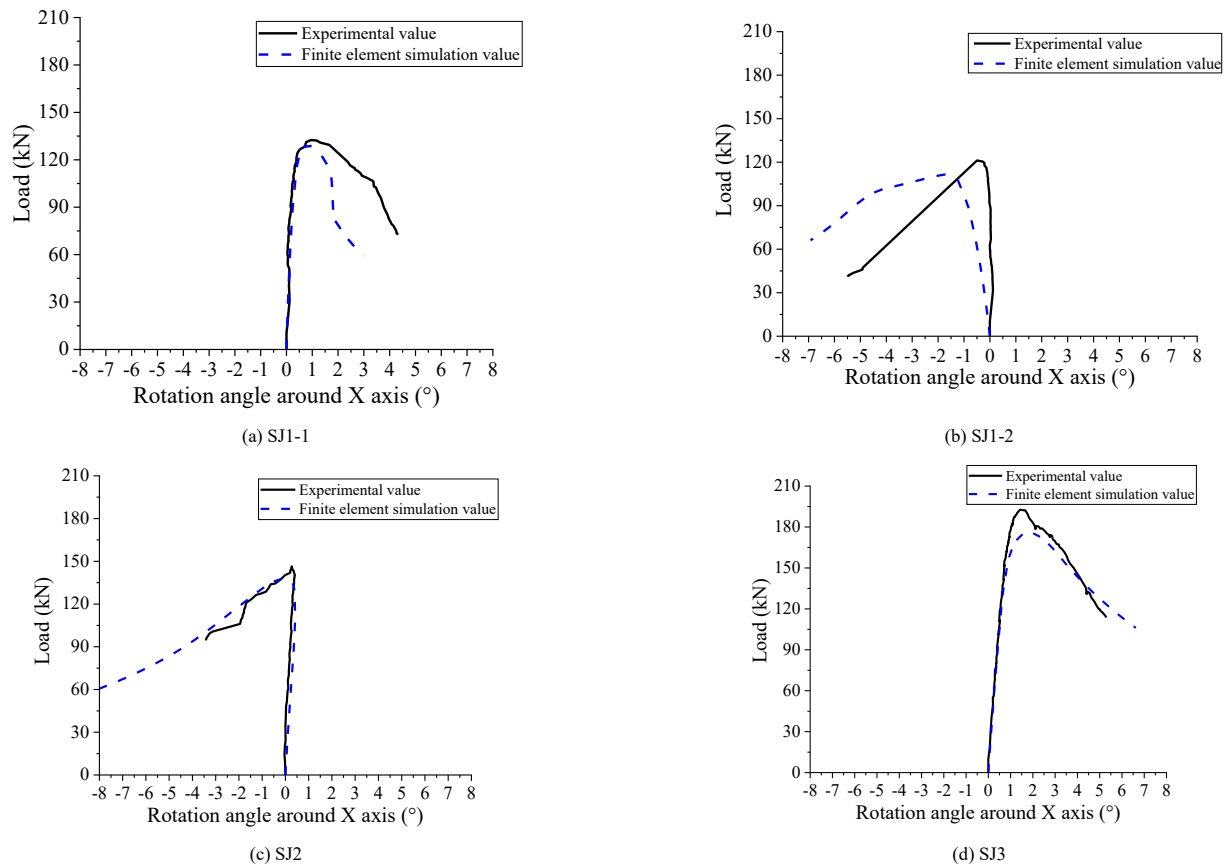


Fig. 13 Finite element results of load-axial compression displacement curve

The compressive specimens of the single-limb Ohmic column have various degrees of rotation in the X and Y axes, whereas the compressive specimens of the double-limb composite column primarily rotate in the X axis. The curves of various columns are summarized using the rotation angle around the X axis, and the finite element and experimental data are compared and examined (Fig. 14). The experimental and finite element values of the load-rotation curves of all

column specimens are nearly identical; the initial slope of the test curve is greater than the initial slope of the simulated value curve, indicating that the rotation speed of the test value is slow at the start of the rotation angle. The test findings demonstrate that the rotation process is caused by the spherical hinge's non-ideal state. The rotation is limited by a certain amount of resistance.



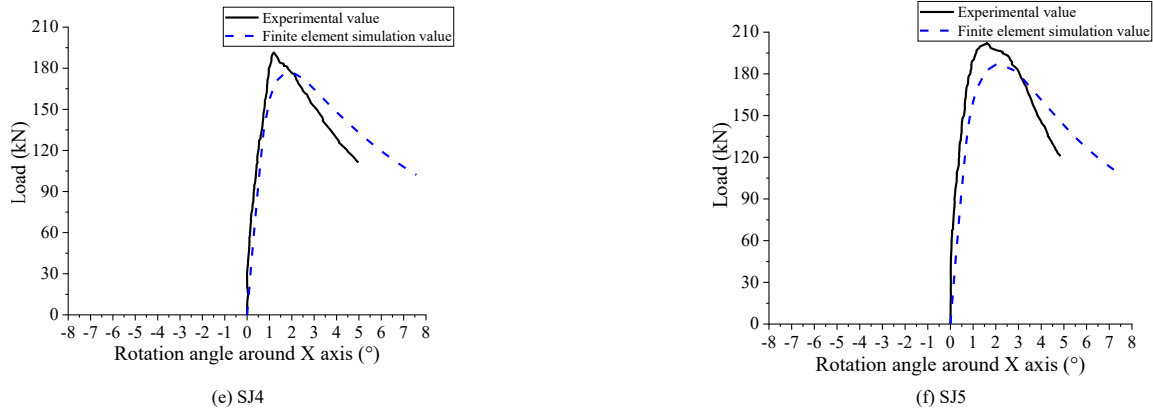


Fig. 14 Finite element results of load-rotation curve

3.3. Ultimate capacity analysis

In addition to comparing and assessing experimental and finite element values, a finite element model without starting flaws is created for computation,

Table 2

The column test results are compared with the finite element analysis results

Classification	Specimens Number	Mode of Failure (D: Distortional buckling; L: Local buckling)		Ultimate Bearing Capacity			Error/% ($P_T - P_{FE}$)/ P_T
		Test	Finite Element	P_T /kN	P_{FE} /kN	P_0 /kN	
Single Limb Column	SJ1-1	D	D	132.54	129.77	131.36	2.08
	SJ1-2	D	D	121.19	111.86	115.31	7.70
Double-leg column	SJ2	D	D	146.42	137.84	141.56	5.86
	SJ3	L	L	192.69	176.02	183.64	8.64
	SJ4	L	L	191.49	177.11	188.28	7.51
	SJ5	L	L	202.24	186.90	195.70	7.59
Average Error							6.56

The table demonstrates that the final failure modes of each column specimen in the test and the finite element simulation results are virtually identical. In this test, the variation between column test and simulation results ranges from 2% to 9%. The test value for each column's ultimate bearing capacity exceeds the simulation value. The lowest error is 2.08% in the single-limb ohmic column SJ1-1, the worst is 8.64% in SJ3, and the average is 6.56%. The error is within the acceptable range.

By developing a better finite element model of the shell element, column tests can be replicated more precisely. A set of load displacement curves can be created by converting and computing the data from the finite element simulation results.

4. Research on the influence of parameters

When the finite element simulation results are compared to the real test results, they are almost identical, demonstrating that the column may be successfully simulated if the column section is carefully drawn and the finite element parameters are properly specified. In this chapter, the SJ4 cross-section column (cold-formed thin-walled constructed double-limb composite column) is used as the main model, and more parametric research is carried out on its foundation.

The slenderness ratio of the column(λ), the number of batten plates(n), the thickness of the column(t_c), the length(l) and spacing of the discontinuous welds(d), and the thickness of the dowel plate(t_d) will all have an impact on the ultimate bearing capacity and failure mode of the cold-formed thin-walled assembled double-limb composite column. The preceding test and finite element analysis results indicate that the column's slenderness ratio will influence the component's final failure mode.

When $\lambda \leq 85$, the final failure mode is local buckling failure. The failure section consists mostly of the column's middle and upper parts, with the upper end plate rotating along the X axis. When $85 \leq \lambda \leq 95$, the specimen's final failure mode is between local and overall buckling failure. The column's failure is influenced by both buckling modes. When $\lambda \geq 95$, the specimen's final failure mode becomes general instability failure, with increased lateral bending

with the understanding that adding initial faults results in a lower finite element simulation value. The ultimate bearing capacity value P_0 is compared to the experimental value P_T and the finite element value P_{FE} . The results are shown in Table.2.

increases. The column's failure point is predominantly located in the middle, with no significant change near the ends.

The increase in batten plate has a more evident positive influence on local buckling instability. Welding the batten plate to the column's local buckling failure can increase the final bearing capacity by around 5% while also boosting the region's cross-sectional strength. Furthermore, expanding the batten plate can have a more noticeable impact on the column's local stability, but the effect on the column's overall stability is unknown.

The following three influencing factors will have a substantial impact on the cold-formed thin-walled assembled double-limb composite column's ultimate bearing capacity and failure mechanism. As a result, in order to accurately analyze the specific change process of each influencing factor on the column, as well as provide the influence law and related suggestions for each key factor, a detailed parametric analysis of the double-limb composite column is required to lay the groundwork for the column's research and design in the project.

4.1. Thickness of column(t_c)

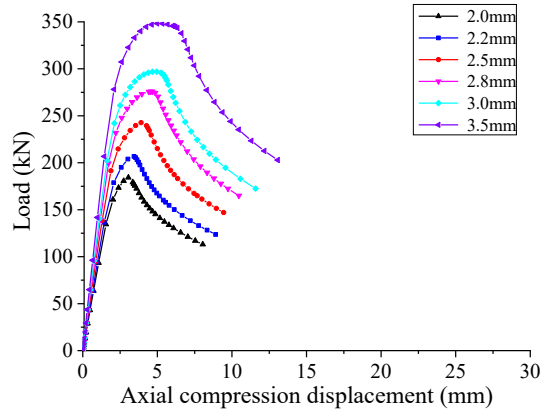
The average thickness of a steel shelf structure in industry is between 2.0 mm and 3.5 mm. When the thickness is less than 2.0 mm, the column's bearing capacity rapidly drops, resulting in reduced safety performance. If the thickness is too large for cold-formed thin-walled steel members, the difficulty of cold-formed rolling of thick plates in the factory will skyrocket, and when the material thickness exceeds 3.5mm, the section will be more likely to produce fine cracks after cold bending, which is detrimental to structural safety and negates the economic benefits of cold-formed thin-walled members.

Based on the specimen SJ4, this portion selects component heights $H = 1.5m$ to ensure that the remaining test conditions are identical to the previous ones. The specimen's boundary conditions are changed so that it can hinge at either end. The spacing between the intermittent welds is 300mm, and their length is 50mm. Change the thickness of the component's column and generate a collection of finite element parametric models for analysis.

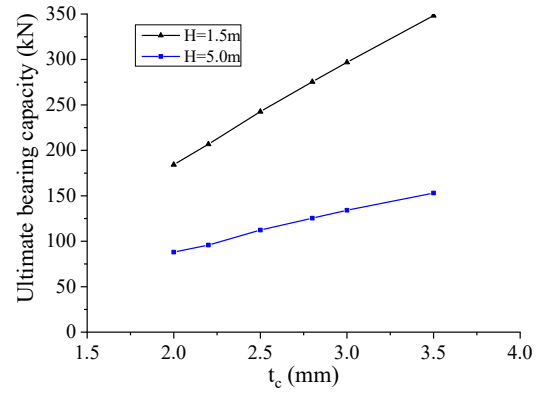
The simulation results in Fig.15 clearly show that the ultimate bearing

capacity of the double-limb composite column gradually increases as the column's wall thickness increases, which is essentially linear; however, the

column's final failure mechanism is independent of wall thickness.



(a) Load-axial displacement curves of specimens with different column thicknesses



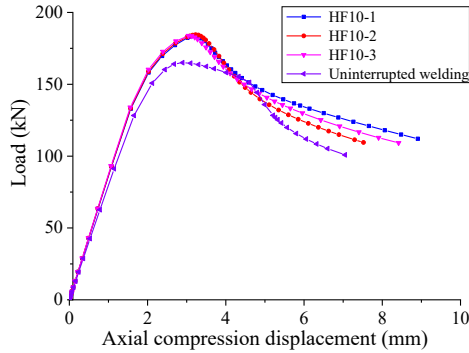
(b) Comparison curves of ultimate bearing capacity of specimens with different wall thicknesses

Fig. 15 Analysis of the influence of column thickness

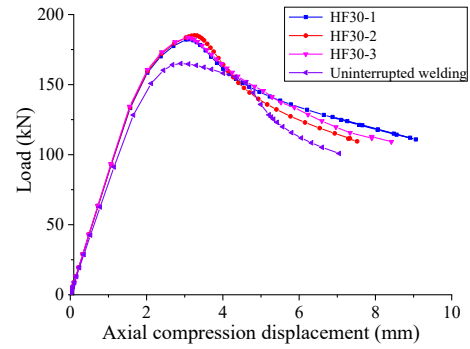
Table 3

Intermittent weld parametric model specification table

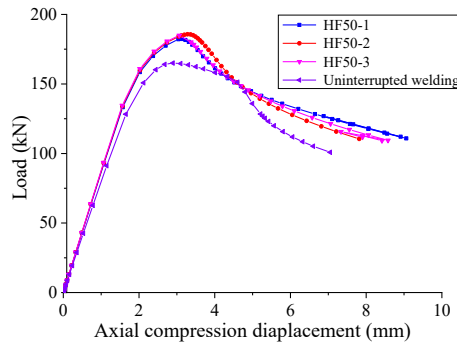
l (mm)	d (mm)	No.
10	750	HF10-1
	500	HF10-2
	300	HF10-3
30	750	HF30-1
	500	HF30-2
	300	HF30-3
50	750	HF50-1
	500	HF50-2
	300	HF50-3



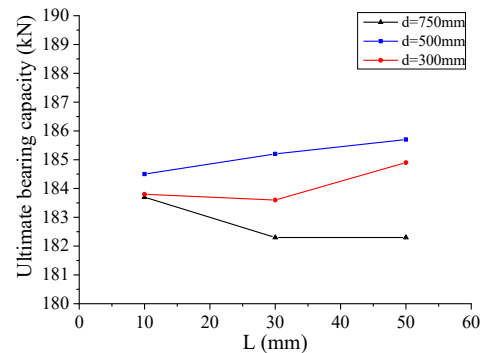
(a) $L=10\text{mm}$



(b) $L=30\text{mm}$



(c) $L=50\text{mm}$



(d) Ultimate bearing capacity of weld parameters at different heights

Fig. 16 Analysis of the influence of weld length and spacing

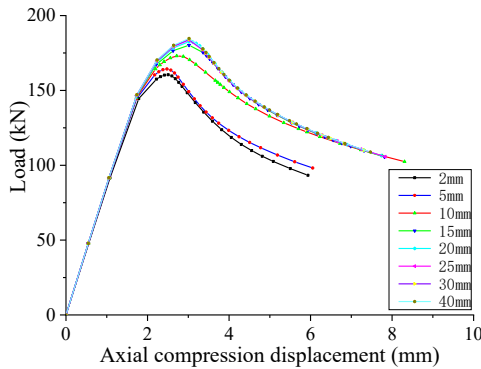
4.2. Column weld length(l) and spacing(d)

The load test and finite element simulation analysis of the cold-formed thin-walled assembly shelf column under consideration in this study show that there are no fixed standards or specifications, and the length and intermittent weld spacing are empirical values. The estimated values from the project are used in the preceding test and finite element analysis. In terms of cross-section, the intermittent welding between the inner and outer limb columns provides the primary support for the double-limb composite column based on SJ4. Thus, in this section, we will look at the bearing capacity of the cold-formed thin-walled assembly shelf column, as well as the effects of modifying the weld spacing and intermittent weld length.

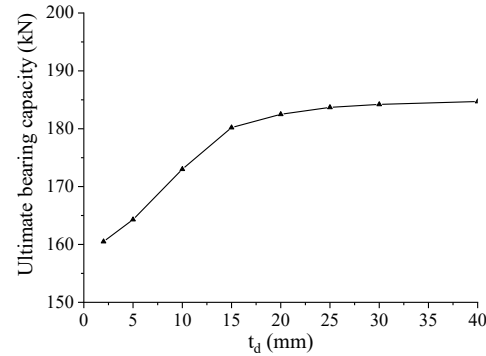
The components are divided into three groups based on their weld length: 10 mm, 30 mm, and 50 mm, in that order. The weld spacing changes from large to tiny under the left and right symmetrical intermittent welding arrangements, depending on the type of weld length. The column is 2mm thick, and the other properties are identical to those of the SJ4 section. Table.3 shows the individual model parameter changes.

As seen in Fig.16, it is:

- (1) When the weld spacing is the same, the constructed double-limb composite column's bearing capacity is not improved by the length of a single weld, and the weld's length has no effect on the column's final bearing capacity. The column's bearing capacity is mostly determined by its own bearing capacity.
- (2) When the same weld length is utilized, the load bearing capacity rises as the weld spacing reduces. That is, the ultimate bearing capacity of the column



(a) Load-axial displacement curves of specimens with different thickness of force transfer plate



(b) Comparison curves of ultimate bearing capacity of specimens with different thickness of dowel plate

Fig. 17 Analysis of the influence of the thickness of the force plate

As seen in Fig.17, it is:

- (1) At the commencement of loading, the load-axial displacement curve for a double-limb composite column with different force plate thicknesses is virtually equal to the finite element model. The ultimate bearing capacity increases with the thickness of the dowel plate, suggesting that increasing the thickness of the dowel plate helps the top structure to distribute the weight more uniformly to the double-limb composite column, allowing the column to withstand greater load.

- (2) The thickness of the dowel plate impacts the column's final bearing capacity in several ways. At 0 ~ 20mm, the curve slopes to a straight line, indicating a large improvement in ultimate bearing capacity. At the 20-40mm stage, the slope is gentle, and the column's ultimate bearing capacity increases slowly. For optimal results, choose a dowel plate thickness of 15-25 mm. Because 20 mm is the normal size, it is the most economical to use 20 mm thickness.

5. Conclusions

In summary, the following conclusions can be drawn:

- (1) The cold-formed thin-wall double-limb composite column is suited for shelf projects due to its compact design, ease of manufacturing, high bearing capacity, and strong anti-side ability. The two-limb composite column's force performance is higher after application and testing in the actual project, saving cargo storage space in the strong axis while boosting lateral stiffness in the weak axis.
- (2) The directly spliced two-limb composite column SJ2 (no force transfer plate) has distortion buckling failure in the test, and the ultimate bearing capacity is improved to some extent compared to the single-limb ohm column, but the co-working performance of the inner and outer limbs of the two-limb composite column is not fully realized. The failure of the

increases with a denser surface weld arrangement, but the range of enhancement is limited.

- (3) Whether or not there are continuous welds has a considerable impact on bearing capacity. At a 1.5-meter column height and a 750-millimeter weld spacing, the ultimate bearing capacity of weld lengths of 10 mm, 30 mm, and 50 mm is 9.2%, 9.1%, and 9.0% higher than that of the non-welded column, respectively.

- (4) The weld configuration varies with the height of the column. The final bearing capacity of the column is greatest and most cost-effective when the spacing between the long column's discontinuous welds is 300 mm and the weld length is 30 mm. The short column's discontinuous weld spacing is best configured at 500 mm, and the longer the weld length, the greater the ultimate bearing capacity.

4.3. Thickness of the dowel plate(t_d)

In the previous test, specimen SJ3 had a 31.4% higher ultimate bearing capacity than SJ2, demonstrating that adding the dowel plate can significantly increase the bearing capacity of the double limb composite column. To fully study the influence of dowel plate thickness on the bearing capacity of the SJ3 section, the column force is measured as the thickness of the dowel plate is varied. The thicknesses of the dowel plates are 2mm, 5mm, 10mm, 15mm, 20mm, 25mm, 30mm, and 40mm, respectively. Aside from the dowel plate, the remaining attributes are equivalent to SJ3. The upper short column is 8mm thick, while the lower double-limb composite column is 2mm.

two-legged composite columns SJ3 with force transfer plate and composite column, SJ4 with force transfer plate, and SJ5 with force transfer plate and composite plate was caused mostly by local buckling. In comparison to the SJ1 and SJ2 sections, the ultimate bearing capacity is significantly increased. The final bearing capacity of the two-limb composite column can be raised to a certain extent by placing plates on both sides.

- (3) The bearing capacity of the two-limb composite column increases with the thickness of the column plate, and the relationship is nearly linear; nevertheless, increasing the thickness does not change the column's final failure mode. Columns with $\lambda \leq 85$ typically fail due to local buckling, primarily in the middle and upper sections of the column. A column with $\lambda \geq 95$ will fail due to overall instability, with the failure spot located in the middle. The column section with a thickness of 3.5mm is the most efficient and cost-effective.
- (4) The spacing and weld size of the discontinuous welds have no effect on the column's ultimate failure mode, but they do have an impact on its final bearing capacity. The welding influence of upper and lower end plates affects columns with $\lambda \leq 85$, hence increasing weld spacing and size has no effect on the column's final bearing capacity. The column's ultimate bearing capacity increases significantly with $\lambda \geq 95$. The recommended spacing for intermittent welds in the project is 300mm-500mm, with a weld length of 30mm being the most cost-effective choice.

Funding

This work was supported by the National Natural Science Foundation of China [Grant No.52278150].

References

- [1] H. Mashaly, A. H. A. Abdelrahman, F. A. Salem, N. S. Mahmoud. EVALUATION OF LOCAL-PLATE BUCKLING COEFFICIENT FOR THE DESIGN OF COLD-FORMED STEEL-LIPPED CHANNEL CROSS SECTIONS: NUMERICAL SIMULATIONS AND DESIGN RECOMMENDATIONS. *Advanced Steel Construction*. (2024): 20, 30-38.
- [2] Affolter Ch., Piskoty G., Wulschleger L. Collapse of a high storage rack. *Engineering Failure Analysis*. (2009): 16: 1846-1855.
- [3] Tian Y.S., Godley M.H.R., Wang J. Racking strength and stiffness of cold-formed steel wall frames. *Journal of Constructional Steel Research*. (2004), 7: 1069-1093.
- [4] Gao, W, Wan, J & Liu, S 2021. A Stability Design Theory for the Steel Members Using Asymmetric Thin-Walled Open-Sections. *Progress in Steel Building Structures*. (2021) vol. 23, no. 5, pp. 53-62 and 72.
- [5] Trouncer, Adam Nevil and Kim J.R. Rasmussen. Flexural-torsional buckling of ultra light-gauge steel storage rack uprights. *Thin-walled Structures*. 81 (2014): 159-174.
- [6] Kilar, Vojko et al. Seismic analysis of an asymmetric fixed base and base-isolated high-rack steel structure. *Engineering Structures*. 33 (2011): 3471-3482.
- [7] Obst, Maciej et al. Experimental investigation of four-point bending of thin walled open section steel beam loaded and set in the shear center. *Scientific Reports*. (2022): Vol:12, No.1:7275.
- [8] Pala, Yaşar et al. Improvement of Buckling Behavior of Cold Formed Steel Uprights with Open Cross Section Used in Storage Rack Systems. *World Academy of Science, Engineering and Technology, International Journal of Civil and Environmental Engineering*. (2017): Vol:4, No:5.
- [9] Davies, J. Michael et al. The design of perforated cold-formed steel sections subject to axial load and bending. *Thin-walled Structures*. 29 (1997): 141-157.
- [10] Shanmugam, N. E. and M. Dhanalakshmi. Design for openings in cold-formed steel channel stub columns. *Thin-walled Structures*. 39 (2001): 961-981.
- [11] Freitas, Arlene Maria Sarmanho et al. Analysis of steel storage rack columns. *Journal of Constructional Steel Research*. 61 (2005): 1135-1146.
- [12] Moen, Cristopher Dennis and Benjamin W. Schafer. Elastic buckling of cold-formed steel columns and beams with holes. *Engineering Structures*. 31 (2009): 2812-2824.
- [13] Baldassino, Nadia et al. An experimental investigation on solid and perforated steel storage racks uprights. *Journal of Constructional Steel Research*. (2019): Vol.155: 409-425.
- [14] Talebian N, Gilbert B P, Pham C H, et al. Parametric Studies and Design Rules for Local and Distortional Biaxial-Bending Capacity of Cold-Formed Steel Storage-Rack Uprights. *Journal of Structural Engineering*. (2020): 146(3).
- [15] Ren C, Wang B, Zhao X. Numerical predictions of distortional-global buckling interaction of perforated rack uprights in compression. *Thin-Walled Structures*. (2019): Vol.136:292-301.
- [16] GB/T228.1-2021. *Metallic materials—Tensile testing—Part 1: Method of test at room temperature*.
- [17] EN15512:2022. *Steel static storage systems - Adjustable pallet racking systems - Principles for structural design*.
- [18] Zhao G. Study on stability performance of axial compression members of H-section of Q345GJ steel. Chongqing University. (2011).
- [19] Qin Y. Theoretical and experimental study on axial compressive properties of cold-formed thin-walled steel low-rise residential wall column system. Tongji University. (2006).
- [20] Shen Z, Guo X. Stability coefficient of compression rod of aluminum alloy extrusion profile with symmetrical cross-section. *Journal of Building Structures*. (2001): (04): 31-36+48.
- [21] Casafont M, Roure F, Pastor M. Distortional buckling test for steel storage rack columns. *Structures and Buildings*. (2013): 166(8):392-402.
- [22] Gu M, Zhang Q. Research on the introduction of first-order buckling modes as initial defects. *Proceedings of the Fifth National Symposium on Modern Structural Engineering*. (2005).
- [23] GB50017-2017. *Standard for design of steel structures*.
- [24] EN1993-1-5. *Design of steel structures-Part1-5: Plated structural elements*.
- [25] Claudio Bernuzzi, Alice Pieri. Warping influence on the static design of unbraced steel storage pallet racks. *Thin-Walled Structures*. (2014), Vol.79:71-82.
- [26] Claudio Bernuzzi, Castiglioni Carlo A. Experimental Analysis on the Cyclic Behavior of Beam-to-column Joints in Steel Storage Pallet Racks. *Thin-Walled Structures*. (2001): (39):841-859.
- [27] J. J. Moy, C. S. Tan, EXPERIMENTAL STUDY OF SCISSOR FRAME STRUCTURES WITH FEM VALIDATION OF LOAD IMPACT ON MANUAL LOCKING MECHANISM. *Advanced Steel Construction*. (2024):20, 160-168.
- [28] Aguirre C. Seismic Behavior of Rack Structures. *Journal of Constructional Steel Research*. (2005): 61(5): 607-624.
- [29] Alavi B, Gupta A. Performance-Based Seismic Design of an Industrial Storage Rack System. *Structures Congress*. (2008):1-10.
- [30] Aktepe, Rafet and Burcu Guldur Erkal. State-of-the-art review on measurement techniques and numerical modeling of geometric imperfections in cold-formed steel members. *Journal of Constructional Steel Research*. (2023): Vol.207:107942.

SEISMIC PERFORMANCE OF PU-PAI FANG-DOVETAIL TENON JOINTS WITH VARYING LOOSENING DEGREES REINFORCED BY STEEL SLEEVE CLAMP HOOPS

Sen-Long Tan¹, Yun-Peng Chu¹, Yao-Peng Liu^{2,*}, Jia-Hao Wang¹, Si-Qi Wang¹, Zheng Zhang³ and Bo Si⁴

¹ School of Civil Engineering and Architecture, Southwest University of Science and Technology, Mianyang 621010, China

² School of Civil Engineering and Transportation, South China University of Technology, Guangzhou 510641, China

³ Tongji Architectural Design (Group) Co., Ltd, Shanghai 200092, China

⁴ Beijing Building Construction Research Institute, Beijing 10039, China

* (Corresponding author: E-mail: yaopengliu@scut.edu.cn)

ABSTRACT

The Pu-pai Fang-dovetail tenon joint, an enhanced form of the traditional dovetail joint, is commonly used at beam-column connections in traditional beam-lifting timber structures. However, long-term environmental exposure and seismic loading often lead to wood shrinkage and joint loosening, reducing structural integrity. This study proposes a reinforcement method for Pu-pai Fang-dovetail tenon joints with varying degrees of looseness using steel sleeve clamp hoops. Quasi-static tests were conducted on one intact specimen and three specimens with different looseness levels to examine their failure modes and seismic behavior. Results indicate that tenon pull-out in the reinforced joints causes tearing of wood fibers at the mortise and Pu-pai Fang, yet the flexural capacity continues to increase without exhibiting a descending branch. The energy dissipation capacity and stiffness degrade rapidly at first and then stabilize. Compared with unreinforced joints, the reinforced specimens exhibited a lower tenon extraction rate and higher ultimate flexural capacity. A finite element model was subsequently developed, showing good agreement with the experimental results. Parametric analysis revealed that selecting an appropriate friction coefficient (0.3–0.5) and clamp-hoop thickness (5–7mm) can effectively improve the seismic performance of Pu-pai Fang-dovetail tenon joints.

ARTICLE HISTORY

Received: 15 June 2025
Revised: 28 July 2025
Accepted: 11 August 2025

KEYWORDS

Ancient timber buildings;
Pu-pai Fang-Dovetail tenon joints;
Loosening degrees;
Quasi-static test;
Parametric analysis

Copyright © 2025 by The Hong Kong Institute of Steel Construction. All rights reserved.

1. Introduction

The dovetail tenon joint is a commonly used key joint form for the connection between beams and columns in traditional beam-lifting timber structures [1]. Under the action of earthquakes, the tenon and mortise effectively prevent the tenon from being pulled out and falling off by mutual friction, sliding and compression deformation. This structural form belongs to a typical "semi-rigid" connection and has a good energy dissipation and shock absorption effect [2,3,4,5]. However, the cutting behavior at the end of the column to achieve the connection between the column and the beam frame layer significantly weakens the load-bearing capacity of the column and also provides the initial conditions for the invasion of microorganisms into the wood. Due to the long-term exposure of ancient timber structures to the natural environment and the characteristic of wood materials that they tend to shrink easily, cracks generally occur in the beam and column components under the long-term load and the influence of wind and rain, as shown in Fig. 1(a), and the connection points of the joints become loose, as shown in Fig. 1(b). These deterioration phenomena cause the seismic performance of timber structures to deteriorate, making them prone to premature damage during earthquakes. The failure of key joints may lead to the overturning and collapse of the entire structure.

In recent years, some scholars have carried out a large number of experimental studies on the mechanical properties and seismic resistance of traditional mortise and tenon joints caused by loose damage [6]. The bending moment, stiffness and energy dissipation capacity of the loose joints were all lower than those of the intact joints. Moreover, the greater the degree of looseness of the loose joints, the lower the bearing capacity, and the more obvious the degradation of stiffness and strength. However, they still had good deformation capacity. Zhang et al. [7] found through numerical analysis that the extrusion deformation of the joints was mainly concentrated at the tenon of the dovetail tenon, the equivalent plastic strain of the tenon increased linearly, the failure at the end of the tenon was the least, and the failure at the neck of the tenon was the greatest. Yu et al. [8] established the geometric deformation characteristics and geometric model of the dovetail tenon and found that the bending moment of the dovetail tenon connection is directly proportional to the height and length of the tenon. Considering the gap effect caused by loosening is of great significance for performance degradation and the establishment of bending moment models [9]. Bai et al. [10,11] explained how loosening damage affects the failure mode and mechanical properties of dovetail joints. He et al. [12] proposed a theoretical bending moment model for loose joints and verified it through the deformation characteristics and lateral resistance of the timber frame. At present, the research on loose joints mainly focuses on traditional mortise and tenon joints. The ingenious design of ancient architectural timber structures is to design Pu-pai Fang on the upper part of beam components to

enhance the bending resistance of the structure. Such joints are called Pu-pai Fang - dovetail tenon joints [13]. At present, some scholars have conducted relatively few studies on the mechanical properties of Pu-pai Fang components [14,15]. The Pu-pai Fang can significantly enhance the rotational stiffness and bending moment of joints. The force mechanism of this type of joint is significantly different from that of other traditional joints, but it also faces problems such as the deterioration of structural performance state under environmental influence, as shown in Fig. 1(c). Therefore, conducting research on the Pu-pai Fang-Dovetail tenon joint with different degrees of looseness is of great significance for quantitatively assessing the damage state of the timber structures of ancient buildings.

The timber structures of ancient buildings have problems such as deformation, cracking, decay, tenon pull-out and damage by wood-boring insects during long-term use, which seriously affect the structural safety and protection and inheritance [16]. Meanwhile, the damage to timber structures often occurs at the joints, which in turn significantly affects the stability of the overall structure. Therefore, there is an urgent need to formulate effective protective measures for timber structures, especially for joints. The common reinforcement methods for joints in ancient buildings mainly include steel components [17,18,19], fiber cloth, dampers [20,21,22], et al. By comparing the above-mentioned reinforcement methods, it is found that the steel components assembled with flat steel, iron hooks and clips are complex and prone to cause significant damage to wood. However, CFRP reinforcement usually requires wrapping the entire mortise and tenon joint. Dampers are relatively expensive. These reinforcement methods are prone to causing damage to the cultural relics themselves and subsequent pollution, which is contrary to the principles of protection and restoration of cultural relic buildings, and the improvement in their mechanical properties is limited. He et al. [23] used wooden wedges to reinforce the straight tenons, which did not cause damage to the main body of the cultural relic building. The rotational stiffness and load-bearing capacity were significantly improved, but new deterioration risks may occur in the natural environment. Therefore, it is urgent to provide a reinforcement method that is convenient to implement, inexpensive, and does not cause deterioration to the main body of cultural relic buildings.

This paper presents a steel sleeve clamp hoop reinforcement device and conducts Quasi-static test tests on one intact specimen and three specimens with different loosening conditions. The working mechanism and seismic performance of reinforcing the Pu-pai Fang - dovetail tenon joint under different loosening degrees are systematically studied. In addition, a finite element model was established to conduct parametric analysis on the friction coefficient, bolt preload, and thickness of the Pu-pai Fang clamp hoop, and the influence of these factors on the seismic performance of the joints was discussed.



Fig. 1 Typical damage conditions of mortise-and-tenon joints in ancient timber structures

2. Joint characteristics and force mechanism

2.1. Joint characteristics

According to the records in the Song Dynasty's "Yingzao Fashi" [24], in the official-style buildings, the beam and column components were often connected by dovetail tenon joints. The column ends were successively stacked with Lu-Tou and Tou-Kung and other components upwards through Man-Tou tenon joint, forming an important anti-lateral system [25]. The structural features are shown in Fig. 2. The tenon has a structure that is wider on the outside and narrower on the inside, with the mortise being larger on the inside and smaller on the outside. The tenon is precisely embedded into the mortise of the column, forming an interlocking connection. The traditional dovetail tenon joint, as shown in Fig. 3(a), there is a Pu-pai Fang component designed above the dovetail tenon, as shown in Fig. 3(b). The upper part of the Pu-pai Fang components can be classified into dovetail tenon joints and Pu-pai Fang-dovetail tenon joints. The Pu-pai Fang-dovetail tenon joint suppresses rotational deformation through the enhanced stiffness provided by the common

parapet beam, and the geometric constraints formed effectively prevent the tenon from being pulled out. The Pu-pai Fang-dovetail tenon joint is widely used in traditional timber structure buildings.

2.2. Force mechanism

For the standardized description, forward loading is defined as the clockwise rotation of the beam, reducing the Angle between the beam and the column to below 90° , while reverse loading occurs during counterclockwise rotation, causing the Angle to exceed 90° , as shown in Fig. 4. Under forward loading, as shown in Fig. 4 (a), the beam is constrained and rubbed by the mortise during rotation, and the tenon is locally embedded and pressed, forming horizontal pressure and reverse resistance. The wood in the compressed area is crushed. The Pu-pai Fang rotates in the same direction as the beam. Due to the limiting effect of the mortise of the Man-Tou tenon joint, the Pu-pai Fang first generates reverse resistance and effectively restricts the rotation behavior of the beam. This behavior is not tying but eventually leads to the separation of the beam and the Pu-pai Fang. Under reverse loading, as shown in Fig. 4(b), during the rotation of the Pu-pai Fang, it first comes into contact with the column end and forms resistance and horizontal shear force. Meanwhile, the tenon forms an outward horizontal shear force on the mortise during the rotation process. This behavior also prevents the beam and the Pu-pai Fang from rotating synchronously, eventually resulting in the separation at the connection point. However, the further increase in the rotation of the joints causes the wood to enter the plastic deformation stage. During the mutual compression process between the tenon and the mortise, the tenon is gradually pulled out, resulting in cumulative plastic deformation of the tenon. Due to insufficient restraint capacity, the wood fibers at the mortise tear, as shown in Fig. 4(c). The Pu-pai Fang becomes the main load-bearing component during the process of restricting the structural rotation. The main occurrence of wood fiber tearing and end shear damage along the wood grain direction of the Pu-pai Fang.

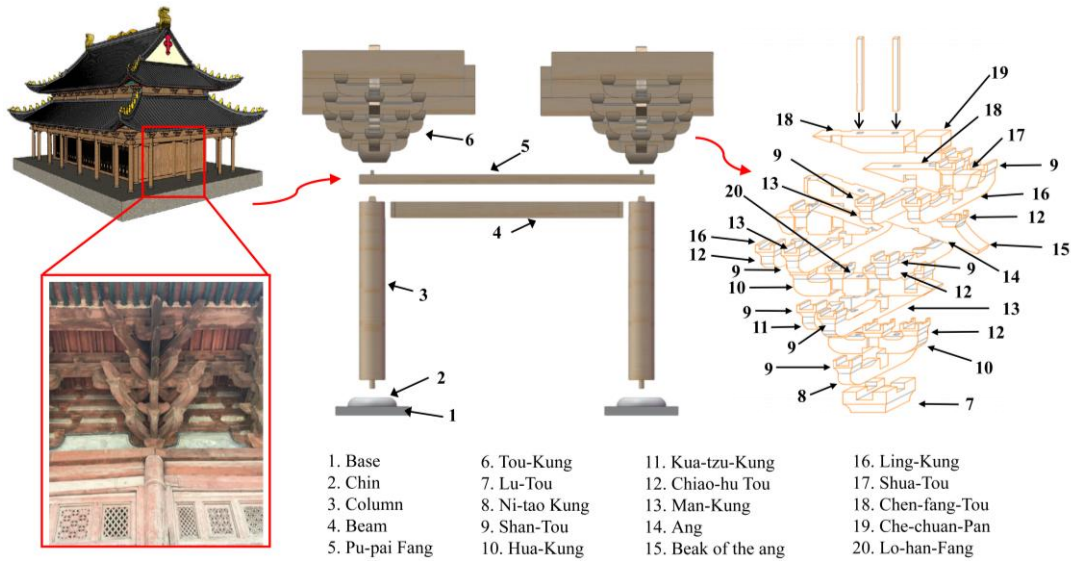


Fig. 2 Structural features of timber structures in ancient buildings

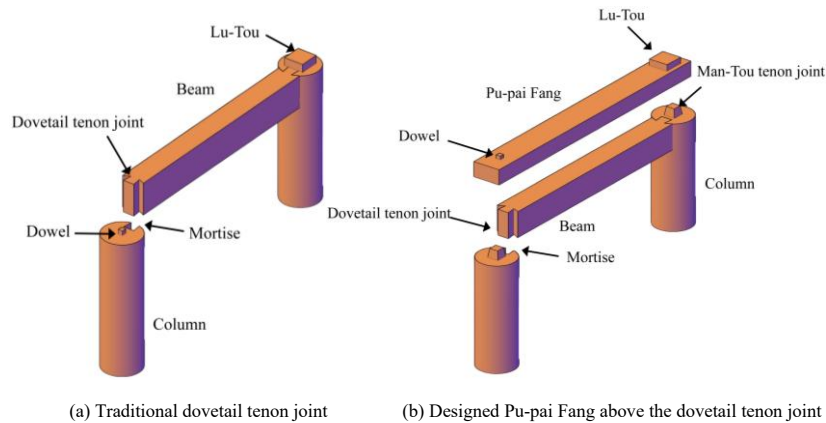


Fig. 3 Construction characteristics of Pu-pai Fang-dovetail tenon joints

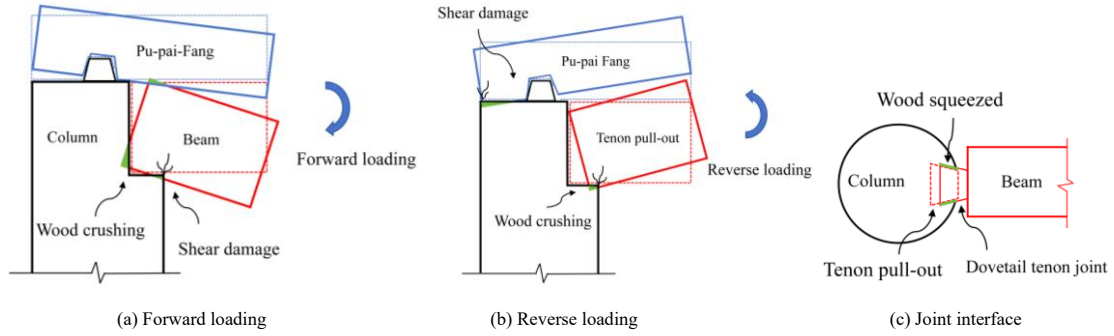


Fig. 4 Force mechanism of the Pu-pai Fang-dovetail tenon joint

3. Quasi-static test

3.1. Specimen design

This test mainly focuses on the use of a steel sleeve clamp hoop reinforcement device that is simple, portable, low-cost and will not cause secondary damage to the cultural relics buildings themselves. The purpose of the test is to research the seismic performance of the steel sleeve clamp hoop reinforcement of Pu-pai Fang - dovetail tenon joints with different degrees of looseness. The design of the joint reinforcement is shown in Fig. 5. According to the secondary wood size standards stipulated in the Song Dynasty architectural classic "Yingzao Fashi", the specimens were made at a scale of 1:3.52. The specific dimensions are shown in Fig. 6. The side view and top view of the Pu-pai Fang-dovetail tenon joint are shown in Fig. 6(a) and Fig. 6(b), respectively. Due to the fact that bolts have strong ultimate resistance and ductility [26]. The joints are fixed by a reinforcing device composed of beam-column support component, Pu-pai Fang clamp hoops and column clamp hoop. The beam-column support component and column clamp hoop are connected by movable bolts. The Pu-pai Fang clamp hoops are formed by welding rectangular clamps with bolts [27,28]. The Pu-pai Fang clamp hoops and beam-column support component are connected by welded bolts. The specific dimensions are shown in Fig. 7, Fig. 8 and Fig. 9. The side view, front view and top view of the beam-column support component are shown in Fig. 7(a), Fig. 7(b) and Fig. 7(c), Side view, front view and top view of Pu-pai Fang clamp hoop, as shown in Fig. 8(a), Fig. 8(b) and Fig. 8(c), Top view, front view and

side view of column clamp hoop, as shown in Fig. 9(a), Fig. 9(b) and Fig. 9(c). Due to the differences in the degree of shrinkage and aging of wood, the Pu-pai Fang - dovetail tenon joints became loose to varying degrees. The specimens were made by reducing the length of the tenon to simulate different degrees of loosening, and one intact joint and three specimens with different loose joints were fabricated (Table 1).

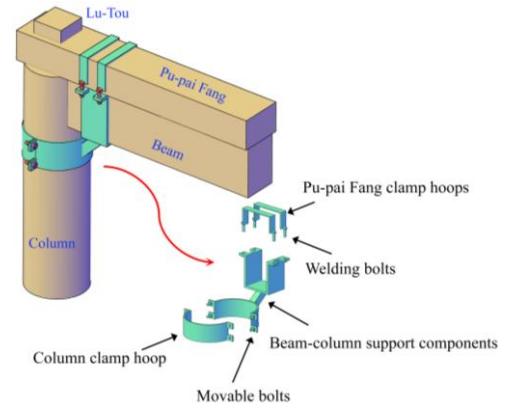


Fig. 5 Steel sleeve clamp hoops reinforce the Pu-pai Fang - dovetail tenon joint design

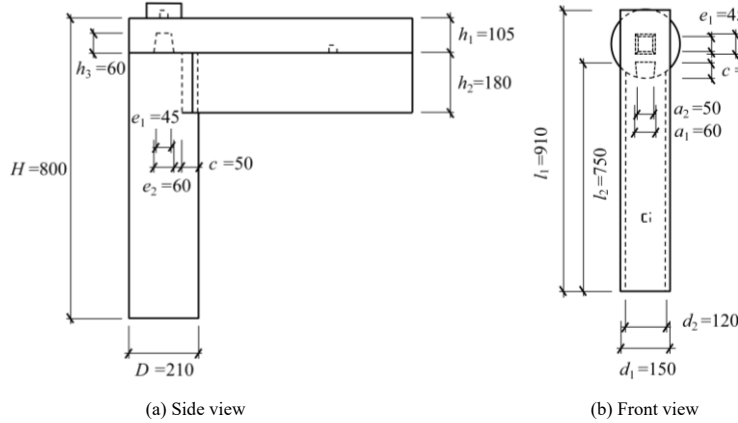


Fig. 6 Detailed dimensions of Pu-pai Fang-dovetail tenon joint

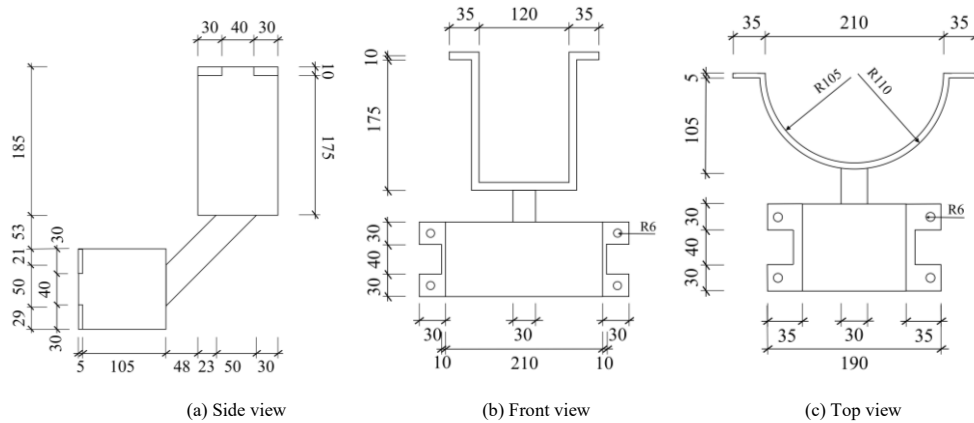


Fig. 7 Detailed dimensions of beam-column support component

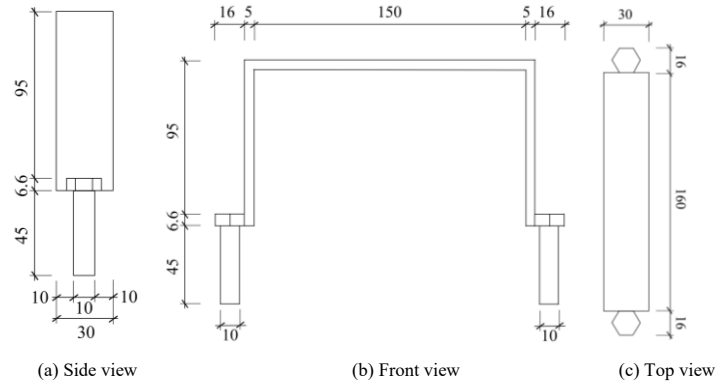


Fig. 8 Detailed dimensions of column clamp hoops

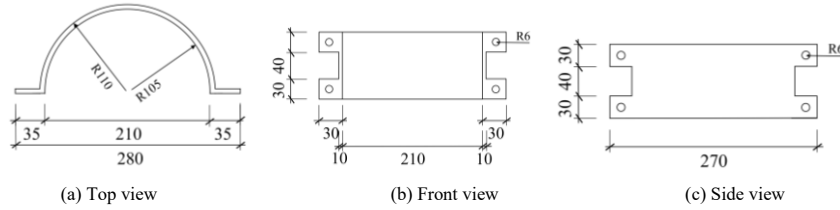


Fig. 9 Detailed dimensions of Pu-pai Fang clamp hoops

Table 1

The degree of looseness of the dovetail mortise and tenon joint

Specimen	Dovetail mortise & tenon size(mm)			Reduction of tenon length (mm)	Degrees of loosening(%)
	c	a ₁	a ₂		
JR1	50	0	—	0	—
JR2	45	5	10%	5	10%
JR3	40	10	20%	10	20%
JR4	35	15	30%	15	30%

3.2. Test scheme

3.2.1. Loading equipment

The test loading device is shown in Fig. 10. The wooden column is placed horizontally on the base platform. Limit covers are installed respectively in the middle and at the end of the column to prevent the specimen from overturning and twisting during the loading process. The loading point is set at a distance of 500 mm from the upper edge of the column, and the low-cycle repeated load is jointly applied to the beam and the Pu-pai Fang by the test system (MTS actuator). To simulate the axial compression load formed by the transfer of the self-weight of the frame layer to the wooden columns, jacks are arranged in the horizontal direction of the columns, and a constant load of 20 kN is pre-applied to the column ends. A stable axial pressure is maintained throughout the entire cyclic loading process.

3.2.2. Measurement solution

The axial pressure of the column is measured by the load sensor integrated in the hydraulic jack. The displacement and load at the beam end are recorded by the load sensor within the MTS system. The load and displacement data were obtained by the DH3816 data acquisition instrument. The layout of the displacement meter is detailed in Fig. 10. The joint rotation θ is calculated by the difference between displacement meters W1 and W4, and the tenon pull-out and extrusion amounts are measured by W2 and W3.

3.2.3. Loading system

The quasi-static test loading system is designed in accordance with ISO 16670 [29] and adopts the loading mode of staged displacement control. The ultimate displacement of the joint is set at 50 mm, and the displacement amplitude is determined based on the ultimate displacement obtained from the monotonic loading test of the component. Single cycle loading was carried out respectively at 1.25 % (0.625 mm), 2.5 % (1.25 mm), 5 % (2.5 mm), and 10 % (5 mm) of the set limit displacement. The three cycles of loading were carried out at 20 % (10 mm), 40 % (20 mm), 60 % (30 mm), 80 % (40 mm), 100 % (50 mm), and 120 % (60 mm) of the ultimate displacement respectively. The

loading system is shown in Fig. 11.

If the following situations occur during the test: obvious plastic deformation or shear tearing occurs at the tenon or mortise; The rotation Angle significantly exceeds the limit value of 1/30 stipulated in the "Technical Standard for Maintenance and Reinforcement of timber Structures of Ancient Buildings" [30]. When the load drops to 80% of the peak load, the test should stop loading.

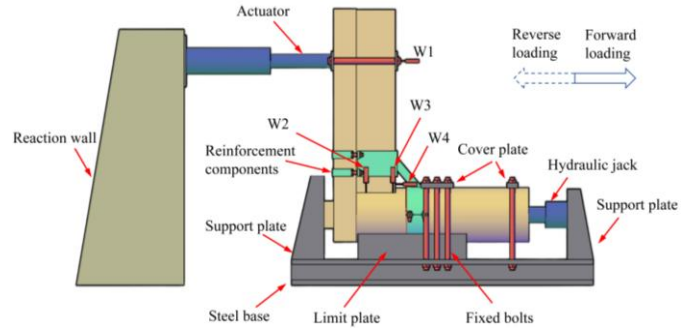


Fig. 10 Loading equipment

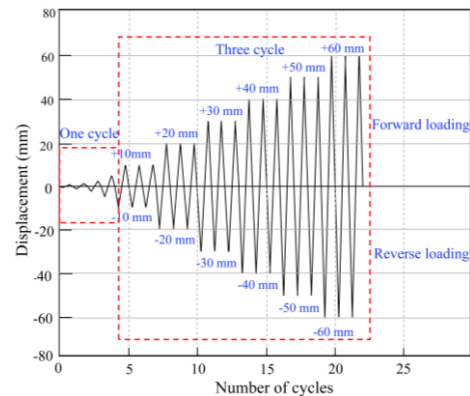


Fig. 11 Loading system

4. Test result and analysis

4.1. Test phenomenon

At the initial stage of loading, under the forward loading of JR1, the actuator drives the beam components to rotate, and the column and beam support components rotate synchronously, generating the sound of the column and beam support components being compacted. When reverse loading occurs, the tenon and the mortise generate extrusion friction along the contact surface, making a slight "creaking" sound of extrusion friction. The joint area remains in the elastic stage and no obvious plastic deformation has occurred.

When the rotation reaches 0.03rad, extrusion deformation occurs between the tenon and the mortise during forward loading, accompanied by the continuous sound of the column and beam supports being pushed and squeezed, as shown in Fig. 12(a). When loading in reverse, as the joints are constantly squeezed during the forward loading, only the squeezing and friction sounds of the wood being continuously pulled out can be heard during the reverse loading, while the clamps of the Pu-pai Fang are in an active state.

As the rotation continuously increases, the tenon constantly exhibits alternating pull-out and insertion behaviors during the loading process, and the wood fibers at the mortise are torn, as shown in Fig. 12 (b). At this time, when loading in reverse, the clamping members of the Pu-pai Fang and the Pu-pai Fang continuously restrain the rotational deformation by adjusting the Angle, as shown in Fig. 12 (c). But when a "bang bang" sound was heard from the

wood, it was speculated that the fibers of the Pu-pai Fang had broken during its rotation.

When the joint rotation reaches 0.12rad, the tenon is continuously pulled out, with a tenon pulling amount of 18 mm, as shown in Fig. 12 (d). At the mortise, the wood fibers are obviously lifted, resulting in significant deformation and damage. A continuous squeezing and stretching sound can be heard from the wood fibers of the Pu-pai Fang. During the loading process, the clamps of the Pu-pai Fang are in an active state, ensuring that the joints maintain the inherent seismic resistance and energy dissipation effect of the wood in the early stage of loading. In the later stage of loading, the clamps of the Pu-pai Fang can limit the free rotation of the joints through their own adjustment, significantly enhancing the tensile strength of the joints and reducing the pulling out of the tenons.

The test phenomena of JR2-JR4 are similar to those of the JR1 model, and the wood fibers at the joints all show severe warping. The difference lies in that no obvious sound of wood cracking occurred during the loading process. Meanwhile, for joints with different degrees of loosening, the pull-out amount in the later stage of loading was similar, but the pull-out rate of the tenon kept increasing as the degree of loosening increased.



(a) Initial loading stage (b) Onset of fiber tearing at the mortise (c) Progressive tenon pull-out under cyclic loading (d) Localized crushing & separation at joint interface

Fig. 12 Test phenomena of the Pu-pai Fang–dovetail tenon joint specimens

4.2. Analysis of seismic performance

4.2.1 Moment-rotation hysteretic curve

The Moment-Rotation hysteresis curves of specimens JR1-JR4 can be calculated respectively by Eqs. (1) and (2) :

$$M = FL \quad (1)$$

$$\theta = \frac{\Delta}{L} \quad (2)$$

where F is the horizontal load at the loading point of the MTS system, Δ is the horizontal displacement at the loading point, and L is the distance from the loading point to the surface of the column.

The moment-rotation hysteresis curves of JR1-JR4 are shown in Fig. 13(a), Fig. 13(b), Fig. 13(c) and Fig. 13(d), respectively. It is not difficult to find that the hysteresis curves of all joints all present an inverse Z-shaped feature and have obvious shrinkage characteristics, which is closely related to the material properties of timber structures. The hysteresis curve of the joint is relatively full at the initial stage of loading, and it has a good energy dissipation capacity. One reason is that during forward loading, the wood structure achieves structural energy dissipation through the compression and friction between components. On the other hand, during reverse loading, the beam-column support component has a large initial stiffness to limit the rotation of the joint. As the rotation of the joint increases, the interface sliding effect between the tenon and the mortise increases, and stiffness degradation and irreversible plastic deformation occur in the joint domain, with the hysteresis curve shrinking and narrowing. However, when the joint was loaded to the later stage, it did not enter the descent phase. This is because the Pu-pai Fang clamp hoops exerted a constraint on the reverse rotation of the joint, further increasing the overall load-bearing capacity of the structure.

By comparing the M_y and M_u of JR1-JR4 (Table 2), it is found that the yield bending moment and ultimate bending moment of JR2 are relatively large due to the overly tight installation process of the specimen. The remaining specimens show that the greater the degree of looseness of the joint, the greater the bending moment when entering the yield state. This is because the reduction of the tenon causes the Pu-pai Fang to need to provide greater structural resistance. The greater the degree of looseness of the joints, the greater the forward ultimate bending moment and the smaller the reverse ultimate bending moment. This is because when loading in the forward direction, the tenon pull-out rate increases, and the contact surface provided by the tenon to resist bending moment decreases, forcing the common beam to provide greater resistance to bending moment. However, when loading in the reverse direction, the tenon pull-out rate of JR1 is smaller, and the tenon can then provide greater resistance to bending moment.

Table 2

Comparison of characteristic values of the specimens

Specimen	Yield bending moment M_y (kN·m)	Ultimate bending moment M_u (kN·m)	Loading direction
JR1	1.09	12.42	Forward
	-4.58	-17.13	Reverse
JR2	4.01	16.51	Forward
	-6.58	-19.03	Reverse
JR3	3.00	13.06	Forward
	-4.23	-16.38	Reverse
JR4	2.72	14.99	Forward
	-6.54	-15.38	Reverse

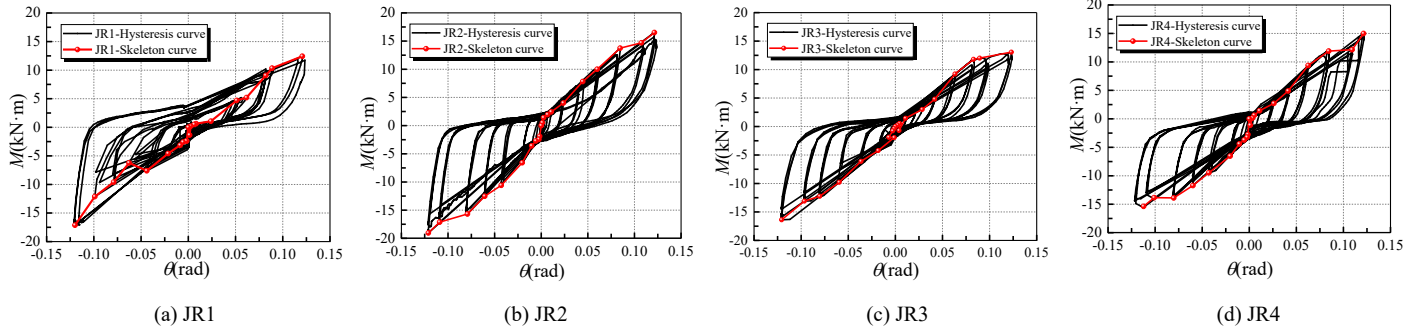


Fig. 13 Moment-rotation hysteresis curve of the joints

4.2.2. Moment-rotation skeleton curve

The envelope curves of the first maximum bending moment point in the moment-rotation curve under each stage displacement were taken as the skeleton curves, and a comparative analysis was conducted with the skeleton curves of the Pu-pai Fang - dovetail tenon joint in reference [13]. The comparison of the skeleton curves of JR1-JR4 and DJ1-DJ4 are shown in Fig. 14(a), Fig. 14(b), Fig. 14(c) and Fig. 14(d), respectively. The positive ultimate bending moment and negative ultimate bending moment of the intact joint JR1 have increased by 51.49% and 60.1% respectively. The positive ultimate bending moments and negative ultimate bending moments for the loose joints JR2-JR4 are respectively JR2: 96.58% and 89.39%. JR3: 50.89%, 164.58%;

JR4: 92.16%, 58.96%. Compared with DJ1-DJ4, the bending moment values of JR1-JR4 in the early stage of loading are similar. However, in the later stage of loading, the overall flexural bearing capacity of the structure is significantly improved. The forward and reverse ultimate flexural bearing capacities of the reinforced specimens with different degrees of loosening exceed 50% compared with the unreinforced specimens. It indicates that the steel sleeve clamp hoops reinforcement can fully exert the energy dissipation and vibration reduction effect of the timber structure in the early stage of loading, and in the later stage of loading, the steel sleeve clamp further enhances the overall seismic performance of the structure.

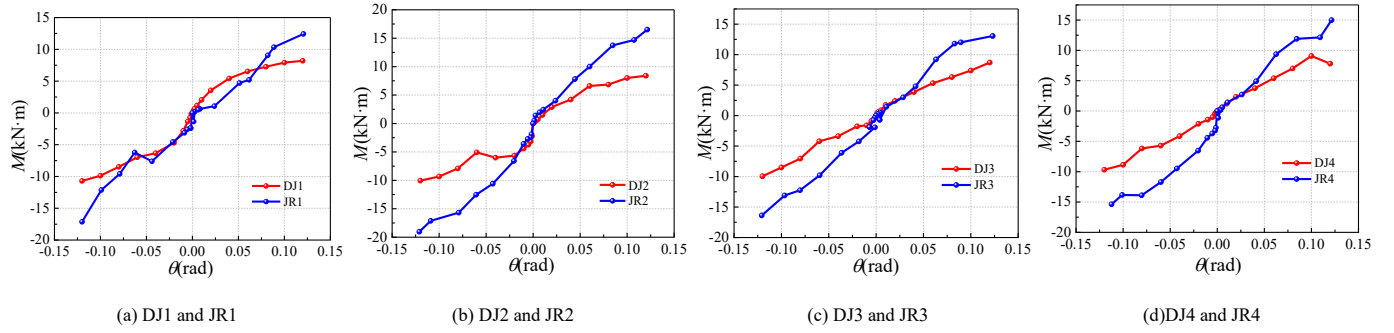


Fig. 14 Moment-rotation skeleton curve of specimens

4.2.3. Energy dissipation capacity

The equivalent viscous damping coefficient h_e directly reflects the energy dissipation capacity of the joint and can be calculated according to Eq. (3):

$$h_e = \frac{1}{2\pi} \frac{S_{(\Delta ABC + \Delta CDA)}}{S_{(\Delta EDO + \Delta FBO)}} \quad (3)$$

where $S_{(\Delta ABC + \Delta CDA)}$ represents the area enclosed by the shaded portion of the hysteresis loop (Fig. 15), and $S_{(\Delta EDO + \Delta FBO)}$ denotes the triangular area corresponding to the hysteresis curve.

The equivalent viscous damping coefficient curves are shown in Fig. 15. The energy dissipation capacity of all specimens evolves similarly, initially rising rapidly to a peak value, followed by a gradual decline until reaching a stable state. However, when the rotation reaches 0.01 rad, h_e drops significantly. This is because energy dissipation occurs through compression and friction between components during rotation; as the gap between mortise and tenon gradually increases, the available free movement space expands, causing the joint to enter a loose state, thus leading to a progressive reduction in energy dissipation capacity. Subsequently, h_e continues to decrease and eventually stabilizes around 0.15. Comparing JR1-JR4 with DJ1-DJ4, it is observed that both types of joints exhibit similar trends in h_e , but the energy dissipation capacity of JR1-JR4 is superior to that of DJ1-DJ4, confirming the effectiveness of steel sleeve clamp hoops confinement in enhancing energy dissipation performance.

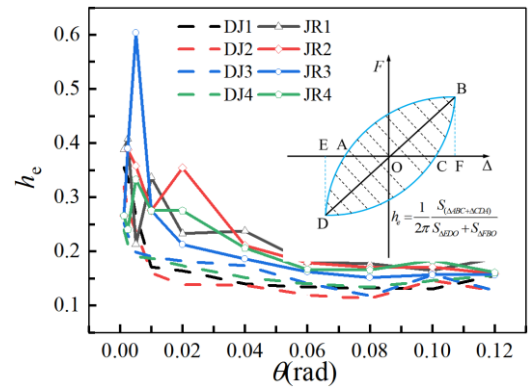


Fig. 15 Equivalent viscous damping coefficient of the joints

4.2.4. Stiffness degradation

The variation of secant stiffness at different deformation levels can reflect stiffness degradation. The secant stiffness K_i at each deformation level can be calculated according to Eq. (4):

$$K_i = \frac{|+M_i| + |-M_i|}{|+\theta_i| + |-\theta_i|} \quad (4)$$

where M_i is the peak bending moment of the first cycle under the i -th load level; θ_i is the rotation corresponding to M_i .

The stiffness degradation curve of the joint is shown in Fig. 16. During forward loading, the overall variation trends of JR1-JR4 are slightly different.

Generally, the initial stiffness of the joints rapidly deteriorates, then slowly increases and tends to a stable state to an average of $117.12 \text{ kN}\cdot\text{m}\cdot\text{rad}^{-1}$. JR1 has a relatively high resistance due to the resistance of the beam-column support components. Subsequently, during the rotation of the beam components, they are embedded with the beam-column support components, causing the material to soften and a large movable gap to appear at the contact interface. As a result, the stiffness rapidly decreases, among which the initial stiffness of JR1 deteriorates most obviously. The greater the degree of looseness of the joint, the larger the initial gap it already has, so the initial stiffness degradation is not obvious. This further indicates that steel sleeve clamp hoops are more suitable for reinforcing loose joints and can still maintain a certain initial stiffness at the joints.

When reverse loading is applied, the stiffness degradation trend of JR1-JR4 is generally consistent. The overall manifestation is that the initial stiffness of the nodes rapidly deteriorates, and then the stiffness degradation tends to stabilize to an average of $143.15 \text{ kN}\cdot\text{m}\cdot\text{rad}^{-1}$. This is because the Pu-pai Fang clamp hoops and beam-column supports form an active connection, and the initial loading does not interfere with the structure. To maximize the energy dissipation and shock absorption effect of the timber structure, the stiffness is kept stable in the later stage of loading by relying on the constraints of the Pu-pai Fang clamp hoops.

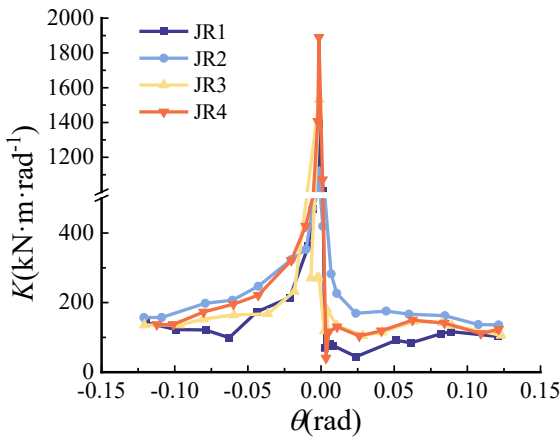


Fig. 16 Stiffness degradation curve of the joints

4.2.5. Deformation ability

The "GB 50165-2020 Technical Standard for Maintenance and Reinforcement of timber Structures in Ancient Buildings" clearly stipulates that the limit value of the displacement Angle at the beam-column joints of timber structures is $1/30$. During the test loading process of JR1-JR4, the maximum rotation all reached 0.12 rad , and the joints maintained good bearing capacity. Their deformation capacity significantly exceeded the specification limit, fully verifying that this reinforcement method has excellent anti-deformation ability.

Fig. 17 shows the curve graph of the joint rotation and the tenon pull-out amount (γ). The average maximum tenon pull-out amount of JR1-JR4 is only 20.24 mm , and the tenon pull-out rates are 37.14% , 50.74% , 51.44% and 54.25% respectively. The tenon pull-out rate of JR1 is the lowest, indicating that the tenoning rate of the joint increases with the increase of the degree of loosening. By comparing the tenon pull-out rates of JR1-JR4 with those of DJ1-DJ4, it is not difficult to find that the overall tenon pull-out rate of JR1-JR4 is much lower than that of DJ1-DJ4, reducing by 53.51% , 13.41% , 46.89% and 46.25% respectively. Except for the fact that DJ2 is installed too tightly, The tenon extraction rates of the remaining joints can all be significantly reduced. During the reverse loading process of the joint, at the initial stage of loading, the joint is used for restraint, and energy is consumed through the compression and friction between the joint and the tenon. In the middle stage of loading, the Pu-pai Fang can provide resistance to bending moment for the rotation of the beam component. As the wood at the joint and the Pu-pai Fang is torn, the Pu-pai clamp hoop takes effect to achieve the function of constraining the rotation of the joint. At the same time, This also indicates that the steel sleeve clamp reinforcement has a significant effect on restricting the tenon pull-out.

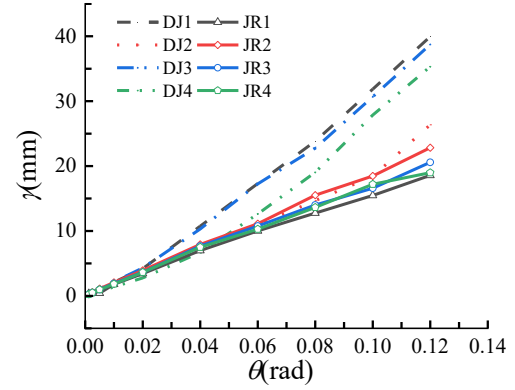


Fig. 17 Curves showing the relationship between joint rotation & tenon pull-out amount

5. Establishment of the finite element models

5.1. Model establishment

The finite element model (FEM) material was made of Masson pine. The material property parameters were obtained through tests. Its physical and mechanical properties were determined and completed by the members of the same research group [31] in accordance with the small sample testing methods stipulated in the Chinese National standard "Standard Test Methods for Physical and Mechanical Properties of Wood" [32-34]. The mechanical property parameters of this batch of Masson pine are shown in Table 3.

The model is established using the C3D8R type 8-node entity unit in ABAQUS, as shown in Fig. 18. As wood is an orthotropic material, the compression along the grain and transverse grain is simplified to a double-fold line model, and the tension is simplified to a single-fold line model. The elastic modulus of anisotropic materials in the elastic stage is defined using engineering constants. During the plastic stage, the yield stress of the material in different directions is determined by combining the potential function in ABAQUS with the Hill yield criterion. Steel and bolts are simulated as ideal elastoplastic materials. During the assembly process, assembly shall be carried out in accordance with the test design. A 2 mm contact gap tolerance shall be reserved between the Pu-pai Fang and the Pu-pai Fang clamp hoops during the test process. The contact attributes between each component of the joint are defined through the interaction of surface-to-surface contact. Normal contact adopts "hard" contact to allow interface separation. The tangential behavior adopts a penalty function friction model. The friction coefficients between woods and between woods and steel are set at 0.3 , and the friction between steel is set at 0.15 . The model loading mode and boundary constraint conditions are consistent with the test conditions. The upper and lower ends of the column are respectively set as hinged and fixed connections, and the force application point is set at a position 500 mm away from the column surface. The boundary conditions are applied by coupling constraints through the initial analysis step. The test is divided into 4 analysis steps in total. It includes applying preload to the bolts, fixing the bolt length, applying axial load at the column end and low-cycle repeated load at the loading point, and setting the preload guarantee load $F_p=25500 \text{ N}$ for the bolts [35].

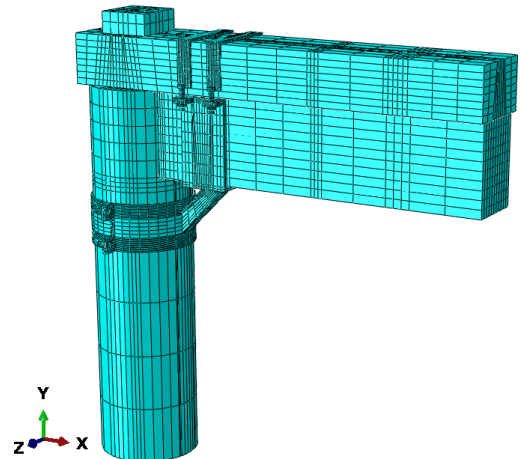


Fig. 18 Meshing details of finite element model

Table 3
Mechanical properties of *Pinus massoniana* Lamb

Parameter	Adopted value in FE model		
Density (kg/m ³)	$\rho=542$		
Moisture content (%)	$W=17$		
Elasticity modulus (MPa)	$E_L=19411$	$E_R=1465$	$E_T=762$
Poisson ratio	$\mu_{LR}=0.28$	$\mu_{LT}=0.48$	$\mu_{RT}=0.62$
Shear modulus (MPa)	$G_{LR}=1456$	$G_{LT}=1165$	$G_{RT}=349$
Yield stress (MPa)	$f_{tL}=120.9$	$f_{cL}=31.08$	$f_{cR}=3.62$
Yield stress ratio	$R_{11}=1$	$R_{22}=0.12$	$R_{33}=0.12$
	$R_{12}=0.56$	$R_{13}=0.56$	$R_{23}=0.13$

Note: ρ and W denote the density and moisture content; L, R, and T denote the longitudinal, radial, and tangential directions of wood grain, respectively; μ is the Poisson ratio; E is the elastic modulus; G is the shear modulus; f_{tL} is the tensile strength parallel to the grain; f_{cL} is the compressive strength parallel to the grain; f_{cR} is the compressive strength perpendicular to the grain.

5.2. Model verification

The stress distributions of the finite element model failure modes under forward loading and reverse loading are shown in Fig. 19(a) and Fig. 19(b) respectively. The finite element model and the test results were compared. The hysteresis curves of JR1-JR4 are shown in Fig. 20(a), Fig. 20(b), Fig. 20(c), and Fig. 20(d). Except for JR2 which was too tight during the test installation process, the comparison results at M_E and M_T of the other specimens are in good agreement (Table 4), and the error ratio between the test results and the finite element prediction results is all less than 20%. It indicates that the finite element results are in good consistency with the experiments. The hysteretic curves of the test specimens are fuller than those of the finite element model. This is because during the test, the wood fibers at the common beam and the joint of

the specimen successively cracked and broke, the movable gap of the tenon increased, and the sliding effect of the contact interface at the joint increased during the reciprocating loading process.

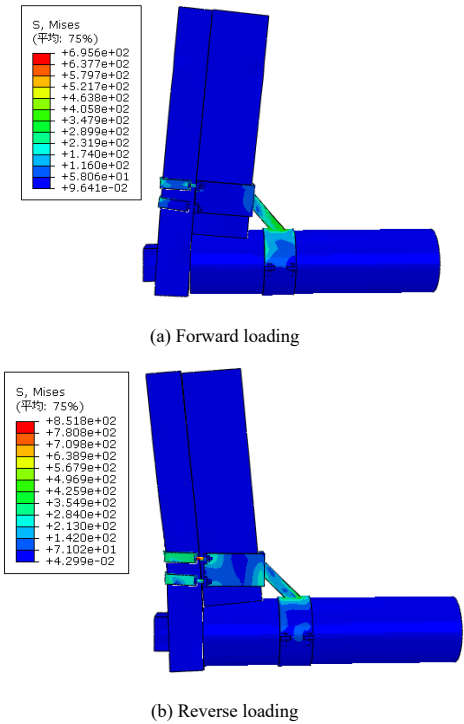


Fig. 19 Stress contour with the failure modes

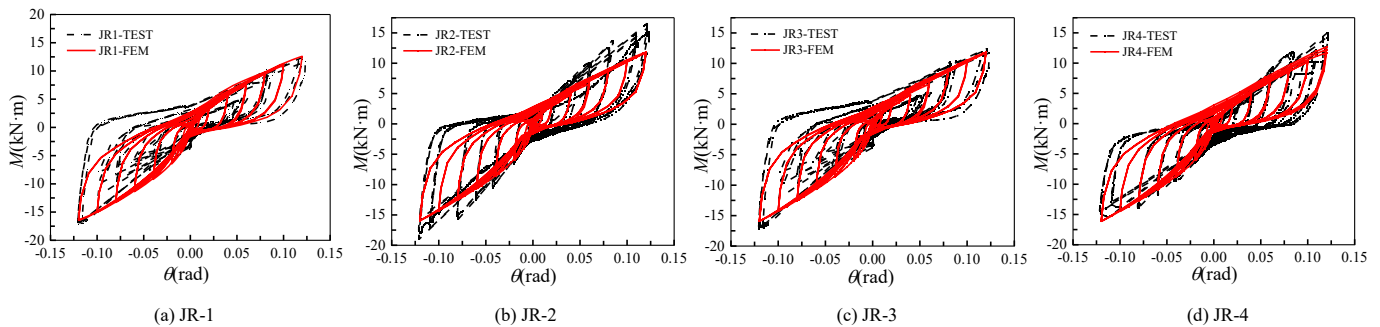


Fig. 20 Comparison between the finite element model and test results

Table 4
Comparison between experimental and FE results

Specimen	M_E (kN·m)	M_T (kN·m)	Error rate (%)
JR1	-16.43	-17.13	4.22
	12.59	12.42	1.35
JR2	-15.93	-19.03	16.31
	11.82	16.51	28.41
JR3	-15.93	-16.38	2.73
	11.82	9.47	9.47
JR4	-16.14	-15.38	4.72
	12.65	14.99	15.63

5.3. Parameters influence analysis

5.3.1. Friction coefficient

The friction coefficients of $\mu=0.1, 0.3, 0.5$ and 0.7 were selected for analysis respectively, as shown in Fig. 21. When subjected to reverse loading, the flexural bearing capacity of the joint increased from $14.91 \text{ kN}\cdot\text{m}$ to $18.94 \text{ kN}\cdot\text{m}$, an increase of 27.04%. This indicates that the flexural bearing capacity of the joint increases with the increase of the friction coefficient. During forward

loading, the high friction characteristic can provide stiffness at the initial stage of loading, but it may cause brittle failure of the structure in the later stage of loading, reducing the seismic toughness. Meanwhile, the high friction characteristic is contrary to the principle of using Pu-pai Fang clamp hoops for movable reinforcement. However, when the friction coefficient is within the range of 0.3 to 0.5, the structure strikes a balance between strength and ductility, improving rotational stiffness. Enhancing the moment bearing capacity can effectively achieve energy dissipation. Therefore, it is recommended that the friction coefficient be selected as 0.3 to 0.5, which is more appropriate.

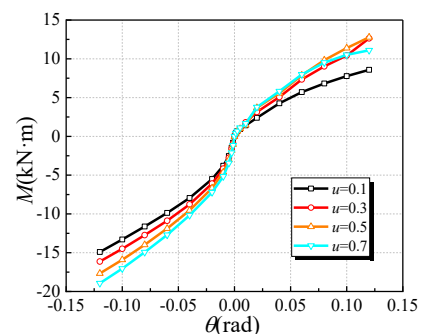


Fig. 21 Friction coefficients of joints

5.3.2. Bolt preload

The preload forces of the welding bolts were selected as $f_1=0.25 F_p$, $f_2=0.5 F_p$, $f_3=0.75 F_p$ and $f_4=F_p$ respectively, as shown in **Fig. 22**. It can be seen that the preload force of the welding bolts has little effect on the bearing capacity under reverse loading, while under forward loading, the flexural bearing capacity increases with the increase of the preload force. The increase was from 12.27 kN·m to 12.65 kN·m, representing only a 3.07 % increase. This indicates that applying preload to bolts is an important step in the reinforcement of steel sleeve clamp hoops. However, the magnitude of the preload has a relatively small impact on the flexural bearing capacity of the structure. This also suggests that the key point of this reinforcement device lies in reducing intervention in the early stage of loading. This purpose of providing protective effects on the structure in the later stage of loading is consistent.

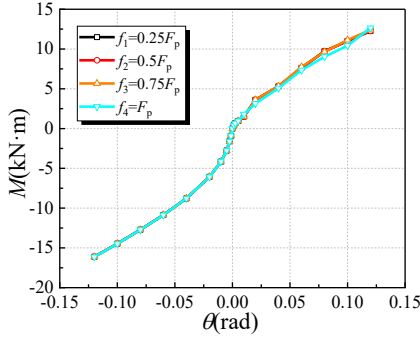


Fig. 22 Bolt preload of the joints

5.3.3. Pu-pai Fang Clamp hoop thickness

The thicknesses h of the Pu-pai Fang clamp hoops was selected as 3 mm, 5 mm, 7 mm and 9 mm, as shown in **Fig. 23**. When reverse loading was applied, the flexural bearing capacities of the models with $h=3$ mm, $h=5$ mm, and $h=7$ mm were similar. However, when the thickness increased to 9 mm, the flexural bearing capacity of the models decreased from 16.14 kN m to 13.32 kN m, a reduction of 17.4 %. When subjected to forward loading, the flexural bearing capacities of the models $h=5$ mm and $h=7$ mm are 12.40 kN·m and 12.28 kN·m respectively. These flexural bearing capacities are significantly better than those of the models $h=3$ mm and $h=9$ mm, indicating that a thickness range of 5-7 mm is more suitable for the clamp hoop parts of the Pu-pai Fang.

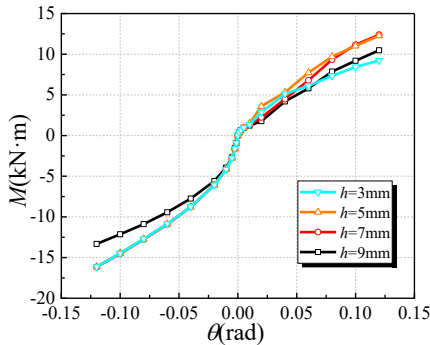


Fig. 23 Pu-pai Fang clamp hoop thickness of joints

6. Conclusions

This study investigated the seismic performance of Pu-pai Fang–dovetail tenon joints with different degrees of looseness reinforced by steel sleeve clamp hoops through quasi-static testing and finite element (FE) simulation. The main conclusions are summarized as follows:

(1) Due to the continuous alternating pull-out and insertion of the intact specimens, the wood fibers at the mortise and the Pu-pai Fang were torn. In the later stage of loading, the Angle of the Pu-pai Fang clamp hoops was adjusted to restrict the free rotation of the joints, enhancing the tensile pull-out capacity of the joints and reducing the pull-out of the tenons. The damage phenomenon of the loose joints was similar to that of the intact specimens, and the pull-out amount of the tenons was also similar. However, the tenon pull-out rate keeps increasing as the degree of loosening increases.

(2) The hysteresis curve of the joint shows an inverse Z-shaped feature. There is a significant shrinkage characteristic in the later stage of loading. However, the steel sleeve clamp hoop exerts a constraint on the reverse rotation of the joint, further increasing the flexural bearing capacity, and no decline stage

occurs. The greater the degree of joint loosening, the greater the forward ultimate bending moment and the smaller the reverse ultimate bending moment. The forward and reverse ultimate flexural bearing capacities of the reinforced specimens exceed 50% compared with those of the unreinforced specimens.

(3) The energy consumption capacity characteristic of the joint is characterized by a rapid increase to the peak in the initial stage, followed by a slow decline and a gradual stabilization. The stiffness degradation characteristics of the joint are manifested as a rapid initial stiffness degradation, followed by a slow increase and a tendency towards a stable state. The average maximum tenon extraction amount of the joints was only 20.24 mm, and the tenon extraction rates were 37.14 %, 50.74 %, 51.44 % and 54.25 % respectively. Compared with the unreinforced joints, the tenon extraction rates decreased by 53.51 %, 13.41 %, 46.89 % and 46.25 % respectively. The main reason lies in the fact that the steel sleeve clamp reinforcement maintains the energy dissipation of the wooden structure in the early stage of loading and constrains the energy dissipation in the later stage of loading. (4) It is recommended that the coefficient of friction be set within the range of 0.3 to 0.5, and the thickness of the Pu-pai Fang clamp hoop be set within the range of 5 to 7 mm. This can balance the structural strength and ductility, improve the rotational stiffness, enhance the moment bearing capacity, and effectively achieve energy dissipation. Applying preload to bolts has no obvious effect on the reinforcement of steel sleeve clamp hoops.

Acknowledgements

The work was financially supported by the grant from the Basic and Applied Basic Research Foundation of Guangdong Province (Grant No. 2025A1515010443) and the Scientific and Technological Achievements Transformation Project of the Scientific Research Institutes of Science and Technology Department of Sichuan Province (Grant No. 2024ZHYS0008).

References

- [1] Pan Y., An R.B. and You W.L., "A review on mechanical performance of mortise-tenon joints in traditional timber structures", *Journal of Building Structures*, 45(07): 226-241, 2024.
- [2] Wu Y.J., Wang L., Lin H.S., Zhang L.P. and Xie Q.F., "Effect of shear force on the rotational performance of straight mortise-tenon joints", *Structures*, 44: 501-10, 2020.
- [3] Wang J., Cui Z.H., Yu L., Xu R.W. and Yang Q.S., "Analysis of the seismic behavior of traditional Chinese timber structures in the tang dynasty", *Structures*, 41: 447-62, 2022.
- [4] Wang S.Y., Guo T., Deng H. and Zhou H.B., "Study on seismic performance of straight Tenon-type joints in Chuan-dou style timber structure", *Chinese Journal of Wood Science and Technology*, 36(01): 57-62, 2022.
- [5] Wang Q.L., Ye J.H. and Su M.Z., "Cyclic behavior and shear capacity of a single-frame modular steel structure-cold-formed steel wall with semi rigid connections", *Advanced Steel Construction*, 21(4):304-315, 2025.
- [6] Bai F.Y., Fan Z.K., Xue J.Y., Wu C.W., Hu C.M. and Li J.X., "Experimental study on seismic performance and deformation damage of loose dovetail-tenon joints in ancient timber structures", *Structures*, 54: 541-555, 2023.
- [7] Zhang J., Li Y.H., Li Y.J., Xu W.T. and Yao L.H., "Research on Stress Analysis of Dovetail Joints of Timber Building", *China Forest Products Industry*, 58(03): 21-26, 2021.
- [8] Yu P., Li T.Y., Yang Q.S., Meng X.J., Shi X.W. and Chen J.Y., "Analytical model and rotational performances of dovetail mortise-tenon connection at the column head of traditional wooden frame", *Structures*, 57:105256, 2023.
- [9] Zhang B.Z., Xie Q.F., Li S.Y., Zhang L.P. and Wu Y.J., "Effects of gaps on the rotational performance of traditional straight mortise-tenon joints", *Engineering Structures*, 260: 114231, 2022.
- [10] Bai F.Y., Fan Z.K., Xue J.Y., Wu C.W., Hu C.M. and Li J.X., "Experimental study on seismic performance and deformation damage of loose dovetail-tenon joints in ancient timber structures", *Structures*, 54: 541-55, 2023.
- [11] Bai F.Y., Dong F., Sui Y., Xue J.Y., Wu C.W., Song D.J. and Hu C.M., "Experimental study on fracture damage and seismic performance of loose through-tenon joints in ancient timber structures", *Construction and Building Materials*, 394: 132228, 2023.
- [12] He J.X., Yu P., Wang J., Yang Q.S., Han M. and Xie L.L., "Theoretical model of bending moment for the penetrated mortise-tenon joint involving gaps in traditional timber structure", *Journal of Building Engineering*, 42, 103102, 2021.
- [13] Chu Y.P., Tan S.L., Gu S. and Wang S.Q., "Seismic performance of Pu-Pai Fang- Dovetail mortise and tenon joints at different degrees of looseness: experimental tests and theoretical analysis", *International journal of architectural heritage*, 1-24, 2025.
- [14] Wu Y.J., Lin H.S., Xie Q.F., Wang L. and Zhang L.P., "Influence of Pu-pai Fang on lateral performance of columns in ancient timber structures", *Journal of Building Structures*, 44(11): 170-180, 2023.
- [15] Chu Y.P., Li Q., Zeng M.Q., Wang J.H. and Gu S., "Seismic performance of cross hoop-head mortise and tenon joints under different degrees of looseness", *Structures*, 81, 110268, 2025.
- [16] Dong H.Y., Jin Y.J., Cao W.L., Liang X., Liu S.Y., "Seismic performance of wooden straight-tenon joints reinforced with lightweight steel members", *Engineering Structures*, 282, 115825, 2023.
- [17] Xue J.Y., Wu C.W., Zhang X.C. and Zhang Y.T., "Experimental study on seismic behavior of mortise-tenon joints reinforced with shape memory alloy", *Engineering Structures* 218: 110839, 2020.
- [18] Xue J.Y., Wu C.W., Zhang X.C. and Qi Z.D., "Experimental and numerical study of mortise-tenon joints reinforced with innovative friction damper", *Engineering Structures*, 230: 111701, 2021.
- [19] Chen J., Wang W., Ding F.X., Xiang P., Yu Y.J., Liu X.M., Xu F., Yang C.Q. and Long S.G., "Behavior of an advanced bolted shear connector in prefabricated steel-concrete composite beams", *Materials*, 12(18): 2958, 2019.

- [20] Xie Q.F., Zhang L.P., Zhou W.J., Wang L. and Zhou. T.G., "Cyclical behavior of timber mortise-tenon joints strengthened with shape memory alloy: experiments and moment-rotation model". *International journal of architectural heritage*, 13(8): 1209-22, 2018.
- [21] Latour M., Piluso V. and Rizzano. G., "Experimental analysis of beam-to-column joints equipped with sprayed aluminium friction dampers". *Journal of Constructional Steel Research*, 146: 33-48, 2018.
- [22] Tan J.P., Pan D.G. and Fu X.Q., "Seismic Performance Evaluation of Steel Frames with Dampers Added on Existing Structures", *Advanced Steel Construction*, 18 (2) 552-560, 2022.
- [23] He J.X., Liu K., Xie L.L., Wang. X.J., Yang W.Y. and Zhao W.L., Experimental and numerical studies on influences of wedge reinforcement on seismic performance of loose penetrated mortise-tenon joints, *Journal of Building Engineering*, 91, 109610, 2024.
- [24] Li Jie. *Yingzao fashi (standards and Models for Architecture)*. Royal. Kaifeng: Press; 1950.
- [25] Yu P., Yang Q.S., Li T.Y., Meng X.J., Shi X.W. and Chen. J.Y., "Quantitative contribution assessment of joints and components to the load-carrying capacity of ancient timber frame", *Structures*, 59, 105739, 2024.
- [26] Qin Z.C., Moriyama H., Yamaguchi T., Shigeishi M., Xing Y.Y. and Hashimoto. A., "Ultimate strength, ductility, and failure mode of high-strength frictional bolted joints made of", *Advanced Steel Construction*. 19, 117-22, 2023.
- [27] Gan D., Tang H.X., Li W., Zhou Z., Zhou X.H. and Chen. Z.M., "Analysis and design of axial analysis and design of axially loaded square CFST column to RC beam joints stiffened by diagonal ribs", *Advanced Steel Construction*, 19(1):38-45, 2023.
- [28] Jakovljević I., Spremić M. and Marković. Z., "Shear behaviour of demountable connections with bolts and headed studs", *Advanced Steel Construction*, 19(4): 341-352, 2023.
- [29] ISO-16670. Timber structure-Joints made with mechanical fasteners-Quasi-static. reversed cyclic test method. International Organization for Standard; 2003.
- [30] GB 50165-2020. Technical standard for maintenance and reinforcement of ancient timber structures, Beijing, China, 2020.
- [31] Chu Y.P., Shi B.X. and Gong. Y.D., "Experimental study on compressive behavior of intermediate slender timber columns with local damage and the retrofitting techniques for the damaged columns", *Structures*, 46, 1709-1725, 2022.
- [32] GB/T 1927.1-2021. Test methods for physical and mechanical properties of small clear wood specimens-Part 9: determination of bending strength, Beijing, China, 2021.
- [33] GB/T 1927.1-2021. Test methods for physical and mechanical properties of small clear wood specimens-Part 10: determination of bending modulus of elasticity, Beijing, China; 2021.
- [34] GB/T 1927.1-2021. Test methods for physical and mechanical properties of small clear wood specimens-Part 12: determination of radial compressive strength. Beijing, China; 2021.
- [35] GB/T 3098.1-2010. Mechanical properties of fasteners-Bolts, screws and studs. Beijing, China, 2010.

EXPERIMENTAL AND NUMERICAL STUDY ON CONNECTION JOINTS APPLIED TO AUTOMATIC CONSTRUCTION DEVICE

Xian-Feng Wang¹, Qian-Xi Zhang¹, Zhi-Peng Fu¹, Wei-Lun Wang^{1,*}, Jian Liu¹, Xiao-Gang Zhang¹ and Shan-Bai Dong²

¹ Guangdong Provincial Key Laboratory of Durability for Marine Civil Engineering, State Key Laboratory of Intelligent Construction and Healthy Operation and Maintenance of Deep Underground Engineering, College of Civil and Transportation Engineering, Shenzhen University, Shenzhen 518060, China

² Excellence Group Co. Ltd. Shenzhen 518052, China

* (Corresponding author: E-mail address: wang_weilun@hotmail.com)

ABSTRACT

To meet the demands of intelligent and green construction, the development of automatic construction devices is of practical significance. In this study, a novel connection joint was designed for its supporting column and investigated experimentally and numerically based on static load tests, which were carried out on five joint specimens with different axial pressure ratios, flange thicknesses, and insertion depths. It was found that the failure of all specimens was due to the bolted connection, especially the failure of the thread. However, no apparent damage was found on the tube wall of the joint, indicating that the damage mainly occurred at the bolt connection. Additionally, a finite element analysis (FEA) model was established to investigate the joint's failure process, revealing intricate stress and strain conditions under loading. Notably, the highest stress and strain were identified at the central bolt, indicating its critical role in joint failure. The parameters of tube wall thickness and flange outside diameter in the finite element model were analyzed, and the results showed that 10 mm wall thickness and 252 mm outer diameter of flange were the best choices. This study may provide an experimental and numerical basis for the practical application of automatic construction devices.

ARTICLE HISTORY

Received: 21 September 2024
Revised: 22 February 2025
Accepted: 22 February 2025

KEYWORDS

Automatic construction device;
Steel joint;
Static load tests;
Finite element analysis;
Moment-rotation relationship

Copyright © 2025 by The Hong Kong Institute of Steel Construction. All rights reserved.

1. Introduction

Currently, the civil construction industry is facing various challenges, including substandard construction site conditions, high hazards, environmental pollution, and elevated construction costs [1-4]. Increasing automation in the construction process is a vital strategy to address these issues. The development of automation and intelligent technologies has significantly changed the construction industry [5-9]. Various construction robots, such as wheeled robots, wall-building robots, and welding robots, have been invented by researchers. Advanced automation devices have played a critical role in protecting workers from hazardous and physically demanding tasks [10] while markedly increasing productivity [11]. However, these robots are generally limited to specific tasks within the construction process. To further enhance automation across the entire construction process, improve working conditions, and reduce costs, highly integrated automated construction devices have been progressively applied by various countries since the late 20th century [12-17]. These devices aim to increase the overall automation level of the construction process.

In the last century, an automated construction device known as Big Canopy was developed in Japan [13], which was used in the construction of concrete buildings. This device utilized precast concrete (PC) components installed using remote control, significantly reducing the required labor force. Bar codes marked on the components enabled precise monitoring of their positions during construction, significantly improving construction efficiency. In recent years, several automated construction devices have been independently developed in China [17, 18]. These devices predominantly use cast-in-situ reinforced concrete to ensure structural stability and safety. Material transport, formwork operations, and concrete pouring are all controlled by computer programs. This high level of automation has significantly enhanced construction efficiency and reduced costs. However, deficiencies remain in the design of the connection joints of the support columns in current automated construction devices. These joints do not adequately support the continuous lifting of support columns as building height increases. Additionally, the connection process of the support columns presents many inconveniences, resulting in low installation efficiency. Given the existing issues of the support column device in the current automatic construction device, a new type of joint has been designed in this paper, which aims to enhance the automation level of the automatic construction device.

There have been numerous researches on beam-column connection joints, which share similarities with the support column connection joints in automatic construction devices in terms of structural form and mechanical characteristics. For steel beam-column joints, researchers have studied different configurations of reinforced panels and flange panels to identify joints with enhanced energy consumption [19-23]. Some researchers have introduced replaceable energy dissipation devices at beam-column joints to enable reparability in case of joint damage. Test results have shown that these devices exhibit good energy

dissipation capacity and reparability [24]. Another connection method involves the use of sleeves and bolts for convenient installation. Zhang et al. [25] proposed a design method for core tube flange column joints, where the separation of connecting flange plates was further controlled by incorporating prestressed tendons into the column joints, yielding positive outcomes in joint performance. Fan et al. [26] presented a square steel tubular column-column joint with a blind bolt connection. The upper and lower columns were connected to the joint using four connecting plates and bolts, verifying good sliding resistance and ultimate bearing capacity.

The demonstration project of an automatic construction device currently utilizes a joint connection form depicted in Fig. 1. However, the connection exhibits relatively low connection strength as it only relies on the three bolts within the connection. Additionally, the necessity for attaching the connecting bracket to the building entails drilling into the concrete. These requirements render field installation both inconvenient and time-consuming.

This study proposed a novel connection joint designed explicitly for the automatic construction device, aiming to elevate its automation level, as illustrated in Fig. 2. The primary objective of this design is to enhance the installation convenience of the lifting column standard section while accommodating the lifting requirements of the support column. During installation, the bolt holes automatically align when the four corners of the upper and lower lifting column standard sections are properly aligned and inserted. The two lifting column standard sections are then connected by bolts. This joint design not only facilitates easier installation but also meets the demands of the support column lifting installation inherent to the automatic construction device. Furthermore, a pulley has been integrated at the end of the horizontal support frame of the automatic construction device, as illustrated in Fig. 3. This pulley interfaces with the track affixed to the building, enabling the entire support structure to be lifted upward as each lattice column standard section is installed from below. This feature facilitates the construction of higher floors, enhancing the overall efficiency and versatility of the device and also meeting the needs of a high automation level of the automated construction device.

In this paper, the mechanical behaviors of the newly designed connection joint, focusing on five steel joint specimens with distinct geometric parameters, were systematically analyzed and compared. Both static load tests and finite element analysis were employed to examine the mechanical properties and failure modes of the specimens. The experimental data were subsequently corroborated and expanded upon using finite element analysis to provide a more comprehensive understanding of the performance of the joint under diverse conditions, such as varying tube wall thickness and flange outside diameter. The impact of these additional parameters on the mechanical properties of the joints was estimated using the finite element method. By understanding the performance of these joints under various conditions and parameters, it became feasible to optimize their design and enhance the safety and reliability of the

automatic construction device during construction operations.

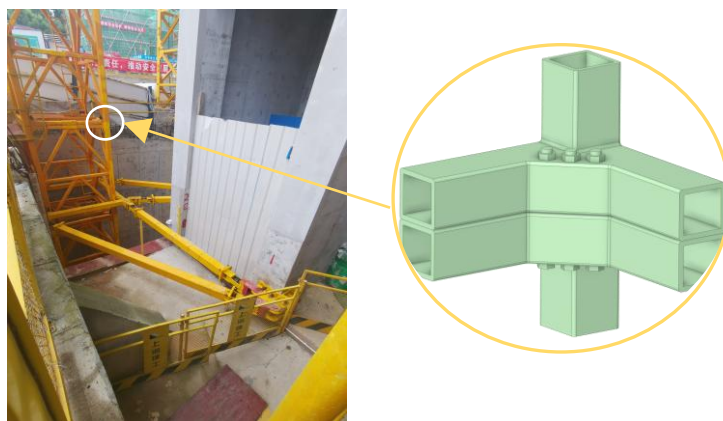


Fig. 1 Connecting joint of automatic construction device project

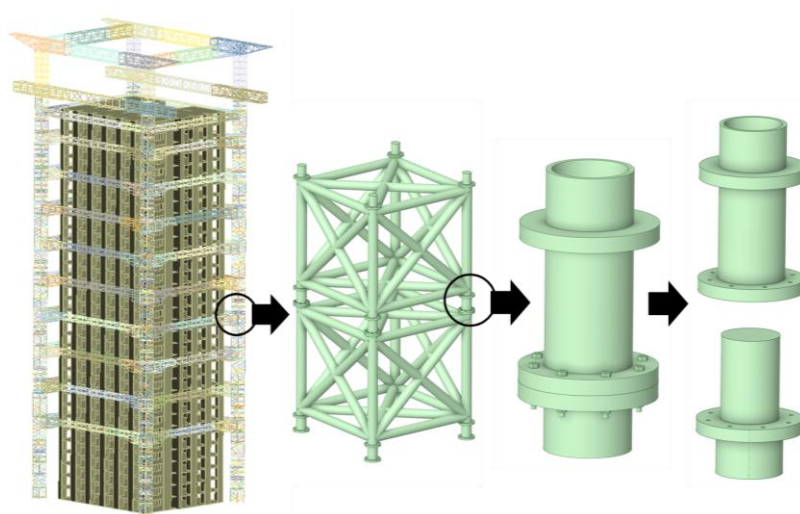


Fig. 2 A new type of connection joint for the automatic construction device

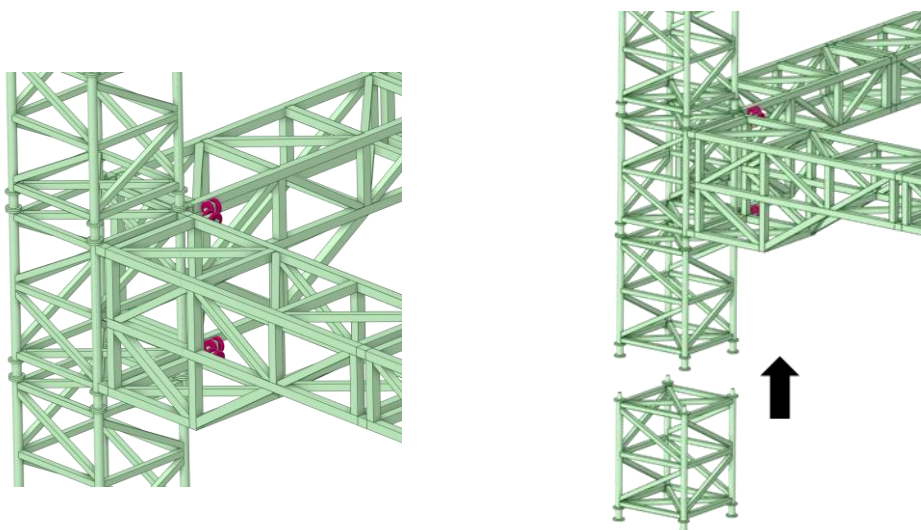


Fig. 3 Schematic diagram of the lifting process of the automated construction device

2. Experimental study

2.1. Test specimens

A novel connection joint was designed to enhance the automation level of the automated construction device, as illustrated in Fig. 4. The connection joint

was assembled from two parts. The upper part, a seamless steel tube, was welded to the flange-A at its bottom, while the lower part, also a seamless steel tube, was welded to the inserting portion with the flange-B at the welding site. Notably, during assembly, the inserting portion, a top-closed seamless steel tube, was inserted into the cavity of the upper seamless steel tube at the joint. The upper and lower parts of the joint were then connected by eight high-strength bolts.

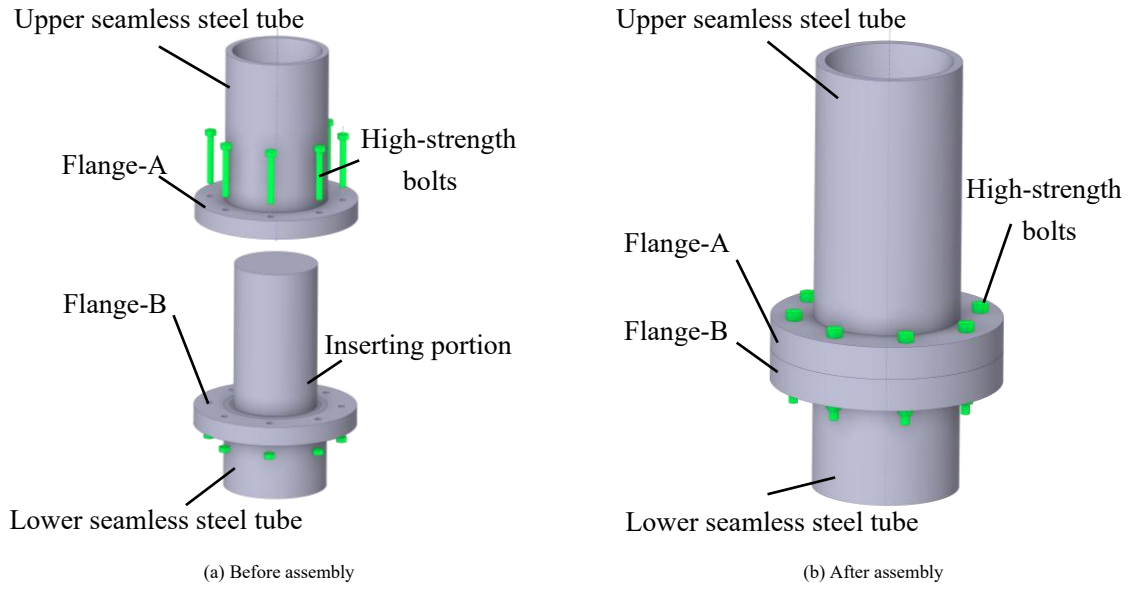


Fig. 4 Configuration of connection joint

Whether dealing with seamless steel tubes or flange plates, the curved outer surface posed a challenge when connecting to the horizontal actuator of the testing machine. To address this, a circular ring was welded on the outer surface of the seamless steel tube at the upper part of the joint. Subsequently, a horizontal connector was designed, as illustrated in Fig. 5. This connector, consisting of two bolt-connected parts, formed a circular cavity that snugly encased the welded ring on the upper part of the joint, thus facilitating the connection between the horizontal actuator and the joint. Additionally, an end plate with pre-designed bolt holes was welded to the top of the joint, enabling connection

to the vertical actuator. During loading, the material experienced increasing bending moments further from the horizontal loading position, leading to substantial bending moments at the bottom of the joint. A single-end plate welded at the bottom of the joint proved insufficient, often resulting in weld failure before the joint was fully stressed [27]. To overcome this, two flanges (Flange-C and Flange-B) were welded at the bottom of the joint, and eight stiffeners were interposed between them. These plates allowed eight bolts to pass through, effectively securing the bottom of the joint.

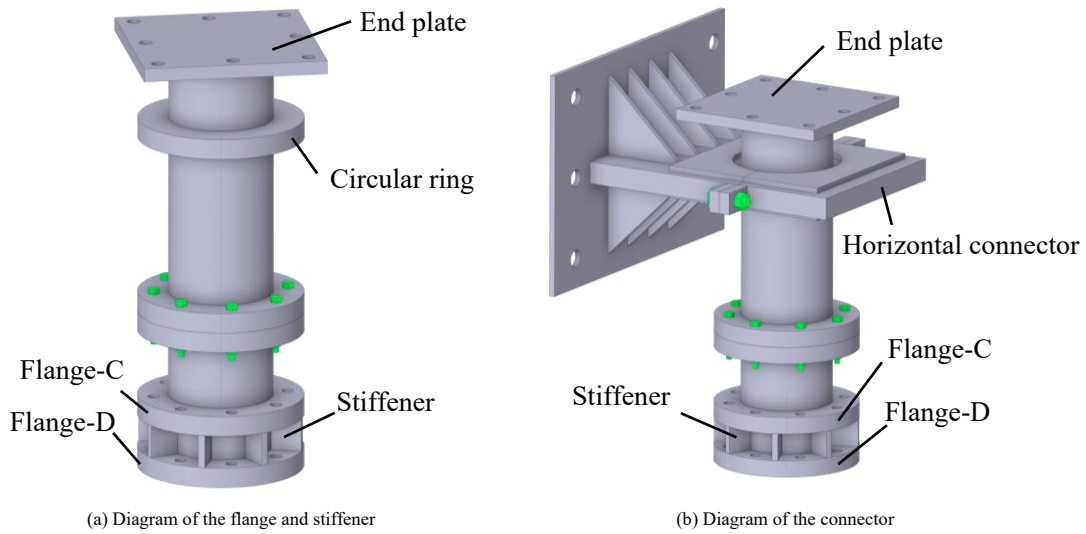


Fig. 5 Joint connected to the testing device

In this study, five steel joint specimens were tested. These specimens were designed to have the same height and outside diameter as the seamless steel tube. The length of the upper seamless steel tube of all specimens is 420 mm, and the length of the lower seamless steel tube of all specimens is 470 mm. All specimens are constructed from 20# seamless steel tubes specified in GB/T 8162-2018 [28], and all the flanges and stiffeners of all specimens are made of Q345B steel specified in GB/T 1591-2018 [29]. For specific material properties, see Tables 1 and 2.

The five specimens differed in the parameters of the flange-A and flange-B thickness, the axial compression ratio, and the inserting portion depths. Notably, the change in axial compression ratio was achieved by varying the vertical axial force magnitude. These parameters significantly influenced the mechanical properties of the joints [30-34]. The specific size parameters of all specimens are shown in Fig. 6 and Table 3, where t is the wall thickness of the seamless steel tube, h is the thickness of flange-A and flange-B, and F is the magnitude

of the vertical axial force acting on the top of the joint specimen.

The axial pressure was estimated based on the specific application scenario. By considering the combined dead weight of the entire framework, along with the additional loads from the upper equipment, materials, and personnel, the vertical force exerted at the bearing column joint has been calculated to be 600 kN. To analyze the structural performance under varying loads, two additional vertical axial force values of 400 kN and 800 kN were selected. Regarding the flange thickness, given that a range of 15-30 mm was typically utilized for steel structure end plates and similar components, thicknesses of 20 mm and 30 mm were chosen for further investigation [35-42].

Eight high-strength bolts between flange-A and flange-B are 10.9 s M10 ones [26]. A torque wrench was used to apply torque to the bolt. The designed pretension was 55 kN, and the actual pretension ranged from 46.7 kN to 63.6 kN, calculated by the actual torque applying the bolt preload, according to GB/T 1231-2006 [43].

Table 1
Material properties of the steel plate

	Chemical component (%)							Yield strength (MPa)	Ultimate strength (MPa)	Elongation (%)
	C	Si	Mn	P	S	Cu	Nb			
Steel	0.1600	0.2100	1.3900	0.0150	0.0020	0.0400	0.0030	407	555	26.5
Q345	V	Ti	Cr	Mo	Ni	Als	CEV			
	0.0010	0.0230	0.0400	0	0.0017	0.0005	0.4000			

Table 2
Material properties of the seamless steel tube

Specification (Outer diameter * thickness.) (mm)	Chemical component (%)								Yield strength (MPa)	Ultimate strength (MPa)	Elongation (%)
	C	Si	Mn	P	S	Ni	Cr	Cu			
133*10	0.210	0.190	0.480	0.028	0.009	0.009	0.023	0.011	300	497	23
159*10	0.200	0.200	0.560	0.011	0.008	0.020	0.060	0.020	374	632	18

Table 3
Detailed information of the specimens (Fig. 6)

Specimen No.	t (mm)	h (mm)	s (mm)	F (kN)
J-1	10	30	200	400
J-2	10	30	200	600
J-3	10	30	200	800
J-4	10	20	200	400
J-5	10	30	100	400

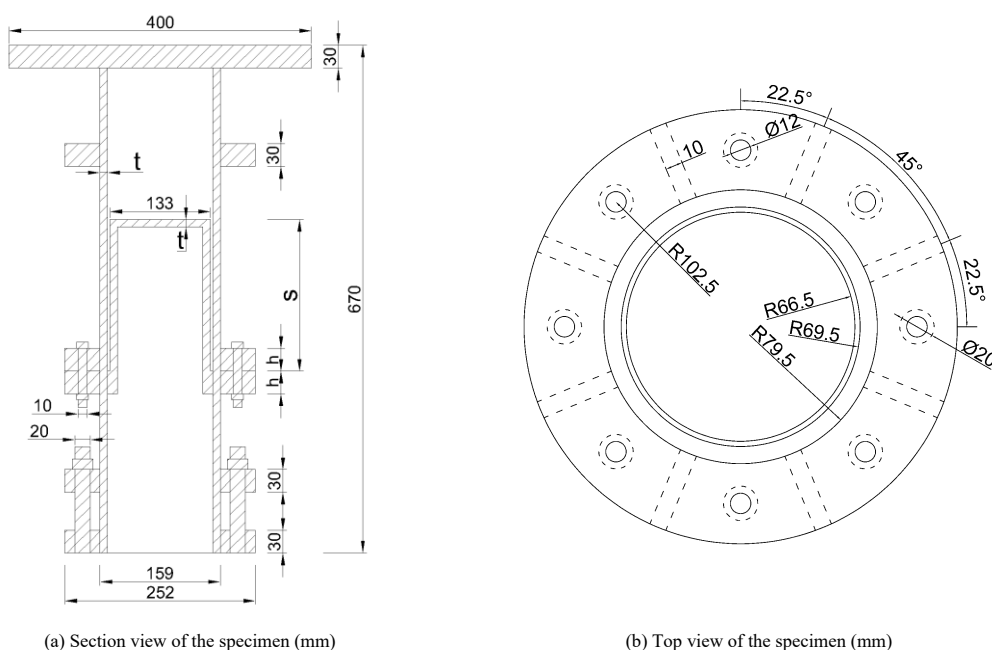


Fig. 6 Structural diagram of a connection joint

2.2. Test setup and loading scheme

The experiment was performed in the Structural Laboratory of the College of Civil and Transportation Engineering at Shenzhen University, as shown in Fig. 7.

The vertical actuator with a load capacity of 2000 kN was connected to the top-end plate of specimens by eight high-strength bolts and exerted a constant vertical force on the top of the specimens. Similarly, a horizontal actuator, capable of exerting up to 1500 kN, was connected to the specimens by a horizontal connector and applied a horizontal force or displacement.

Before the horizontal static loading test, an axial force was constantly applied to the specimen by a vertical actuator throughout the entire test loading process. The specimen was preloaded by the horizontal actuator, which first applied horizontal thrust from 0 to 20 kN through the force control mode and then unloaded to 0. The slippages between the steel plate at the lower fixed end and each bolt were eliminated by the preloading process. A horizontal displacement was then applied to the specimen by the horizontal actuator through the displacement control mode, and a loading rate of 1 mm/min. The loading process was terminated until the force applied was reduced to 85% of the ultimate bearing capacity of the specimen.

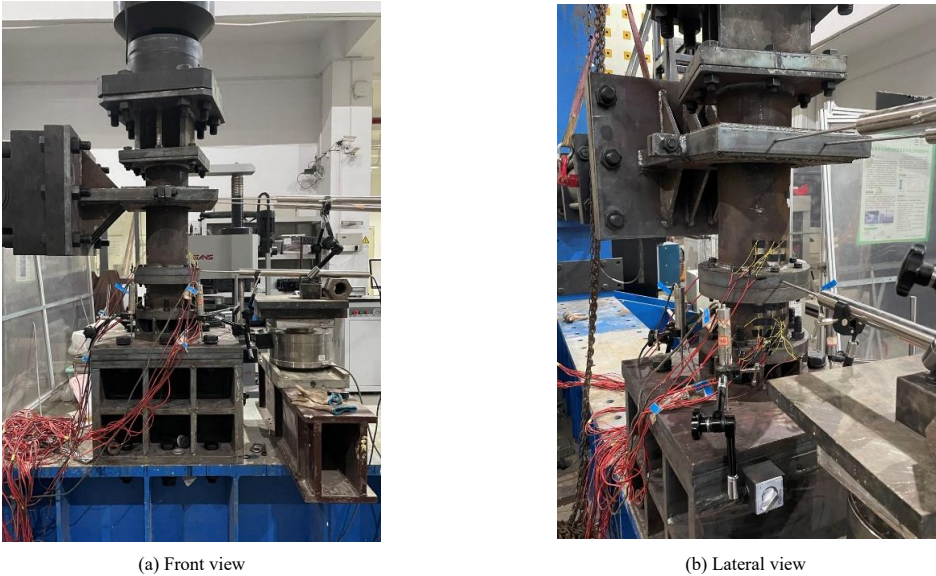


Fig. 7 Test setup for a connection joint

Note:  Displacement sensor

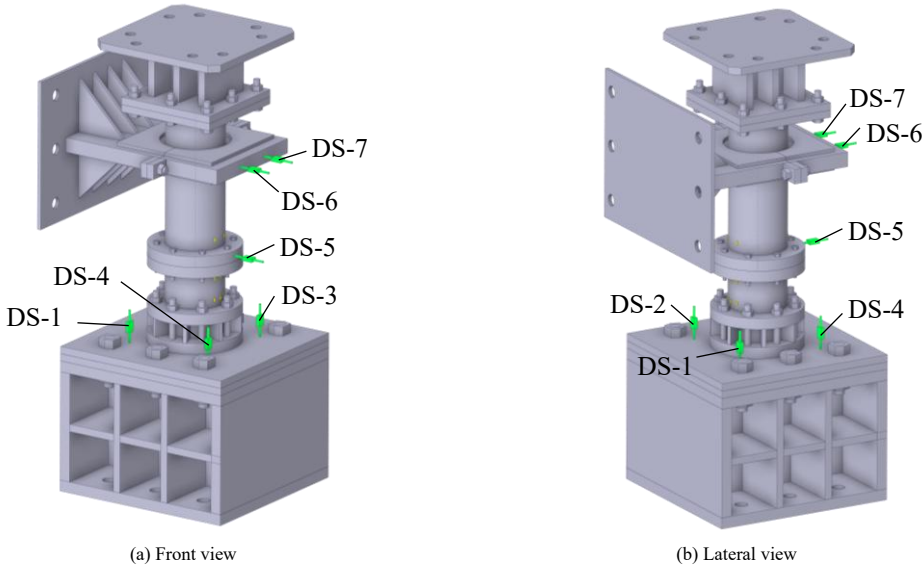
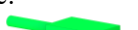



Fig. 8 Displacement sensor layout of the specimen

Note:  Displacement sensor
 Strain gauge

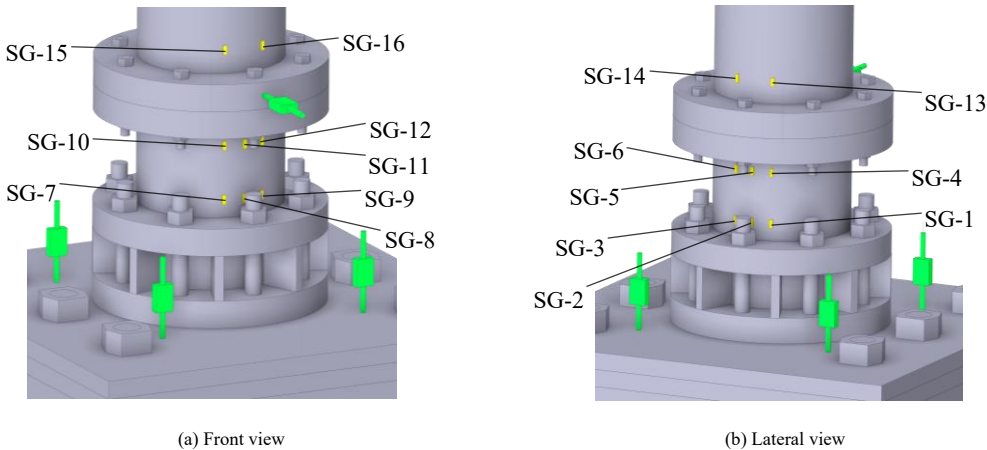


Fig. 9 Strain gauge layout of the specimen

2.3. Measurement scheme

The measurement scheme of the five specimens is identical, and the layout of displacement sensors is shown in Fig. 8. The vertical height of the two displacement sensors (DS-6 and DS-7) was the same, and they were placed at the front and back sides to measure the horizontal displacement at the loading

position, with the average value used as the horizontal displacement. Four displacement sensors were placed around the lower fixed part of the specimen to measure the buckling that might occur in the bottom plane of the specimen.

Each specimen in the study was outfitted with 16 strain gauges. These gauges were strategically distributed on the outer surface of the circular tube of the specimens. The precise locations of the strain gauges are depicted in Fig. 9.

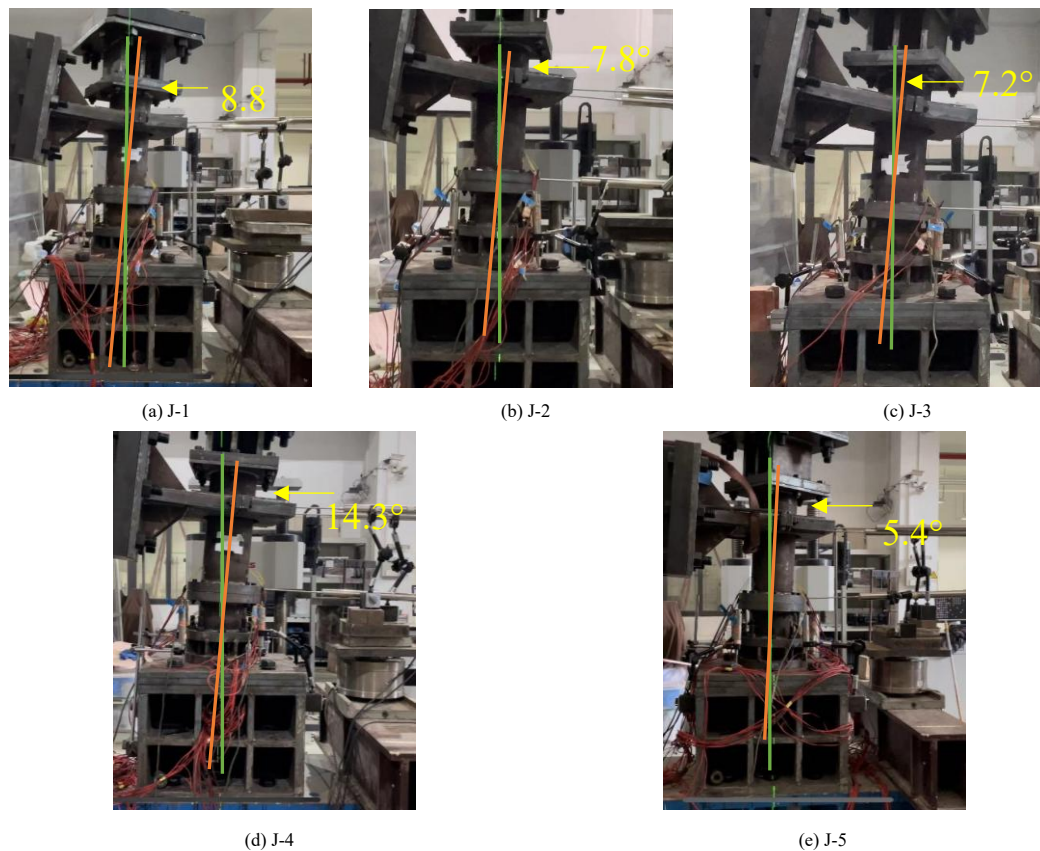


Fig. 10 Rotation angle of the joints after loading. (In the figures, the green line represents the specimen's initial axial position, determined based on the light emitted from a gradienter before the experiment. The orange line indicates the vertical line of the middle flange plate of the joint specimen after the experiment.)

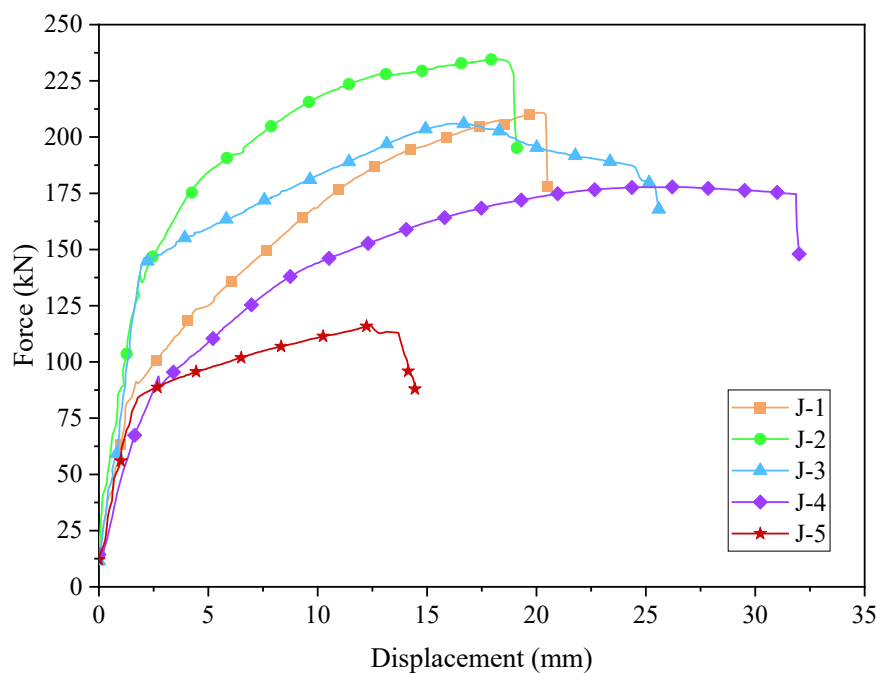


Fig. 11 Load-displacement curves of the specimens

3. Experimental results

3.1. Observed joint performance and discussion

During the experiment, different specimens exhibited varying rotation angles upon the application of the horizontal actuator, as illustrated in Fig. 10. The angular difference between the green and yellow lines signifies the extent

of the specimen's rotation.

Notably, as the axial pressure ratio increased, the rotation angle of the joint decreased sequentially from 8.8° to 7.8°, and ultimately to 7.2°, with corresponding reduction rates of 11.4% and 18.2%, respectively, indicating a diminishing rotational capacity of the joint. Conversely, reducing the flange thickness of the joint by 10 mm significantly increased the rotation angle to 14.3°, a rise of 62.5%, thereby enhancing the rotational ability of the joint. Furthermore, halving the length of the inserting portion of the joint reduced the rotation angle to 5.4°, a decrease of 38.6%, thus weakening the rotational capability of the joint. Observation of the test indicated that none of the specimens exhibited apparent signs of damage after testing. However, during the disassembly process, it was discovered that the bolts between flange-A and flange-B in the middle of the joints had loosened.

3.2. Load versus displacement curves

The average value of the results of the two parallel displacement sensors (DS-6 and DS-7) on both sides of the upper part of the specimen was taken as the horizontal displacement of the specimen, and the load-displacement curve of the specimen was drawn, as shown in Fig. 11. As the ultimate bearing capacity of the specimen dropped to 85%, the test was stopped, so the load-displacement curve only had a small decreasing section. However, in the actual loading process of the specimen, the bearing capacity of the specimen showed a zigzag and repeated decreasing trend. The yield displacement, yield strength, ultimate displacement, and ultimate strength of each specimen were listed in Table 4. Among them, yield displacement and yield strength refer to the transverse and longitudinal coordinate values at the apparent turning point of the load-displacement curve of the specimens.

From the load-displacement curves of each specimen, a linear segment characterized the initial loading stage, indicating the elastic behavior of the specimens. As loading progressed, the curves evolved into nonlinear segments, reflecting the onset of local plastic deformation in the joints. In load-displacement curves of the J-3 specimen exhibited a gradual decline compared to the other four specimens, which showed a sharp decrease after reaching their ultimate bearing capacity.

Table 4
Mechanical parameters of the specimens

No.	Yielding strength (kN)	Yielding displacement (mm)	Ultimate strength (kN)	Ultimate displacement (mm)
J-1	91.3	1.695	210.9	20.209
J-2	139.1	1.873	234.6	18.711
J-3	146.3	2.082	206.0	16.591
J-4	93.6	2.724	177.8	26.580
J-5	84.1	1.771	116.2	12.345

With the progressive increment of axial pressure ratio, a significant escalation in the yield strength of the joint was observed, rising from 91.3 kN to 139.1 kN, and ultimately reaching 146.3 kN, marking increases of 52.4% and 60.2%, respectively. Correspondingly, the yield displacement of the joint demonstrated a parallel upward trend, registering increases of 10.5% and 22.8%. These findings indicated a positive correlation between the axial pressure ratio and yield strength and displacement within a defined range, with a notably more

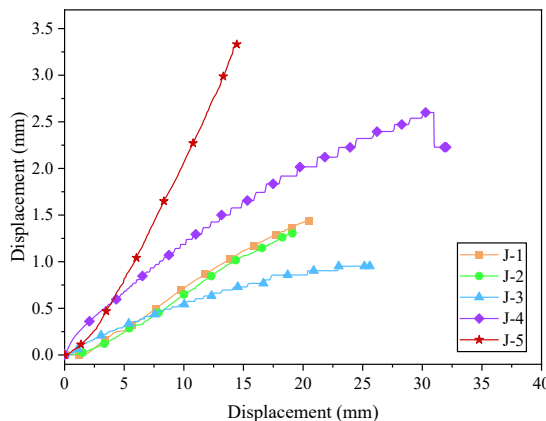
substantial influence on the yield strength. Conversely, the relationship between axial pressure ratio and ultimate strength and ultimate displacement exhibited a distinct pattern. As the axial pressure ratio increased, the change rate in ultimate strength was relatively small, recorded at 11.2% and -2.3%, respectively. This modest variation could be further influenced by potential eccentricity effects at the initial stage, suggesting that axial force exerted a limited impact on the ultimate strength of joints. Moreover, an increase in axial force was associated with a continual decrease in ultimate displacement, indicating an earlier joint failure. This was attributed to the influence of second-order effects caused by the vertical load.

When the thickness of the joint flange was decreased by 10 mm, an increase of 2.5% in the yield strength and a significant increase of 60.7% in yield displacement were observed. The specimen exhibited a 15.7% decrease in ultimate strength and a 31.5% increase in ultimate displacement when it reached the limit state. These changes suggested that a reduction in flange thickness markedly enhanced the ductility of the joint. Conversely, when the insertion depth of the joint was halved, the yield strength of the specimen decreased by 7.9%, yield displacement increased by 4.5%, ultimate strength decreased by 44.9%, and ultimate displacement reduced by 38.9%. These results indicated a substantial reduction in both the strength and ductility of the joint due to the halving of insertion depth, an unfavorable outcome in practical applications.

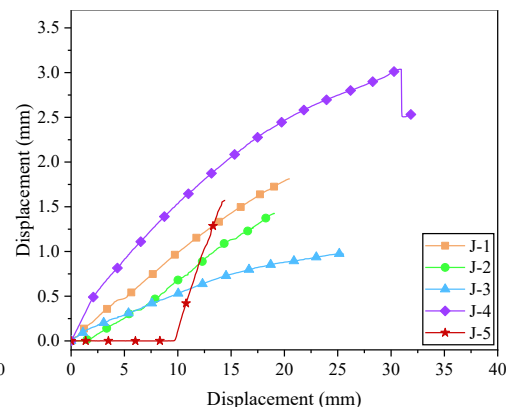
3.3. Deformation curve of the bottom plate

Displacement measurements captured by sensors DS-1, DS-2, DS-3, and DS-4 on the bottom plate of various specimens are shown in Fig. 12. According to the positions of the four displacement sensors in Fig. 8, it can be found that under ideal conditions, the values of the sensor DS-1 and DS-2 on the tension side are the same and positive, while the values of the sensor DS-3 and DS-4 on the compression side are the same and negative. If the values of the four displacement sensors are not this law, it indicates that the bottom plate is bulging.

As shown in Fig. 12a and b, sensors DS-1 and DS-2, positioned on the tension side of the material, registered positive values due to the base plate being stretched upward. A reduction in the displacement on the tension side of the base plate was observed as the axial pressure ratio increased. This reduction was attributed to the downward force exerted by the axial pressure, which limited the tensile displacement of the base plate. This observation aligned with the phenomenon noted in the test, where an increase in the axial pressure ratio resulted in a reduction of the rotation angle of the joint. For joint J-4, the measurement values from DS-1 and DS-2 were significantly higher. This indicated that a decrease in the thickness of the flange correlated with an enhancement in the bulging of the bottom plate, consistent with the observed increase in the rotation angle during the test. Fig. 12c and d demonstrated that DS-3 and DS-4 were positioned on the compression side of the material, where the bottom plate experienced downward compression, yielding negative displacement values. For joint J-5, torsion of the specimen was observed, causing a significant discrepancy between the measurements of displacement sensors DS-1 and DS-2, and a positive displacement value for DS-3. As depicted in Fig. 12c and d, the displacement measurements for each specimen did not exhibit a clear pattern of regularity. This lack of uniformity was attributed to the base plate not being perfectly planar, with bumps or depressions on its surface. These irregularities resulted in non-uniform displacement when the bottom plate was compressed. This issue was not observed on the tension side of the base plate. This should be attributed to losing contact with the ground when the base plate was stretched. Consequently, any surface defect on the base plate did not influence its displacement under this condition.



(a) Displacement value of DS-1



(b) Displacement value of DS-2

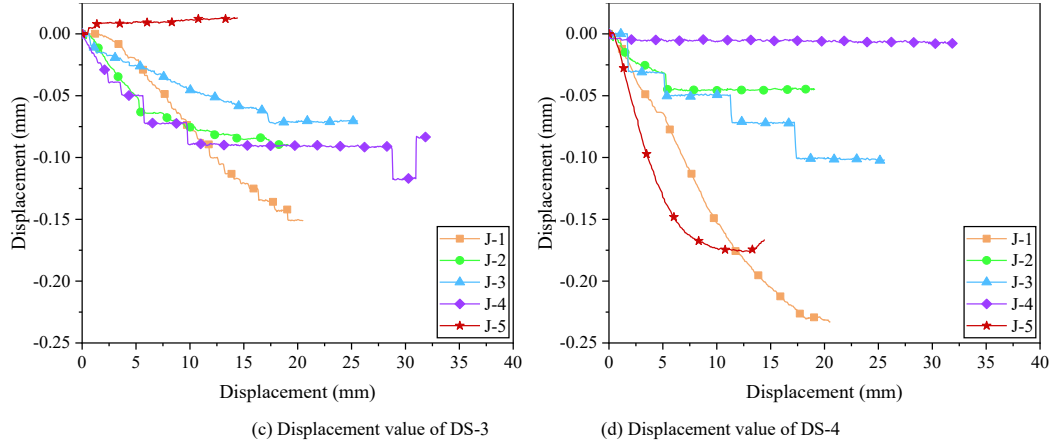


Fig. 12. Deformation displacement curve of the bottom plate. (In the figure, the horizontal coordinate is the average value of DS-6 and DS-7, and the vertical coordinate is the measured value of DS-1, DS-2, DS-3, and DS-4, respectively)

3.4. Moment versus rotation curves

In the analysis presented in the abovementioned section, it was observed that warping of the bottom plate resulted in an increased angle at the joint. To accurately determine the actual rotational capacity of the joint and construct the moment-angle curve, the rotation attributable to the buckling of the bottom plate was approximately eliminated using methods depicted in Eqs. (1) and Fig. 13. Notably, due to the progressive horizontal displacement at the top, the ground rotation center of the joint did not align with the central axis of the joint. Instead, it shifted towards the compression area.

$$\theta = \frac{L_a}{L_h} - \frac{L_t + L_p}{L_s} \quad (1)$$

where L_t is the mean value of DS-1 and DS-2 displacement sensor; L_p is the mean value of DS-3 displacement sensor and DS-4 displacement sensor; L_a is the mean value of DS-6 displacement sensor and DS-7 displacement sensor; L_h is the distance from the middle of the ring to the top of flange-C; L_s is the distance between DS-1 and DS-4 (the distance between DS-2 and DS-3) that is 250 mm. θ is the actual rotation of the joint.

The moment-rotation curves of the joints are shown in Fig. 14, and the mechanical properties of each specimen are given in Table 5, where K_0

represents the initial rotational stiffness of the joint (the slope of the line segment in the moment-rotation curve), K_1 represents the tangent stiffness of the joint (the tangent slope of the load-displacement curve at the initial stage of bending), M_y represents the yield moment, θ_y represents the yield rotation, M_u represents the ultimate moment, θ_u represents the ultimate rotation.

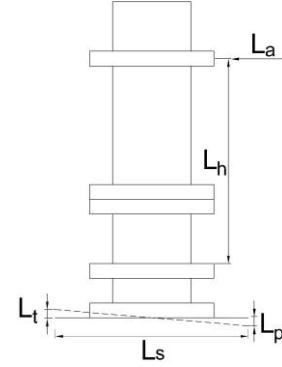


Fig. 13 Definition of L_t , L_p , L_a , L_h , L_s

Table 5
Mechanical parameters of the specimens

Specimen No.	K_0 (kN·m/rad)	K_1 (kN·m/rad)	$\frac{K_1}{K_0}$	M_y (kN·m)	θ_y (rad)	M_u (kN·m)	θ_u (rad)
J-1	11615	2783	0.240	47.93	0.0037	110.72	0.0457
J-2	15944	4273	0.268	73.03	0.0038	123.17	0.0403
J-3	15973	1196	0.075	76.81	0.0047	108.15	0.0350
J-4	6037	1826	0.302	49.14	0.0073	93.35	0.0613
J-5	10509	732	0.070	44.15	0.0037	61.01	0.0313

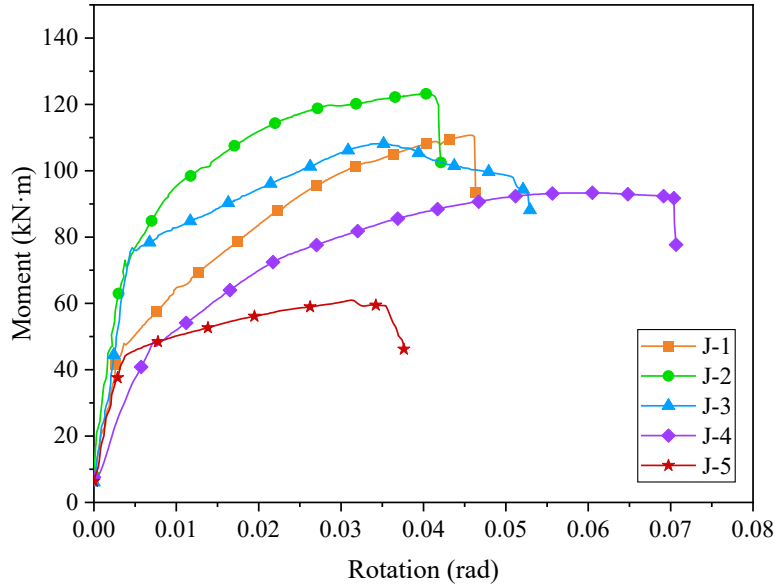


Fig. 14 Moment-rotation curves of the joints

As axial pressure increased, the initial stiffness, yield moment, and yield displacement of the joint rose, indicating enhanced elastic strength and deformation capacity. Compared with specimen J-1, the ultimate bending moment of the joint increased by 11.2% and subsequently decreased by 2.3%, suggesting that the effect of axial pressure on the ultimate bending moment initially escalated and then diminished under a specific axial force. A reduction of 11.8% and 23.4% in the limit angle was observed, implying that higher axial pressure precipitated the earlier failure of the joint. A notable decrease in the stiffness of the specimen was observed once it entered the plastic state. As evidenced in Table 5, an increase in axial force to 800 kN markedly reduced the stiffness of the joint, with its tangential stiffness being just 0.075 times its initial stiffness. Despite no significant variation in the load-bearing capacity of the joint, this abrupt decline in stiffness invariably accelerated joint failure. A decrease in the flange thickness of the joint resulted in higher yield bending moments and angles, while the initial stiffness dropped by 48.0%, nearly halving. The ultimate load-bearing capacity decreased by 15.7%, while its ultimate angle rose by 34.1%. This indicated a trade-off in the joint, sacrificing ultimate strength for greater rotational capacity. The ratio of tangential to initial stiffness of the joint rose to 0.302, indicating a lesser decrease in the stiffness of the joint. Halving the insertion depth of the joint led to reduced load bearing and rotational capacities, making it inadvisable in practical applications.

4. Finite element analyses

4.1. Finite element model

The finite element models simulating the loading of joints were built as shown in Fig. 15. The hexahedral element of twenty nodes was used to mesh circular steel tubes, flanges, stiffeners, and bolts. The global mesh size was 10 mm, and the refinement size was 5 mm and 2 mm for the bolts and bolt holes. In this study, the high-strength bolts were simplified into a dumbbell-shaped solid model, and the bolt modeling excluded the gaskets. The stress-strain model of steel and high-strength bolts is shown in Fig. 16. The elastic modulus of steel and high-strength bolts was 206 GPa, and Poisson's ratio was 0.3. The pretension force within all the high-strength bolts in the finite element model adopted a design value of 55 kN. In the finite element model, the bolt pretension force was applied to the surface of the bolt rods. The boundary condition of the lower part of the finite element model was simplified to consolidation, constraining the displacement in all directions, in which the degrees of freedom in the vertical direction of the upper part of the specimen and the rotation direction of the bending plane were released.

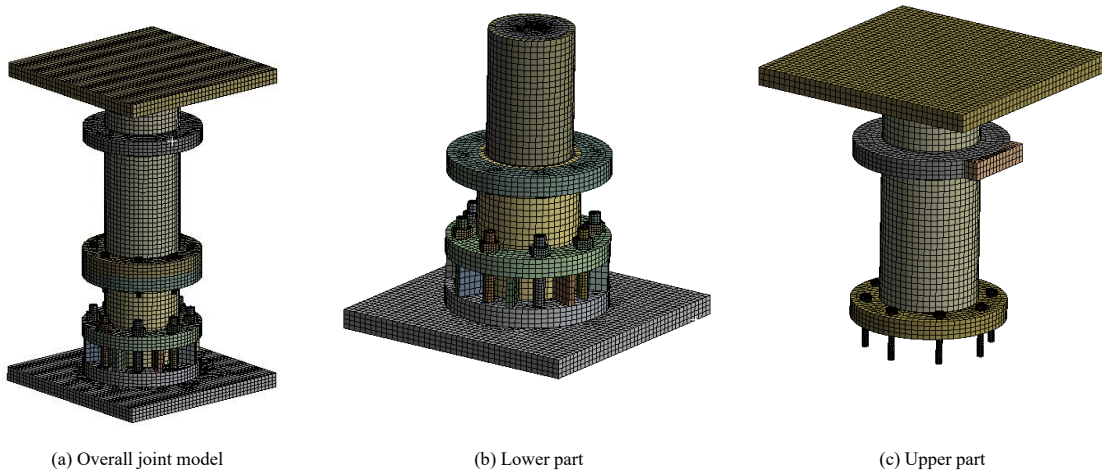


Fig. 15 Finite element models for the proposed joint

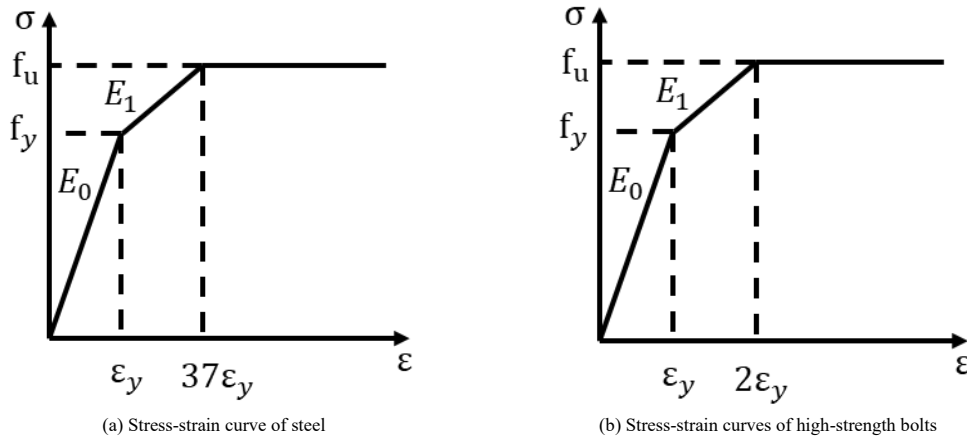


Fig. 16 Constitutive model of the materials

4.2. Finite element model validation

The mechanical behavior of all five specimens was simulated using the finite element method (FEM). Fig. 17 compared the load-displacement curves between the test and finite element results for the specimens. The mechanical parameters obtained by simulation and the comparison between test parameters and simulation parameters are shown in Table 6. As can be seen from Fig. 17

and Table 6, the simulation results were in good agreement with the test results, though there were still some gaps, which might have resulted from the initial defects in the test specimens and the gaps between the combined structures. Additionally, in the process of numerical simulation modeling, the simplification of the bolt model in the simulation and the selection of the norm value of the friction coefficient also contributed to the difference between the experimental and simulation results.

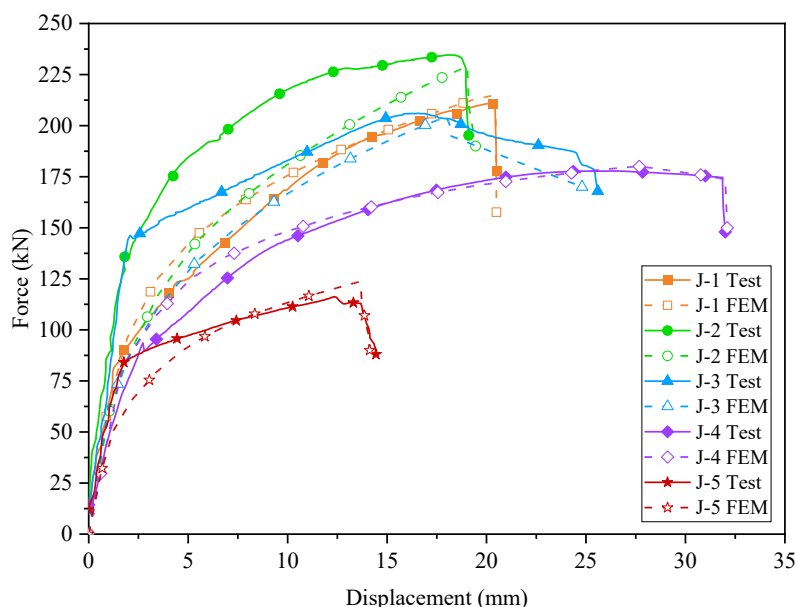


Fig. 17 Comparison of load-displacement curves between test and simulation

Table 6

Comparison between test result parameters and simulation result parameters

Specimen No.		J-1	J-2	J-3	J-4	J-5
K_0 (kN/mm)	Test results	57.08	58.98	61.77	46.92	51.92
	Simulation results	56.85	58.99	62.95	46.34	48.69
	Deviation (%)	-0.40	0.02	1.91	-1.24	-6.22
Peak strength (kN)	Test results	210.91	234.61	206.00	177.81	116.20
	Simulation results	215.00	229.00	204.33	180.01	123.57
	Deviation (%)	1.94	-2.39	-0.81	1.24	6.34
Peak displacement (mm)	Test results	20.21	18.71	16.59	26.58	12.34
	Simulation results	20.45	19.04	17.96	27.52	13.60
	Deviation (%)	1.19	1.76	8.25	3.54	10.17

4.3. Finite element results analysis

The stress-strain distribution characteristics of each test specimen were obtained via the aforementioned finite element simulation. For the joint specimen, the middle bolt and the compression side of the lower steel pipe were

identified as potential locations for higher stress and strain occurrence. Therefore, the stress-strain distribution of these two places was analyzed and was detailed below. The schematic diagram of the middle bolt and the lower steel pipe compression zone is shown in Fig. 18.

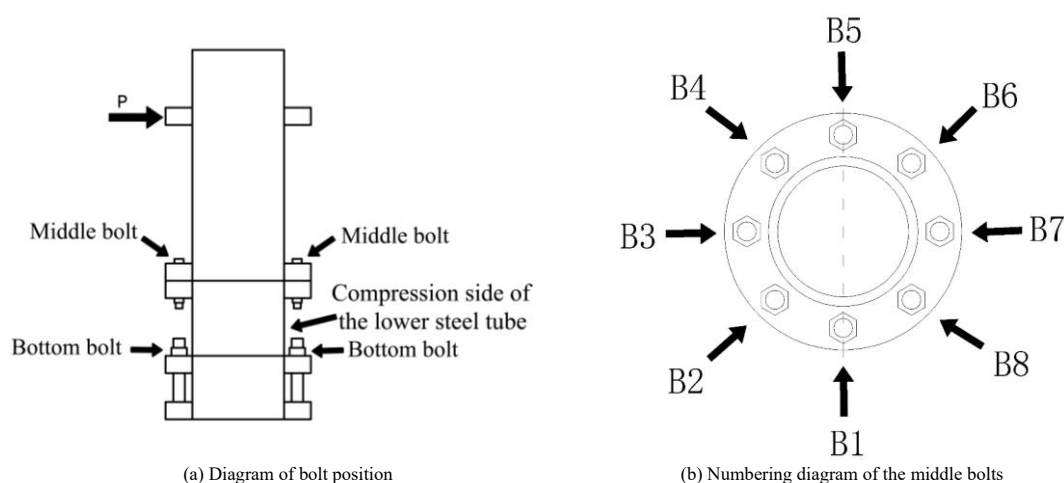


Fig. 18 Position diagram of bolts and steel pipe pressure zone

As shown in Fig. 18, owing to the application of a horizontal force on one side of the specimen, the material of the specimen was stretched on the side facing the horizontal force and compression on the opposite side. Fig. 18(b) presents the top view of Fig. 18(a). B1 to B8 represent eight middle bolts. Bolts B2 to B4 experience tensile stress, whereas bolts B6 to B8 experience compressive stress. The stress-strain analysis of the middle bolt below refers to the bolt subjected to the most significant tensile force, the B3 bolt.

4.3.1. Stress analysis

The equivalent stress nephogram of the B3 bolt between flange-A and flange-B for each tested specimen is shown in Fig. 19. The peak stress in specimens J-1 and J-5 was observed to be centrally located within the bolt, diminishing progressively towards the ends of the bolt. In contrast, in specimens J-2 and J-4, the peak stress deviates slightly from the center. This variation is attributed to the differing contact degrees between the bolts and bolt-hole walls

during loading.

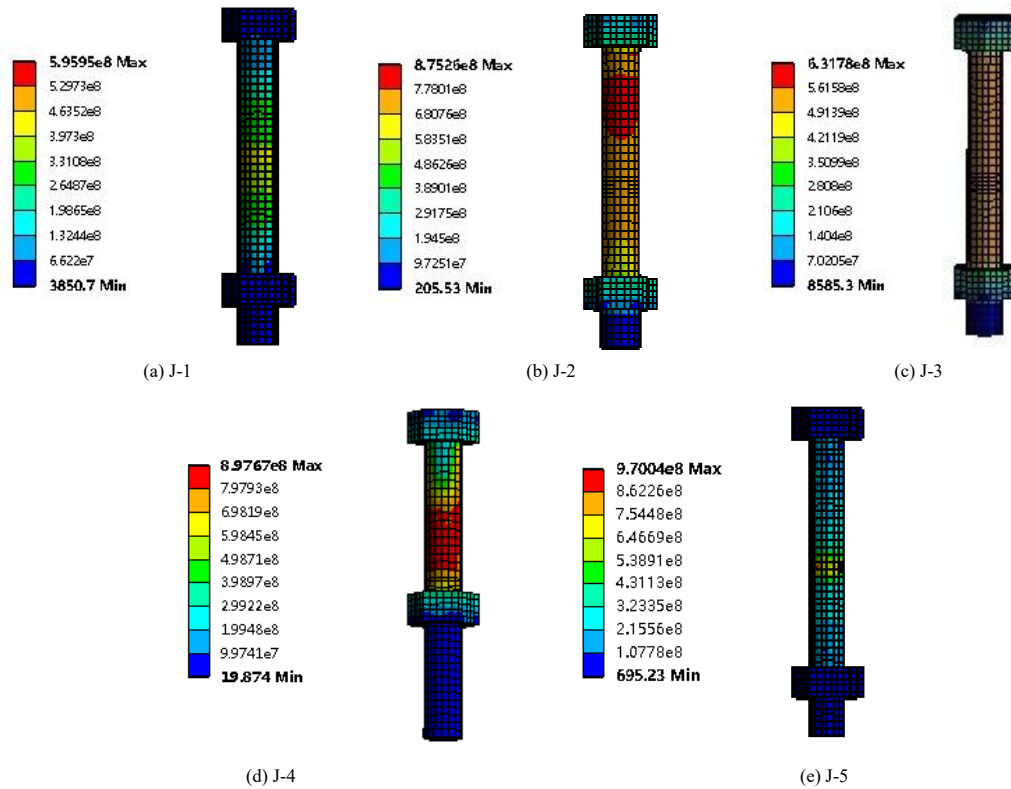


Fig. 19 Equivalent stress nephogram of the B3 bolt between flange-A and flange-B

The maximum equivalent stress experienced by the B3 bolt between flange-A and flange-B in each specimen is shown in Fig. 20. Notably, among specimens J-1, J-2, and J-3, specimen J-2 exhibits the highest stress value 946.49 MPa. This indicates that the correlation between axial pressure and the maximum equivalent stress of the B3 bolt is not a direct linear relationship but exhibits an extremum at 600 kN. A reduction in flange thickness resulted in an elevated maximum equivalent stress at the bolt, reaching 950.96 MPa, 3.1% higher than specimen J-1. When the insertion depth is halved, the maximum equivalent stress of the B3 bolt escalated to 970.04 MPa, the highest among all specimens examined and 5.2% higher than specimen J-1. It is evident that diminishing the thickness of the flange, along with halving the insertion depth, induces considerable stress in the B3 bolt.

The equivalent stress nephogram for the compression side of the lower steel tube of each specimen is shown in Fig. 21. Examination of the figure reveals that the maximum equivalent stress for specimens J-1 and J-3 is located near

flange-C at the bottom of the circular tube. In contrast, for specimens J-2, J-4, and J-5, the location of the maximum equivalent stress is less distinct, manifesting across a broader area.

The maximum equivalent stress identified in the compression side of the lower steel tube of each specimen is shown in Fig. 22. The data analysis reveals that specimens J-1, J-2, and J-3 exhibit similarly elevated stress levels. Specifically, specimen J-2 registers the minimum stress value at 474.58 MPa, while specimen J-3 records the maximum at 609.32 MPa. It is observed that reducing the flange thickness of the specimen results in the lowest equivalent stress on the compression side of the lower steel tube, measured at 356.05 MPa, which is 29.6% lower than that of specimen J-1. Furthermore, halving the insertion depth leads to a decrease in equivalent stress within this region to 367.31 MPa, which is 27.4% lower than that of specimen J-1, although the extent of reduction is less pronounced than that observed in specimen J-4.

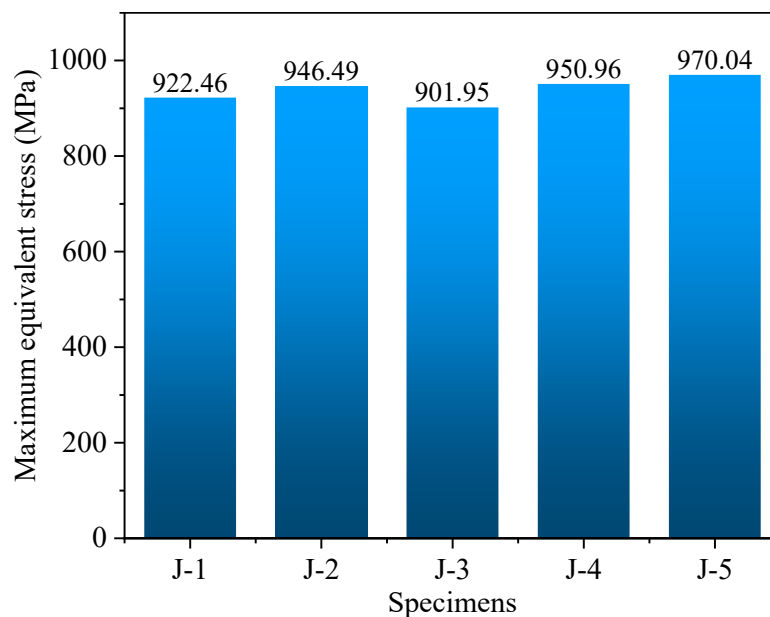


Fig. 20 Maximum equivalent stress at B3 bolt between flange-A and flange-B of each specimen

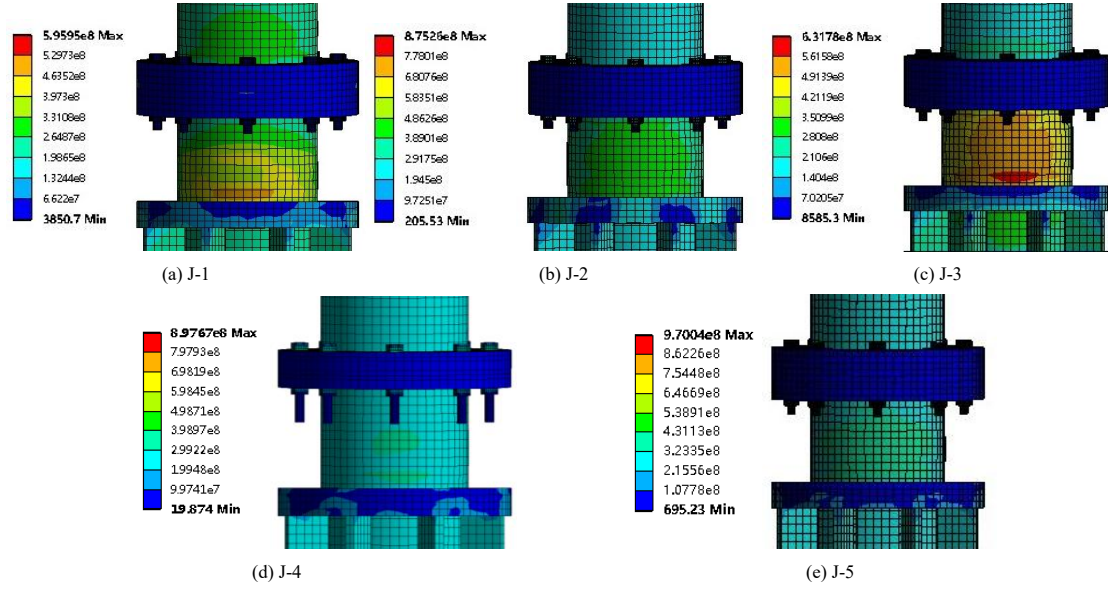


Fig. 21 Equivalent stress nephogram of the compression side of the lower steel tube

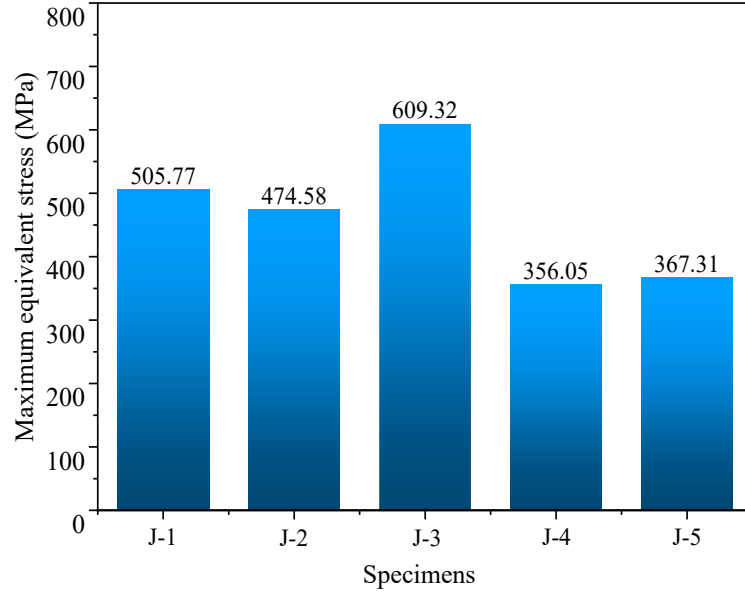
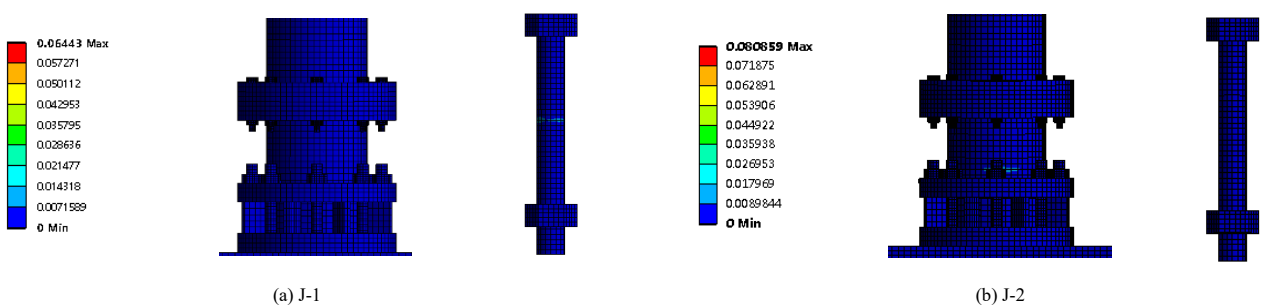


Fig. 22 Maximum equivalent stress at the compression side of the lower steel tube of each specimen

A critical observation concerns the contrasting pattern in the maximum equivalent stress observed at the B3 bolt compared to that at the compression side of the lower steel tube. Notably, at the B3 bolt, the stress value under an axial force of 600 kN surpasses those observed at 400 kN and 800 kN. Conversely, the stress values at the compression side of the lower steel tube exhibit an opposite trend. Furthermore, while reducing the flange thickness and halving the insertion depth elevate the stress at the bolt, these modifications lead to a reduction in stress at the compression side of the lower steel tube. This inverse correlation underscores the intricate interplay between structural alterations and their impact on the internal stress distribution within the specimens.

4.3.2. Strain analysis

The equivalent plastic strain of each specimen on the compression side and the B3 bolt at the turning point is shown in Fig. 23. It can be seen that plasticity only occurs in a small part of specimens J-1, J-2, and J-3, and most of the other parts do not enter the plasticity stage. Specimens J-1 and J-3 enter the plastic state from the middle of the B3 bolt, while specimen J-2 enters the plastic stage from the bottom of the steel tube near flange-C. The plastic development of specimens J-1, J-2, and J-3 at the turning point obtained by numerical simulation is in good agreement with the load-displacement curve obtained by the test, as it is evident from the curve that the specimens are transitioning from the elastic stage to the plastic stage at this time. The plastic deformation of joints in the numerical simulation occurs earlier than in the test.



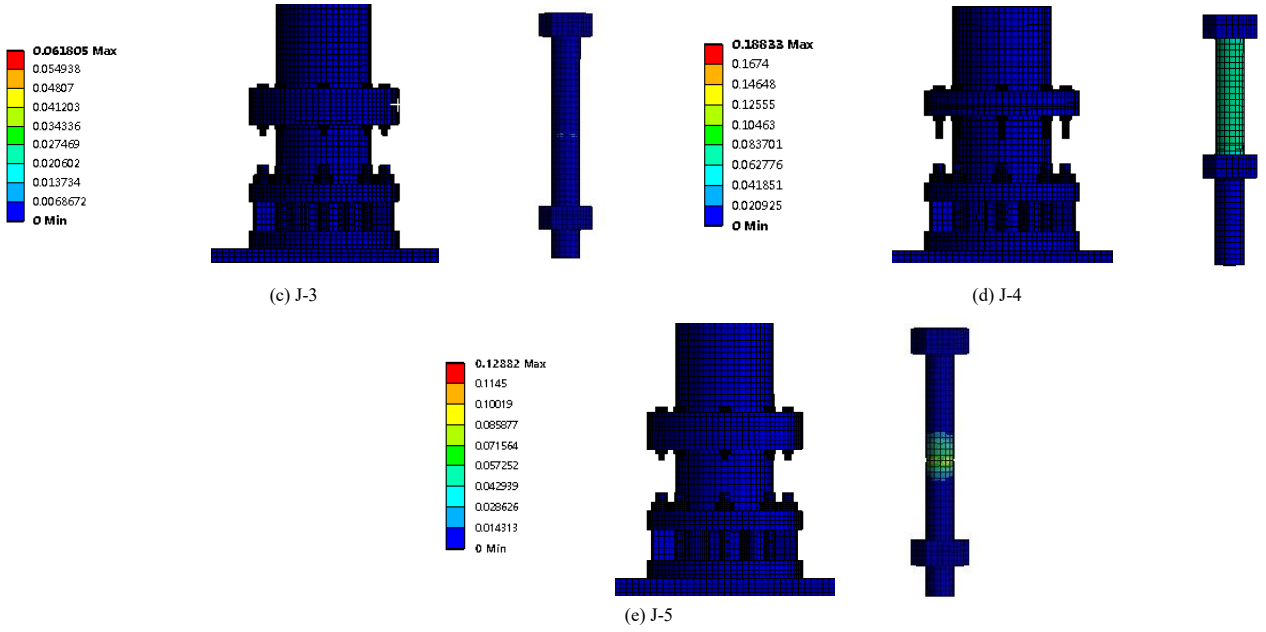


Fig. 23 Equivalent plastic strain nephogram of the joints on the compression side and the B3 bolt at the turning point

The equivalent plastic strain nephogram of the B3 bolt between flange-A and flange-B for each specimen was shown in Fig. 24. As observed in the figure, the plastic strain in specimens J-1 and J-5 is confined solely to the midsection of the bolt. This localization of plasticity correlates with the observed stress distribution within the bolt. Specimen J-3 exhibits minimal plastic deformation, with only a small portion of the bolt undergoing plasticity. Notably, specimens

J-2 and J-4 demonstrate plastic deformation throughout the entire bolt rod, indicating a more widespread strain distribution under the applied conditions. This variation in plastic strain among the specimens aligned with the differences in stress distribution, highlighting the impact of structural and loading variations on the deformation characteristics of the bolt.

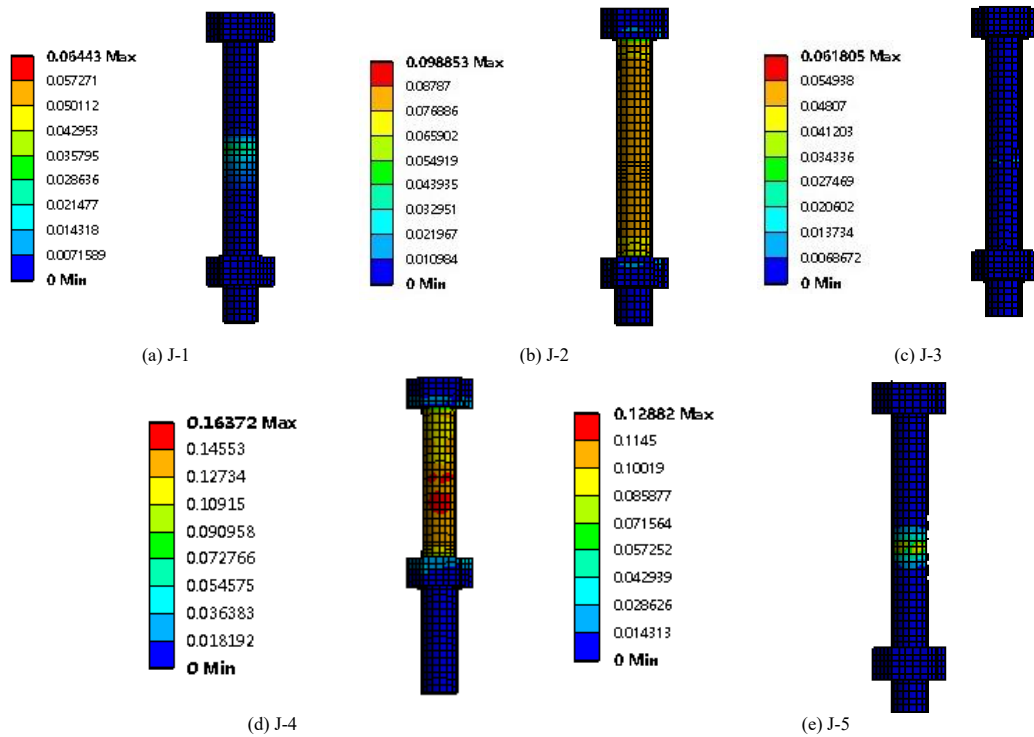


Fig. 24 Equivalent plastic strain nephogram of the B3 bolt between flange-A and flange-B

The maximum equivalent plastic strain value of the B3 bolt between flange-A and flange-B of each specimen is shown in Fig. 25. As can be seen from the figure, the maximum equivalent plastic strain value of the B3 bolt for specimens J-1, J-2, and J-3 with different axial pressure parameters is at a low level, not exceeding 0.1. When the flange thickness of the specimen decreases, the maximum equivalent plastic strain at the bolt of the specimen reaches 0.1483,

which is 5.2 times that of the specimen J-1. After the insertion depth of the specimen is halved, the maximum equivalent plastic strain at the bolt of the specimen is 0.1259, which is 4.4 times that of the specimen J-1. In both cases, the strain of the bolt reaches a considerable value, indicating relatively sufficient plastic deformation.

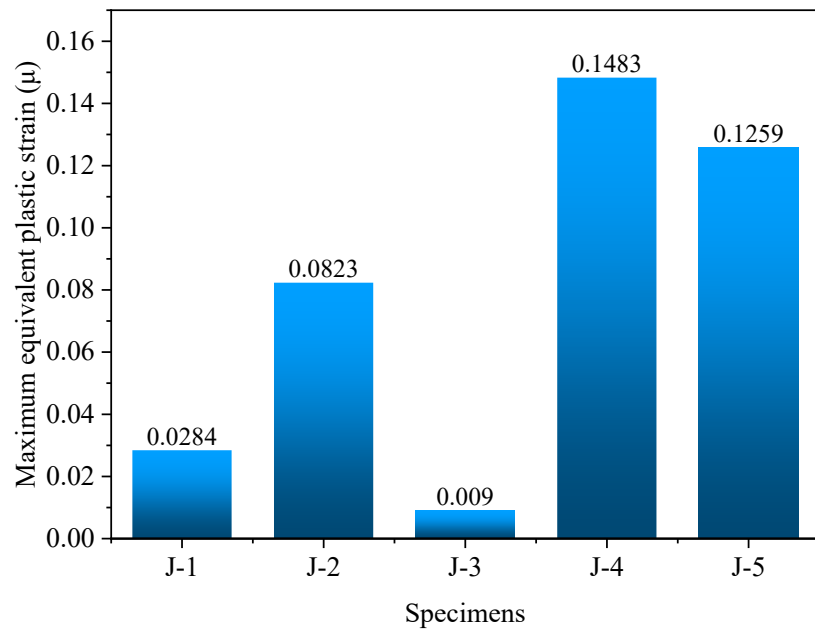


Fig. 25 Maximum equivalent plastic strain at the B3 bolt between flange-A and flange-B of each specimen

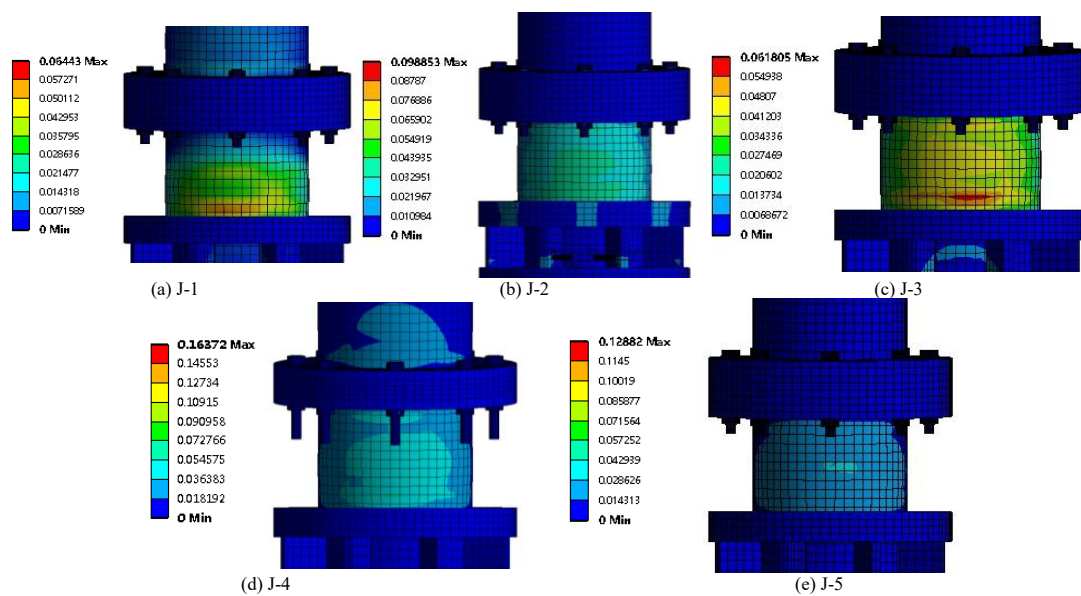


Fig. 26 Equivalent plastic strain nephogram of the compression side of the lower steel tube

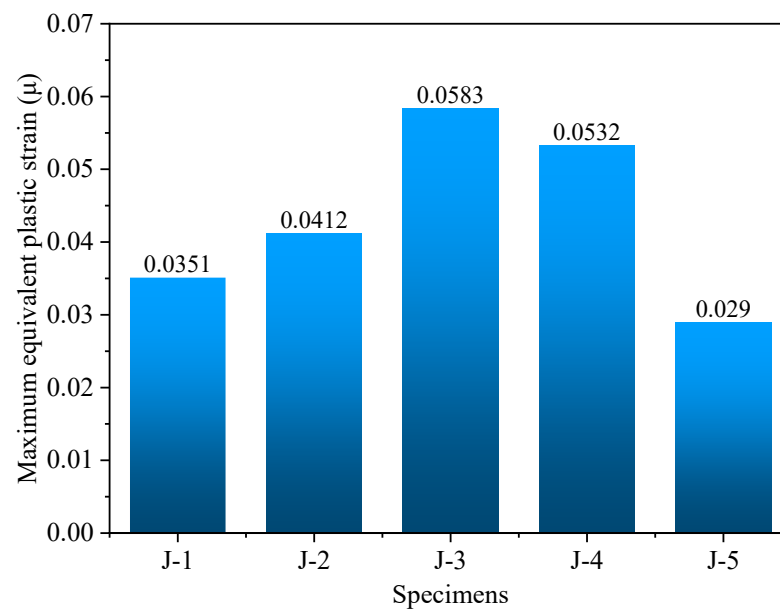


Fig. 27 Maximum equivalent plastic strain at the compression side of the lower steel tube of each specimen

The equivalent plastic strain distribution on the compression side of the lower steel tube is shown in Fig. 26. It is evident from the figure that all specimens have entered a plastic state. Specimens J-1 and J-4 exhibit plastic deformation on both the upper and lower sides of flange-A and flange-B, and the maximum plastic strain is observed at the bottom of the steel tube near flange-C. The distribution of plastic strain in specimen J-3 is similar to specimen J-1, with the maximum value of plastic strain also appearing at the bottom of the steel tube near flange-C. The distribution of plastic strain in specimen J-3 is similar to specimen J-11, with the maximum value of plastic strain also appearing at the bottom of the steel tube near flange-C. However, no plastic strain is evident on the upper side of flange-A. For specimen J-4, when the plastic strain appears on the upper side of flange-A, there is no distinct extreme value, and the plastic strain distribution is relatively uniform. The strain distribution of specimens J-3 and J-5 is similar, with plastic strain only appearing on the lower side of flange-B.

The maximum equivalent plastic strain on the compression side of the lower steel tube of each specimen is illustrated in Fig. 27. It is evident from the figure that as the axial pressure on the specimen increases, the plastic strain of the compression side of the lower steel tube increases. This is due to the rise of the axial pressure acting on the top of the joint. The magnitude of the axial pressure directly affects the stress condition at the bottom of the joint. The maximum equivalent plastic strain of specimen J-4 reaches 0.0532, which is 51.6% larger than specimen J-1. Reducing the thickness of the flange increases the plastic strain on the compression side of the lower steel tube of the joint. The maximum equivalent plastic strain of specimen J-5 is 0.0290, which is a reduction of 17.4% compared to specimen J-1. Reducing the inserting depth decreases the plastic deformation on the compression side of the lower steel tube of the joint.

5. Parametric analysis

To further investigate the influence of various parameters on the mechanical strength and rotation capacity of the proposed joints, multiple sets of specimens

were prepared in each group for numerical analysis, considering the two parameters of tube wall thickness and the outside diameter of flanges A and B.

5.1. Effect of tube wall thickness

Seven joint specimens with varying tube wall thicknesses were analyzed using the finite element method. The tube wall thicknesses are 6 mm, 8 mm, 10 mm, 11 mm, 12 mm, 13 mm, and 14 mm, respectively. All other parameters of the specimens are identical to those of specimen J-1. The specific sizes of all specimens are shown in Table 7.

The moment-rotation curve derived from the numerical simulation results of the specimens is shown in Fig. 28. The Farthest Point Method was adopted [44] to determine the mechanical properties of the joints, as shown in Fig. 29, and the initial stiffness, yield moment and corresponding yield rotation, and ultimate moment and corresponding ultimate rotation of each joint were given, as shown in Table 8.

The data presented in Table 8 clearly show that the mechanical parameters of the joints exhibit a specific trend as the joint wall thickness increases. Initially, as the wall thickness increases from 6 mm to 10 mm, all the mechanical parameters, including the initial stiffness, yield moment, yield rotation, ultimate moment, and ultimate rotation, continuously increase, reaching a local maximum value at 10 mm. This indicates that a thicker wall enhances the overall mechanical performance of the joint. However, a different pattern emerged as the wall thickness increased from 10 mm to 12 mm. In this range, all the mechanical parameters of the joint start to decrease continuously, reaching a local minimum value at 12 mm. This indicates that there is an optimal range for the wall thickness, beyond which increasing the thickness is not advantageous for enhancing the mechanical properties of the joint. Interestingly, when the wall thickness increased from 12 mm to 14 mm, the mechanical parameters of the joint started to increase again, continuing to rise and reaching the maximum value at 14 mm. This suggests that there may be additional benefits to increasing the wall thickness beyond the optimal range.

Table 7
Detailed information of the specimens

Specimen No.	t (mm)	h (mm)	F (kN)	s (mm)
J-t-6	6	30	400	200
J-t-8	8	30	400	200
J-t-10	10	30	400	200
J-t-11	11	30	400	200
J-t-12	12	30	400	200
J-t-13	13	30	400	200
J-t-14	14	30	400	200

Note: The naming rule of the seven specimens is J + t + tube wall thickness, where J stands for joint and t for wall thickness.

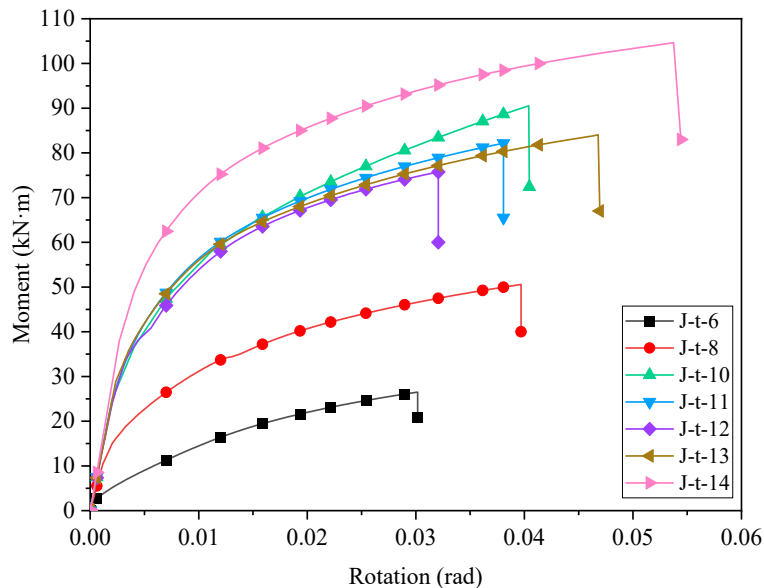


Fig. 28 Moment-rotation curve of the joints

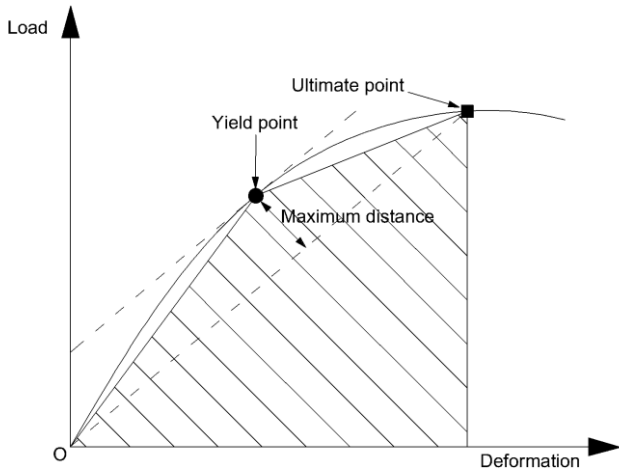


Fig. 29 Farthest Point Method for determination of yield points of members

Table 8
Mechanical properties of the specimens

Specimen No.	K_0 (kN·m/rad)	M_y (kN·m)	θ_y (rad)	M_u (kN·m)	θ_u (rad)
J-t-6	4428	2.69	0.00061	26.50	0.03017
J-t-8	8788	32.56	0.01103	50.58	0.03970
J-t-10	12395	58.03	0.01119	90.54	0.04040
J-t-11	11957	55.63	0.00965	82.15	0.03807
J-t-12	11815	52.85	0.00957	75.75	0.03207
J-t-13	12150	58.21	0.01119	84.05	0.04680
J-t-14	14289	74.34	0.01155	104.66	0.05374

Considering both the joint performance and economical cost, selecting a wall thickness of 10 mm as the most appropriate value is advisable. At this thickness, the mechanical properties of the joint reach their local maximum,

indicating optimal performance and choosing a thickness of 10 mm balances the mechanical capabilities and the economic cost of manufacturing. It is important to note that the specific performance requirements, design constraints, and application context should be considered when determining the suitable wall thickness for a joint in a practical situation.

5.2. Effect of flange outside diameter

Five joint specimens with different outer diameters of flange-A and flange-B were analyzed using the finite element method. The outer diameters of the flanges are 252 mm, 264 mm, 276 mm, 288 mm, and 300 mm, respectively. Other parameters of the specimens are identical to those of J-1. The specific dimensions of all specimens are shown in Table 9.

Table 9
Detailed information of the specimens

Specimen No.	d (mm)	t (mm)	h (mm)	F (kN)	s (mm)
J-d-252	252	10	30	600	200
J-d-264	264	10	30	600	200
J-d-276	276	10	30	600	200
J-d-288	288	10	30	600	200
J-d-300	300	10	30	600	200

Note: The naming rule of the five specimens is J + d + flange diameter, where J stands for joint and d for diameter.

Based on the numerical analysis results, the moment-rotation curves of five joint specimens were plotted, as shown in Fig. 30. The farthest point method was applied to determine the yield moment and corresponding yield rotation, ultimate moment and corresponding ultimate rotation, and initial stiffness of the joint specimens, as shown in Table 10. From the information provided in Fig. 30, it is evident that the joint labeled J-d-252 exhibits the highest initial stiffness and ultimate bending moment. As the outer diameters of Flange-A and Flange-B increase, the bearing capacity of the joints decreases compared to the J-d-252 joint. Specifically, when the outer diameter of the joint flange increases from 264 mm to 300 mm, the yield strength and ultimate strength remain nearly unchanged at approximately 54 kN·m and 80 kN·m, respectively. Additionally, the yield and ultimate rotation do not significantly differ, except for a slight reduction in the yield and ultimate rotation of J-d-300.

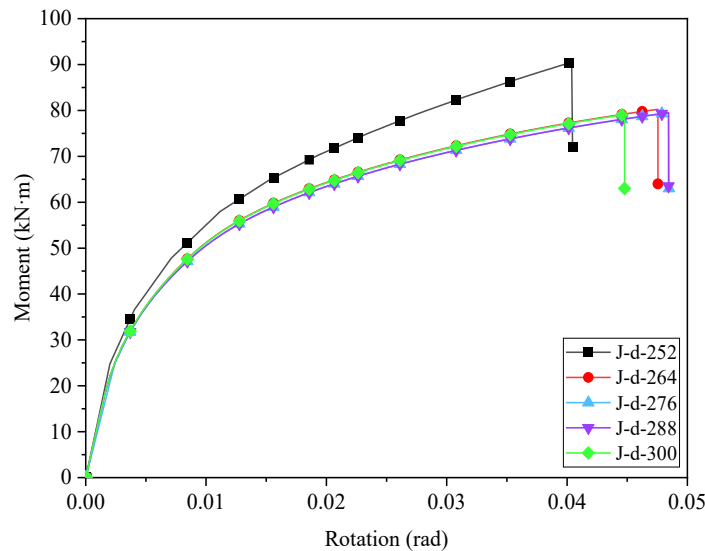


Fig. 30 Moment-rotation curves of the joints

Considering both the mechanical properties of the joint and economic factors, selecting the outer diameter of the flange as 252mm is recommended. The J-d-252 joint exhibits the most significant initial stiffness and ultimate bending moment among the tested joints. While increasing the outer diameter of the flange may not significantly impact the yield strength, ultimate strength, yield angle, or ultimate rotation, it results in a decrease in bearing capacity

compared to the joint J-d-252.

However, it is essential to note that the specific application, design requirements, and constraints should be carefully considered when determining the appropriate outer diameter of the flange for a joint. Other factors, such as cost-effectiveness and additional performance considerations, should also be considered when making the final decision.

Table 10

Mechanical properties of the specimens

Specimen No.	K_0 (kN·m/rad)	M_y (kN·m)	θ_y (rad)	M_u (kN·m)	θ_u (rad)
J-d-252	12395	58.03	0.01119	90.54	0.04040
J-d-264	11349	54.31	0.01167	80.23	0.04755
J-d-276	10397	53.61	0.01167	79.48	0.04843
J-d-288	11483	53.33	0.01152	79.48	0.04843
J-d-300	11455	53.59	0.01129	79.09	0.04478

6. Conclusions

In this study, the experimental research and finite element analysis of the proposed joint used for advanced automation devices were conducted under combined vertical and lateral loads. Based on the experimental observation and finite element analysis, the following conclusions can be drawn:

1. Axial force has a limited impact on the ultimate moment of the joint but significantly reduces the ultimate rotation. Thinner flanges A and B cause a 15.7% drop in the ultimate moment and a 34.1% rise in the ultimate rotation. Halving the insertion depth leads to a 44.9% rise in the ultimate moment and a 31.5% rise in the ultimate rotation. Additionally, the failure of all specimens is due to the bolt connection, specifically the failure of the threads. However, no significant damage is found in the joint tube wall, indicating that the failure primarily occurs in the bolt connection.
2. The moment-rotation curve and mechanical parameters derived from the experimental and numerical simulation studies exhibit a high degree of consistency. At the turning point, the progression of plastic deformation in simulated specimens with different axial forces aligns well with the experiment results. However, in the numerically simulated specimens with thinner flanges and shorter insertion depth, the onset of plastic deformation of the joint occurs earlier than in the experimental specimens. This discrepancy may be due to the simplification of the bolt model and the selection of the standard friction coefficient.
3. The maximum equivalent stress at the B3 bolt initially increases by 2.6% and then decreases by 2.2% with increasing axial force. The thinner flange increases the stress at the B3 bolt by 3.1 % due to the diminished contact area between the bolt and flange resulting from decreased flange thickness, which enhances the stress concentration. A shorter inserting depth increases the stress at the B3 bolt by 5.2%, a consequence of the diminished support provided by the inserting portion to the upper steel tube, necessitating the bolts to withstand increased loads. Conversely, the maximum equivalent stress evolution trend on the compression side of the lower steel tube is opposed to that of the B3 bolt.
4. The maximum equivalent strain at the B3 bolt initially increases and then decreases with the increasing axial force, while on the compression side of the lower steel tube, it consistently increases. The equivalent strain at the B3 bolt in three of the five specimens exceeds that on the compression side of the lower steel tube, suggesting a higher failure risk at the bolts, which aligns with observed bolt loosening in the experiments. When the axial pressure is 800 kN, the compression side of the lower steel tube may fail earlier due to the high axial pressure. When the axial pressure is 400kN, this discrepancy may be attributed to the simplification of bolt modeling and the selection of the standard friction coefficient values.
5. The mechanical properties of the joint fluctuate with increasing tube wall thickness, peaking at 10 mm, which optimally balances the mechanical properties and economic cost. The bearing capacity of the joint decreases with increasing outer diameters of flange-A and flange-B. Considering both the mechanical performance and the financial cost of the joint, selecting a flange with an outer diameter of 252 mm is recommended.

The findings in this study indicate the influence of various factors and parameters, such as bolt connection, axial force, flange thickness, wall thickness of the circular tube, and flange diameter, on the bearing and rotation capacities of the joint. Understanding these relationships should be beneficial to designing and optimizing the joint for the desired performance. Although this paper has made efforts to study the joint of the automated construction device, there are still some shortcomings that need to be addressed. Future research could focus on exploring the mechanical response of the joint under dynamic loads or investigating the mechanical properties of the joint when utilizing new materials. Such studies will provide a deeper understanding of joint performance and durability, potentially leading to further improvements in the design and functionality of automated construction systems.

Acknowledgments

The authors gratefully acknowledge the financial support provided by the National Key R&D Program of China (2022YFE0109300), Shenzhen Natural Science Foundation (JCYJ20240813141827036), Shenzhen Housing and Construction Bureau - Science and Technology Program in Engineering Construction Field (2021-R&D), Guangdong Provincial Key Laboratory of Durability for Marine Civil Engineering (2020B1212060074), and Shenzhen Key Laboratory for Low-carbon Construction Material and Technology (ZDSYS20220606100406016).

References

- [1] Elkhaila A., "The magnitude of barriers facing the development of the construction and building materials industries in developing countries, with special reference to Sudan in Africa", *Habitat International*, 2016, Vol. 54, PP. 189-198.
- [2] Jiang, Z.Y., Sun, X.P., Luo, Y.Q., Fu, X.L., Xu, A. and Bi, Y.Z., "Recycling, reusing and environmental safety of industrial by-product gypsum in construction and building materials", *Construction and Building Materials*, 2024, Vol. 432.
- [3] Senthamizh, S.S., Anandh, K.S., "Navigating leadership styles through qualitative exploration for enhanced safety in the construction sector", *Safety Science*, 2024, Vol. 175.
- [4] Zhang, M., Shi, R. and Yang, Z., "A critical review of vision-based occupational health and safety monitoring of construction site workers", *Safety Science*, 2020, Vol. 126.
- [5] Zhao, X., Jin, Y., Selvaraj, N.M., Ilyas, M. and Cheah, C.C., "Platform-independent visual installation progress monitoring for construction automation", *Automation in Construction*, 2023, Vol. 154.
- [6] Zhang, M., Xu, R., Wu, H., Pan, J. and Luo, X., "Human-robot collaboration for on-site construction", *Automation in Construction*, 2023, Vol. 150.
- [7] Xiao, B., Chen, C. and Yin, X., "Recent advancements of robotics in construction", *Automation in Construction*, 2022, Vol. 144.
- [8] Oke, A.E., Aliu, J., Oluwasefunmi, F.P., Akanni, P.O. and Stephen, S.S., "Attaining digital transformation in construction: An appraisal of the awareness and usage of automation techniques", *Journal of Building Engineering*, 2023, Vol. 67.
- [9] Bogue, R., "What are the prospects for robots in the construction industry?", *Industrial Robot-An International Journal*, 2018, Vol. 45, PP. 1-6.
- [10] Rosa, M., Cury, J.E.R. and Baldissera, F.L., "Supervisory Control in Construction Robotics: in the Quest for Scalability and Permissiveness", *IFAC-PapersOnLine*, 2020, Vol. 53, PP. 117-122.
- [11] Gharbia, M., Chang, R.A., Lu, Y., Zhong, R.Y. and Li, H., "Robotic technologies for on-site building construction: A systematic review", *Journal of Building Engineering*, 2020, Vol. 32.
- [12] Yu, Y., "What is Aerial Building Mechaine?", *Hoisting Conveying Mach*, 2017, Vol. 2017, PP. 39.
- [13] Wakisaka, T., Furuya, N., Inoue, Y. and Shiokawa, T., "Automated construction system for high-rise reinforced concrete buildings", *Automation in Construction*, 2000, Vol. 9, PP. 229-250.
- [14] Pan, C.L., Chen, S.M., Wang, G.F., Zhang, D.D. and Wei, X.H., "Construction technology of building structure under construction condition of integrated platform of Shenyang Baoneng Global Financial Center", *Construction Technology*, 2017, Vol. 46, PP. 18-20.
- [15] Li, T.Z., "A new path for prefabricated construction—Aerial Building Mechaine", *Construction Architecture*, 2016, Vol. 22, PP. 43-44.
- [16] Kudoh, R., "Implementation of an Automated Building Construction System", in *Proc of 13th International CIB World Building Congress*, Amsterdam, 1995.
- [17] Dong, S.B., "Research on cast-in-situ prefabricated construction technology of Aerial Building Machine", *Urban Architecture Space*, 2017, Vol. 24, PP. 55-59.
- [18] Pan, C.L., Quan, W.B., Zhang, W.S., Wang, G.F. and Chen, M.S., "Integrated platform technology for construction equipment of super high-rise building", *Construction Technology*, 2017, Vol. 46, PP. 1-4.
- [19] Yin, L., Niu, Y., Quan, G., Gao, H. and Ye, J., "Development of new types of bolted joints for cold-formed steel moment frame buildings", *Journal of Building Engineering*, 2022, Vol. 50.
- [20] Wei, J.P., Tian, L.M., Guo, Y., Qiao, H.Y., Bao, Y., Jiao, Z.A. and et al., "Numerical study of the seismic performance of a double-hinge steel frame joint", *Journal of Constructional Steel Research*, 2021, Vol. 187.
- [21] Wang, H., Zhang, B., Qian, H., Liu, J., An, B. and Fan, F., "Experimental and numerical studies of a new prefabricated steel frame joint without field-welding: Design and static performance", *Thin-Walled Structures*, 2021, Vol. 159.
- [22] Gao, J.D., Du, X.X., Yuan, H.X. and Theofanous, M., "Hysteretic performance of stainless steel double extended end-plate beam-to-column joints subject to cyclic loading", *Thin-Walled Structures*, 2021, Vol. 164.
- [23] Chen, Z., Niu, X., Liu, J., Khan, K. and Liu, Y., "Seismic study on an innovative fully-bolted beam-column joint in prefabricated modular steel buildings", *Engineering Structures*, 2021, Vol. 234.
- [24] Ma, Y., Qi, A., Yan, G., Zheng, L., Xue, P. and Wang, F., "Experimental study on seismic performance of novel fabricated T-joint with replaceable steel hinges", *Structures*, 2022, Vol. 40, PP. 667-678.
- [25] Yan, X.Z., Zhe, W.H., Yang, L.L., Bo, W.J., Xiao, T.C. and Meng, Y.C., "Experimental and

- numerical investigation of prefabricated prestressed vertical steel strand core tube flange column connection joint", *Journal of Constructional Steel Research*, 2022, Vol. 190, PP. 107-124.
- [26] Fan, J., Yang, L., Wang, Y. and Ban, H., "Research on seismic behaviour of square steel tubular columns with deconstructable splice joints", *Journal of Constructional Steel Research*, 2022, Vol. 191.
- [27] Havula, J., Garifullin, M., Heinisuo, M., Mela, K. and Pajunen, S., "Moment-rotation behavior of welded tubular high strength steel T joint", *Engineering Structures*, 2018, Vol. 172, PP. 523-537.
- [28] GB/T8162-2018, "Seamless steel tubes for structural purposes", China. Beijing, Architecture & Building Press, 2018.
- [29] GB/T1591-2018, "High strength low alloy structural steels", China. Beijing, Architecture & Building Press, 2018.
- [30] Mou, B., Yan, X., Yu, Y. and Wang, Z., "Composite CFST column to H-shaped steel beam joint: Experimental and numerical investigation", *Engineering Structures*, 2024, Vol. 299.
- [31] Li, Q., Xu, C., Luo, Z., Huang, F., An, Y., Zhang, D. and et al., "Experiment and design methodology of an IODR flange connection under bending load", *Journal of Constructional Steel Research*, 2023, Vol. 201, PP. 107-144.
- [32] Fidalgo, A. and Packer, J.A., "Evaluation of bolted CHS flange-plate connections under axial tension", *Journal of Constructional Steel Research*, 2022, Vol. 196.
- [33] Aydemir, C., Eser, A.M. and Arslan, G., "Seismic performance of RC columns under combined cyclic flexural and constant axial loadings", *Structures*, 2023, Vol. 54, PP. 196-208.
- [34] Higgoda, T.M., Elchalakani, M., Kimiaci, M. and Guo, X., "Experimental and numerical investigation of bolted steel endplate with bonded sleeve end connections for pultruded GFRP circular tubular hollow beams", *Thin-Walled Structures*, 2023, Vol. 192, PP. 111-133.
- [35] Longo, A., Montuori, R. and Piluso, V., "Seismic reliability of chevron braced frames with innovative concept of bracing members", *Advanced Steel Construction*, 2009, Vol. 5, PP. 367-389.
- [36] Jiang, Z.Q., Yan, T., Zhang, A.L., Yang, X.F., Yu, C. and Li, R., "Experimental study of plate-buckling type earthquake-resilient prefabricated steel beam-column joints with replaceable double flange cover plates", *Structures*, 2023, Vol. 50, PP. 110-113.
- [37] Kashan, K. and Yan, J.B., "Numerical studies on the seismic behaviour of a prefabricated multi-storey modular steel building with new-type bolted joints", *Advanced Steel Construction*, 2021, Vol. 17, PP. 1-9.
- [38] Sorace, S. and Terenzi, G., "Fluid viscous damper-based seismic retrofit strategies of steel structures: General concepts and design applications", *Advanced Steel Construction*, 2009, Vol. 5, PP. 325-342.
- [39] Wang, H., Zhang, B., Qian, H., Liu, J., An, B. and Fan, F., "Experimental and numerical studies of a new prefabricated steel frame joint without field-welding: Design and static performance", *Thin-Walled Structures*, 2021, Vol. 159.
- [40] Qin, Y., Chen, Z., Wang, X. and Zhou, T., "Seismic behavior of through-diaphragm connections between CFRT columns and steel beams-experimental study", *Advanced Steel Construction*, 2014, Vol. 10, PP. 351-371.
- [41] Zhang, C. and Su, M., "Bearing capacity of bolted longitudinal seams of corrugated steel structures under compression", *Journal of Constructional Steel Research*, 2024, Vol. 213.
- [42] Chen, Z., Qin, Y. and Wang, X., "Development of connections to concrete-filled rectangular tubular columns", *Advanced Steel Construction*, 2015, Vol. 11, PP. 408-426.
- [43] GB/T1231-2006, "Specifications of high strength bolts with large hexagon head, large hexagon nuts, plain washers for steel structures", China. Beijing, Architecture & Building Press, 2006.
- [44] Peng, F., Han, L.Q. and Lie, P.Y., "Discussion and definition on yield points of materials, members and structures", *Engineering Mechanics*, 2017, Vol. 34, PP. 36-46.